Development of 3D Printed Biomimetic Bilayer Scaffold for Osteochondral Tissue Engineering and Reconstructive Surgery

Fiona Verisqa

DDS, MClinDent (Oral and Maxillofacial Surgery)

Thesis submitted to UCL in partial fulfilment of the requirements for the degree of

Doctor of Philosophy.

Division of Biomaterials and Tissue Engineering

Eastman Dental Institute

UCL

2023

Declaration

I, Fiona Verisqa, confirm that the work presented in this thesis is my own. Where information has been derived from other sources, I confirm that the thesis has indicated this.

SIGN

DATE

And He found you lost and guided you.

QS 93: 7

Acknowledgements

Alhamdulillah Rabbil'Alamin

This PhD journey has been an amazing experience for me, and it would not have been possible without the support of people who showed me the way, companions who walked beside me and those who always had my back. I would like to take this opportunity to express my immense gratitude to them.

I am deeply grateful to my primary supervisor, Prof. Jonathan Campbell Knowles, for the opportunity to pursue a doctoral degree at UCL and for his unwavering guidance, supervision, and encouragement throughout the entire journey of this PhD. Insights and constructive feedback from him have been instrumental in shaping this thesis.

I extend my appreciation to my secondary supervisor, Dr. Linh Nguyen, for her valuable perspective and support. Her expertise and thoughtful input have significantly enriched the depth and quality of this work.

My acknowledgement also goes to EDI BTE academic lecturers Dr. David Chau, Dr. Alessandro Poma, and Prof. Anne Young for their valuable insights and assistance that played a role in elevating the quality of this thesis.

My gratitude extends to the EDI BTE lab technicians, Dr Graham Palmer, Dr. George Giorgiu, Dr Nicola Mordan, Dr. Georgia McDonald, and Dr. Isabel Kingston, whose technical expertise and assistance played a pivotal role in conducting experiments and collecting data. Their tireless efforts behind the scenes have contributed to the foundation of this thesis.

I would like to acknowledge our esteemed collaborators, Prof. Haewon Kim, Dr. Nandin Mandakhbayar, Dr. Jeonghui Park, Dr. Seongjin Shin and the

ITREN team at Dankook University, South Korea for conducting the in vivo studies. This partnership added a valuable dimension to my research.

To my fellow BTE PhD students and alums, especially Nik Alia Syahirah, Mohammad Al Jaber, and Lady Barios Silva, your camaraderie and stimulating discussions have been both motivating and enlightening. PhD can be a lonely journey, but the friendships made during the four years made me feel not alone.

I am profoundly thankful for my husband's unwavering support and understanding, Imaduddin Abdullah, a fellow PhD student. I could not ask for a better partner in this academic journey, life, and beyond. Your constant companionship and encouragement have been my pillars of strength. I am forever grateful to you.

To my precious son, Thariq, your innocent laughter and unconditional love provided solace and inspiration during the challenging phases of this academic pursuit. I hope my journey can make you believe you can achieve your dreams, and I hope I can make you proud.

My heartfelt appreciation goes to my parents, my parents-in-law, and my family in Indonesia. Their love and support have been my source of determination from the beginning.

A special thanks to my cherished friends who were there for the high and low. Our friendship, meme-sharing, and occasional study breaks provided a much-needed balance to my PhD journey.

Finally, I sincerely thank LPDP – Ministry of Finance of the Republic of Indonesia for the invaluable support in funding my PhD. Their belief in my potential has been instrumental in making this endeavour possible.

Publications

Peer-Reviewed Publications

Patel, K.D., Padalhin, A.R., Franco, R.A.G., **Verisqa, F**., Kim, H.W. and Nguyen, L., 2021. Basic concepts and fundamental insights into electrospinning. In *Biomedical Applications of Electrospinning and Electrospraying* (pp. 3-43). Woodhead Publishing.

Verisqa, F., Cha, J.R., Nguyen, L., Kim, H.W. and Knowles, J.C., 2022. Digital Light Processing 3D Printing of Gyroid Scaffold with Isosorbide-Based Photopolymer for Bone Tissue Engineering. *Biomolecules*, *12*(11), p.1692.

Aljaber, M.B., **Verisqa, F.**, Keskin-Erdogan, Z., Patel, K.D., Chau, D.Y. and Knowles, J.C., 2023. Influence of Gelatin Source and Bloom Number on Gelatin Methacryloyl Hydrogels Mechanical and Biological Properties for Muscle Regeneration. *Biomolecules*, *13*(5), p.811

Conference Proceedings (Oral Presentations)

- **Verisqa, F**., Cha, J. – R., Linh, N., Knowles, J., & Kim, H. -. W. (2023). High-Resolution Gyroid Bone Scaffold Manufactured via Digital Light Processing 3D Printing. Presented at: Tissue Engineering and Regenerative Medicine International Society European Chapter Conference (TERMIS-EU).
- **Verisqa, F**., Knowles, J., Linh, N., & Kim, H. -. W. (2022). 3D printed isosorbide-based polymer and gelatin methacrylate bilayer scaffold for osteochondral tissue engineering. Presented at: Tissue Engineering and Regenerative Medicine International Society Asia Pacific Chapter Conference (TERMIS-AP).
- **Verisqa, F.**, Linh, N., & Knowles, J. (2022). 3D Printed Osteogenic Scaffold for Cleft and Craniofacial Defect Reconstruction. Presented at 14th International Congress of Cleft Lip, Palate & Related Craniofacial Anomalies.

- **Verisqa, F.**, Linh, N., Kim, H. -. W., & Knowles, J. (2022). Optimisation of 3D printable GelMA for temporomandibular joint cartilage regeneration. Presented at Face Ahead AOCMF.

Funding and Prizes

PhD funding – Indonesia Endowment Funds for Education (LPDP), Ministry of Finance, Republic of Indonesia (2019-2023)

3MT Competition Winner of UCL Faculty of Medical Sciences 10th annual Dean's Research Prize (2022)

3MT Competition Winner of UCL Eastman Dental Institute Research Away Day (2022)

Postgraduate Research Presentation Winner of UCL Faculty of Medical Sciences 11th annual Dean's Research Prize (2023)

Editor's Choice Article of Biomolecules Journal (2023)

Abstract

Introduction: An osteochondral defect requires a tissue-mimicking scaffold due to the bone and cartilage layers' structural, physiological, and functional differences. This study aimed to develop a biomimetic bilayer scaffold by combining 3D-printed isosorbide-based novel CSMA-2 polymer and gelatin methacrylate (GelMA).

Methods: The osseous layer was fabricated by 3D printing CSMA-2 polymer with different hydroxyapatite (HA) filler concentrations using the Digital Light Processing (DLP) method. The gyroid structure was chosen due to its unique physical and mechanical properties. GelMA with optimised concentrations was prepared and light-cured on top of the 3D-printed CSMA-2 scaffold to create the chondral layer. Both material and solid scaffold characterisation were conducted to evaluate their chemical, mechanical, and rheological properties. In-vitro and in-vivo studies were performed to analyse the scaffold's biocompatibility.

Results: Each scaffold layer demonstrated similar mechanical properties to native cancellous bone and cartilage tissue. The co-culture of MC3T3-E1 and ATDC5 cells on the bilayer scaffold showed the cells resided on their designated layers. The bilayer scaffolds maintained their structural integrity during the long-term dynamic cell culture period in a perfusion bioreactor. CSMA-2 layer and GelMA layer were able to support human adipose-derived stem cell (hADSC) osteogenic and chondrogenic differentiation. The in vivo result showed good biocompatibility, new bone growth, and satisfactory angiogenic properties of the scaffolds.

Discussion and Conclusions: The combination of 3D printed CSMA-2 and GelMA biomimetic bilayer scaffolds created the cartilage and bone tissue-specific environment. The bilayer scaffolds supported the growth of progenitor cells in a co-culture system and promoted stem cells' chondrogenic and osteogenic differentiation. It also had good mechanical properties and showed the potential to maintain its structural integrity during surgical implantation and integration with the recipient site.

Impact Statement

Osteochondral diseases such as osteoarthritis affect more than 8 million people in their productive age in the UK (NICE, 2017). These lesions have limited self-healing capacity, and larger defects often require interventional treatment, such as osteochondral allograft transplantation (Sherman *et al.*, 2014). This thesis addresses clinical challenges associated with the current treatment of osteochondral defects. The challenges include tissue availability, risk of disease transmission, graft-to-recipient size matching and reduced tissue viability due to the harvesting-to-transplantation interval. Thus, developing a biomimetic bilayer 3D printed scaffold offers a potential treatment option to benefit the research community and broader society.

The combination of novel and commercial biomaterials allows the scaffolds to imitate the natural structure of the joint and provide a suitable environment for bone and cartilage cells that facilitate cell proliferation and differentiation. The isosorbide-based CSMA-2 polymer also provides a sustainable alternative to petroleum-based materials, whilst GelMA offers excellent tunability. In addition, the structural integrity observed in the composite GelMA/CSMA-2 scaffolds during the long-term cell culture can propose a relatively straightforward method of combining different materials with different physical properties to fabricate a gradient structure. The findings in this thesis can enhance our understanding of osteochondral tissue engineering. They may pave the way for further innovations and applications in diverse fields such as organ transplantation and wound healing.

The scaffold can be tailored to accurately match the individual's anatomical requirement through a patient-specific and customisable design process enabled by 3D printing. The possibility of incorporating patient-derived

cells through the preconditioning process further enhances tissue compatibility, reducing the risk of rejection and post-surgical complications. With the biocompatibility shown by the scaffolds, the joint function can be restored and ultimately extend the joint longevity.

The 3D-printed biomimetic bilayer osteochondral scaffolds can considerably reduce the burden on healthcare systems. Around one thousand people are diagnosed with joint disease daily (NICE, 2017). This condition might require costly joint replacement surgeries that need to be followed by extensive rehabilitation. By offering a less invasive approach and delaying the need for joint replacement, the synthetic scaffold can reduce hospital stay, rehabilitation periods, and subsequent medical expenses, easing the strain on healthcare resources.

Therefore, by combining innovative technologies and patient-centric approaches, this thesis can contribute to improving treatments in orthopaedic and related fields, offer better patient outcomes, reduce the healthcare burden, and expand scientific knowledge.

Index of Abbreviations

β-TCP	Beta-tricalcium phosphate
ACAN	Aggrecan
ACI	Autologous chondrocyte implantation
AD-MSC	Adipose-derived mesenchymal stem cells
Akt Or PKB	Protein kinase B
ALP	Alkaline phosphatase
ANKRD1	Ankyrin repeat domain 1
BAPO	Bis(2,4,6-trimethylbenzoyl) phenylphosphine oxide
BAPO	Phenylbis(2,4,6-trimethyl benzoyl)phosphine oxide
BHIS	Bis(2-hydroxyethyl) isosorbide)
BM-MSC	Bone marrow mesenchymal stem cells
BMP	Bone morphogenetic protein
BS	Bone surface
BSA	Bovine serum albumin
BSD	Bone surface density
Bsp	Bone sialoprotein
BV	Bone volume
BV	Blood vessels
Ca	Calcium
CAD	Computer-aided design
CAM	Chicken *egg* chorioallantoic membrane
cDNA	Complementary Deoxyribonucleic acid
Col I	Collagen I
Col X	Collagen X
CQ	Camphorquinone
CSMA-2	((3R,3ar,6S, 6ar) - hexahydrofuro[3,2-b] furan-3,6-diyl)bis(oxy)) bis(ethane-2,1-diyl))bis(oxy))bis(carbonyl))bis(azan ediyl))bis(3,3,5 - trimethylcyclohexane - 5,1-diyl))bis (azanediyl))bis(carbonyl))bis(oxy))bis(ethane - 2, 1 - diyl) bis(2-methylacrylate)).
DAPI	4′,6-diamidino-2-phenylindole
DBTBL	Dibutyltin dilaurate

DLP	Digital light processing
Dlx5	Distal-less homeobox
DoF	Degree of functionalisation
EB	Extrusion based
ECM	Extracellular matrix
eNOS	Endothelial nitric oxide synthase
EO	Ethylene oxide
EPC	Endothelial progenitor cells
ERK	Extracellular *signal*-Regulated Kinase
FAK	Focal adhesion kinases
FBS	Fetal bovine serum
FDA	Food and Drug Administration
FDM	Fused deposition modelling
FTIR	Fourier transform infrared spectroscopy
GAG	Glycosaminoglycan
GAPDH	Glyceraldehyde 3-phosphate dehydrogenase
GelMA	Gelatin methacrylate
Gla	Bone γ-carboxyglutamic acid
HA	Hydroxyapatite
hADSC	Human adipose-derived stem cells
HE	Hematoxylin and Eosin
HEMA	2-hydroxyethyl methacrylate
HUVEC	Human umbilical vein endothelial cells
ICRS	International cartilage repair society
IPDI	Isophorone diisocyanate
ISDN	Isosorbide dinitrate
ISMN	Isosorbide mononitrate
I-WP	I-graph-wrapped package
LAP	Lithium phenyl(2,4,6-trimethylbenzoyl)- phosphinate
Micro-CT	Micro computed tomography
MRI	Magnetic resonance imaging
MSC	Mesenchymal stem cells
Msx2	Homeobox homologue-2
MT	Masson’s trichrome
NFATc1	Nuclear Factor of Activated T Cells 1

NMR	Nuclear magnetic resonance
OA	Osteoarthritis
OAT	Osteochondral autograft transfer
OCA	Osteochondral allograft
OCN	Osteocalcin
OPN	Osteopontin
Osx	Osterix
P	Phosphate
P/S	Penicillin/streptomycin
PBS	Phosphate buffered saline
PCL	Polycaprolactone
PEG	Polyethene glycol
PEGDA	Polyethylene glycol diacrylate
PG	Proteoglycans
PI3K	Phosphoinositide-3-kinase
PISEB	Poly(isosorbide sebacate)
PLA	Polylactic acid
PLA	Polylactic acid
PLGA	Poly(lactic-co-glycolic acid
PPF	Poly(propylene fumarate)
RAS	Rat sarcoma
RGD	*Arginine*–glycine–aspartic acid
RhoA	Ras homolog family member A
RNA	Ribonucleic acid
ROCK	Rho-associated kinase
RT-qPCR	Real-time quantitative polymerase chain reaction
RUNX2	Runt-related transcription factor-2
SD	Sprague-dawley
SEM	Scanning electron microscopy
SER-THR	*Serine/threonine*
SLA	Stereolithography
SMAD	Suppressor of Mothers against Decapentaplegic
SOX9	SRY-box transcription factor 9
TAZ	Transcriptional coactivator with PDZ-binding motif
TEAD	Transcriptional enhancer factor domain

TEGDMA	Triethylene glycol dimethacrylate
TGF-β	Transforming growth factor β
TPMS	Triply periodic minimal surface
TV	Tissue volume
UC-MSC	Umblical cord mesenchymal stem cells
UV	Ultraviolet
VEGF	Vascular endothelial growth factor
YAP	Yes-associated protein
α MEM	α modified Eagle's medium

Table of Contents

Index of Figures

Index of Tables

Chapter 1. Introduction

1.1. Literature Review

1.1.1. Osteochondral Unit

Human joints have complex structures that connect adjacent bones to allow smooth joint motion. The joint consists of articular cartilage that covers the subchondral bone, synovial lining, ligaments, and tendons. The composite structure formed by articular cartilage and subchondral bone is known as the osteochondral unit (Goldring and Goldring, 2016). This unit can transfer loads during weight-bearing and joint motion. Changes in the structure or composition of the osteochondral unit result in disrupted joint integrity and motion.

1.1.1.1. Osteochondral Unit: Cartilage

Cartilage comprises chondrocytes in the lacunae of the extracellular matrix (ECM) they produce (van Dijk *et al.*, 2010). This cartilaginous matrix contains collagen, proteoglycan, hyaluronic acid and glycoprotein. The electrostatic connection between collagen fibres and the glycosaminoglycan (GAG) contributes to the elastic properties of the cartilage, along with the water content resulting from the negative GAG and the flexibility of the collagen fibres (Sophia Fox, Bedi and Rodeo, 2009). The elasticity of cartilage provides the ability to resist compressive forces. Cartilage is avascular, and the intra-articular fluid provides its nutrition. The lack of vascularisation and direct nourishment contributes to the slow regeneration of cartilage. The joint's articular cartilage has various zones: superficial, middle, deep, and calcified (figure 1.1).

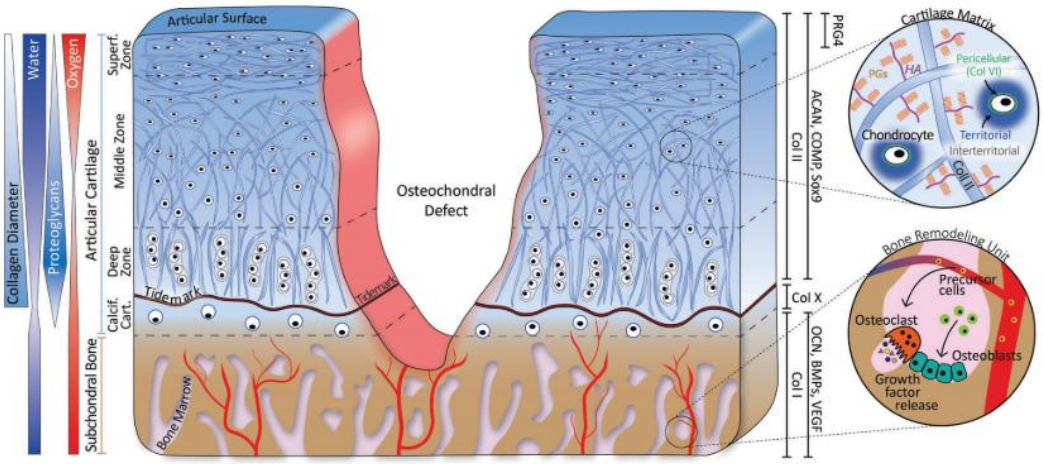

Figure 1. 1. Schematic cross-sectional image of ICRS grade IV osteochondral defect.

Regions of the osteochondral unit are presented on the left, along with the composition of water, proteoglycans, and oxygen. The common osteogenic and chondrogenic markers are shown on the left. The circles are magnified images of cartilage and bone tissue. Source: (Lesage et al.*, 2022).*

1.1.1.1.1. Cartilage Zone

The superficial zone protects the deeper layer from shear stress by resisting the shear, tensile, and compressive forces from articulation. It comprises tightly packed, parallel-aligned collagen fibres (mainly type II and IX)(Sophia Fox, Bedi and Rodeo, 2009). This layer also contains flattened chondrocytes. The superficial zone represents 10 – 20% of articular cartilage volume.

The middle zone of the cartilage acts as a transition zone between the superficial and deep zones (Sophia Fox, Bedi and Rodeo, 2009). It represents 40 – 60% of articular cartilage's total volume and contains proteoglycans (PG). The collagen in this layer is oblique to the articular surface, and the chondrocytes are spherical.

The deep zone provides significant resistance to compressive forces since the collagen in this layer is organised perpendicular to the surface of the articular cartilage (Doyle *et al.*, 2021). It contains the largest collagen fibres, the highest proteoglycan percentage, and the lowest water content. The chondrocytes are in

a columnar arrangement. This zone represents approximately 30% of the articular cartilage's total volume.

The calcified zone secures the cartilage to the bone by anchoring the deep zone's collagen fibrils to the subchondral zone (Sophia Fox, Bedi and Rodeo, 2009). The chondrocytes in this zone are hypertrophic. The zone has a tidemark, a line that separates the calcified from the uncalcified cartilage. Calcified cartilage also serves as a physical barrier between bone and cartilage to prevent blood vessel invasion from the subchondral bone, bringing osteogenic signals for ossification (Lesage *et al.*, 2022).

1.1.1.1.2. Cartilage Components

The chondrocyte is the only cell that resides in the cartilage. It originates from mesenchymal stem cells and represents 2% of the articular cartilage's total volume. They vary in shape, size, and number, depending on the zones of the articular cartilage. Chondrocytes' potential for replication is limited, contributing to the limited intrinsic healing capacity of the cartilage defect (Naujoks et al., 2008; Onderková and M. Kalaskar, 2023).

Water contributes up to 80% of cartilage's wet weight. The water flow through the cartilage zones allows the transport and distribution of nutrients to the chondrocytes and provides lubrication. Meanwhile, collagen makes up about 60% of the cartilage's dry weight. Collagen is the most abundant macromolecule in the ECM, and type II collagen represents 90 – 95% of ECM collagen(Sophia Fox, Bedi and Rodeo, 2009).

The second largest macromolecules in the ECM are proteoglycans, with aggrecan as the most abundant and the largest. Aggrecan provides osmotic properties to the cartilage, contributing to compressive load resistance due to its

anionic nature (Lesage *et al.*, 2022). The hydrostatic pressure accumulates in the deep cartilage region.

Unlike the rest of the cartilage regions, calcified cartilage consists of Collagen X (Col X) and calcium phosphate crystals. This different composition makes the calcified cartilage zone stiffer than non-calcified cartilage zones but still softer than the subchondral bone beneath. This gradient of mechanical properties allows a stress-reducing mechanism at the interface of the osteochondral unit (Lesage *et al.*, 2022). In addition to the chondrocyte's limited proliferative ability, Collagen II, with a half-life of 117 years, also contributes to the limited regenerative properties of the cartilage (Lesage *et al.*, 2022).

Articular cartilage has unique viscoelastic properties. It provides a lubricated smooth surface for articulation with low friction and facilitates load transmission to the subchondral bone. It can withstand high cyclic loads with insignificant degenerative change. During joint loading, the interstitial fluid pressure of the cartilage increases and causes the fluid to flow out from the ECM. When the load is removed, the fluid returns to the ECM.

Hydrostatic pressure has been identified as one of cartilage's most important mechanical stimuli. It provides signals for normal articular cartilage homeostasis and chondroprotective effects from inflammatory stimulus for chondrocytes (Tamaddon *et al.*, 2018). Joint cartilage is typically exposed to forces between 3 – 10 MPa, with the highest stress recorded in the hip joint (Tamaddon *et al.*, 2018). Different bodily movements also expose the articular cartilage to various mechanical loads, ranging from lower loads of walking to higher loads of running or jumping. More than 90% of the applied joint load is supported by interstitial water content.

The ageing process can affect the composition of ECM, the distribution of chondrocytes within the zones, and their response to external factors (Sophia Fox, Bedi and Rodeo, 2009). Hydration of the matrix decreases as age increases. Lower water content in the cartilage then increases compressive stiffness, which causes a reduced ability to withstand deformation.

1.1.1.2. The Osteochondral Unit: Bone

1.1.1.2.1. Bone anatomy

Bone comprises compact and trabecular bone. Compact or cortical bone is in direct contact with the periosteum and acts as the primary weight-bearing structure of the skeleton. It makes up approximately 80% of skeletal mass. These cortical bones are made from the aggregation of osteons, their multicellular unit. Osteon or haversian systems consist of a central or haversian canal surrounded by concentric rings or lamellae of the matrix. The bone cells or osteocytes reside in spaces called lacunae. Small channels called canaliculi radiate from the lacunae to provide pathways through the hard matrix. Unlike cartilage, bone is vascularised with blood vessels in the Haversian canals. Cortical bones contain microscopic pores to allow vascularisation (Fuchs, Warden and Turner, 2009). Their bone porosity depends on the anatomical site, age, exposure to injury, diseases, and pharmacological interventions. On average, compact bones demonstrate approximately 10% porosity.

On the other hand, trabecular bones have high porosity, ranging from 50% to 90% of trabecular bone volume. Trabecular or cancellous bone also contains osteocytes in lacunae, found in a lattice-like pattern called trabeculae. The trabeculae are strategically placed along the lines of stress to add strength to the bone by directing force to the more solid, compact bone. The spongious structure of the trabecular bone makes the bone lighter and easier to move by muscles.

The space of some spongious bone also contains red bone marrow and serves as a site for haematopoiesis. The detailed bone structure can be seen in figure 1.2.

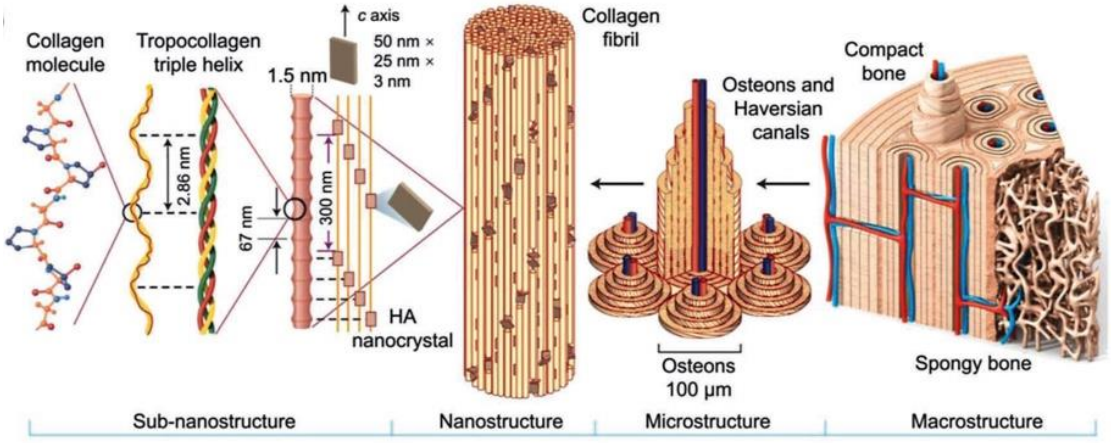

Figure 1. 2. The structural organisation of bone.

The sub-nano structure comprises collagen and HA, which form the collagen fibrils that build the osteon unit. The trabecular or spongy bone shows a porous macrostructure, and the cortical bone has a laminated compact structure macroscopically. Source: (Wang et al.*, 2022)*

Bones are covered by endosteum and periosteum for their inner and outer surfaces, respectively (Fuchs, Warden and Turner, 2009). The outer layers of the periosteum comprise collagen and elastin fibres, fibroblasts, and nerve and microvascular networks. The inner layer of the periosteum contains mesenchymal stem cells with osteogenic and chondrogenic differentiation potential. The endosteum is lined with mature osteoblasts that form a membrane to enclose the bone marrow. Osteoclasts can be present in the endosteum of the active bone resorption region.

The joint's subchondral bone is located beneath the calcified cartilage zone. It has cortical plates and cancellous bone. The bone in the cortical plate merges into the cancellous bone, which is more metabolically active than the cortical bone (Goldring and Goldring, 2016). The trabeculae of the cancellous bone have different orientations depending on their location. The dependency of bone structure on the local mechanical environment follows Wolff's hypothesis,

which is also applied to subchondral bone (Goldring and Goldring, 2016). Wolff's hypothesis states that the direction and magnitude of the force applied to the subchondral bone determine its intrinsic architecture and the bone adapts to the force through the cell-controlled remodelling process (Goldring and Goldring, 2016). This remodelling process involves bone resorption mediated by osteoclast and bone formation by osteoblast. The process provides a replacement mechanism for damaged bone. It enables bone adaption in response to local mediators, systemic hormones, and biomechanical factors. Bone formation is initiated by osteoid deposition, an organic bone matrix that undergoes rapid mineralisation and a slow mineral accretion phase (Goldring and Goldring, 2016).

Due to vascularisation, subchondral bone attenuates the load forces and metabolic exchange between the bone and the calcified cartilage region (Lesage *et al.*, 2022). Soluble nutrients are also transferred from the underlying subchondral bone, especially to the deeper layers of the cartilage (Goldring and Goldring, 2016). It also has stem cells in the bone marrow that serve as a reservoir for progenitor cells. Subchondral bone is also innervated by sensory neurons, providing nociception (Jacob, Shimomura and Nakamura, 2020).

1.1.1.2.2. Bone Composition

Bone matrices comprise organic and inorganic components. Most organic matrix is collagen, with more than 90% being type I collagen (Col I) (Lin *et al.*, 2020). Collagen contributes to bone flexibility and resilience, whereas minerals provide stiffness to the bone. The porous structure created by the Col I fibrils arrangement also contributes to the bone yield strength (Lesage *et al.*, 2022). The rest of the organic bone matrix are fibronectin, osteopontin (OPN), osteocalcin (OCN), bone sialoprotein (Bsp), and proteoglycans. These non-

collagenous proteins play essential roles during cell adhesion, osteoblast differentiation, tissue mineralisation, and bone remodelling (Lin *et al.*, 2020). The inorganic matrix serves as a reservoir of calcium, phosphorus, sodium, and magnesium ions. The crystalline structures formed by these ions provide stiffness to the bone. Most of these crystals are in the form of calcium hydroxyapatite (Nguyen *et al.*, 2022).

Bone-forming cells or osteoblast development begins with the local proliferation of mesenchymal stem cells (MSC) in the bone marrow and periosteum. Runt-related transcription factor-2 (RUNX2), distal-less homeobox-5 (Dlx5) and homeobox homologue-2 (Msx2) expression are required to shift the progenitor cells to the osteoblast lineage. After the MSC is committed to the osteoblast lineage, the preosteoblast expresses Col I and Bsp. The differentiation of preosteoblast into osteoblast requires the expression of RUNX2, components of the Wnt signalling pathway, and osterix (Osx). The mature osteoblast expresses Col I, OCN, and alkaline phosphatase (ALP). Osteoblasts become osteocytes by incorporating themselves into the unmineralised matrix. As the matrix mineralises, the osteocytes mature, express a new set of genes, and occupy the lacunae. Osteocytes have been reported as the sensor for mechanical stimuli in the bone and can regulate mineral metabolism (Polo-Corrales, Latorre-Esteves and Ramirez-Vick, 2014).

1.1.2. Osteochondral Defects and Treatments

An osteochondral defect is a lesion involving articular cartilage and the subchondral bone (figure 1.1)(van Dijk *et al.*, 2010). It is mainly caused by trauma to the joint. However, repetitive, excessive loading and diseases can also alter the structure of osteochondral tissue, resulting in severe defects. According to the International Cartilage Repair Society (ICRS) classification, cartilage defects vary from mild structural change, as in grade I, to severely abnormal damage involving both cartilage and the subchondral bone, or grade IV. Grade IV or osteochondral defects can cause debilitating pain and functional impairment.

Osteoarthritis (OA) is the most common type of joint disease that involves the cartilage and the bone. The condition occurs due to the imbalance between joint tissue damage and repair (Litwic *et al.*, 2013). OA can develop anywhere but mainly affects the knees, hands, hips, feet, and facet joints. OA lesions on weight-bearing joints often lead to reduced physical functions and disabilities that interfere with daily activities. This condition eventually requires surgical intervention to restore the quality of life. It has been estimated that more than 8 million people aged over 45 in the UK need treatment for osteoarthritis, and around one thousand people are diagnosed with it daily (NICE, 2017).

The osteochondral lesion can be diagnosed by combining clinical findings and radiological imaging from X-ray to magnetic resonance imaging (MRI) (Jacob, Shimomura and Nakamura, 2020). The lesions have limited repair capacity, particularly in adults with mature skeletal development (Pearce *et al.*, 2012). Chondrocytes in the injured area have altered metabolism, resulting in the disorganisation of collagen. This change shifts the transmission of load toward the subchondral bone. When the transmitted load exceeds the subchondral bone capacity, the damage to the cartilage can be more severe, since the resistance

from the cartilage is reduced. With its limited capacity, chondrocytes proliferate and produce a new matrix that is inadequate to restore the native surface. Stem cells from the medulla of subchondral bone then produce type I collagen fibres to fill the defect with fibrocartilage. However, fibrocartilage does not have the damping function of the articular cartilage (Fuentes-Mera *et al.*, 2019). Hence, osteochondral tissue restoration is needed.

The treatment to restore the joint's bone and cartilage damage depends on several factors, including the lesion size. Smaller lesions < 2 cm^3 can benefit from microfracture treatment, whilst lesions larger than that will require different types of treatment such as autologous chondrocyte implantation (ACI), osteochondral autograft transfer (OAT), or osteochondral allograft (OCA) transplantation (Matthews *et al.*, 2022). OCA transplantation has been the gold standard for extensive injuries (4 cm^3) with significant bone loss (figure 1.3).

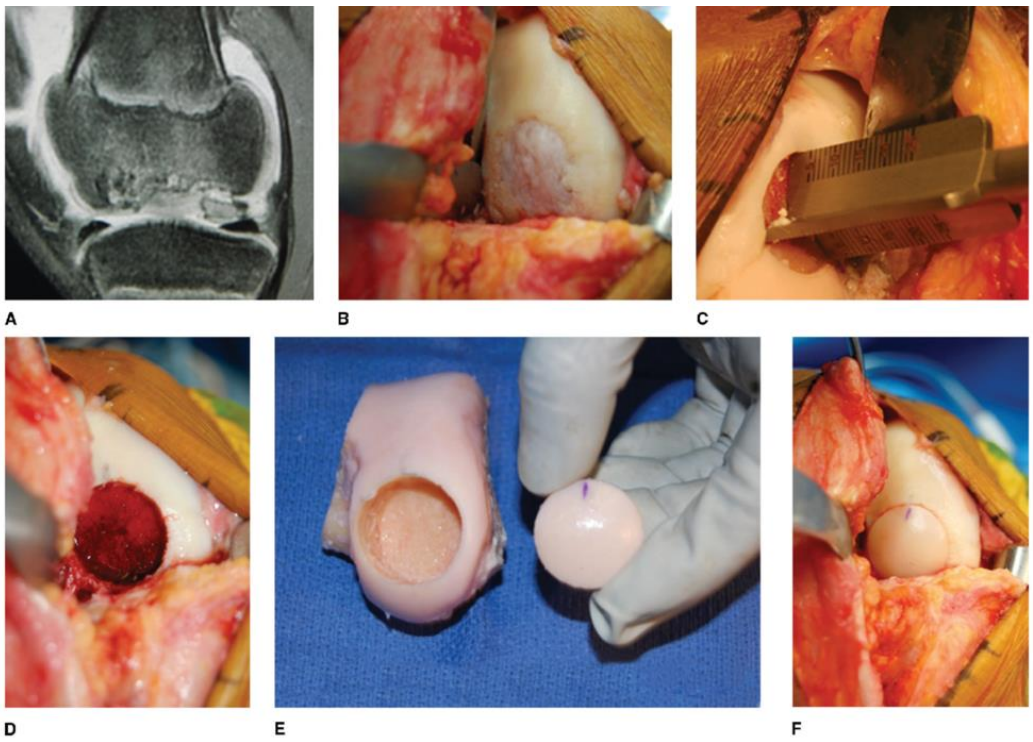

Figure 1. 3. Osteochondral allograft transplantation on a knee defect.

A. MRI image of the defect. B. Clinical presentation of the defect. C. Surgical site preparation. D. Recipient site. E. donor site and the allograft. F. Transplanted osteochondral allograft. Source: (Sherman et al.*, 2014).*

OCA provides a viable cartilage and bone layer with metabolically active cells that allow the remodelling process. The full-thickness graft offered by the OCA technique can restore the defect architecture accurately (Briggs *et al.*, 2015). OCA has been used in joint structures such as ankles, femoral condyles, tibial plateau, patella, elbow, and shoulder. Successful OCA transplantation can delay the need for joint replacement in severe cases (Lai *et al.*, 2022). The treatment also demonstrated satisfactory long-term outcomes (Lai *et al.*, 2022). However, as an allograft, OCA has several classic limitations, including donor tissue availability, the potential for disease transmission, limited time from harvesting the graft to the transplantation, and graft-to-recipient size matching. It has been reported that the average osteochondral defect size is 4.1 cm^2, which can be considered an extensive injury that requires tissue substitutes (Doyle *et al.*, 2021).

To overcome these limitations, synthetic grafts are developed to offer benefits such as more straightforward single-stage surgery and avoiding healthy donor morbidity. Commercial osteochondral substitutes can be made from polymers, including polylactic acid (PLA), polycaprolactone (PCL), and poly(lactic-co-glycolic acid (PLGA). Unfortunately, prefabricated osteochondral substitutes have fixed dimensions that might not match the patient's defect. They are also acellular, which can increase their failure rates and reduce tissue remodelling.

1.1.3. The Current State of Tissue Engineering Approaches for Osteochondral Defect Repair

Osteochondral tissue has a stratified architecture that is challenging to be replicated. Scaffolds are developed to imitate the hierarchical structure since it has been reported that the scaffold's geometry influences cell behaviours (Holmes *et al.*, 2015). Therefore, a single-layer strategy cannot provide optimum cartilage and bone tissue regeneration. Bone tissue stiffness of the osteochondral unit has been reported to vary from 1.6 to 3.9 GPa, depending on the joint, whilst cartilage demonstrates significantly lower stiffness, ranging from 0.1 to 6.2 MPa (Lesage *et al.*, 2022). Several studies have reported better bilayer scaffold outcomes than the single-layer counterpart in animal models (Lesage *et al.*, 2022). Various methods are applied to produce the layered structure, such as electrospinning, solvent casting, freeze drying, and particle leaching (Lesage *et al.*, 2022). However, these conventional methods do not provide accuracy and control over scaffold architecture, including pore size, interconnectivity, and distribution of the pores. 3D printing is a promising method for developing scaffolds with intricate biomimetic structures. 3D printing methods can accurately fabricate objects based on computer-aided design (CAD) models.

To be successfully integrated into the defect, scaffolds need to be put in cell culture for a certain period to allow the cells to secrete adequate ECM. In addition, the ECM will facilitate the integration of scaffolds into the surrounding host tissue. Therefore, a cytocompatible scaffold is necessary. Good mechanical properties are also essential to ensure scaffold integration. Inferior mechanical properties cause a mechanical imbalance in the defect area, exposing the defect to an excessive load that might lead to degenerative processes (Fuentes-Mera *et al.*, 2019).

Different strategies can be applied to develop scaffolds for osteochondral defect repair. Scaffolds can be made with a single material but have stratified layers or different materials to create the bilayer structure (Martin *et al.*, 2007). Multiphasic bone and cartilage scaffolds not only mimic the nature of the native tissue but also benefit from the bone layer healing capability. Due to the porous structure, the bone layer allows vascularisation and stem cell migration, promoting implant integration.

Different biomaterials representing each layer have been combined to develop these multiphasic scaffolds. At the time of writing, ceramics were still the most frequently used for the bone layer. Around 50% of recent studies in osteochondral regeneration used Calcium phosphate to mimic the subchondral bone (Lesage *et al.*, 2022). Conversely, collagen and collagen derivatives, such as gelatin, were widely used for the cartilage layer (Lesage *et al.*, 2022).

Based on these findings, the combination of ceramics and hydrogels was extensively developed for osteochondral scaffolds. After undergoing clinical trials, some of these scaffolds are currently available in the European Union market (figure 1.4). CartiHeal Agili-C® combines hyaluronic acid as the cartilage phase and calcium carbonate-based aragonite as the bone phase (Jacob, Shimomura and Nakamura, 2020). The combination of the polylactide-coglycolide copolymer for the cartilage layer and calcium sulphate for the bone layer is commercially available as TruFit CB® plug (Bedi *et al.*, 2010). Another available product is MaioRegen®. It combines type I collagen and magnesium-hydroxyapatite as cartilage and bone layer, respectively (Yan *et al.*, 2015). ChondroMimetic® also utilises collagen, type I and type II, with chondroitin sulfate for the chondral phase and calcium phosphates for the bone phase. Bovine collagen is used for the

cartilage phase of BioMatrix CRD, whilst β-TCP is used for the bone phase (Fu *et al.*, 2022).

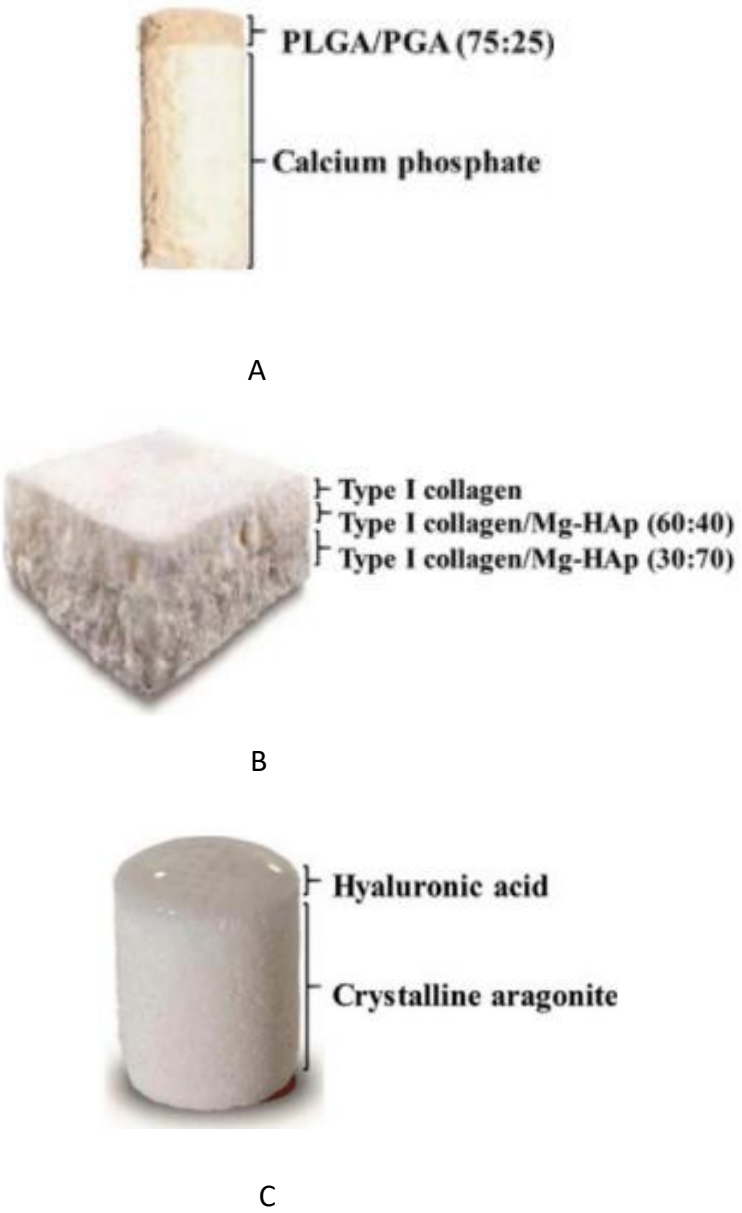

Figure 1. 4. Commercially available and EU-approved products for osteochondral tissue regeneration with their composition.

The combination of softer polymers and bioceramics is used in these products.
A. TrufFit CB. B., MaioRegen C. Agili-C. Source: (Fu et al.*, 2022).*

Most commercially available products have organic source-derived materials for the chondral layer and inorganic bioceramics for the bone layer, as shown in table 1.1. Naturally derived polymers are commonly used due to their capability to hold a significant volume of water that replicates the hydrated 3D environment of the native ECM (Doyle *et al.*, 2021). As mentioned, collagen or collagen-derived materials are used in clinically approved products. Their weak mechanical properties are often improved by combining them with synthetic polymers such as PLGA and PLA (polylactic acid). Bioceramics, on the other hand, show mechanical properties comparable to bone. Their brittle properties are addressed by combining them with polymers, like BioMatrix CRD®, which combines β-TCP with PLA. It has been suggested that a mechanical match between the native tissue and the implanted scaffold might induce improved tissue regeneration and integration (Yang *et al.*, 2021).

Table 1.1. Summary of commercially available and EU-approved products for osteochondral tissue regeneration with specific material for each layer.

Product name	Bone layer	Cartilage layer
CartiHeal Agili-C®	Calcium carbonate-based aragonite	Hyaluronic acid
TruFit CB®	Calcium sulphate	Polylactide-coglycolide copolymer
MaioRegen®	Magnesium-hydroxyapatite	Collagen type I
ChondroMimetic®	Calcium phosphate	Collagen (type I and II) with chondroitin sulfate
BioMatrix CRD®	β-TCP	Bovine collagen

Inferior restoration of subchondral bone has been reported with mechanically inferior bone layer scaffolds (Zhang *et al.*, 2013). This insufficient repair of subchondral bone negatively affected cartilage tissue repair. It has been

suggested that the cartilage repair should start from the subchondral area. As the ossification of the subchondral bone progresses, the new cartilage tissue is brought up to the joint surface. By providing stable mechanical support, the scaffold's bone layer can prevent fibrotic tissue growth, which is conducive to chondral tissue regeneration. The structure of the subchondral bone is also essential. Adequate porosity of the bone layer enables better diffusion across the osteochondral interface (Pouran *et al.*, 2017).

These commercially available products indicate the importance of developing each layer to correspond to the native tissue structure. In addition, the biochemical and biophysical properties of the native osteochondral structure are challenging to recreate with a single material. These multiphase scaffolds have been reported to improve the patient's clinical symptoms, resulting in approval for clinical use (Delcogliano *et al.*, 2014). However, several problems remain, including incomplete integration with the surrounding host tissue and graft-to-recipient size matching(Wei and Dai, 2021). Cutting out the commercial implants has been performed to match the lesion size. Nevertheless, osteochondral defects often have irregular edges, making the press-fit retention method difficult. MaioRegen® was one of the most investigated products with good clinical outcomes in young patients but also showed deformation, dislodgement, and delamination when implanted with the press-fit method and exposed to continuous passive motion in a cadaver human knee model (Kon et al., 2014). On the other hand, studies investigating Trufit CB® reported controversial results, including the lack of long-term durability evaluation and the findings of fibrous vascularised tissue at 1-year follow-up biopsy (Kon *et al.*, 2014). Clinical reports on Agili-C® in larger defects were also limited. A case report in 2013 describes

the promising result of Agili-C implantation in a smaller (2 cm^2) femoral condyle lesion (Kon *et al.*, 2014).

These limitations regarding the structural integrity and implantation method necessitate exploring alternative fabrication methods for osteochondral scaffolds, such as additive manufacturing or 3D printing (figure 1.5). According to previous studies, using 3D printing as an implant shaping method was less common than the moulding method, which provides the opportunity to develop personalised implants with complex structures (Lesage *et al.*, 2022). Moreover, the materials used in the existing products are not commonly used for osteochondral tissue 3D printing. In 3D bioprinting of osteochondral unit, alginate is the material of choice for both bone and cartilage due to its printability, followed by PCL and methylcellulose (Santos-Beato *et al.*, 2022). However, alginate is also known for its low cell attachment and inferior mechanical properties (Santos-Beato *et al.*, 2022). Considering the main limitation of the approved existing product, which is the deformation and delamination of the implant, alternative 3D printable materials that can fabricate an osteochondral scaffold with good structural integrity and mechanical properties are necessary.

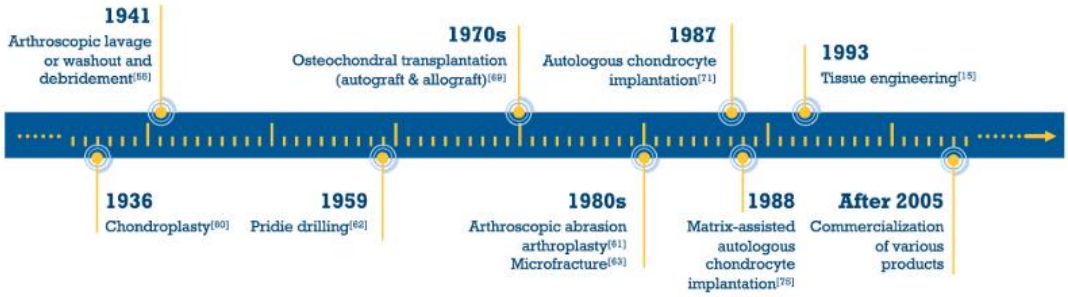

Figure 1. 5. The advancement of articular cartilage and osteochondral defect treatment.

Source: (Wei and Dai, 2021).

1.1.3.1. 3D Printing

Additive manufacturing or 3D printing allows the personalisation of joint damage treatment. It enables the fabrication of patient-specific implants that increase defect size matching. Anatomically sized with defect-specific shapes could be fabricated using a patient's imaging scan that can be converted into computer-aided design (CAD). Scaffolds are made layer-by-layer, allowing the production of implants with a high degree of architectural complexity. Gradients, oriented channels, and multilayer structures of osteochondral tissue fabrication are made possible with 3D printing. According to recent review studies of osteochondral scaffold fabrication, the most used 3D printing techniques are extrusion- and lithography-based printing (Doyle *et al.*, 2021; Wei and Dai, 2021; Lesage *et al.*, 2022).

1.1.3.1.1. Extrusion-based Printing (EB)

The extrusion-based printing mechanism involves extruding material through a nozzle, depositing it to a printing bed in the XY plane fashion, and then depositing the material in the Z plane or vertical direction, layer by layer (figure 1.6). This method uses materials that can be printed using thermosensitive polymers, hydrogels, and bioceramics. This method requires fine-tuning the 3D printing parameters, such as extrusion pressure, printing speed, and temperature. Despite the tunability and broad range of printable material, the 3D printing designs of EB are limited due to the extrusion mechanism that does not allow the fabrication of more complex structures. The diameter of cylindrical filaments extruded from the nozzle ranges from 150 to 350 µm (Wang *et al.*, 2022). These filaments are crosslinked further using light, chemicals, heat, or enzymes.

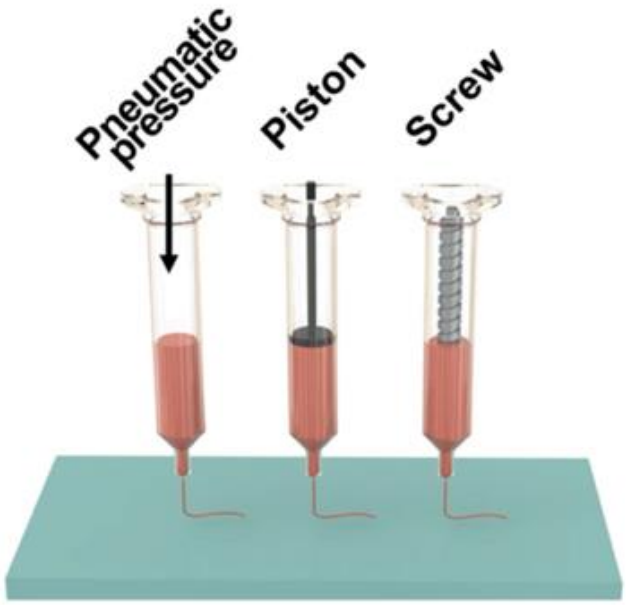

Figure 1. 6. Schematic image of extrusion-based 3D printing.

Different mechanisms of extrusion, such as pneumatic pressure, piston, and screw, can be applied to deposit the 3D printing material. Source: (Yi et al.*, 2021).*

EB printing is currently the most prevalent method used for bioprinting due to the availability of various cytocompatible materials with rheological properties suitable for extrusion mechanisms (Santos-Beato *et al.*, 2022). Viscoelastic inks are extruded in a transient shear process. The shear thinning property allows smooth extrusion and good recoverability (Zhou, Fu and He, 2020). When the inks are extruded and deposited, their viscosity increases and recovers to their initial state, and the structure can retain its shape. Since the EB method can tolerate various materials, it allows multi-material printing with multiple dispensers and inks. However, the printing resolution, around 200 – 1000 µm, is lower than other 3D printing methods (Wang *et al.*, 2022). The printing speed is also one of the disadvantages. The highest printing speed of direct ink writing has been reported to be around 100 mm/s, slower than vat polymerisation.

1.1.3.1.2. Lithography-based Printing

Lithography-based printing that includes stereolithography (SLA) and Digital Light Processing (DLP) fabricates 3D structures layer by layer with liquid material by exposing them to the light source (figure 1.7). These methods are also known as vat polymerisation. SLA is one of the first rapid prototyping methods developed in the 1980s (Chia and Wu, 2015). The main difference between SLA and DLP is the light source. SLA uses a laser, whilst DLP uses a projector as the light source. Reactive species, such as free radicals, are generated by photo initiators after UV or visible light exposure. The exposure polymerises the resin material in the X-Y plane, followed by the Z-plane layer-by-layer stacking. These methods are known for their outstanding accuracy and precision. The curing kinetics of photo polymerisation can be controlled by the power intensity of the light source, scanning speed, monomer amount, and photoinitiator percentage (Chia and Wu, 2015). Resins typically used in SLA methods are acrylates, methacrylates, epoxy, and vinyl monomers. Resin viscosity, additives, irradiation time, and light intensity can affect the quality of the 3D-printed structure (Shaukat, Rossegger and Schlögl, 2022).

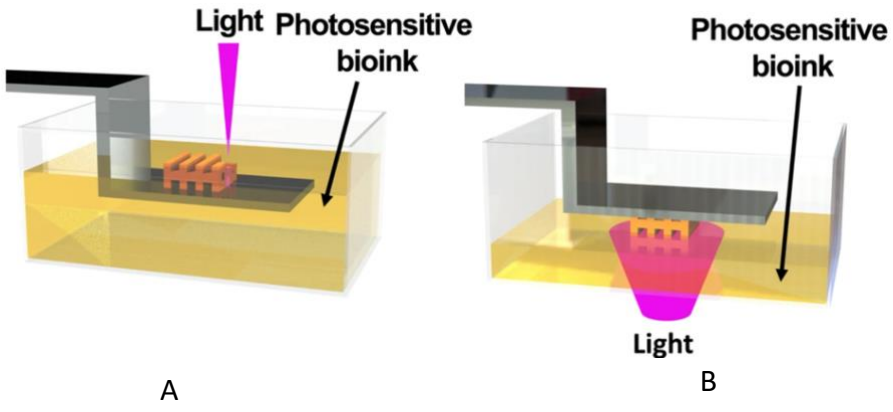

Figure 1. 7. Schematic illustration of lithography-based 3D printing.

A. SLA. B. DLP. SLA uses a laser as the light source, while a projector is the light source in DLP. Source: (Yi et al.*, 2021).*

Due to the lithography-based 3D printing mechanisms, faster printing speeds than other 3D printing techniques, particularly for DLP, have been reported. DLP can achieve a printing resolution of <50µm, superior to extrusion-based printing resolution of around 150 µm (Schoonraad *et al.*, 2021). However, the development of cytocompatible material for lithography-based 3D printing is not as extensive as the extrusion-based ones. Vat photo polymerisation requires materials with photo curability and fluidity.

Photocurability of the materials is induced by a photoinitiator that can react under the light source (Zhou, Fu and He, 2020). Both SLA and DLP use photo resins with rheological properties that allow the flow of the resin before repeating the photo-polymerisation process for the next layer. The viscosity of the material influences this free fluid movement (Bedell *et al.*, 2022). The addition of ceramic materials to the DLP bio-ink has been reported to have a light-scattering effect, affecting printing accuracy. DLP bioprinting also demonstrated more viable cells than extrusion-based methods due to the lower shear forces applied by DLP printing. The DLP method easily reproduces complex architectures, such as overhang features and interlacing structures. These designs cannot be fabricated by extrusion-based printing. Fabrication of complex geometry allows the improvement of the scaffold's mechanical properties. The combination of 3D-printed PEGDA (Polyethylene Glycol Diacrylate) and ECM via stereolithography has been reported to show osteochondral tissue repair in the rat femur (Zhu *et al.*, 2020). Despite its superiority, DLP has disadvantages, including limited build volume compared to other 3D printing methods and difficulties printing with more than one material.

Combining different 3D printing techniques to fabricate an osteochondral scaffold is also possible. Scaffolds with a gradient layer can be fabricated using

lithography-based printing with ceramic materials as the bone layer. Extrusion of a hydrogel was then applied to the construct to create the cartilage layer. The combination of hydrogel and hydroxyapatite on multiphasic scaffolds demonstrated the differentiation of human MSC towards the osteogenic and chondrogenic lineage that corresponds to the scaffold gradient (Groen *et al.*, 2017). Defect fitting and patient-specific design have been reported to influence the successful implantation of collagen-PCL scaffolds (Groen *et al.*, 2017).

1.1.3.1.3. 3D Printing Material

Developing 3D printing material involves formulating chemicals with properties that allow the fabrication of an accurate and stable 3D-printed construct. The accuracy and stability of the finished construct contribute to the desired mechanical properties and favourable architecture for cell viability (Bakhtiary, Liu and Ghorbani, 2021). Furthermore, a material's printability and shape fidelity are determined by its rheological properties (Schwab *et al.*, 2020)

Fluids can be categorised into Newtonian and non-Newtonian fluids based on their rheological properties. Newtonian fluids have constant viscosity throughout different shear rates, whilst non-Newtonian fluids demonstrate a viscosity change with different shear rates. Non-Newtonian fluids show different behaviour when stress is applied. If the viscosity increases with increased stress, it is a shear-thickening material. On the other hand, if the viscosity decreases with increased stress, it is a shear-thinning material. Higher viscosity has been reported to result in better shape fidelity and indicates superior mechanical properties. Material with lower viscosity requires lower injection force that might result in better cell viability for bioprinting. Viscosity itself is the resistance of a

fluid to flow under stress exposure. The main factors influencing the viscosity of material are molecular weight and concentration.

Different printing techniques require materials with different rheological properties. For example, non-Newtonian materials are suitable for 3D printing with extrusion mechanisms, whilst DLP and SLA work well with Newtonian materials. 3D printing material should show viscoelastic properties to control the surface's tension, support adhesion, and maintain the integrity of each layer (Bakhtiary, Liu and Ghorbani, 2021). To keep each layer's integrity, the material should also demonstrate resistance against the flowing mechanism during the 3D printing process. After the material deposition control is achieved, the shape fidelity of the 3D-printed construct resulting from the stacking of multiple layers should be evaluated. Structural integrity, geometric accuracy, and layer stacking are some parameters of the 3D printing shape fidelity (Schwab *et al.*, 2020). The deviation of these parameters is often caused by the time-dependent flow behaviour of the material before stabilisation, surface tension, and gravity. These factors mainly affect extrusion-based printing. Therefore, rheological modifiers and viscosity enhancers have been used to optimise material printability.

Lithography-based printing methods are developed to improve the shape fidelity of 3D printing results. The absence of a nozzle and the possibility of printing with lower viscosity material improves the printing resolution. Solutions with viscosity ranging from 0.25 – 10 Pa.s have been reported to be easily printed with lithographic printing. These materials can flow effortlessly and allow the removal of unreacted monomers from pores, holes, or other negative features, improving the resolution. However, cross-linking efficiency and post-printing structural stability of lithographic printing materials affect shape fidelity. Thus, materials with rapid cross-linking and showcasing high light absorption are

preferred. In addition, the curing depth of a photo-sensitive material should ideally be higher than the printing layer height or the selected resolution to ensure accurate polymerisation and integration between layers.

Nevertheless, light penetration over the selected layer thickness might cause undesired polymerisation of parts that should not be cured. Therefore, controlling the curing depth, irradiation dosage, and wavelength is essential. Photo absorbers can be mixed with the photo-sensitive material to limit light scattering and avoid over-curing to achieve accurate irradiation.

Hydrogels are the most used 3D printing material for tissue engineering purposes. Synthetic hydrogels like Gelatin Methacrylate (GelMA) have been developed for regenerative purposes (figure 1.8). GelMA exhibits tunability that can provide improved mechanical strength. In addition, it has lower immunogenicity than its natural counterpart, gelatin (Jiang *et al.*, 2021). Since GelMA is a denatured product of collagen, it demonstrates hydrophilicity and has an aqueous phase that can transform into gel under specific stimuli such as temperature (Dong *et al.*, 2019). It can produce 3D structures under UV irradiation with the help of a suitable photoinitiator by forming covalently crosslinked hydrogels. The double bonds in GelMA can conjugate intermolecularly, resulting in a rapid 3D architecture fabrication within seconds to several minutes, depending on the size of the construct.

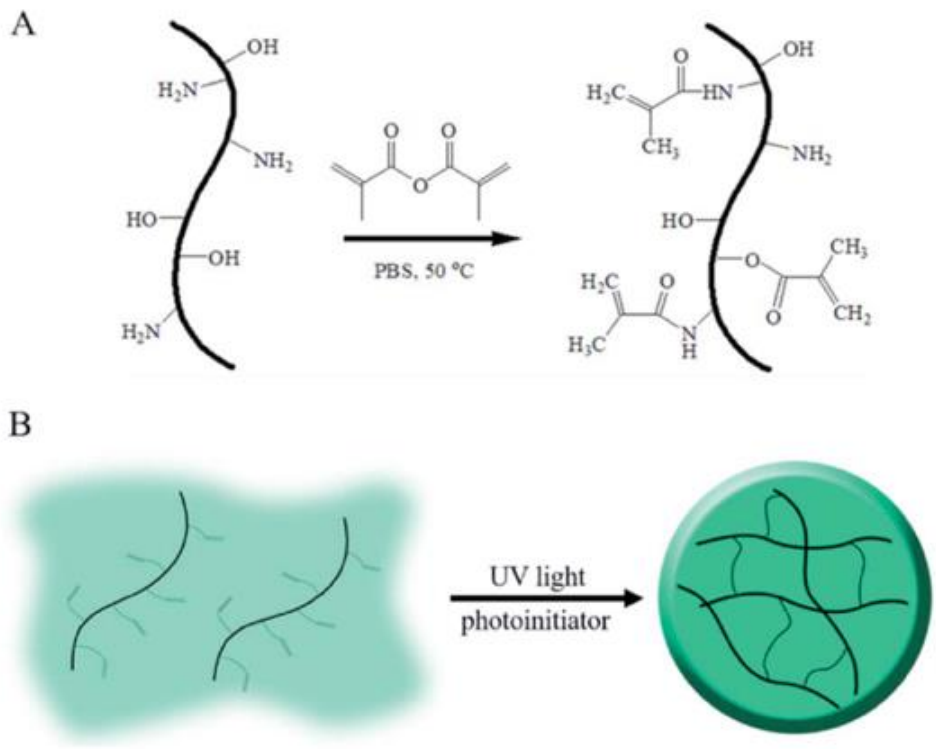

Figure 1. 8. Schematic illustration of (A) GelMA synthesis and (B) polymerisation.

Source: (Dong et al.*, 2019).*

Nevertheless, when used in extrusion-based 3D printing, GelMA's 3D printing resolution is low and shows poor shape fidelity. In addition, it has been reported that lower GelMA concentrations showed higher porosity and pore size, which allows higher extracellular matrix calcification (Dong *et al.*, 2019). Another synthetic hydrogel that has the potential for tissue engineering is polyethene glycol (PEG). PEG also offers tuneable mechanical properties but has a low viscosity that might not be suitable for 3D printing, particularly with the extrusion-based method.

Previous studies have suggested that tuneable hydrogels are more suitable as 3D printing material for soft tissue. However, hard tissues such as bones require material that can fabricate strong constructs for implants. Bioceramics have been used as bone grafts and substitutes due to their excellent biocompatibility and osteoconductive properties. To achieve osseointegration, it

is necessary to provide a customisable bone implant to match the defect. 3D printing can fabricate patient-specific implants with high precision and favourable mechanical properties. It has been reported that bioceramics such as calcium phosphate were made as suspensions to increase their tunability and printability (Yao, Sha and Zhao, 2019a). The preparation of suspensions is essential to achieve desirable rheological properties for 3D printing.

There are three types of particle interaction in a suspension: strongly aggregated, weakly aggregated, and well-dispersed (Zhou *et al.*, 2021). A well-dispersed suspension is required for ceramic lithography-based printing such as SLA and DLP. Conversely, a strongly aggregated suspension is needed for extrusion-based printing (Zhou *et al.*, 2021). Combining two or more monolithic materials has been performed to create a composite photopolymer with improved properties. These composites include the incorporation of complex ceramics into a photocurable resin. Mechanical mixing, sonication, shear mixing, or combining these methods are conducted to achieve homogeneous suspension of such composite with an acceptable viscosity (Manapat *et al.*, 2017).

1.1.3.1.4. Alternative and Novel 3D Printing Materials

The majority of commercially available photopolymers originated from unsustainable petrochemical sources (Mondal, Diederichs and Willett, 2022). Plant-derived polymers have been developed to reduce the harmful carbon emissions from fossil-based materials. Moreover, these plant-based materials are more renewable and sustainable than animal-derived natural polymers. One of the potential candidates for plant-based 3D printing material is isosorbide. Isosorbide is a monomer derived from sugar, available from starch and cellulose. It has desirable stiffness for hard tissue engineering due to its ring structure

(figure 1.8). The good optical transparency of isosorbide is also advantageous for its development as a 3D printing material. Isosorbide can serve as the backbone for polymers with methacrylate or acrylate groups as the functional group (Mondal, Diederichs and Willett, 2022). Several studies demonstrated successful 3D printing with various isosorbide-based composites (Mondal, Diederichs and Willett, 2022; Owji *et al.*, 2022; Verisqa *et al.*, 2022).

Isosorbide methacrylate showed a compressive modulus that reached 4 GPa, similar to native bone compressive modulus. In addition, the mechanical properties offered by isosorbide-based polymers were higher than petroleum-based or natural-origin composites such as poly(methyl methacrylate) (PMMA) and epoxy resin (Mondal, Diederichs and Willett, 2022). Moreover, isosorbide-derived polyesters have shown elasticity and high tensile strength, unlike other materials that exhibit high compressive strength but are brittle (Lammel-Lindemann *et al.*, 2020; Tejeda-Alejandre *et al.*, 2022). Previous studies also reported the addition of bioceramics such as calcium phosphate and hydroxyapatite to isosorbide-based photopolymers (Owji *et al.*, 2022). The impressive mechanical properties of the 3D printed structure make isosorbide a promising 3D printing material for osteochondral tissue substitutes.

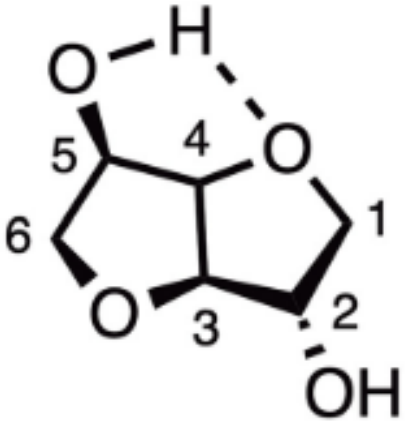

Figure 1. 9. Structure of isosorbide.

Source: (Saxon et al.*, 2020).*

Methacrylate-based photopolymers, including isosorbide methacrylate, are polymerised via a radical system (Bagheri and Jin, 2019). A radical system has three main steps: radical generation, initiation, and propagation. The radical generation occurs under light irradiation, where the photoinitiator converts photolytic energy into reactive species, initiating photo-polymerisation. The most commonly used photoinitiator with a radical system includes camphorquinone (CQ). The utilisation of UV light-sensitive photoinitiators in 3D printing applications is common since their light absorption wavelengths are suitable with most 3D printer light sources. For example, Bis(2,4,6-trimethylbenzoyl) phenylphosphine oxide (Irgacure 819; BAPO) with wavelength 295 nm and 370 nm has been reported to initiate photo-polymerisation of PEGDA in DLP 3D printing (Bagheri and Jin, 2019). Irgacure 2959 is often used for polymerising hydrogels like GelMA. It is water soluble and has low cytotoxicity. However, its peak absorption is at 280 nm, which is more suitable for UV-B than UV-A. Exposure to UV-B irradiation has been reported to have a more significant genotoxic effect (Nguyen *et al.*, 2019). Meanwhile, more water-soluble lithium phenyl(2,4,6-trimethylbenzoyl)- phosphinate (LAP) with light absorption at 375 nm showed faster gelation than Irgacure 2959 (Nguyen *et al.*, 2019). Faster gelation will reduce the length of UV exposure to cells, increasing cell viability.

1.1.3.3. Scaffold Design for 3D Printing

New bone formation and mechanical properties are important parameters for orthopaedic scaffolds. Factors affecting new bone formation in the scaffolds include porosity, pore size, shape, and distribution (Chen *et al.*, 2020). 3D printing allows the fabrication of porous structures with high precision. Geometry-based designs such as octahedrons and rhombic dodecahedrons have been

successfully 3D printed. Other complex porous structures that can be 3D printed are Triply Periodic Minimal Surface (TPMS) and Voronoi. Due to the printability of these structures, they have been explored for the 3D printing of bone scaffolds (Kanwar and Vijayavenkataraman, 2021). Based on their unit designs, the CAD for bone scaffolds can be classified into non-parametric designs, such as diamond, polyhedron, and honeycomb, as well as parametric designs, which include Voronoi and TMPS (Kanwar and Vijayavenkataraman, 2021). A hexagonal design like honeycombs has been reported to show high cell viability and strength compared to the 3D printed bone scaffold with conventional designs that have rectangular or triangular pores (Roohani-Esfahani, Newman and Zreiqat, 2016; Yazdanpanah et al., 2022). The maximum contact area and the obtuse angle of the hexagonal design contributed to the high compressive strength and high cell growth (Roohani-Esfahani, Newman and Zreiqat, 2016a; Yazdanpanah *et al.*, 2022)

Most conventional existing designs have straight edges and sharp turns due to the Boolean intersection of the geometric primitives (Chen *et al.*, 2020). The sharp angles of these geometric structures are not favourable for cells to attach, spread, and proliferate. TPMS, on the other hand, has smooth infinite surfaces with symmetrical concave and convex curvatures. The structure also has a higher surface-to-volume ratio than strut-based structures (Abueidda *et al.*, 2019). Therefore, TPMS is a promising porous structure for cell proliferation.

The most commonly used TPMS designs are diamond surface, primitive surface, I-graph-wrapped package (I-WP) and gyroid surface. Previous studies have shown that these designs matched the mechanical properties of cortical and cancellous bone (Chen *et al.*, 2020). At high porosity, TPMS structures had Young's modulus similar to cancellous bone, whilst TPMS designs with low

porosity showed compressive strength that resembled cortical bone. Moreover, the mechanical properties of the TPMS structure were not inferior to those of strut-based structures such as the rhombic dodecahedron. The spring shape design of the gyroid might provide isotropic resistance to mechanical loading and elasticity (Germain *et al.*, 2018).

Based on finite element analysis (FEA), the TPMS gyroid structure (figure 1.9) could provide uniform mechanical stimuli to the cells seeded on the scaffold (Yousefi *et al.*, 2015). Another simulation also reported that the pore size on gyroid architectures might also affect cell differentiation, whilst the pore shape was found to influence the fluid movement and mechanical load distribution. The interconnectivity and fluid permeation of the gyroid facilitated nutrient transport and the ease of cell seeding (Ma *et al.*, 2019). The open architecture of the gyroid surface allowed cell suspension infiltration, resulting in better cell distribution all over the scaffold surface (Melchels *et al.*, 2010). The permeability of a gyroid structure also allows a longer cell culture period since the cells residing on the scaffold can still access adequate nutrients and oxygen.

Regarding CAD, the gyroid structure has a self-supporting feature that eliminates the requirement of building the support structure. This feature enables 3D printing with vat photo polymerisation methods, such as SLA and DLP, using photopolymers (Voet *et al.*, 2018; Shaukat, Rossegger and Schlögl, 2022). Furthermore, vat photo polymerisation allows 3D printing of high-resolution gyroid structures, which is important to ensure smooth surfaces and curvatures.

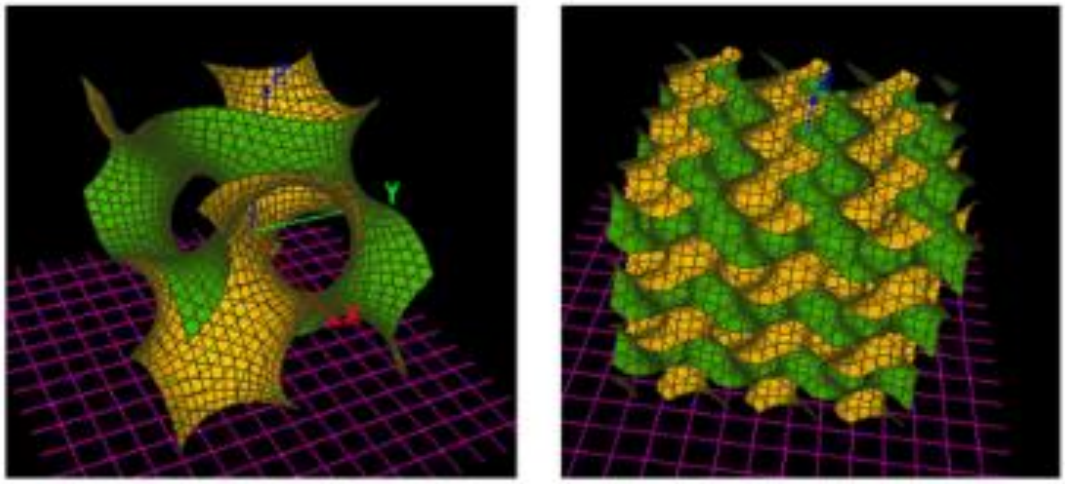

Figure 1. 10. CAD of TMPS Gyroid structure.

Left: a single unit of gyroid. Right: the gyroid structure. Source: (Jin et al.*, 2019).*

1.1.3.3. Cell Sources

Cells are major tissue engineering components often loaded into the scaffolds to promote better tissue integration and repair. These cells should have properties that enable in vitro cell culture for a longer period and scaffold implantation. Progenitor cells, like stem or tissue-specific cells, are commonly used for osteochondral repair (Seo *et al.*, 2014). Corresponding to each layer of the osteochondral unit, chondrocytes are used for cartilage tissue regeneration, whilst osteoblasts are utilised for the same purpose for bone. However, mature and differentiated cells have a limited quantity, which poses a challenge to the culturing process and obtaining the desired number of cells.

MSCs then become an alternative source due to their multipotency and rapid proliferation. Bone marrow MSCs (BM-MSC) are the most widely used for osteochondral tissue engineering since both chondrocytes and osteoblasts are derived from the stem cells in the bone marrow. Disadvantages of BM-MSC include a highly invasive harvesting process and the decline in their viability over time, i.e., they become senescent once differentiated (Fu *et al.*, 2022).

Umbilical cord MSCs (UC-MSC) can offer more stem cells per unit harvest than BM-MSC. They have broad multipotency, but the harvesting, collection, and storing processes are expensive. On the other hand, harvesting adipose tissue-derived MSCs (AD-MSC) is minimally invasive with low morbidity. It can be easily repeated to obtain more cells (Frese, Dijkman and Hoerstrup, 2016). AD-MSC are also multipotent and show low immunogenicity. It has been reported that BM-MSC and UC-MSC seeded on a PLGA scaffold show no significant difference regarding the biochemical properties (Zhang *et al.*, 2016). Meanwhile, AD-MSCs cultured on PCL scaffolds demonstrated chondrogenic differentiation (Rose and De Laporte, 2018).

Chondrogenic differentiation is evaluated by analysing chondrogenic markers, such as SOX9, Aggrecan, Col I and Col II (figure 1.11) (Wu *et al.*, 2017). SOX9 is an early marker, whilst Aggrecan is expressed at the late stage of differentiation. Aggrecan is upregulated during the formation of cartilage matrices and promotes ECM deposition. COLI is a marker found in the pre-cartilage matrix phase and diminishes after the mature cartilage tissue is formed. In contrast, COLII presents as the late-stage marker after the maturation of cartilage tissue (Wu *et al.*, 2017).

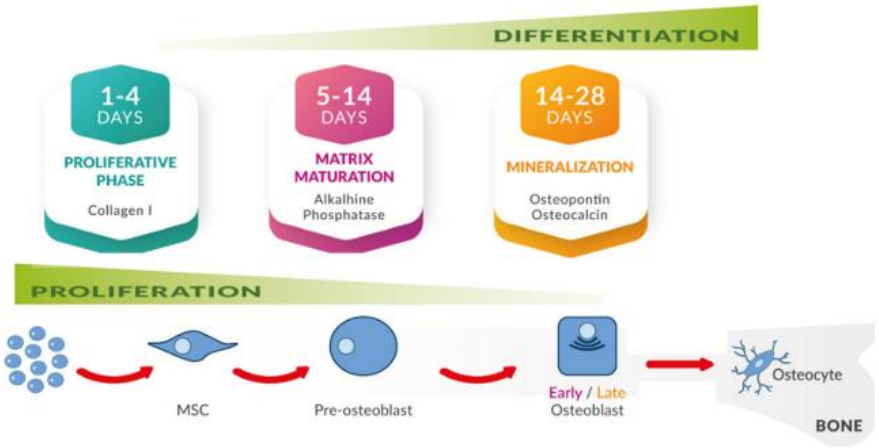

Figure 1. 11. Schematic illustration of stem cells osteogenic differentiation.

Timeline and corresponding differentiation stages with their correlating markers are shown. Source: (Carluccio et al.*, 2020).*

Osteogenic differentiation has different markers, including RUNX2, which can be detected at the early phase of differentiation and osteopontin (OPN), expressed in the middle or later stage (figure 1.12) (Fu *et al.*, 2017). Lower RUNX2 expression has been reported to correlate with lower osteoblast proliferation (Kawane *et al.*, 2018). OPN regulates the hydroxyapatite crystal nucleation (Olivares-Navarrete *et al.*, 2017; Hwang and Horton, 2019). Other osteogenic markers are alkaline phosphatase (ALP), COLI, Bsp, and OCN. The early stage is marked by a decreased proliferation rate, where the committed stem cells or early osteoblasts start to express ALP. Approaching the final stage, ALP expression declines and expression of OPN and OCN, secreted by late osteoblasts, increases. The mineralisation phase then follows this stage. At the later stage of differentiation, osteoblasts become osteocytes (Carluccio *et al.*, 2020).

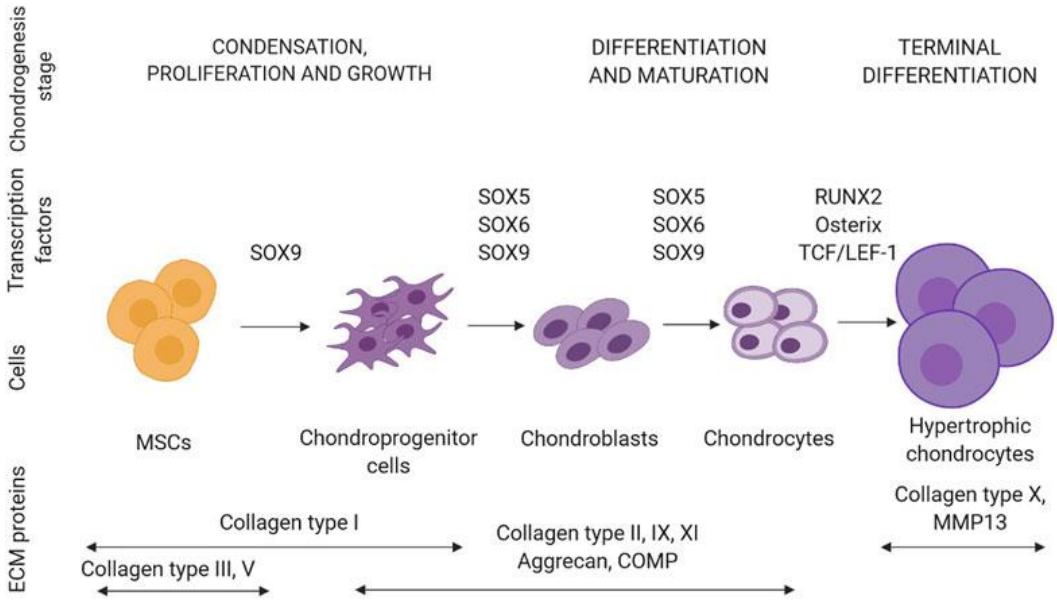

Figure 1. 12. Schematic illustration of stem cells chondrogenic differentiation.

Different markers are shown to correspond to the phases of differentiation.
Source: (Szustak and Gendaszewska-Darmach, 2021).

Recent cell culture methods have been developed for improving cell differentiation. Three-dimensional (3D) culture and scaffolding have been reported to improve cell proliferation (Baruffaldi *et al.*, 2021). High-density cell cultures have demonstrated superior chondrogenic differentiation since the culture resembles the embryogenesis microenvironment (Jacob, Shimomura and Nakamura, 2020).

One of the problems that need to be addressed regarding the implantation of the scaffold with cells is the long-term viability of the implant. Cells residing in the centre of the scaffolds were believed to die before the vascularisation from the surrounding host tissue could penetrate the graft (Ng, Bernhard and Vunjak-Novakovic, 2016). Therefore, promoting pre-vascularisation of the graft in a bioreactor facilitates rapid vascularisation after the implantation.

1.1.3.3. Three-Dimensional Cell Culture and Bioreactor

The 3D-printed scaffold is a construct generated in vitro. While 3D printing can fabricate a patient-specific graft, successful implantation and integration depend on the cellular response. 3D cell culture can mimic the cell's physiological environment. This technique includes scaffold-free or anchorage-independent and scaffold-based or anchorage-dependent cell methods.

Scaffold-free methods are considered simple and cost-effective. They rely on the auto-aggregation of cells in specialised culture plates, such as cell-repellent plates and hanging drop microplates that promote spheroid formation (Langhans, 2018). However, producing the co-culture with these methods has disadvantages since it is difficult to locate the different types of cells precisely. Their size and ability to remain stable are also problems in the collection process (Temple *et al.*, 2022). Spheroid cultures need to be maintained at an optimum

size. Large spheroids can result in insufficient nutrient supply, leading to necrosis (figure 1.12) (Langhans, 2018). The nutrient and gas exchange diffusion limit ranges from 200 to 300 μm (You *et al.*, 2023).

On the other hand, scaffold-based methods offer location control and allow periodic cell seeding (Temple *et al.*, 2022). Scaffolds are more visible than spheroids and can be harvested manually. The physical supports provided by the scaffold vary from basic mechanical structures to ECM-like structures (Wanigasekara *et al.*, 2023). The disadvantage of these methods is the difficulty of ensuring homogenous cell distribution. It has been reported that cells encapsulated within a 3D matrix could create structures resembling in vivo organisation with better intercellular contact and communication (Law *et al.*, 2021). This communication is enabled due to the topology of the 3D matrix that mimics the 3D architecture of the native tissue. In addition, cell-to-ECM interaction also occurs in 3D cell culture.

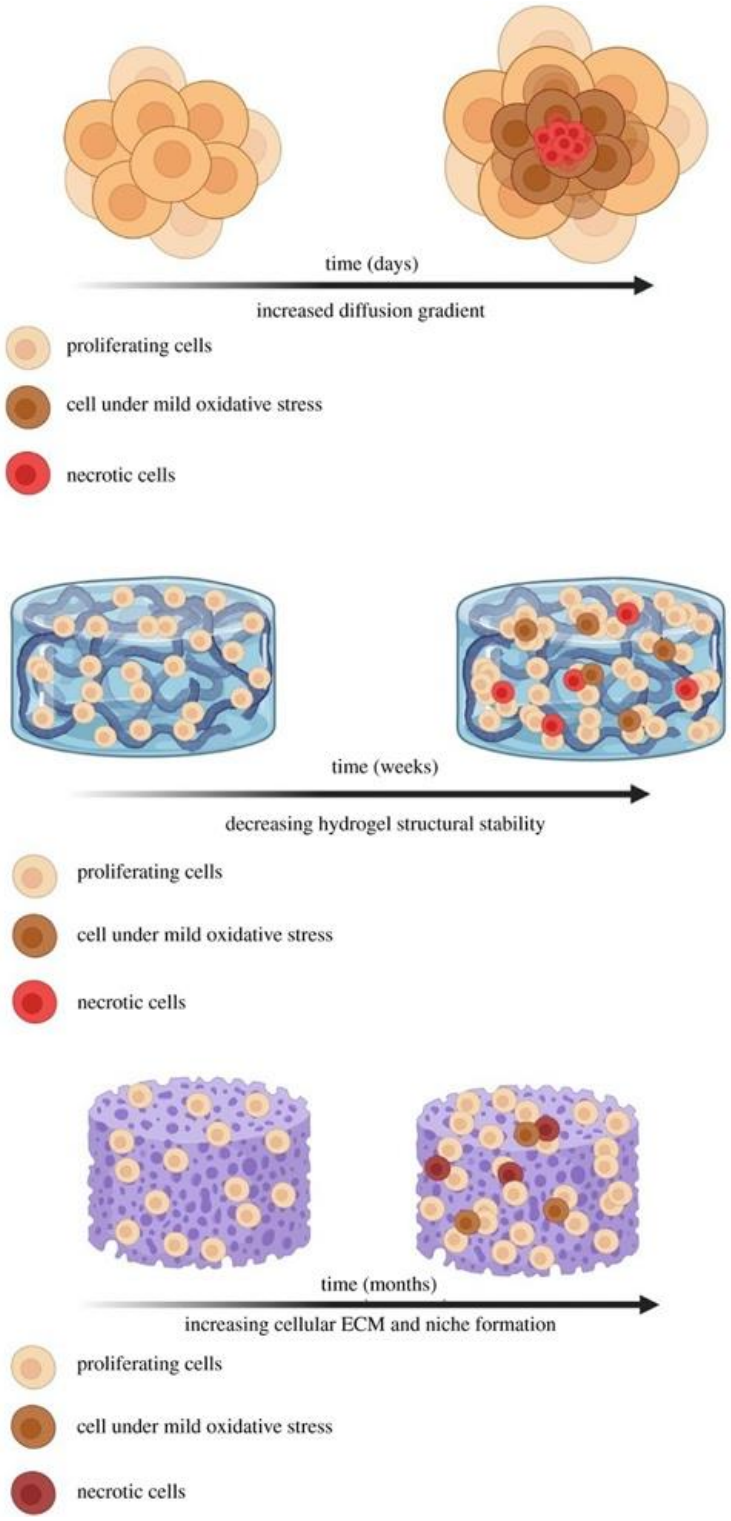

Figure 1. 13. Schematic illustration of 3D cell culture methods.

Top: scaffold-free method. Middle: hydrogel-based method. Bottom: scaffold-based method. Cells are shown to experience different conditions due to their location. The cells in the inner part of the spheroid or construct are necrotic, whilst those on the outer part can keep proliferating. The necrosis timeline differs among different culture methods. Source: (Temple et al.*, 2022).*

High cell density 3D culture plays an important role in developing tissue-like cell-to-cell interactions (Da Conceicao Ribeiro *et al.*, 2018). Native human tissues have a cell density of 1 to 3 billion cells/ml. (You *et al.*, 2023). Therefore, artificial tissues require high cell densities to improve physiological compatibility and increase implantation potential (You *et al.*, 2023). It is also essential for the formation of functional bone microtissues. The optimum cell seeding for 3D cultures depends on the cell type and the 3D matrix.

Establishing a bioreactor reproducing a physiochemical environment under controlled conditions can achieve favourable cellular events leading to functional tissue regeneration. Bioreactors allow cell seeding with high density, which leads to improved tissue formation in 3D constructs. A higher number of cells allows higher extracellular matrix production and increased bone mineralisation (Wendt, Jakob and Martin, 2005).

The dynamic conditions in a bioreactor also increase the transport of nutrients and metabolic waste products. Static culture is found to distribute media inhomogeneously, resulting in the hypoxic and necrotic central region, with most viable cells residing in the peripheral area. It has been reported that fluid flow in the perfusion bioreactor improved cell growth, differentiation, and mineralised matrix deposition (Wendt, Jakob and Martin, 2005).

A perfusion system is expected to balance the rate of nutrient transport and waste product removal, retain the synthesised extracellular matrix components, and provide necessary shear stress to maintain a physiological state for the cells. Thus, perfusion bioreactors, among other types, are commonly used for musculoskeletal tissue engineering. Perfusion bioreactors demonstrate a more uniform mixing of the media compared to others, resulting in better physical stimulation and environmental control (Gaspar, Gomide and Monteiro,

2012). This type of bioreactor uses a pump system that perfuses the media through the scaffolds. The perfusion system consists of a pump, a tubing circuit, a media reservoir, and the perfusion chamber (figure 1.14)(Flaibani *et al.*, 2009). These bioreactors can precondition the scaffold by developing mature tissue before implantation (Ng, Bernhard and Vunjak-Novakovic, 2016).

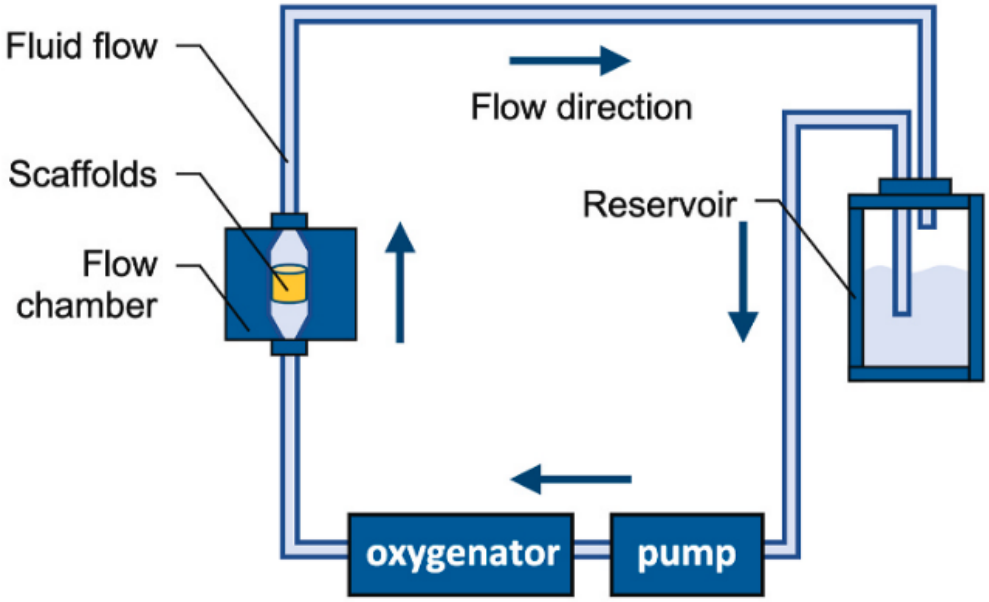

Figure 1. 14. Schematic illustration of perfusion bioreactor components.

The perfusion system comprises a reservoir to contain the medium, a pump to circulate the medium, an oxygenator for gas exchange, and a flow chamber to contain and perfuse the scaffold.
Source: (Wei and Dai, 2021)

MSCs cultured on scaffolds in the perfusion bioreactor have been reported to show accelerated osteogenic differentiation. Osteogenic markers like ALP and OPN were increased, indicating the facilitation of differentiation by the flow perfusion dynamic culture environment (Gaspar, Gomide and Monteiro, 2012). It has been known that physical stimuli can modulate chondrocytes and osteoblast metabolism. Previous studies demonstrated upregulated ECM production and increasing mechanical properties by applying stimuli (Wendt, Jakob and Martin, 2005). Optimum mineralisation has been reported to occur in bioreactors with a flow rate of 0.5 – 5 $ml.min^{-1}$ (Zhao *et al.*, 2018).

Cyclical hydrostatic pressure application on MSCs has demonstrated increased cartilage matrix production without chondrogenic growth factors (Jacob, Shimomura and Nakamura, 2020). Chondrogenesis also improved in cultures exposed to mechanical loading. Grafts produced with a bioreactor system have been reported to show accelerated repair of osteochondral defects compared to scaffold grafts without cell embedding (Vukasovic *et al.*, 2019). Recirculating flow-perfusion bioreactor has been shown to produce new cartilage with a better resemblance to native cartilage (Wei and Dai, 2021). Immediate post-surgery joint loading might be possible due to the accelerated repair, which allows a shorter rehabilitation period, return to normal activities and improved quality of life.

1.2. Problem Statement and Research Objective

1.2.1. Problem Statement

Osteochondral defects, particularly large ones, remain a significant clinical challenge in orthopaedic and related fields. Current treatments for extensive osteochondral defects have significant limitations affecting patients and healthy donors. Synthetic osteochondral tissue substitutes have been utilised to address these limitations. However, the absence of metabolically active cells on commercially available products can cause early implantation failure. Tissue engineering offers a promising approach to osteochondral defect treatment by enabling the combination of biomaterials and cell-based therapy. The main challenge of this approach is the fabrication of scaffolds that mimic the intricate structure and mechanical properties of native osteochondral tissue.

3D printing technology has emerged as a promising method to fabricate the desired scaffold with highly controlled geometries and tissue-like mechanical

properties. 3D printing can fabricate patient-specific constructs that allow a better fit on insertion during the surgical procedure. By printing with 3D printable biomaterials, viable cells can be seeded on the scaffold and increase the successful integration of the scaffold implantation. However, 3D printable biomaterials that can create the biomimetic structure of osteochondral tissue with good mechanical properties are still limited.

In this context, the thesis introduces a pioneering approach by harnessing the synergistic properties of two materials: CSMA-2 and GelMA. CSMA-2 is a recently developed polymer that offers a unique set of characteristics that address the limitations observed in conventional osteochondral 3D printing, namely poor cell growth and weak mechanical properties. CSMA-2's cytocompatibility and bone-like mechanical properties, when combined with GelMA, a well-established and biocompatible hydrogel, can create a tandem with the potential to provide an alternative solution for osteochondral repair.

The novelty of the CSMA-2 and GelMA combination lies not only in their individual advantages but also in the synergistic effect that arises from their integration. The customisable potential of the combination sets it apart from existing materials used in osteochondral repair.

1.2.2. Research Aims and Objectives

Throughout the literature review, significant unmet clinical needs exist in treating osteochondral defects, including the limited availability of customisable osteochondral grafts. To address this challenge, the overarching aim of this thesis focuses on developing a novel 3D-printed bilayer osteochondral scaffold that can mimic the hierarchical structure and mechanical properties of native osteochondral tissue for osteochondral defect reconstruction. Ultimately, the research has led to the development of a new bilayer scaffold's bone layer using CSMA-2 and a cartilage layer using GelMA.

The thesis explores the intricacies of the bilayer scaffold fabrication of bilayer scaffolds with different biomaterials to optimise the process with precision and efficiency. The study also analysed the scaffolds' biological properties using a co-culture technique to mimic the native osteochondral tissue. Furthermore, pre-seeding within a bioreactor equipped with dynamic cell culture is explored to observe the significance of controlled environment conditions in enhancing the scaffold's biological functionality. Lastly, the project investigated key properties needed for the repair and regeneration of osteochondral tissue, including angiogenesis and bone formation in vivo.

Therefore, the objectives and hypothesis of this thesis are as follows:

1. **Objective:** Development and characterisation of a 3D-printed bilayer osteochondral scaffold that can mimic the hierarchical structure and mechanical properties of native osteochondral tissue for osteochondral defect reconstruction.

   Hypothesis: The 3D-printed bilayer osteochondral scaffold will replicate the hierarchical structure and mechanical properties of native osteochondral tissue.

2. **Objective:** Development, characterisation, and optimisation of the scaffold's bone layer using a novel polymer CSMA-2

   Hypothesis: The integration of the novel polymer CSMA-2 as the bone layer of the 3D-printed bilayer scaffold will improve structural integrity and mechanical properties, resulting in an optimised bone layer suitable for osteochondral defect reconstruction.

3. **Objective:** Development, characterisation, and optimisation of the scaffold's cartilage layer using GelMA

   Hypothesis: Incorporating GelMA as the cartilage layer of the 3D-printed bilayer scaffold will improve chondrogenic properties, fostering the development of an optimised cartilage layer suitable for osteochondral defect reconstruction.

4. **Objective:** Simulation of bilayer scaffold precondition for clinical application

   Hypothesis: The preconditioning simulation of the bilayer scaffold by pre-seeding the scaffold with relevant cell type will enhance the scaffold's biological and tissue-like properties.

1.2.3. Thesis Overview

The thesis is structured into the following chapters.

Chapter 1 – Introduction

The introductory chapter provides the fundamental background of the key topics that will be explored. It starts with the osteochondral unit and is followed by the clinical challenges associated with osteochondral defect treatment. The chapter then shifts to the current state of 3D printing and various 3D printing materials, highlighting their potential for osteochondral tissue engineering. The biological components that play essential roles in the regenerative process are discussed to set the foundation for the subsequent chapters.

Chapter 2 – Bone Layer Development

The chapter commences with the synthesis and characterisation of novel CSMA-2 for 3D printing the bone scaffold, underlying the importance of material selection to ensure shape fidelity and structural integrity for the 3D printing process. The chapter then investigates the cytocompatibility of the 3D-printed CSMA-2 bone layer to establish a favourable environment for bone regeneration.

Chapter 3 – Cartilage Layer Development

This chapter discusses the suitability of GelMA as the material of choice for the cartilage layer by analysing its rheological, mechanical, and biological properties. The optimisation of GelMA properties to match the native cartilage tissue was also performed in this chapter.

Chapter 4 – Bilayer Scaffold Development

The chapter explores the fabrication of the bilayer scaffold by combining previously optimised CSMA-2 and GelMA as bone and cartilage layers, respectively. The discussion then moves to preconditioning simulation for clinical

application by conducting co-culture and dynamic culture in a simple perfusion bioreactor.

Chapter 5 – In Vivo Study

In this chapter, an in vivo study centred around the evaluation of novel CSMA-2 was conducted. The 3D-printed CSMA-2 scaffold's performance within the physiological environment of living organisms was analysed through the small animal model study. This chapter focuses on angiogenesis and new bone formation, which are pivotal factors in bone tissue regeneration and osteochondral defect repair.

Chapter 6 – General Discussions, Conclusions and Future Work

This chapter summarises the main conclusions that can be drawn from the experiments performed during this project and highlights areas of the research that require further investigation.

Chapter 2. Bone Layer Development: Synthesis, Characterisation, and 3D Printing of CSMA-2

2.1. Introduction

Bone is one of the most transplanted human body tissues, with autogenous bone graft as the gold standard (*Key Facts* | *Overview* | *Transplant Safety* | *CDC*, no date; Shegarfi and Reikeras, 2009). However, the harvesting process of autologous bone grafting has been reported to cause donor site pain and infection, increased blood loss, prolonged surgery duration, and hospitalisation (Roberts and Rosenbaum, 2012). The graft also has a limited supply since it is harvested from the same patient to reduce the possibility of graft rejection, which is one of the risks of allografts. Synthetic bone grafts have been developed as an alternative to these grafts. Calcium-based bone substitutes are the most used synthetic products, particularly in powder or granule form. This type of synthetic graft is not suitable for the management of large bone defects. Critical size defects require a strong graft that allows osteogenesis and angiogenesis to prevent necrosis and implant failure due to the loading conditions (Kantaros, Chatzidai and Karalekas, 2016). Inducing osteogenesis can be performed by incorporating cells or growth factors into the implants whilst creating graft pores, which will help generate vascularisation (Fernandez de Grado *et al.*, 2018). This approach combines reconstructive surgery and tissue engineering to restore bone defects.

Pores on the scaffold are found to play an important role in bone tissue engineering and bone regeneration. The suitable pore size allows nutrient and metabolite transport and supports cell proliferation. The favourable pore size diameter range for those purposes has been shown to be from 100 – 400 μm

(Cross and Spycher, 2008). Interconnectivity of the pores is also essential for cell migration and maximising nutrient diffusion. A structure with interconnected micropores can be efficiently designed using 3D printing, especially with DLP, which can print at high resolution and complex designs.

The challenge with the DLP method is finding a biocompatible photopolymer suitable for the printing mechanism. Widely available commercial photopolymer resins are toxic and unsuitable as biological implants for the human body. These photopolymers include acrylate-based resin and epoxy systems (Schmidleithner and Kalaskar, 2018). Acrylate-based resins rely on radical photopolymerisation, whilst the epoxy system is based on cationic photopolymerisation (Shirai, 2014; Schmidleithner and Kalaskar, 2018). Acrylate-based resins can cure faster, but epoxy resins show lower shrinkage. Therefore, a new system combining acrylate and epoxy-based resins became a standard in commercial photopolymer products (Schmidleithner and Kalaskar, 2018). CSMA-2 is a novel isosorbide-based polymer with excellent biocompatibility in vitro and in vivo and excellent printability in light-based 3D printing (Owji *et al.*, 2019; Shakouri *et al.*, 2020). Isosorbide is a D-sorbitol derivative demonstrating good mechanical properties due to its bicyclic structure (Nonque *et al.*, 2020). Since isosorbide is derived from sugar, it is a renewable and sustainable bio-based compound (Saxon *et al.*, 2020). It is also inexpensive and non-toxic and has been incorporated into polycarbonates, polyamides, and polyurethane via step-growth polymerisation (Saxon *et al.*, 2019). Good optical clarity makes isosorbide suitable as a monomer for a 3D printing photopolymer (Lai *et al.*, 2019; Saxon *et al.*, 2019).

Light-cured isosorbide-based CSMA-2 has been reported to have mechanical properties similar to human cancellous bone and was non-toxic to

MG63 cell lines (Owji *et al.*, 2019; Shakouri *et al.*, 2020). The previous study successfully and accurately printed solid disc and log pile structures using CSMA-2 as a 3D printing material (Shakouri *et al.*, 2020). ADSC was used in this thesis to explore the cytocompatibility of the 3D printed bone layer scaffold further due to their clinical advantages that include minimally invasive and easily repeatable harvesting procedures (Frese, Dijkman and Hoerstrup, 2016). ADSC is a multipotent adult stem cell that offers more cells in 1 g of tissue than the BM-MSC (Frese, Dijkman and Hoerstrup, 2016). Considering that the age of patients targeted for osteochondral defect treatment is adults over 45 (NICE, 2017), ADSC can be an alternative cell source. However, the final selection of cell type will depend on the accessibility, simplicity of isolation and cultivation, and the associated treatment cost (Yazdanpanah *et al.*, 2022)

Therefore, the objectives of this chapter are:

1. Development of a biomimetic bone scaffold using CSMA-2 as a 3D printing material
2. Optimisation and characterisation of CSMA-2 as a 3D printing material
3. Characterisation of 3D printed CSMA-2 as a bone layer scaffold

2.2. Materials and Methods

2.2.1. Materials

Isosorbide, ethylene carbonate, IPDI (Isophorone diisocyanate), TEGDMA (Triethylene glycol dimethacrylate), DBTBL (dibutyltin dilaurate), HEMA (2-hydroxyethyl methacrylate), penicillin/streptomycin, and L-glutamine were purchased from Sigma Aldrich. α modified Eagle's medium (α MEM), fetal bovine serum (FBS), and MesenPro medium were obtained from Gibco, Life Technologies Ltd., Paisley, UK.

2.2.2. CSMA-2 Synthesis

CSMA-2 synthesis was performed by following previous methods (figure 2.1), and the components involved can be seen in table 2.1 and 2.2. (Owji *et al.*, 2019; Shakouri *et al.*, 2020). The synthesis was started with the synthesis of BHIS (bis(2-hydroxyethyl) isosorbide) by reacting isosorbide (100 g, 684.3 mmol) and ethylene carbonate (132.57 g, 1505.5 mmol) that were degassed under dry nitrogen for 60 minutes. The reaction was then heated on a hot plate for one hour at 70 °C. After the solid components were completely dissolved, the reaction mixture was heated to 170 °C. Then, potassium carbonate (3.0 g, 21.71 mmol) was added, and the mixture was left to react for 48 hours. The resulting BHIS was purified through silica column chromatography using methanol and ethyl acetate (1:9). The purified BHIS was then evaporated in a rotary evaporator to remove the solvents.

The next step was reacting the purified BHIS (32.15 g, 79.37 mmol) with IPDI (57.15 g, 257.07 mmol), TEGDMA (125 g, 436.56 mmol), and five drops (approximately 0.5 ml) of DBTDL at 25 °C for four hours. After that, HEMA (71.42

g, 548.82 mmol) and another 5 drops (approximately 0.5 ml) of DBTDL were added into the reaction mixture and left to react for 12 hours at 25 °C, resulting in the final CSMA-2 monomer as follows:

((3R,3aR,6S,6aR)-hexahydrofuro[3,2-b]furan-3,6diyl)bis(oxy))bis(ethane-2,1-diyl))bis(oxy))bis(carbonyl))bis(azanediyl))bis(3,3,5-trimethylcyclohexane-5,1-diyl))bis(azanediyl))bis(carbonyl))bis(oxy))bis(ethane-2,1-diyl)bis(2methylacrylate)).

Phenylbis(2,4,6-trimethyl benzoyl)phosphine oxide or BAPO (Sigma Aldrich) was used as the photoinitiator to develop photo curability. 2wt% of BAPO was added to CSMA-2 and left to stir for 24 hours. Hydroxyapatite or HA (Captal R, Plasma Biotal, UK) with 1.67 Ca:P ratio and particle size ranging from 6 – 20 µm were added and mixed into CSMA-2 using a speed mixer at 1700 RPM for 2 minutes. HA addition to the CSMA-2 was 5% w/w and 10% w/w. The final CSMA-2 groups were CSMA-2 0HA (without HA), CSMA-2 5HA (5% HA), and CSMA-2 10HA (10% HA).

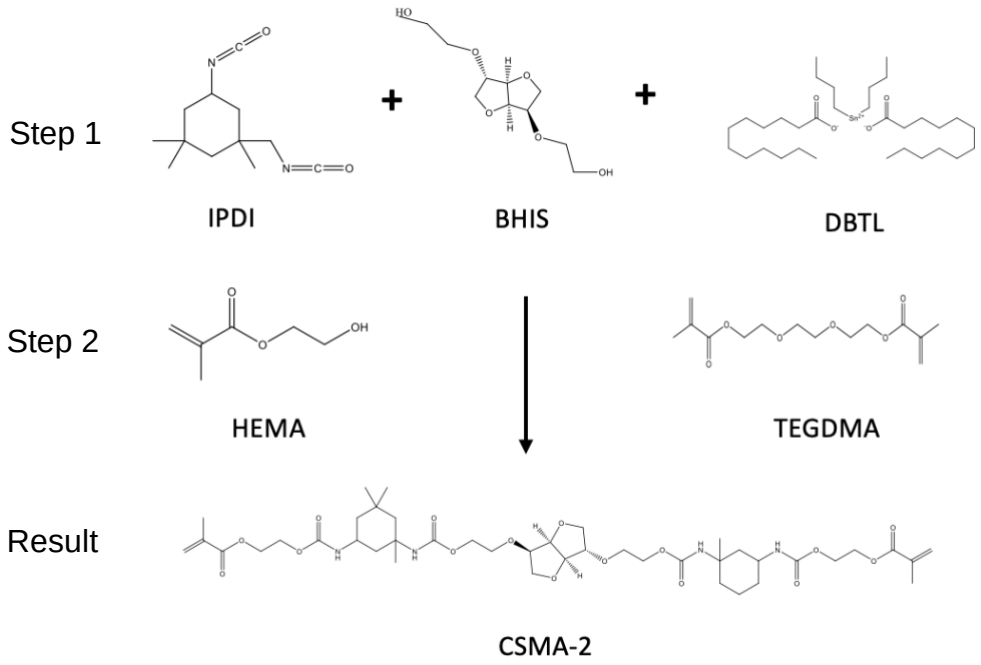

Figure 2. 1. Schematic 2-step reactions of CSMA-2 synthesis.

Step 1. The reaction between IPDI and BHIS creates the monomer backbone with the help of DBTL as the catalyst.
Step 2. The reaction between methacrylate from TEGDMA as the functional group and isosorbide as the backbone. Addition of HEMA as a diluent to help with the dispersion.
Result. Final monomer resulting from the urethan coupling reaction between methacrylate and isosorbide.

Table 2. 1. Components of BHIS synthesis

Components	Amount
Isosorbide	100 g, 684.3 mmol
Ethylene carbonate	132.57 g, 1505.5 mmol
Potassium carbonate	3.0 g, 21.71 mmol

Table 2. 2. Components of CSMA-2 synthesis

Components	Amount
BHIS	32.15 g, 79.37 mmol
IPDI	57.15 g, 257.07 mmol
DBTL	0.5 ml
HEMA	71.42 g, 548.82 mmol
TEGDMA	125 g, 436.56 mmol

2.2.3. CSMA-2 monomer characterisation

2.2.2.3.1. Nuclear Magnetic Resonance

The ^{1}H nuclear magnetic resonance (NMR) spectra were recorded with the AVANCE III 600 spectrometer (600 MHz, Bruker, Germany). $CDCl_3$ was used as a solvent. The data were shown as chemical shifts (δ, ppm) downfield from tetramethylsilane.

2.2.2.3.2. Degree of Conversion

Fourier transform infrared spectroscopy (FTIR series 2000, PerkinElmer, Seer Green, UK) was used to determine the monomer degree of conversion. The CSMA-2 monomer was dropped on the diamond of an attenuated total reflectance accessory (Golden Gate ATR, Specac Ltd., Orpington, UK) and exposed to a Demi Plus LED light-curing unit for 40 seconds at 20 °C. The resolution was set at 4 cm^{-1} with a wavelength range of 800 – 1000 cm^{-1}. The spectra were then recorded to analyse the conversion. Absorbance profiles were measured at 1319 ± 1 cm^{-1} (C-O stretch bond) and 1334 ± 2 cm^{-1} (baseline). The conversion was calculated by using the following formula:

$$C = \left[1 - \left(\frac{Af}{A0} \right) \right] x\ 100$$

C is the conversion, Af is the final absorbance, and A0 is the initial absorbance.

2.2.2.3.3. Rheology

Rheological properties for optimising CSMA-2 formulations were analysed using HAAKE™ Viscotester™ iQ Rheometers (Thermo Scientific, US). A rotational shear test with controlled shear strain from 1 to 1000 $1.s^{-1}$ was performed at 25 °C for 300 seconds. The data were analysed with HAAKE RheoWin software (Thermo Scientific, US).

2.2.4. 3D Printing

Solid and gyroid constructs were fabricated using a Nobel Superfine DLP 3D printer (XYZ Printing, Taiwan) (figure 2.4). Based on existing repositories, the constructs were designed with computer-aided design (CAD) software (Meshmixer, Autodesk, USA). Different scaffold sizes were used for different evaluations. A gyroid scaffold was designed with a 6 mm diameter and a height of 3 mm for cell culture purposes, ensuring compatibility with a standard 96-well plate. A slicing software (XYZware Nobel, XYZ Printing, Taiwan) was used to slice the design and determine the printing setup. The base setup's curing time was 19 seconds with 60 $W.m^{-2}$ power intensity. The curing time for intermediate and model setups was 8.3 seconds with 53 $W.m^{-2}$ power intensity. All setups used 15% of the power level and 0.25 $mm.s^{-1}$ for the speed at 20 °C. The parameter

was determined through a trial-and-error method, considering the impact of high power, which could lead to excessive polymerisation, and low power, which might result in incomplete polymerisation (Zeng, Hsueh and Hsiao, 2023). The detailed setup can be seen in Table 2.3. The printing resolution or layer height was set at 50 μm. After the printing was finished, the samples were washed with 99% methanol (Merck) for 5 – 10 minutes to remove the uncured monomer, then left to dry and underwent a post-curing process with a UV chamber (XYZ Printing, Taiwan) for 1 minute at UV LED power level 3 intensity (16 watt).

Figure 2. 2. The DLP 3D Printer used in this study.

Table 2. 3. 3D printing parameters

Setup	Curing time (s)	Power Intensity ($W.m^{-2}$)	Power Level (%)	Speed ($mm.s^{-1}$)	Temperature (°C)
Base	19	60	15	0.25	20
Intermediate	8.3	53	15	0.25	20
Model	8.3	53	15	0.25	20

2.2.5.1. Printing Resolution and Scaffold Morphology

Scanning electron microscopy (SEM), Zeiss Sigma 300VP (Carl Zeiss Ltd, Cambourne, UK), was used to evaluate the printing resolution and the scaffold morphology. Before the analysis, samples were coated with 95% gold and 5% palladium (Polaron E5000 Sputter Coater, Quorum Technologies, Laughton, UK). Printing resolution was observed by measuring the layer thickness. The printing resolution was set to 100 μm.

2.2.5.2. Wettability

The wettability of the 3D printed scaffold was examined by calculating the surface energy of the 3D printed flat sample surface. Ultrapure water (NANOPure Diamond, Barnstead, US), glycerol (Sigma-Aldrich), and di-iodomethane (GPR) contact angles were obtained using KSV instruments Cam 200 optical contact angle meter (Biolin Scientific, UK). The angles were obtained upon contact with the flat specimen surface with the liquid droplet and measured between the specimen surface-liquid interface and the liquid-air interface.

2.2.5.3. Mechanical Properties

A compressive test was performed using Shimadzu Autograph AGS-X machinery (Shimadzu, Milton Keynes, UK). Preload was performed at 3 $mm.min^{-1}$ speed with a maximum force of 1 N. Next, the cylinders were compressed with a 2 kN load cell and parallel loading plates at a 1 $mm.min^{-1}$ crosshead speed until the sample failed. Gyroid cylinders with six replicates were used as samples. The data was obtained via TRIOS software (TA Instruments, UK).

2.2.5.4. Degradation Rate

3D-printed CSMA-2 scaffolds were incubated in PBS at 37°C. The samples were dried in an oven at 50°C and weighed at each time point. The degradation rate was calculated with the equation below

$$weight\ remaining\ \% = 100 - (\frac{Final\ dry\ weight - Initial\ weight}{Initial\ weight} \text{ x } 100)$$

2.2.6. 3D Printed Scaffold In Vitro Studies

2.2.6.1. 3D cell culture

Human Adipose-Derived Stem Cells (hADSC) were obtained from Lonza and cultured with MesenPRO medium (Gibco), 1% penicillin/streptomycin (P/S) (Sigma-Aldrich), and 1% L-glutamine (Sigma-Aldrich). The cells were incubated at 37 °C and 5% CO_2.

The 3D-printed samples with the gyroid structure were sterilised with 70% alcohol for 15 minutes, washed with PBS (Gibco) twice, and left to dry. UV light sterilisation was then performed for 15 minutes on each side. The samples were soaked with the complete medium and placed in the incubator for 24 hours before cell seeding. After removing the media, passage 5 cells were seeded to the scaffold surface and incubated for 1 hour. Fresh media was added subsequently. The cell density was 5 x 10^3 cells/ scaffold. The media was changed every 2-3 days.

2.2.6.1.1. Metabolic Activity

To analyse metabolic activity, 10% (v/v) alamarBlue (Invitrogen, Thermo Fisher, USA) was added to each well and incubated for 4 hours at 37 °C. Biotek FLx800 microplate reader (BioTek, US) was used to read the fluorescence intensity with 540/35 and 600/40 excitation/emission wavelengths. Four samples were prepared for each scaffold group. The scaffolds were incubated for 21 days.

2.2.6.1.2. Cell Attachment

Cell attachment was analysed by observing hADSC incubated on 3D-printed scaffolds with SEM Zeiss Sigma 300VP (Carl Zeiss Ltd, Cambourne, UK). Scaffolds with cells were fixed in 3% glutaraldehyde and 0.1 M cacodylate buffer and kept at 4 °C for 24 hours. The samples underwent serial ethyl alcohol dehydration and critical drying with hexamethyldisilazane. Samples were coated with 95% gold and 5% palladium. (Polaron E5000 Sputter Coater, Quorum Technologies, Laughton, UK).

2.2.6.2. Osteogenic differentiation

HADSC were cultured with osteogenic media (Mesenchymal Stem Cell Osteogenic Differentiation Medium, PromoCell, Germany) after the cell seeding to induce osteogenic differentiation. Samples were incubated with growth media (see section 2.2.6.1.1) for 1 hour before cell seeding. After cell seeding with 5 x 10^4 cells/scaffold, the samples were incubated for another 1 hour to allow cell attachment. The growth media was removed after 1-hour incubation, and the osteogenic medium was added to the well plate. The osteogenic medium was changed every three days.

2.2.6.2.1. Calcium Deposit

Alizarin red staining (Sigma Aldrich) was performed to evaluate the calcium deposit of hADSC cultured in the 3D-printed scaffold. The staining was carried out on day 7, 14, and 21. First, the media was removed from the samples and washed using PBS three times. Next, 2% w/v alizarin red staining solution was added to the scaffold samples and incubated for 5 minutes at room temperature. The staining was then removed by washing the scaffold using PBS (Gibco). The stained scaffolds were photographed using a Canon EOS camera 1300D, Nikon lens AF Micro NIKKOR 55 mm, 1:2.8, and EOS Utility software 3.0.

2.2.6.2.2. Protein Expression

Immunofluorescence was performed to observe the protein expression of the hADSC. RUNX2 (Runt-related transcription factor 2), OCN (osteocalcin), and OPN (osteopontin) expression were observed as markers of osteogenic differentiation on day 7, day 14, and day 21. The samples were fixed with 4% v/v paraformaldehyde for 10 minutes according to the time points and then washed three times with ice-cold PBS. The samples were incubated for 10 minutes with 0.1% v/v Triton X (BDH Laboratory, UK) and then washed with PBS (Gibco) three times for 5 minutes. The samples were incubated with 1% w/v BSA (Thermo Scientific, US) for 30 minutes to block the unspecific binding of the antibodies. Primary antibody incubation of RUNX2 (1:200)(Ab192256, Abcam, UK), OCN (1:100)(MAB1419, Novus Biological, US), and OPN (1:200)(ab8448, Abcam, UK) was performed overnight at 4 °C in a humidified chamber. The antibody solutions were then removed, and the samples were washed thrice with PBS, 5 minutes each wash. Secondary antibodies AlexaFluor 488 (1:200)(Abcam, UK) and AlexaFluor 594 (1:200)(Abcam, UK)) were added, and the samples were

incubated for one hour at room temperature in the dark. After that, the solution was removed, and the samples were rewashed three times with PBS for 5 minutes. For counterstaining, samples were incubated with DAPI (0.4 μg.ml^{-1})(Invitrogen) for 10 minutes and iFluor 647 (Abcam, UK)) for 30 minutes, then washed with PBS. Images were collected using an Aurox Clarity confocal imaging system (Aurox, Oxfordshire, UK) with an Olympus BX51 microscope (Olympus, Southall, Middlesex, UK), pco.edge 4.2 camera, CoolLED pE-4000 light source (CoolLED, Andover, UK) and Visionary software (Aurox, Oxfordshire, UK).

2.2.6.2.3. Gene Expression

Gene expression assay was performed by isolating the RNA from samples using Direct-zol RNA kits (Zymo Research, US) according to the kit protocol on day 7, day 14, and day 21. Three biological replicates and two technical replicates were used. Isolated RNA from the samples were converted to cDNA using a High-Capacity cDNA Reverse Transcription Kit (Applied Biosystems, ThermoFisher Scientific, US). Real-time quantitative polymerase chain reaction (RT-qPCR) was performed using TaqMan Fast Advanced Master Mix (Applied Biosystems, ThermoFisher Scientific, US) and TaqMan gene expression assay (Applied Biosystems, ThermoFisher Scientific, US). The target genes were RUNX2 (Hs01047973_m1), SPP1 (osteopontin) (Hs00959010_m1), and GAPDH (Hs02786624_g1) as reference. RT-qPCR was processed using Applied Biosystems 7300 Real-Time PCR System (ThermoFisher Scientific, US). The CT value of each target gene was subtracted by GAPDH CT values from the samples. The ΔCT of the sample group was then subtracted by the ΔCT of the hADSC seeded on the tissue culture plate with osteogenic media (control) at the

same time point to obtain ΔΔCT. The final values were $2^{-\Delta\Delta CT}$ or relative gene expression.

Table 2. 4. Target genes for osteogenic gene expression assay

Target gene	Assay ID
GAPDH	Hs02786624_g1
RUNX2	Hs01047973_m1
SPP1/OPN	Hs00959010_m1

$$\Delta Ct = Ct\ (\text{gene of interest}) - Ct\ (\text{housekeeping gene})$$

$$\Delta\Delta Ct = \Delta Ct\ (\text{Sample}) - \Delta Ct\ (\text{Control})$$

$$\text{Fold gene expression} = 2^{-(\Delta\Delta Ct)}$$

2.2.7. Statistical Analysis

Data were presented as a mean and standard variation or box plot. Statistical analyses were conducted using GraphPad Prism 10. One-way ANOVA with Tukey post-test analysis was used.

2.3. Results

2.3.1. CSMA-2 Monomer Characterisation

^{1}H NMR results confirmed the formation of the CSMA-2 monomer (figure 2.3). The three singlets showed at 6.11, 5.58, and 1.92 ppm corresponded to the protons of the methacryl group (CH_2=C−CH_3). The 2.91 and 0.93 ppm signals corresponded to the isophorone's protons.

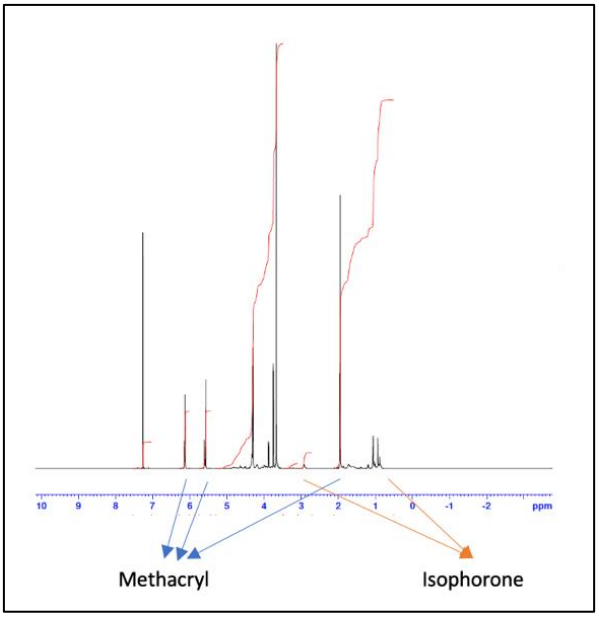

Figure 2. 3.[1]H NMR spectra showing the chemical bond of CSMA-2 monomers.

The blue arrow indicates three singlets corresponding to the methacrylate group's protons. The red arrow depicts signals from the isophorone's proton of the CSMA-2 monomer backbone.

Each CSMA-2 group demonstrated a similar conversion rate and was not significantly different after exposure to UV light. More than 50% of the monomer was polymerised, as can be seen in figure 2.4A. The conversion rates for CSMA-2 0HA, CSMA-2 5HA, and CSMA-2 10 HA were 62%, 56%, and 60% respectively.

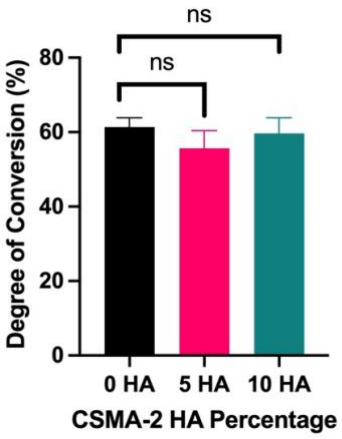

A

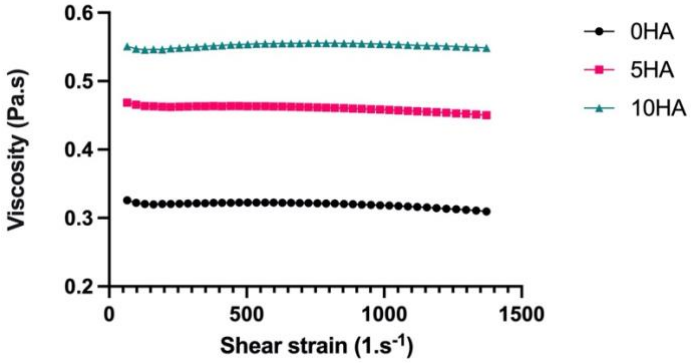

B

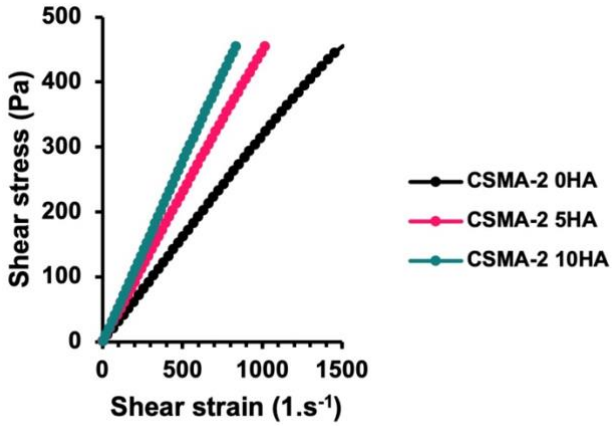

C

Figure 2. 4. Chemical and rheological characterisation of CSMA-2 monomers.

A. The degree of conversions of CSMA-2 monomers with and without HA were above 50%. .The addition of HA did not affect the degree of conversation. NS = not significant
B. Constant viscosity throughout different shear strains of CSMA-2 monomer. The addition of HA increased the monomer viscosity.
C. Linear stress-stain relationship of CSMA-2 monomer.

CSMA-2 rheological properties were then analysed for printability and 3D printing settings. As can be seen from figure 2.4C, the shear stress of CSMA-2 with and without HA is proportional to shear strain. This is a typical Newtonian material flow behaviour. The addition of HA fillers increased CSMA-2 viscosity but did not change its Newtonian properties, as confirmed by figure 2.4B, since the viscosity is constant throughout different shear strains. The viscosity values were approximately 0.3, 0.4, and 0.5 Pa.s for CSMA-2 0HA, CSMA-2 5HA and CSMA-2 10 HA, respectively.

2.3.2. 3D Printing and Scaffold Characterisation

The 3D printing resolution was evaluated by measuring the layer height of a 3D-printed pyramid structure (figure 2.5A). The printing resolution, or the distance between the layers, was set at 100 μm. Based on SEM measurement, the 3D printed resolution for CSMA-2 0HA, CSMA-2 5HA, and CSMA-2 10HA were 86, 83, and 84 μm, respectively (figure 2.5B).

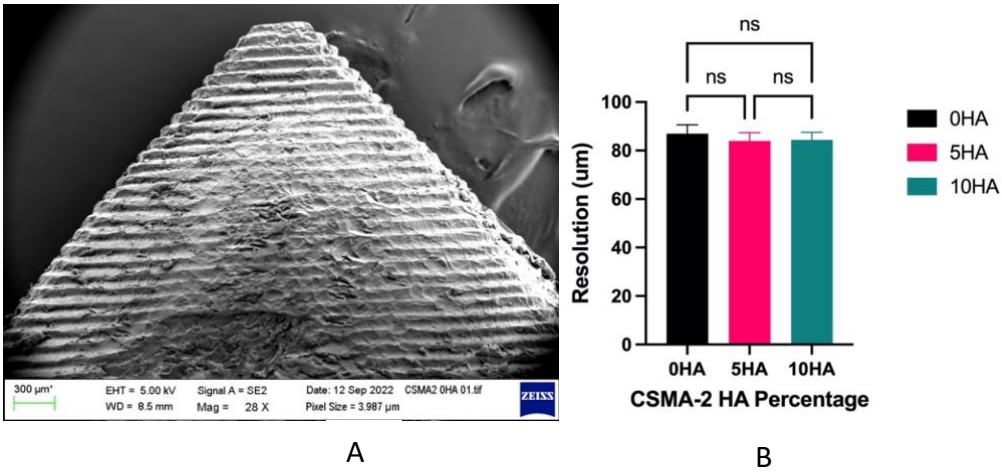

A B

Figure 2. 5. 3D Printing Resolution Evaluation.

SEM image of the pyramid structure used for evaluating the 3D printing resolution. Scale bar = 300 μm. The average layer height of the 3D-printed pyramid structure. There was no significant between CSMA-2 without and with HA addition. The final layer height was approximately 80 μm.
NS= not significant

A complex gyroid structure with interconnected pores was successfully printed using DLP and CSMA-2 as the photopolymer. Figure 2.6A shows CAD and 3D printed scaffolds with apparent similarities between the design and the 3D printed construct in dimension and architecture. Due to the nature of the gyroid structure, it was challenging to measure the size of the pore 2-dimensionally. The average pore diameter on the CAD is approximately 500 μm, whilst the average pore diameter on the 3D-printed structure was around 400 μm. The colour of the 3D-printed scaffold could be described as ivory, with different opacities among the groups. Although adding HA increased the mixture's viscosity, the 3D printing process and the result were not significantly affected. Macroscopically, structure and size were not significantly different among the CSMA-2 groups. However, figure 2.7 A-C showed different surface morphology as expected. The higher the HA content, the roughness of the surface also increased. A relatively smooth surface can be observed on a 3D printed CSMA-2 scaffold without HA, whilst CSMA-2 5HA and 10HA showed rough and irregular surface morphology.

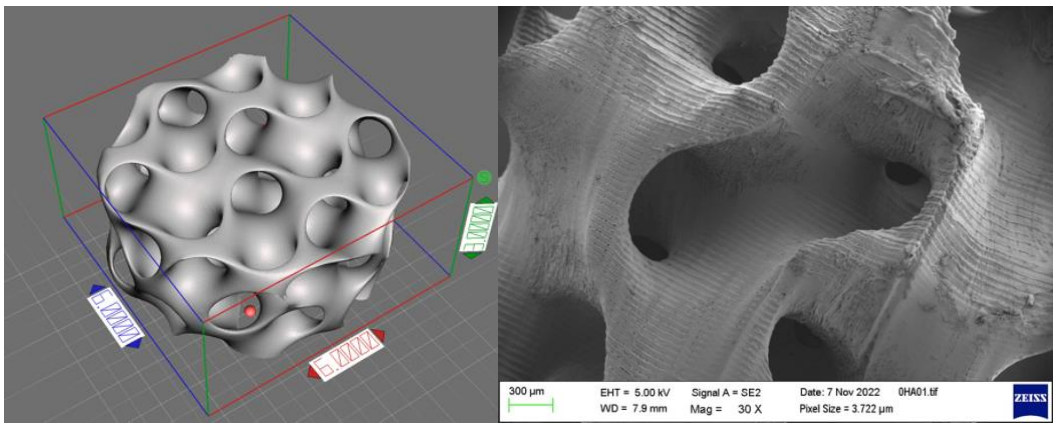

A

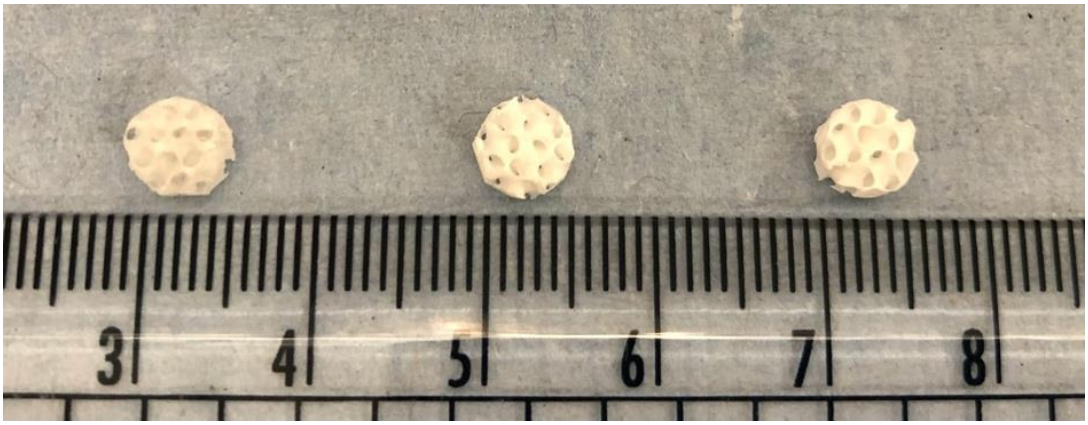

B

Figure 2. 6. The design and 3D-printed gyroid scaffold are used in this chapter.

Left: CAD of the gyroid with 6 x 6 x 3 mm in size. Gridlines are in 0.5 mm.
Right: SEM image of 3D printed gyroid structure with CSMA-2. Scaler bar = 300 μm
3D printed structures of the CAD with different CSMA-2 and HA formulations.
From left to right: 0HA, 5HA, and 10HA.

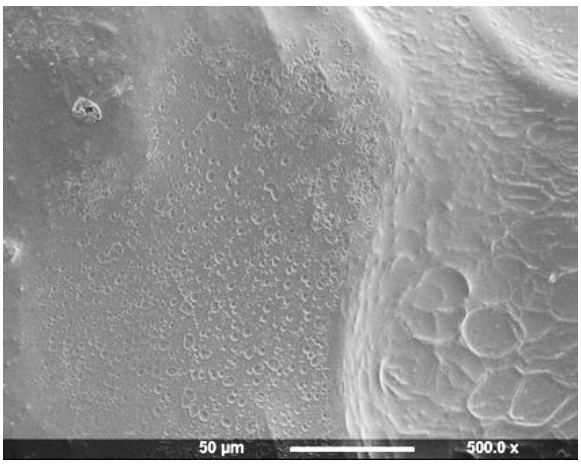

A

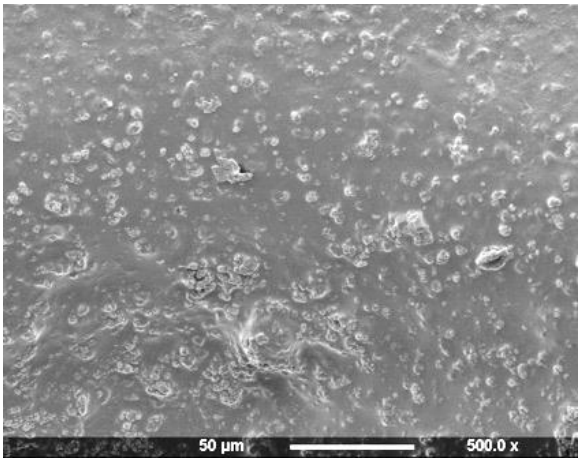

B

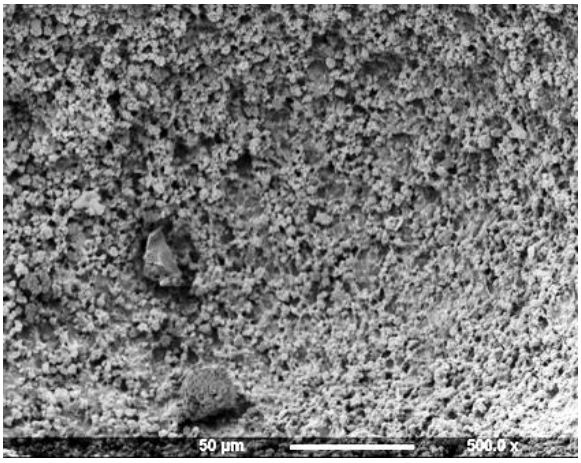

C

Figure 2. 7. SEM images show different surface morphology of 3D printed gyroid scaffolds.

The roughness of the surface increased following the increasing percentage of HA. Scale bar = 50 µm. A. CSMA-2 0HA. B. CSMA-2 5HA, C. CSMA-2 10HA.

The water contact angle was lower on the surface of 3D printed scaffolds with HA, whilst the surface energy was higher. The water contact angle was 76±5.7°, 74°±7,4, and 62°±7.8 for CSMA-2 0HA, CSMA-2 5HA, and CSMA-2 10HA, respectively (figure 2.8A). CSMA-2 0HA, CSMA-2 5HA, and CSMA-2 10HA had surface energy of 41, 47, and 53 $mN.m^{-1}$, respectively (figure 2.8B).

As can be seen from figure 2.8C, CSMA-2 10 HA showed the highest compressive modulus (0.54 GPa) among the group, followed by CSMA-2 with 5HA (0.51 GPa), and CSMA-2 0HA (0.43 GPa).

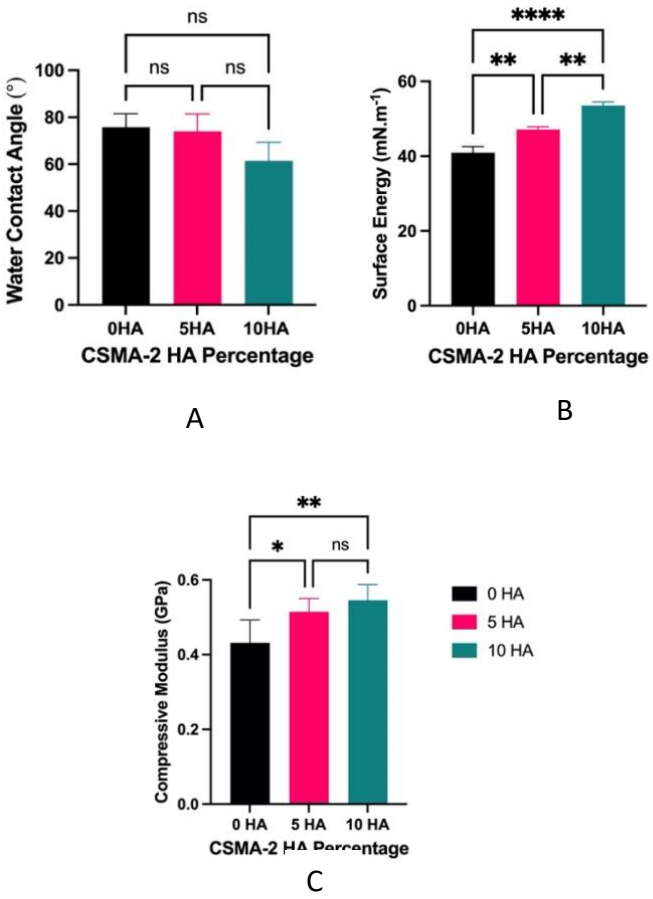

Figure 2. 8. Physical and mechanical properties of the 3D printed CSMA-2 scaffolds.

A. The water contact angle of 3D printed CSMA-2 scaffolds. The hydrophilicity of the 3D printed scaffolds was confirmed with a water contact angle lower than 80°. No significant difference was observed between CSMA-2 without or with HA.

B. The surface energy of 3D printed CSMA-2 scaffolds. The surface energy increased following the increasing percentage of HA. The addition of HA influenced the surface energy significantly.

C. The compressive modulus of 3D printed CSMA-2 scaffolds. The compressive moduli ranged from approximately 0.4 – 0.5 GPa. The addition of HA significantly increased the compressive modulus. There was no significant difference between CSMA-2 with HA groups.

*N = 3. Data presented as mean and ± SD. NS = not significant. * = $p < 0.05$*

As shown in figure 2.9, 3D-printed CSMA-2 scaffolds degraded to approximately 95% of the initial mass over 52 weeks when incubated in the PBS at 37°C. A weight increase can be observed on week 16, followed by a steady decrease until week 48. There was no significant difference in degradation rate between 0HA, 5HA, and 10HA groups.

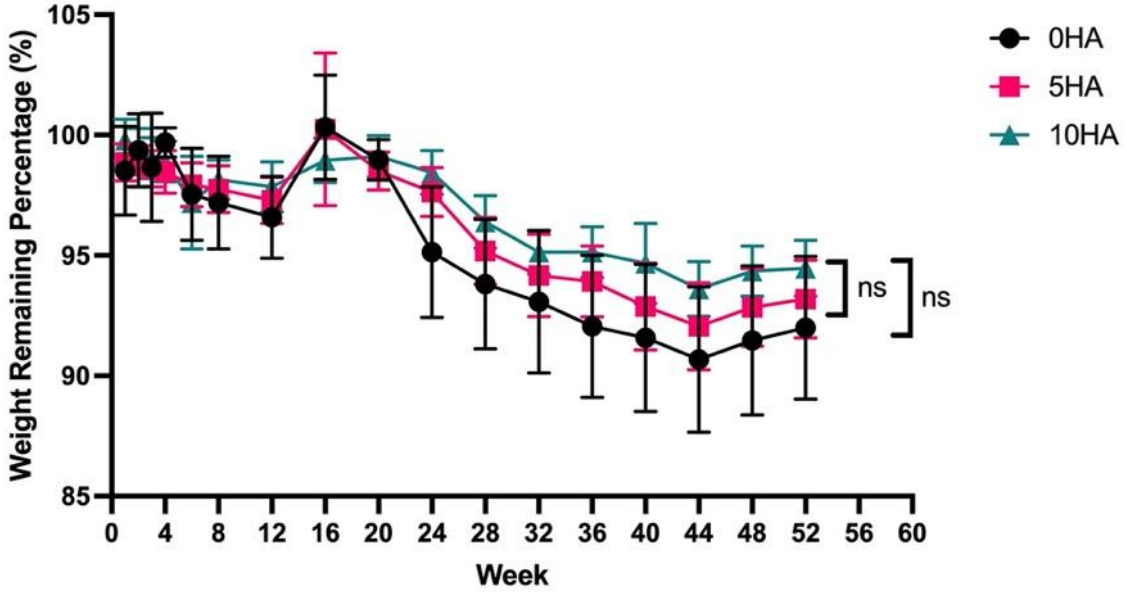

Figure 2. 9. The degradation rate of 3D-printed CSMA-2 scaffolds with various HA percentages.

The scaffolds degraded slowly over the 52-week period. There was an increase in scaffold weight on week 16, followed by a steady decrease until week 44. There was no significant difference between scaffold groups. N = 5. Data presented as mean and ± SD. NS = not significant.

In general, the metabolic activities of hADSC cells were higher when cultured with growth media than with osteogenic media (figure 2.10). CSMA-2 0HA showed the highest cell growth in osteogenic and growth media, particularly on day 21. However, there were differences in metabolic activity trends between osteogenic and growth media scaffold groups. In osteogenic media, hADSC metabolic activity peaked on day 7 and decreased on days 14 and 21. The hADSC incubated in growth media continued to increase and peaked on day 21, except for the CSMA-2 5HA group, which showed the highest metabolic activity on day 14.

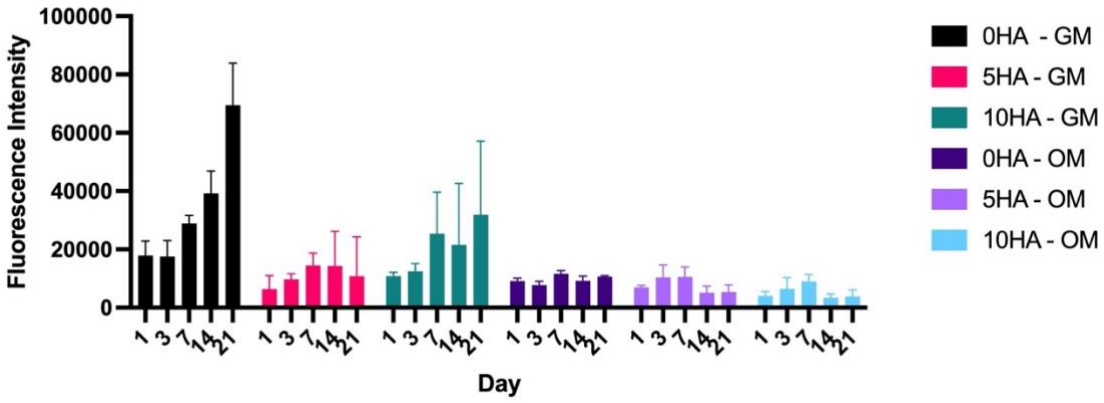

Figure 2. 10. Metabolic activity result of hADSC cells seeded on 3D printed CSMA-2 scaffolds with different media.

The metabolic activity trend differed between scaffolds incubated in osteogenic and growth media. The growth media incubation showed a steady increase in metabolic activity, whilst osteogenic media incubation showed a plateau with minimum change in metabolic activity.
N = 4. Data presented as mean ± SD. OM: osteogenic media, GM: growth media.

Figure 2.11 shows hADSC attachment on 3D printed CSMA-2 scaffolds. The cells were found to attach and spread on the scaffolds. Different surface morphology of scaffold groups was also noticeable, with CSMA-2 5HA and 10HA scaffolds showing rougher surface morphology than CSMA-2 0HA groups.

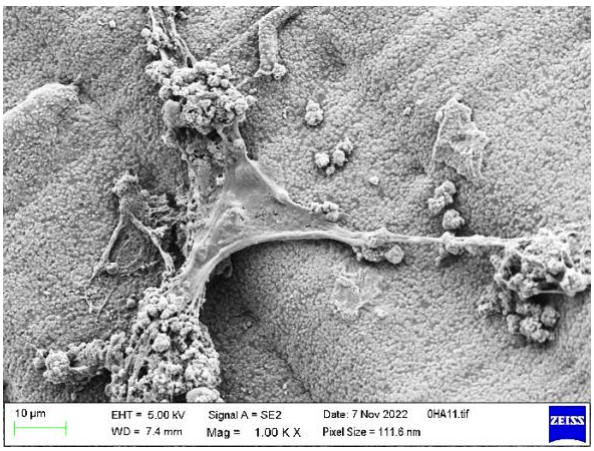

A

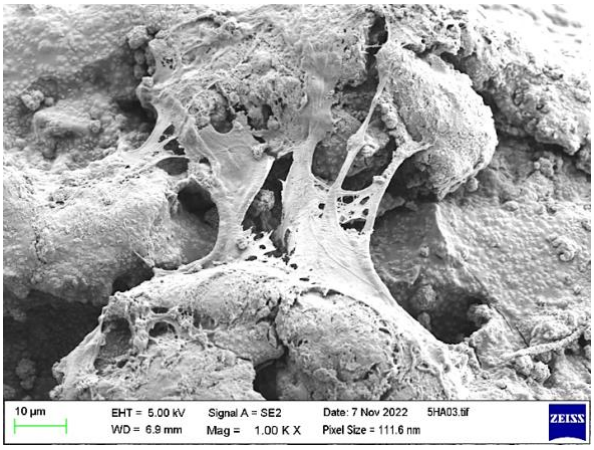

B

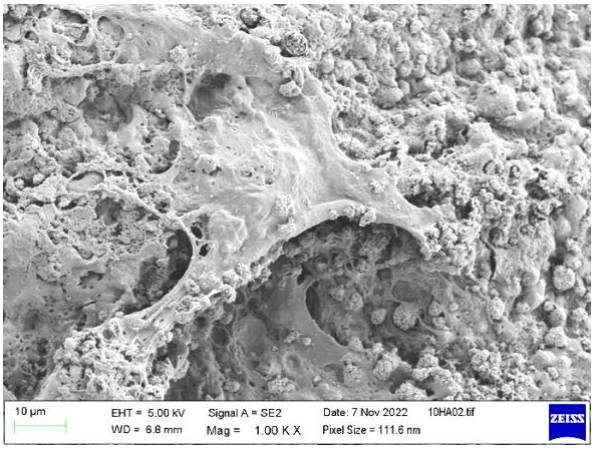

C

Figure 2. 11. Representative SEM images of hADSC attachment on 3D printed CSMA-2 scaffolds.

Cells were found to attach to the scaffold surface. The scaffold surface also showed different roughness, with CSMA-2 5HA and 10HA demonstrating a rougher surface than CSMA-2 0HA. CSMA-2-0HA. B. CSMA-2 5HA. C. CSMA-2 10HA. Scale bar = 10μm

Alizarin red staining images (figure 2.12) show the different staining intensities between various media and scaffold groups. Scaffolds incubated in osteogenic media showed stronger positive staining than growth media ones. The staining was more intense on scaffolds with HA, although the CSMA-2 0HA scaffold incubated in osteogenic media showed increasing intensity on day 14. The staining intensity also increased following the incubation period.

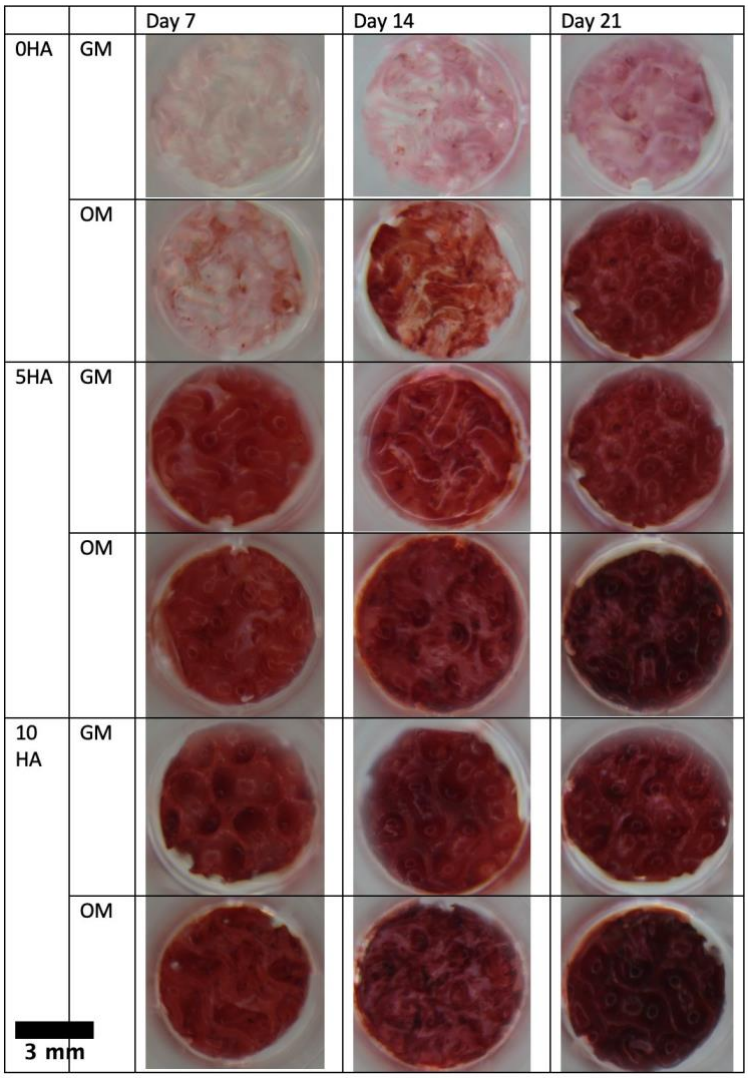

Figure 2. 12. Alizarin red staining results of hADSC incubated on CSMA-2 scaffold.

The staining gradually turned darker with the increasing incubation period. Scaffolds in OM showed relatively stronger positive staining than those incubated in GM. Scaffolds with HA also demonstrated stronger intensity. Scale bar = 3 mm. OM = osteogenic medium. GM = growth medium

Figure 2.13, 2.14, and 2.15 show osteogenic protein marker expression on the CSMA-2 scaffold. RUNX2, OPN, and OCN expressions were detected from day 7 of incubation with osteogenic media. The expression of RUNX2 was relatively stronger on CSMA-2 0HA scaffolds and showed no noticeable difference between the incubation period. OPN expression was also observed on day 7 on all scaffold groups and remained detected until day 21. Similar to OPN, OCN expression can be observed on day 7, with the strongest expression on day 14 and still can be seen on day 21.

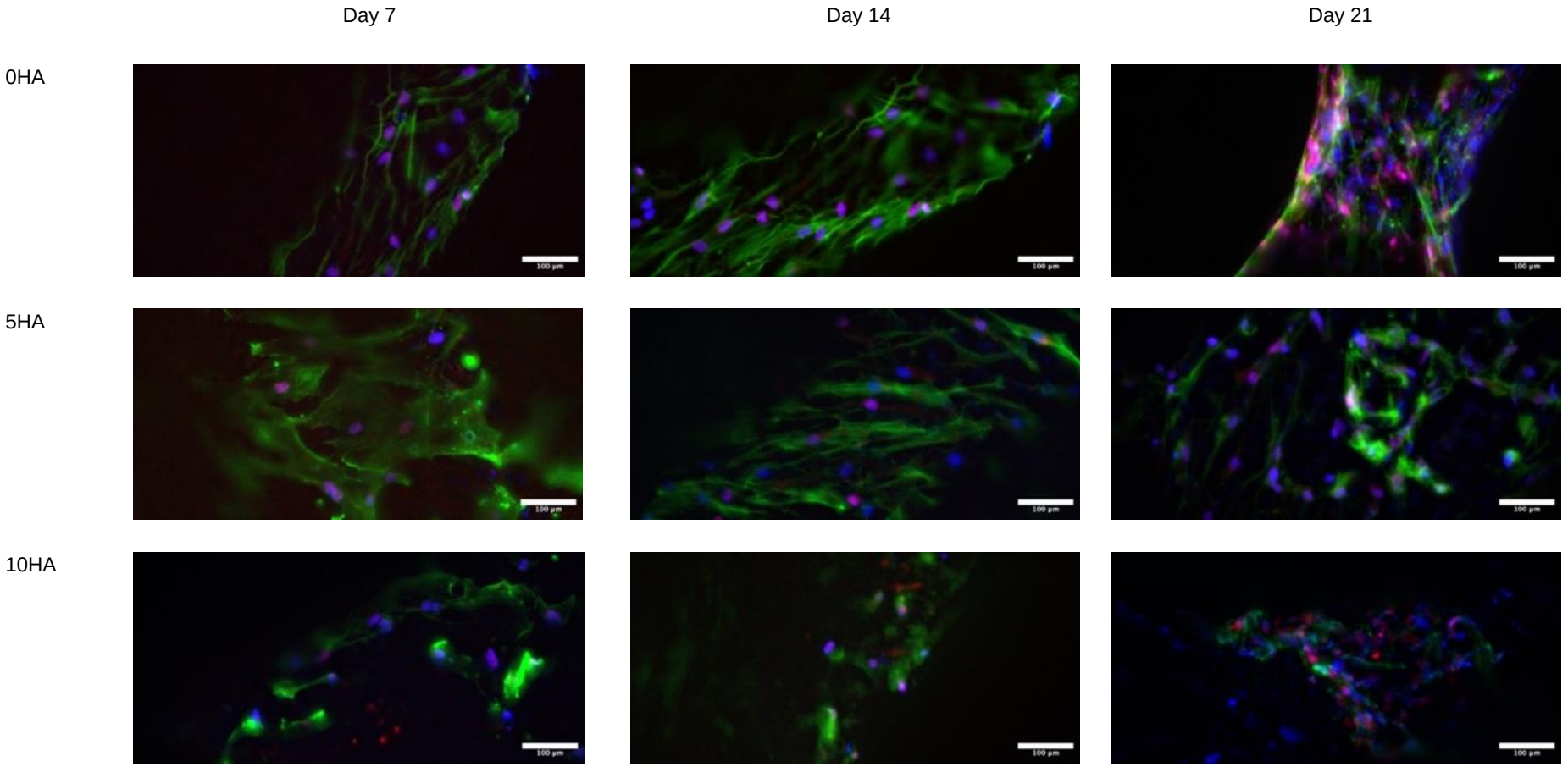

Figure 2. 13. Immunofluorescence images of RUNX2 staining in hADSC cultured on the surface of 3D printed CSMA-2 scaffolds with different HA percentages.

The RUNX2 staining was co-locating with the DAPI staining on the nuclei, hence the purple colour on the images.
RUNX2 (red), DAPI staining on nuclei (blue), and Phalloidin on F-Acting (green). Scale bars: 100 μm.

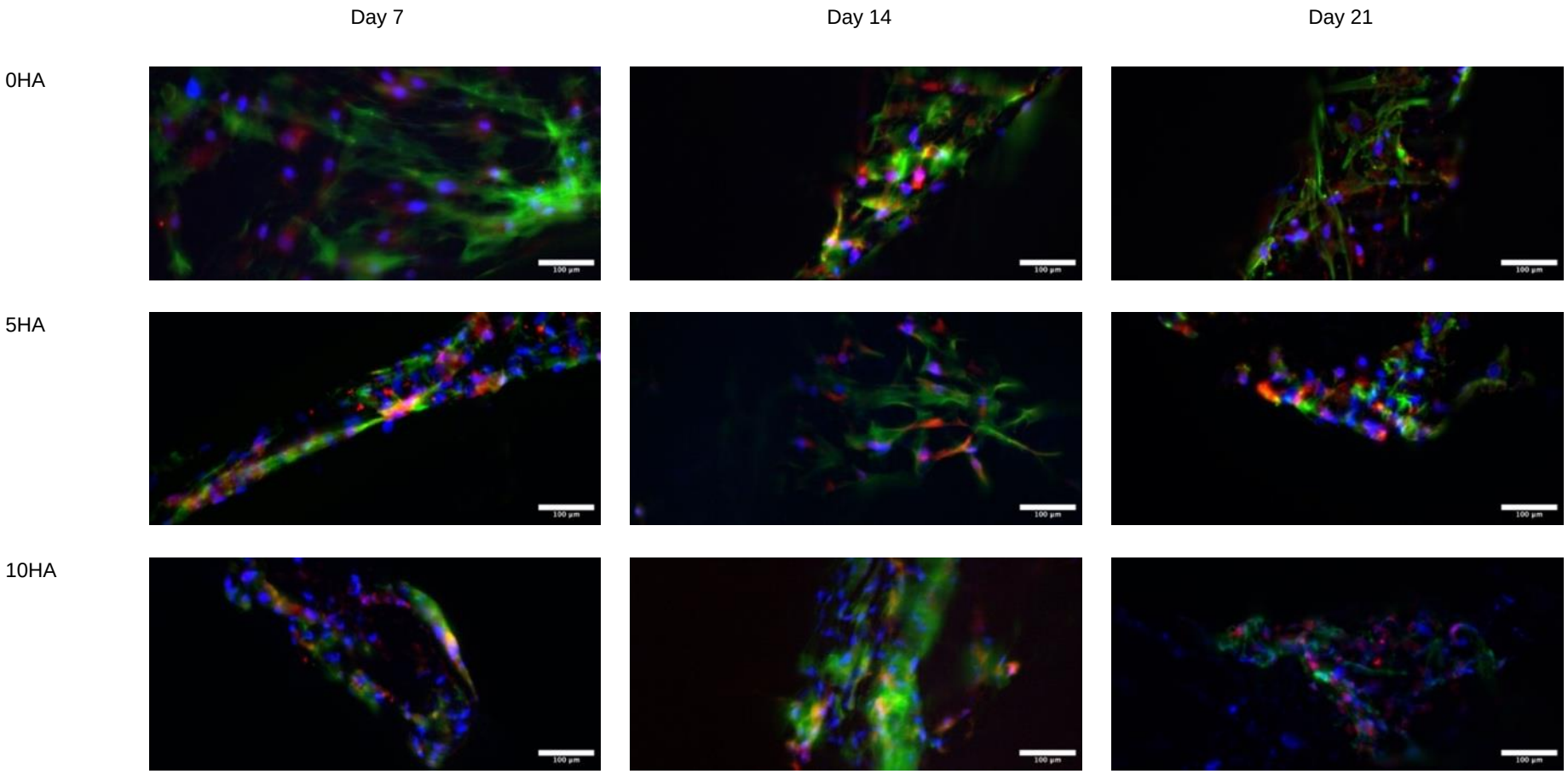

Figure 2. 14. Immunofluorescence images of OPN staining in hADSC cultured on the surface of 3D-printed CSMA-2 scaffolds with different HA percentages.

The OPN staining was relatively less visible on day 7 and getting stronger on day 14 and 21.
OPN (red), DAPI staining on nuclei (blue), and Phalloidin on F-Actin (green). Scale bars: 100 μm.

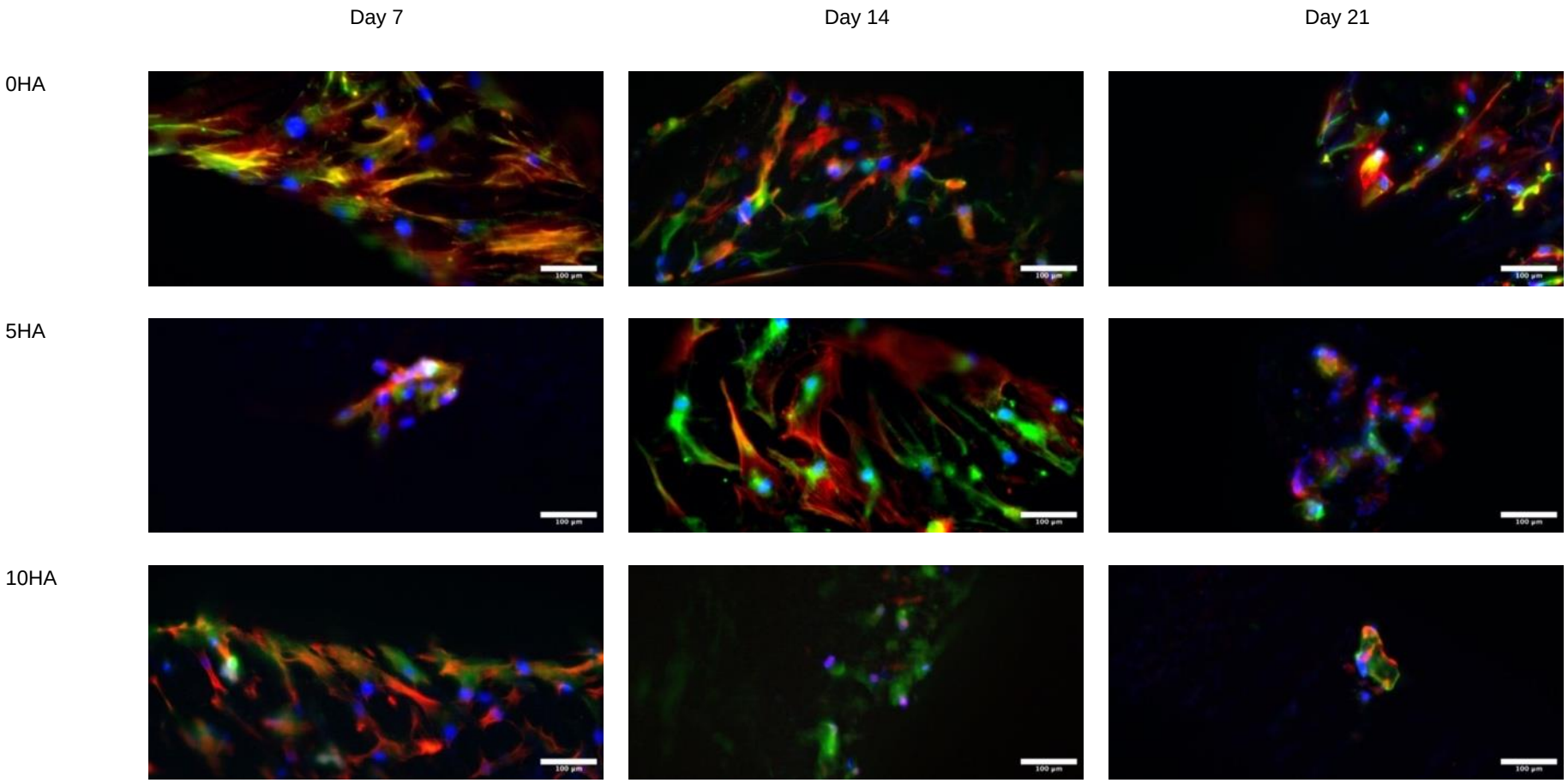

Figure 2. 15. Immunofluorescence images of OCN staining in hADSC cultured on the surface of 3D printed CSMA-2 scaffolds with different HA percentages.

The OCN staining was visibly the strongest on day 14, particularly on CSMA-2 0HA and 5HA.
OCN (green), DAPI staining on nuclei (blue), and Phalloidin on F-Actin (red). Scale bars: 100 μm.

The gene expressions of RUNX2 were not significantly different between CSMA-2 0HA, 5HA, and 10HA (figure 2.16A). However, CSMA-2 0HA scaffolds showed significantly lower OPN gene expression on day 7 and day 21 compared to the CSMA-2 5HA scaffold group. As demonstrated from figure 2.16B, OPN gene expression of hADSC on the CSMA-2 5HA scaffold increased by 2-fold compared to the control at day 7. On day 14, the OPN gene expressions were similar among the scaffold groups

A

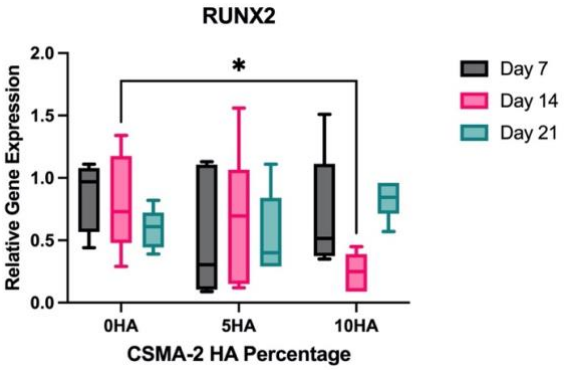

B

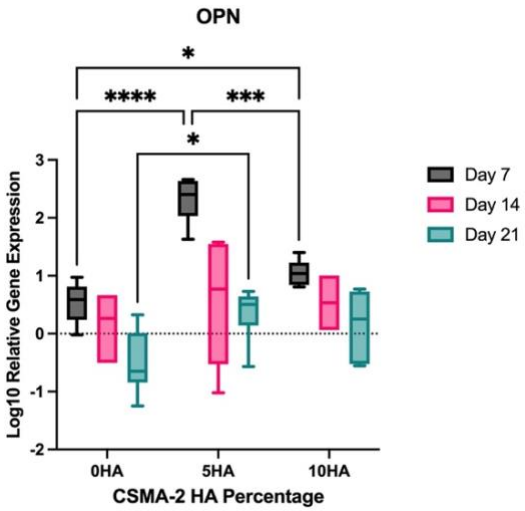

Figure 2. 16. Gene expression of hADSC seeded on 3D printed CSMA-2 scaffolds.

A. RUNX2 gene expression. In general, RUNX2 gene expressions on scaffolds were not different from cells cultured on a well plate in osteogenic media as a control, except for the 10HA group on day 14, which showed significantly lower gene expression.

*B. OPN gene expression. The OPN gene expression was significantly higher on the scaffold with HA. The highest expression can be seen on day 14, then return to the same level on day 7. Biological N = 3, Technical N = 2. Data is presented in a box plot with the line splitting the box representing the median value. * $p < 0.05$.*

2.4. Discussion

CSMA-2 was successfully synthesised by following the previous methods (Owji *et al.*, 2019; Shakouri *et al.*, 2020). The final result of the synthesis was a clear, viscous mixture, which was expected from copolymerising Isosorbide (Lai *et al.*, 2019). This optically transparent mixture enables polymerisation via light curing. The degree of conversion was also similar to previous studies, with more than 50% of the monomer being polymerised after exposure to UV light for less than 1 minute (Owji *et al.*, 2019; Shakouri *et al.*, 2020). This result confirmed that after adding BAPO as a photoinitiator, CSMA-2 could act as a photopolymer suitable for light-based 3D printing. The degree of conversion of dimethacrylate monomer, one of the CSMA-2 components, is also reported to be between 55% and 75% after irradiation (Ozturk *et al.*, 2013). Therefore, it is common for methacrylate monomers to exhibit residual monomers.

Factors that can influence the degree of conversion include the wavelength of the light source. An LED light-curing unit with 450 – 470 nm was used for the degree of conversion analysis with FTIR. The photoinitiator used in this research was BAPO, which has a light absorption ranging from 296 nm to 370nm (Zhang and Xiao, 2018; Bagheri and Jin, 2019). This might affect the degree of conversion since BAPO is more suitable for use with a light source with a lower wavelength, such as a DLP printer with a light source wavelength of 405 nm, which is also why BAPO was chosen. In 3D printing, the residual monomer can be removed following a post-printing process, such as washing with alcohol and post-curing. This process will also improve the quality of the 3D printed structure, particularly those with micropores.

Based on the rheological analysis, CSMA-2 with or without HA was a Newtonian material. Its shear rate was proportional to its shear stress. Every

CSMA-2 mixture group showed constant viscosity throughout different shear rates (figure 2.4b). Different 3D printing methods require different printing materials with different rheological properties. DLP will be more suitable for Newtonian materials since it does not use pressure or extrusion as its printing mechanism. It can fabricate favourable architectures with high resolution that can support bone regeneration, such as interconnected pores with 100 to 400 μm diameter that allow bone ingrowth (Cross and Spycher, 2008; Jia *et al.*, 2021).

Bone architectures also vary in different anatomical structures, e.g. the maxilla and mandible. Jawbones, for example. The maxilla has more trabecular bone than the mandible due to the mandible's dense cortical bone. Therefore, different bone defect requires different bone substitute structure that matches their structure and function. Producing designs with various architectures is relatively straightforward with DLP, which is known for its ability to print fine details with high resolution. 3D printing also allows the fabrication of reproducible and consistent structures within multiple batches and can be based on patient-specific defects.

The structures themselves are produced by photo-polymerisation instead of relying on the material's behaviour and cross-linking after the extrusion for extrusion-based printing or melting for fused deposition modelling (FDM). The bottom-up mechanism of DLP requires materials with the appropriate viscosity. If the viscosity is too low, the surface tension won't be enough to allow the polymer to adhere to the printing platform and undergo base layer curing. It will not allow the uncured excess polymer to drain from the printed layer, reducing the printing resolution if it is too viscous (Lim *et al.*, 2018).

Viscosity is also dependent on additive percentages. Incorporating additives into the photopolymer can improve its mechanical and biological

properties. However, adding HA increased the mixture's viscosity, which might interfere with printing. In addition, additives such as HA can change their rheological and optical properties. Additive particles can scatter the UV light and reduce the printing resolution (Zhou, Fu and He, 2020). Viscous polymers are usually harder to drain, mainly if their design involves micropores. It will be trapped between the micropores and cured along with the subsequent layers. This will result in the loss of fine details, such as pores, that can play an essential role in cell biology.

The 3D printing results showed that the viscosity of CSMA-2 and HA mixtures (0.3 – 0.5 Pa.s) was printable with the DLP method, and complex porous structures like the gyroid could be printed. It has been reported that light-based 3D printing, such as stereolithography, requires viscosity under 5 Pa.s (Yao, Sha and Zhao, 2019b). CSMA-2 could also print at a 0.1 mm resolution setting with a final 3D printed resolution of approximately 0.08 mm. The difference between the printing resolution setting and the final 3D printed resolution of CSMA-2 resin might be caused by the high polymerisation due to UV exposure during the curing process. This shrinkage effect on 3D printing photopolymer is inevitable but can be minimised (Riccio *et al.*, 2021). Since it is known that there was a 0.02 mm difference between the printing resolution and the 3D printed layer thickness, the CAD can be adjusted to take this difference into account. Therefore, CSMA-2 is suitable for light-based 3D printing with high accuracy and precision based on its rheological properties and 3D printing results. It is essential to find the balance between pre- and post-printing properties to ensure the printing-related properties are not significantly affected while improving the 3D printed structure properties.

The colour and opacity of the 3D-printed scaffolds were the only differences observed macroscopically between groups. The colour is nearly similar to human bone; therefore, it is aesthetically acceptable as a biological implant. However, SEM results demonstrated different surface morphology of the scaffolds. In addition, the roughness of the surface increased following the increase in the percentage of HA. These results indicated that although the printing process was not affected, the HA percentage of the polymer affects the surface morphology, particularly the surface roughness.

Since the surface of the 3D printed scaffolds differed, the surface properties such as water contact angle and surface energy also differed. The scaffold groups had a water contact angle of less than 80°, which indicates hydrophilicity (figure 2.8a) (Law, 2014). The angle was higher on the CSMA-2 without HA scaffolds. For surface energy, it was the opposite. CSMA-2 10HA 3D printed structure showed the highest surface energy. Surface energy has been found to affect the hydrophilicity of a material surface. The higher the surface energy, the more hydrophilic the surface. Surface hydrophilicity can also affect cell adhesion and proliferation (Tihan *et al.*, 2009). In addition, surface energy on stiff materials has also been reported to promote osteogenic differentiation of stem cells (Razafiarison *et al.*, 2018). From these results, 3D-printed CSMA-2 scaffolds, with or without HA, demonstrated hydrophilicity that can support cell proliferation and differentiation.

Good mechanical properties are also an essential factor for a successful bone implant. Bones are constantly exposed to mechanical loading, and bone substitutes should be able to withstand the force and surgical implantation procedure. The 3D-printed CSMA-2 porous gyroid scaffold had compressive moduli ranging from 0.4 to 0.5 $N.mm^{-2}$. These values were within the range of

human cancellous bone modulus with porous or trabecular structure (Lai *et al.*, 2015). Ideal scaffolds for bone repair are expected to have compressive strength comparable to native bone, and incorporating isosorbide has been reported to improve the mechanical properties of polymers (Roohani-Esfahani, Newman and Zreiqat, 2016b; Saxon *et al.*, 2020).

The photoinitiator used in this work might also influence the mechanical properties. Previous studies have reported that BAPO was an efficient initiator for polymer crosslinking polymers such as poly(propylene fumarate) or PPF (Timmer, Ambrose and Mikos, 2003). As mentioned before, the light absorption of BAPO is more suitable for most DLP printers with UV projectors that have a 405 nm wavelength. In addition, the match between the material and the 3D printer light source affects the mechanical properties of the 3D printed structure. These findings indicated the suitability of CSMA-2 for high-resolution 3D printing that can fabricate non-toxic scaffolds with adequate strength.

Mechanical strength is essential to maintain the integrity of the bone graft with the surrounding host tissue during the union period. Bone union in large bone defects has been reported to occur up to 33 months after the implantation of bone substitutes (Migliorini *et al.*, 2021; Feltri *et al.*, 2022). 3D-printed CSMA-2 scaffolds remained stable after one year of incubation, with approximately 5% of mass loss. A weight increase in all scaffold groups can be observed on week 16, followed by a steady decrease. This trend signalled the occurrence of bulk degradation. The increasing weight might be caused by increasing water content. This type of degradation usually occurs on hydrophilic polymers (Lin and Anseth, 2013). Since the scaffolds degraded slowly, they could support the union process, particularly for the load-bearing areas. The gyroid structure has been reported to contribute to the integrity of 3D-printed scaffolds (Germain *et al.*,

2018). The layer thickness of the 3D-printed structure was also found to affect the degradation rate, with higher thickness reducing the degradation process.

To analyse the 3D printed CSMA-2 scaffold's cytocompatibility and ability to support osteogenic differentiation, hADSC were seeded. Figure 2.10 shows that the stem cells remained viable for up to 21 days in both media, with those in growth media showing higher metabolic activities. Polymers containing isosorbide, like polyurethane, are known to support cell adhesion, proliferation, and differentiation (Saxon *et al.*, 2020).

Different metabolic activities between stem cells on osteogenic and growth media might be caused by stem cells that were found to reduce their metabolic activity during differentiation (Westhauser *et al.*, 2019). Mature cells like osteocytes slow the production of extracellular matrices that require high energy consumption. During the proliferation period, progenitor cells show high glycolysis, whilst differentiation leads to decreasing glycolysis and increasing mitochondrial oxidation (Shyh-Chang and Ng, 2017). Low glycolysis has also been reported to decrease alamar blue reduction (Abe, Takahashi and Fukuuchi, 2002). These findings could explain why Alamar Blue reduction in samples with osteogenic media was lower than in samples with growth media. hADSC were found to have lower metabolic activities on scaffolds with hydroxyapatite compared to CSMA-2 0HA scaffolds. This result suggested the influence of hydroxyapatite on osteogenic differentiation since the faster the maturation process, the lower metabolic activity was found (Westhauser *et al.*, 2019).

From figure 2.7A-C, it can be seen that CSMA-2 5HA and CSMA-2 10HA had rougher surfaces. Studies have reported that irregular surfaces can affect cell adhesion and morphologies. Scaffolds with a flat surface smaller than the cell size demonstrated elongated cell morphology and slower cell proliferation

(Ramaswamy *et al.*, 2021). This can be caused by the lack of a surface that allows the cells to attach. Cells cultured on planar surfaces showed more mature adhesions than on nano-grooved surfaces (Cassidy *et al.*, 2014). Similar reports also found that adhesion and proliferation of cells on the surface with HA were slower than on smooth and flat culture plates (Deligianni *et al.*, 2000). These findings indicated cell adhesion and proliferation are sensitive to surface roughness that HA addition can affect.

Regarding differentiation, figure 2.12 shows positive Alizarin red staining on the scaffolds, indicating the secretion of calcium phosphate minerals by hADSC. This result also suggested that the cells entered the mineralisation phase, a strong sign of osteogenic differentiation (Rogina *et al.*, 2017). The staining on the scaffolds with HA was stronger than the ones without HA since the HA groups already had calcium in the first place that could react with the staining. However, each scaffold group demonstrated the highest intensity on day 21, in line with the later stage of osteodifferentiation, where matrix mineralisation occurs and calcium deposition increases (Rutkovskiy, Stensløkken and Vaage, 2016).

3D-printed scaffold groups also showed relatively similar expressions of osteogenic protein markers: OCN, OPN, and RUNX2. The expression of these proteins indicates osteogenic differentiation of the cells on the scaffold from stem cells to mature osteoblasts. OCN or bone γ-carboxyglutamic acid (Gla) is non-collagenous and the most abundant protein in the bone that is only expressed by osteoblasts (Moser and van der Eerden, 2019; Komori, 2020). It is also regarded as a differentiation marker of the osteoblast (Nakamura *et al.*, 2009). Since calcium deposition is promoted in the presence of OCN, OCN expression detected from day 7 (figure 2.15) supported the positive result of alizarin red

staining that indicates calcium deposition, which also can be observed from day 7 (Rutkovskiy, Stensløkken and Vaage, 2016).

OPN, or secreted phosphoprotein 1 (SPP1), is a multifunctional protein involved in bone metabolism and remodelling. It is synthesised by osteoblasts, osteocytes, and other hematopoietic cells. OPN gene expression of hASDC was highest on day 7 of incubation on CSMA-2 5HA scaffolds (figure 2.17b). The OPN gene expression decreased on day 14 and day 21 in every scaffold group. The hADSC on CSMA-2 0HA showed the lowest OPN gene expression among the scaffold group. HA has been reported to induce the expression of osteo-specific genes on stem cells quite early by influencing the material surface, leading to gene expression during the first few weeks of the incubation (Lin, Chow and Leng, 2009; Yang *et al.*, 2018). Cell adhesion to HA has been reported to induce signal transduction, leading to sequential expression of genes involved in cell attachment, proliferation, and differentiation (Xu *et al.*, 2016). These gene expressions were caused by Ca^{2+} ion release from the HA (Ma *et al.*, 2017). Ca^{2+} acts as a signalling messenger to induce osteogenic differentiation through BMPs/SMAD and RAS signalling pathways (Viti *et al.*, 2016). The result also suggested that hADSC on CSMA-2 0HA were still proliferating whilst other scaffold groups underwent earlier proliferation arrest and started differentiating. Differentiating cells usually undergo proliferation arrest; this can explain the lower cell number and slower proliferation rate on scaffolds with HA (figure 2.10) (Ruijtenberg and van den Heuvel, 2016).

However, figure 2.17A shows that the RUNX2 gene was expressed quite early by all scaffold groups, including CSMA-2 0HA, similar to RUNX2 protein expression. RUNX2 is a protein essential for osteoblast differentiation and progenitor cell proliferation (Kawane *et al.*, 2018). RUNX2 is required for

preosteoblast proliferation and inducing the commitment of stem cells to differentiate into osteoblast lineage cells (Komori, 2019). Since RUNX2 is weakly expressed in uncommitted mesenchymal stem cells, the expression of RUNX2 in adipose-derived stem cells on CSMA-2 scaffolds indicated their differentiation to immature osteoblasts (Komori, 2019). Unlike OPN and OCN, the RUNX2 gene expressions in our result were unaffected by HA percentage on the scaffold. The presence of aliphatic side chains and cyclohexenes on CSMA-2 that increased the surface charge of the 3D-printed scaffold could promote differentiation without the help of HA (Owji *et al.*, 2022). Furthermore, the metabolic activity was significantly lower in CSMA-2 scaffolds incubated with osteogenic media (figure 2.10). This can be caused by RUNX2 expression that arrests cells in the G0/G1 phase and activates expressions of other genes related to osteogenic differentiation (Xu *et al.*, 2015).

Since CSMA-2 scaffolds can support stem cell differentiation without adding growth factors or protein, future clinical applications will be more straightforward. In clinical application, an osteogenic scaffold can help surrounding progenitor cells from the periosteum or the bone in the recipient site to differentiate into bone cells and initiate bone repair (N. Li *et al.*, 2016). When combined with stem cells as a tissue engineering approach, 3D-printed osteogenic scaffolds can also enable the differentiation process of the incorporated stem cells. Thus, scaffolds promoting osteogenic differentiation have more advantages for the patients.

Nevertheless, certain limitations were encountered during the research regarding this chapter. The study can be improved by adding quantitative analysis, particularly the quantification of alizarin red staining. The absence of a quantitative evaluation limits the confirmation of osteogenic properties of the

bone layer. The gene expression assay also missed OCN as a target gene since it was constrained by the limited time and for experiment optimisation. The absence of OCN gene expression impacted the comprehensiveness of the gene expression analysis designed to parallel the evaluation of protein expression. By recognising these limitations, areas for potential future investigation and refinement can be highlighted.

2.6. Conclusions

This chapter describes the development and optimisation of CSMA-2, an isosorbide-based polymer for bone layer fabrication that showed compatibility with the DLP 3D printing method. The addition of HA fillers did not significantly affect the viscosity of the polymer and was still within the acceptable range of rheological properties for lithography-based 3D printing. The DLP method allows the fabrication of intricate structures with high resolution, accuracy, and precision compared to the commonly used extrusion-based 3D printing. Complex gyroid scaffolds with interconnected pores were successfully printed without a supporting structure that needed removal. The gyroid scaffolds demonstrated mechanical properties similar to the human cancellous bone that shares a similar porous structure. In addition, the 3D-printed scaffolds supported different progenitor cell proliferation and viability. The bone layer scaffold also promoted osteogenic differentiation by showing late markers of osteogenesis. Despite the limitations of this research, these results indicate promising applications in bone tissue engineering.

The work in this chapter was published as:

Verisqa, F.; Cha, J.-R.; Nguyen, L.; Kim, H.-W.; Knowles, J.C. Digital Light Processing 3D Printing of Gyroid Scaffold with Isosorbide-Based Photopolymer for Bone Tissue Engineering. Biomolecules 2022, 12, 1692

Chapter 3. Cartilage Layer Scaffold Development: Characterisation and Optimisation of GelMA

3.1. Introduction

Cartilage differs from bone in physical properties, anatomical structure, and physiology. Cartilage diffuses the mechanical load placed on joints and reduces friction within the synovial joint (Ulici *et al.*, 2022). It also has limited self-regenerative capacity (Li *et al.*, 2019). Articular cartilage pathologies can develop into osteoarthritis, a debilitating joint disease that causes loss of mobility, impaired daily activities, and economic burden in the long run (Litwic *et al.*, 2013).

Cartilage scaffolds are expected to mimic the ECM of native cartilage. Natural polymers such as collagen, gelatin, alginate, and hyaluronic acid are often utilised for cartilage tissue engineering due to their biocompatibility and biodegradability (Medvedeva *et al.*, 2018). However, these natural-derived materials are known for their load-bearing application limitations (Beck *et al.*, 2016). Since articular cartilage is a weight-bearing structure subjected to long-term cyclic loads, providing adequate mechanical properties is essential for cartilage scaffolds (Guo *et al.*, 2020). Tuneable synthetic polymers have been developed to address this requirement. Among hydrogels, gelatin and its derivatives show potential due to their low-cost synthesis, tunable physical and chemical properties, and transparent structure (Yue *et al.*, 2015).

Various techniques have been reported to improve the mechanical properties of synthetic scaffolds, including modifying natural hydrogels with excellent biological advantages. Engineered gelatin-based GelMA is one of the results of this modification. GelMA is synthesised by reacting methacrylate groups with the gelatin's amine group (Lin *et al.*, 2018). Introducing methacryloyl

groups to gelatin enables the photo-polymerisation of GelMA with the help of a photoinitiator and light source. This photocrosslinking process is controllable by adjusting several factors, including the UV-light exposure time (Ding, Illsley and Chang, 2019). Different photocrosslinking conditions' physical, mechanical, and biological results can be significantly different. For example, the stiffness of GelMA can be varied according to the UV exposure time and GelMA concentration. The covalent photocrosslinking in GelMA increases its mechanical properties compared to gelatin (Kulkarni *et al.*, 2022),

GelMA can be synthesised with gelatin from various species (Pahoff *et al.*, 2019). Most of the readily available and commonly used gelatin for GelMA synthesis are porcine type A and bovine type B. Type A GelMA is a product from acid treatment, whilst type B GelMA is produced with alkali treatment (Lee *et al.*, 2016; Pahoff *et al.*, 2019). Type B GelMA has been reported to exhibit higher functionalisation (DoF) than type A since type B has more free amine groups (Pahoff *et al.*, 2019). This free amino group reacts with the methacrylate, producing a higher degree of methacryolation. Several studies have shown that GelMA derived from Bovine type B did not induce an inflammatory response in vivo and in vitro (Sirova *et al.*, 2014; Pahoff *et al.*, 2019). Bovine GelMA also promoted cartilage-like tissue formation more than other hydrogels and accumulated higher GAG than the porcine-derived GelMA (Pahoff *et al.*, 2019). The compressive moduli of bovine-derived GelMA were found to resemble native articular cartilage’s compressive modulus. These favourable properties support the potential of bovine GelMA for cartilage tissue engineering.

Furthermore, the degree of functionalisation (DoF) of hydrogel macromers has been reported as an important determinant of the crosslinking density, which influences a hydrogel’s mechanical properties (X. Li *et al.*, 2016; Pahoff *et al.*,

2019). GelMA with high DoF (above 50%) produces hydrogels with higher stiffness. Prior studies revealed that hydrogel stiffness could affect the morphology of chondrocytes. The stiffer hydrogels could facilitate chondrocyte differentiation, resulting in a typical round cell morphology (X. Li *et al.*, 2016; Pahoff *et al.*, 2019). Elongated cell morphology might indicate that cells are losing the chondrogenic phenotype. It has been reported that round cell morphology is for MSC chondrogenesis (Lin *et al.*, 2019). The spherical organisation of cells can also increase intercellular contact, benefiting chondrogenesis.

Most studies used 10% to 20% GelMA concentration for cartilage tissue engineering (Schuurman *et al.*, 2013; Duchi *et al.*, 2017; Gu *et al.*, 2018, 2020; Onofrillo *et al.*, 2018; Otto *et al.*, 2018). The GelMA concentration percentage is an essential factor in its tunability, and the value is usually determined by the balance between the favourable rheological properties of the GelMA mixture, the crosslinked GelMA scaffold's mechanical properties, and cytocompatibility. According to the previous reports, desired mechanical properties and cytocompatibility have been achieved in GelMA concentrations mentioned above (Schuurman *et al.*, 2013; Duchi *et al.*, 2017; Onofrillo *et al.*, 2018; Otto *et al.*, 2018).

As explained earlier, photo-polymerisation requires a photoinitiator to start the crosslinking process, and lithium phenyl-2,4,6-trimethylbenzoylphosphinate (LAP) is one of the promising photoinitiators (Pahoff *et al.*, 2019). LAP has high water solubility and is easily mixed with hydrogels. It can initiate photo crosslinking at low concentrations and longer light wavelengths (405 nm), thus reducing cytotoxicity in the biological application (Monteiro *et al.*, 2018). Another factor that affects the cytotoxicity of GelMA is the UV exposure time (Ding, Illsley and Chang, 2019). Although UV has been widely used as a light source for

photocrosslinking, it has also been known that prolonged UV exposure reduces cell viability (Monteiro *et al.*, 2018). Therefore, optimising GelMA scaffold fabrication parameters is essential for cartilage tissue engineering. This chapter explored different GelMA concentrations and UV crosslinking time based on previous studies and then determined optimum parameters that provide uncomplicated handling, cartilage-like mechanical properties, and good cytocompatibility. Due to its promising mechanical and biological properties, type B GelMA was used in this thesis.

In summary, the objectives of this thesis chapter are:

1. Characterisation of GelMA solution to find the optimum working condition for cartilage layer scaffold fabrication.
2. Fabrication of GelMA scaffolds with cartilage tissue-like mechanical properties by exploring different GelMA concentrations and UV curing durations.
3. Evaluation of GelMA scaffolds cytocompatibility and their chondrogenic properties.
4. Determination of the optimum GelMA concentration and UV curing duration for the cartilage layer of the bilayer osteochondral scaffolds.

3.2. Materials and Methods

3.2.1. GelMA Preparation

Lyophilised Bovine GelMA with 80% DoF was obtained from Gelomics (Queensland, Australia). The gelMA mixture was made by mixing lyophilised gelMA with PBS at 40°C to give it a liquid form. 0.1% Lithium phenyl-2,4,6-trimethylbenzoylphosphinate (LAP) (Sigma Aldrich) was added as the photoinitiator and stirred until completely dissolved. The pH of the final GelMA mixture was tested to ensure it had a pH of 7.4. The mixture was then exposed to 405 nm UV light (UV curing chamber, XYZprinting, Taiwan) to check whether it was photo cross-linkable. In this experiment, 5%, 10%, and 20% GelMA (w/v) were prepared to determine which concentration has the balance between physical and biological properties for cartilage tissue engineering.

3.2.2. GelMA Characterisation

3.2.2.1. FTIR Analysis

GelMA mixtures were examined by Fourier transform infrared spectroscopy (FTIR, Series 2000, PerkinElmer, Seer Green, UK) in the range of 600-4000 cm^{-1}. The GelMA in liquid form was dropped on the diamond of an attenuated total reflectance accessory (Golden Gate ATR, Specac Ltd., Orpington, UK), and the spectra were then recorded.

3.2.2.2. Rheology

Rheological properties of GelMA solution with different concentrations were analysed using HAAKE™ Viscotester™ iQ Rheometers (Thermo Scientific, US). The GelMA solution was loaded on the plate at 40°C to analyse the temperature-dependent viscosity. The viscosity was recorded at an oscillating

frequency of 1 Hz and 1% strain with temperature ramping from 4 to 40 °C. Further analysis of the solution behaviour was performed with a rotational shear test with controlled shear strain from 1 to 1000 $1.s^{-1}$ at 37°C for 300 seconds. The data were analysed with HAAKE RheoWin software (Thermo Scientific, US).

3.2.3. 3D GelMA Scaffold Characterisation

3.2.3.1. 3D GelMA Fabrication

GelMA solutions were deposited into a mould and light cured with 405 nm UV light (UV curing chamber, XYZprinting, Taiwan) for 1, 2, and 5 minutes. The solid 3D GelMA was then cut with a biopsy punch according to the size requirement for each characterisation.

Table 3. 1. Experimental GelMA concentration and curing time groups.

GelMA concentration (%)	**Curing time (min)**
10	1
	2
	5
15	1
	2
	5
20	1
	2
	5

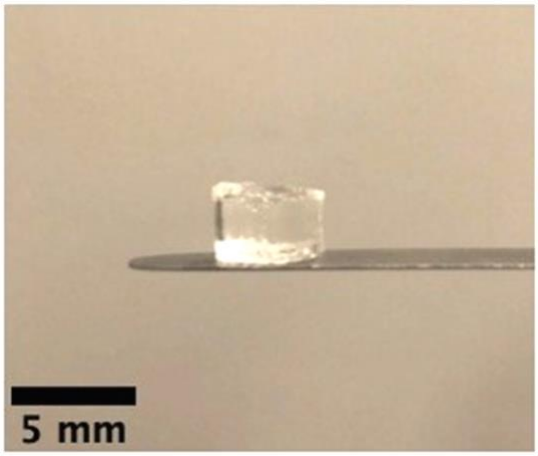

Figure 3. 1. Physical appearance of GelMA scaffold.

After being exposed to UV irradiation, the GelMA mixture solidified into a solid scaffold.

3.2.3.2. Mechanical Properties

Cylindrical 3D GelMA samples underwent the compressive test to analyse the mechanical properties using Shimadzu Autograph AGS-X machinery (Shimadzu, Milton Keynes, UK). Preload was performed at 3 $mm.min^{-1}$ speed with a maximum force of 1 N. Then, the cylinders were compressed at a crosshead speed of 1 $mm.min^{-1}$ until the sample failed. Six replicates were used on this test.

3.2.3.3. Degradability

GelMA samples were incubated in PBS at 37°C. The samples were dried with tissue paper for 5 minutes and weighed at each time point. The degradation rate was calculated using the equation below.

$$weight\ remaining\ \% = 100 - (\frac{Final\ dry\ weight - Initial\ weight}{Initial\ weight}\ \text{x}\ 100)$$

3.2.4. 3D GelMA Scaffold In Vitro Studies

3.2.4.1. 3D Cell Culture

For 3D cell culture, GelMA solutions were filtered with 0.2 μm PES filters before the cell seeding. Two types of cells were used for GelMA in vitro studies. First were the chondrogenic ATDC5 cells, and the second was Human Adipose-Derived Stem Cells (hADSC). ATDC5 cells were obtained from Sigma-Aldrich and cultured with DMEM F12 (Gibco), 10% FBS (Gibco), and 1% penicillin/streptomycin (P/S) (Sigma-Aldrich). hADSC were obtained from Lonza and cultured with MesenPRO medium (Gibco), 1% penicillin/streptomycin (P/S) (Sigma-Aldrich), and 1% L-glutamine (Sigma-Aldrich). The cells were incubated at 37 °C and 5% CO_2. The 3D cell seeding was performed by pipetting 100 μm GelMA solution to the 96 well plates at 37 °C. Passage 5 cells were seeded into the solution, and the well plates were exposed to UV light for 1, 2 and 5 minutes. The cell seeding density was 5 x 10^4 cells/well. Fresh complete growth media was added after the UV curing. The media were changed every 2-3 days.

3.2.4.2. Cell viability

3.2.4.2.1. Metabolic Activity

Cell viability was investigated by analysing the metabolic activity of the 3D cell culture and live cell visualisation. Alamar blue 10% (v/v) Invitrogen, Thermo Fisher, USA) was added to each well and incubated for 4 hours at 37 °C. A Biotek FLx800 microplate reader was used to read the fluorescence intensity with 540/35 and 600/40 excitation/emission wavelengths. Four samples were prepared for each GelMA group.

3.2.3.2.2. Live Cell Visualisation

The GelMA samples were stained using the LIVE/DEAD® Viability/Cytotoxicity Kit (Thermofisher) for live cell visualisation. The working solution was made by adding 20 µL of 2 mM EthD-1 to 10 mL PBS. After vortexing the solution, 5 µL of 4 mM calcein AM was added. The samples were washed with PBS twice and soaked with fresh media before adding 100 – 150 µl of working solution. The samples were then incubated for 30 minutes at 37 °C. Images were obtained using a Leica DM IRB microscope with 10x magnification.

3.2.4.3. Chondrogenic Differentiation

After cell seeding, chondrogenesis was induced by culturing hADSC with chondrogenic media (StemPro, Gibco). Chondrogenic media was added to the crosslinked GelMA after the UV irradiation. The media was changed every three days.

3.2.4.3.1. Glycosaminoglycan Evaluation

Alcian blue (Sigma Aldrich) staining was performed to evaluate the glycosaminoglycan content of the 3D GelMA construct. The staining was carried out on day 7, 14, and 21. The media was removed from the samples and washed using PBS three times. Next, 0.1% alcian blue Staining solution was added to the samples and incubated for 5 minutes at room temperature. Excess staining was removed by washing the samples with PBS several times. The stained samples were photographed using a Canon EOS camera 1300D, Nikon lens AF MICRO NIKKOR 55 mm 1:2.8, and EOS utility software 3.0.

3.2.4.3.2. Protein Expression

Immunofluorescence was performed to observe hADSC protein expression. SOX9 and Collagen II protein expressions were observed as chondrogenic markers on day 7, 14, and 21. The samples were fixed with 4% v/v paraformaldehyde for 10 minutes following the time points and then washed three times with ice-cold PBS. Next, the samples were incubated for 10 minutes with 0.1% v/v Triton X (BDH Laboratory, UK) and washed with PBS (Gibco) three times for 5 minutes. The samples were incubated with 1% w/v BSA for 30 minutes to block the unspecific binding of the antibodies. Primary antibody incubation of anti-SOX9 (CL0639) (1:200) and anti-Collagen IIC (ab34712) (1:200) was done overnight at 4 °C in a humidified chamber. The antibody solutions were then removed, and the samples were washed thrice with PBS, 5 minutes each wash. Secondary antibodies AlexaFluor 488 (1:200) and AlexaFluor 594 (1:200) were added, and the samples were incubated for one hour at room temperature in the dark. After that, the solution was removed, and the samples were washed three times with PBS for 5 minutes. For counterstaining, samples were incubated with DAPI (0.4 µg/ml) for 10 minutes and iFluor 647 for 30 minutes, then washed with PBS. Images were collected using Aurox Clarity confocal imaging (Aurox, Oxfordshire, UK) with an Olympus BX51 microscope (Olympus, Southall, Middlesex, UK), pco.edge 4.2 camera, CoolLED pE-4000 light source (CoolLED, Andover, UK) and Visionary software (Aurox, Oxfordshire, UK).

3.2.4.3.3. Gene Expression

Gene expression assay was performed by isolating the RNA from GelMA samples using Direct-zol RNA kits (Zymo Research, US) according to the protocol on day 7, day 14, and day 21. Three biological replicates and two technical replicates were used. Isolated RNA from the samples were converted to cDNA using a High-Capacity cDNA Reverse Transcription Kit (Applied Biosystems, ThermoFisher Scientific, US). Real-time quantitative polymerase chain reaction (RT-qPCR) was performed using TaqMan Fast Advanced Master Mix (Applied Biosystems, ThermoFisher Scientific, US) and TaqMan gene expression assay (Applied Biosystems, ThermoFisher Scientific, US). The target genes were SOX9 (Hs00165814_m1) and GAPDH (Hs02786624_g1) as reference. RT-qPCR was processed using Applied Biosystems 7300 Real-Time PCR System (ThermoFisher Scientific, US). GAPDH CT values subtracted the CT value of each target gene from the samples, which resulted in ΔCT. The ΔCT of the sample group was then subtracted by the ΔCT of the hADSC seeded on the tissue culture plate with osteogenic media (control) at the same time point to obtain ΔCT. The final values were $2^{-\Delta\Delta CT}$ or relative gene expression.

$$\Delta Ct = Ct\ (\text{gene of interest}) - Ct\ (\text{housekeeping gene})$$

$$\Delta\Delta Ct = \Delta Ct\ (\text{Sample}) - \Delta Ct\ (\text{Control})$$

$$\text{Fold gene expression} = 2^{-(\Delta\Delta Ct)}$$

3.2.5. Statistical Analysis

The data were analysed using one-way and two-way analysis of variance (ANOVA), with post hoc tests of Tukey's on GraphPad Prism 10.

3.3. Results

3.3.1. FTIR

FTIR results of the GelMA mixture and gelatin in figure 3.2 showed a strong and broad peak at 3247cm^{-1}, which can be attributed to -OH groups of the gelatin. N-H bending was detected at 1563 cm^{-1}, which is associated with the backbone structure of gelatin. A strong peak at 1632 cm^{-1} was also observed, indicative of the amide I C=O bond. A peak at 1724 cm^{-1} was only detected on GelMA, suggesting the C=O bond of methacrylic anhydride.

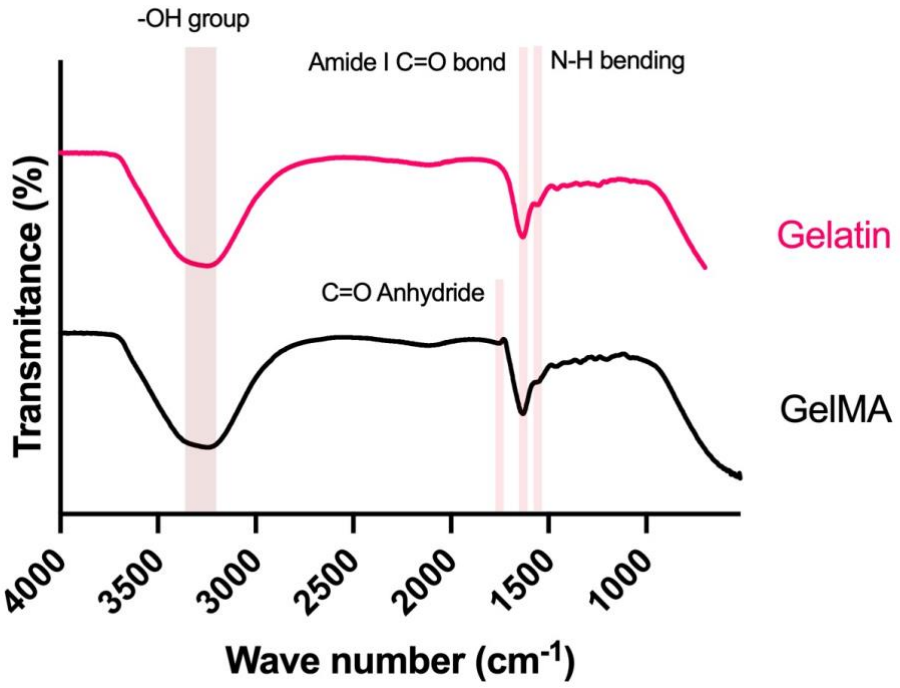

Figure 3. 2. Chemical characterisation of GelMA and gelatin with FTIR.

Gelatin and GelMA shared some peaks at 3247, 1563, and 1632 cm^{-1}, indicating the presence of gelatin. A peak associated with methacrylic anhydride at 1724 cm^{-1} was only detected on GelMA.

3.3.2. Rheology

Rheology results confirmed that GelMA is thermosensitive. Its viscosity changed according to the temperature, as seen in figure 3.3. The higher the temperature, the lower the viscosity of GelMA. The highest viscosity was shown by 20% GelMA at 4 °C (1.7 Pa.s), followed by 15% GelMA (1.4 Pa.s) and 10% GelMA (0.4 Pa.s). Above 25 °C, all the GelMA groups exhibited lower viscosity, 0.003, 0.004, and 0.004 Pa.s for 10%, 15%, and 20% GelMA, respectively. Based on this result, the working temperature of GelMA was set at 37°C, similar to the human body's temperature. At 37°C, all GelMA groups showed Newtonian behaviour since the shear stress was proportional to the shear rate (figure. 3.4). The Newtonian behaviour at low viscosity can reduce the force required of GelMA manipulation, which includes sterilisation and cell encapsulation.

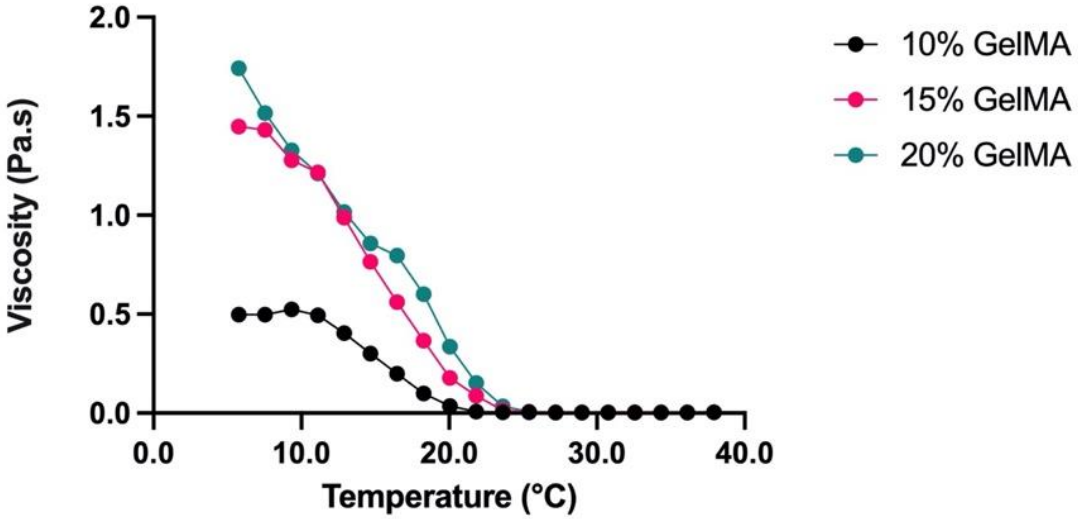

Figure 3. 3. The viscosity changes of GelMA mixtures throughout different temperatures.

The viscosity of GelMA decreased following the increasing temperature. 20% GelMA demonstrated the highest viscosity at 4 °C. The viscosities of different GelMA percentages became similar in higher temperatures, including at 37 °C.

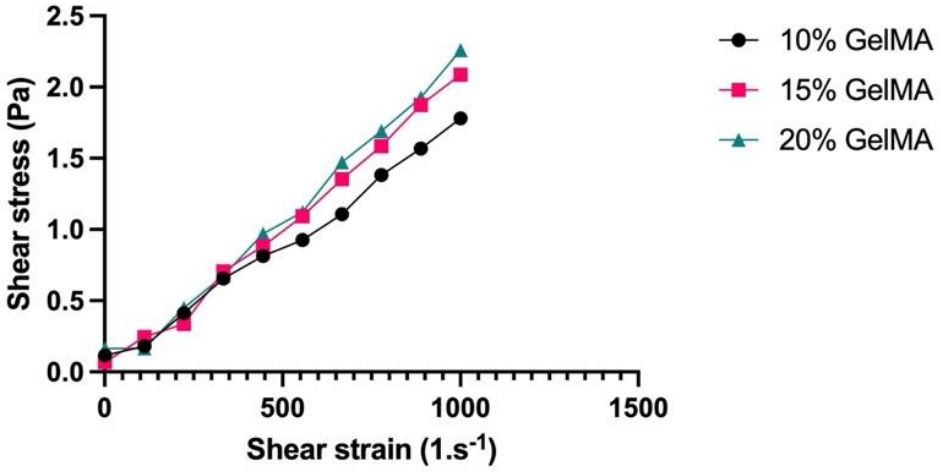

Figure 3. 4. Relatively linear stress-strain relationship of GelMA mixtures at 37 °C.

The proportionality of the stress-strain relation of GelMA at 37 °C confirmed GelMA's Newtonian behaviour.

3.3.3. Compressive Modulus

GelMA samples compressive modulus ranged from 0.5 – 5.1 $N.mm^{-2}$. As can be seen from figure 3.5, The 20% GelMA group generally showed the highest compressive modulus compared to other concentration groups with the same light curing time. The compressive modulus for 20% GelMA exposed to 1 minute, 2 minutes, and 5 minutes of UV light were 4.8, 5.1, and 2.3 $N.mm^{-2,}$ respectively. The 1-minute curing time group demonstrated a higher compressive modulus than other curing time groups, with 10%, 15%, and 20% GelMA showing 0.6, 3.6, and 4.8 $N.mm^{-2}$ of compressive modules. The difference between 10% and 20% GelMA compressive modulus was significant in all curing time groups. Based on the results, the higher the GelMA concentration, the higher the compressive modulus. The lower the light-curing time, the higher the compressive modulus.

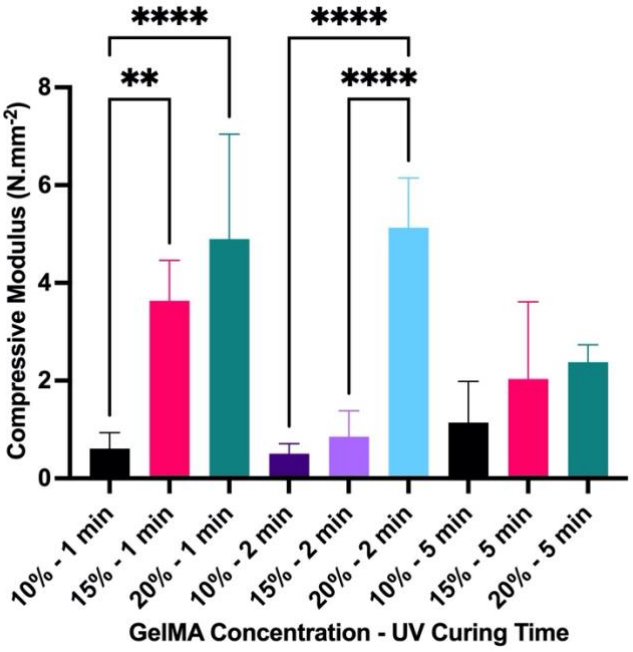

Figure 3. 5. The compressive modulus of different GelMA concentrations and UV curing time.

*10% and 15% GelMA groups showed significantly different compressive modulus with different curing times, implying the influence of UV irradiation duration on the polymerisation and final mechanical properties. Data is presented as mean ± SD. * $p < 0.05$*

3.3.4. Cell Viability

3.3.4.1. Metabolic Activity

The metabolic activities of chondrogenic ATDC5 cells were analysed to evaluate the cytocompatibility of GelMA. Initially, there was no significant difference between the concentration and light-curing groups, with the highest metabolic activity shown by 10% GelMA + 1 minute UV exposure (figure 3.6). However, the rate of metabolic activity increased during the 7-day incubation, which started to differ from day 3. The metabolic activity differences were noticeable on day 3 since there was a significant increase of metabolic activity on 10% GelMA + 1-minute UV and 15% GelMA + 1-minute UV. On day 7, 10% and 15% GelMA + 1-minute UV demonstrated the highest metabolic activity, followed by 10% and 15% GelMA + 2-minute UV. All GelMA that was light-cured for 5 minutes exhibited the slowest increase in metabolic activity.

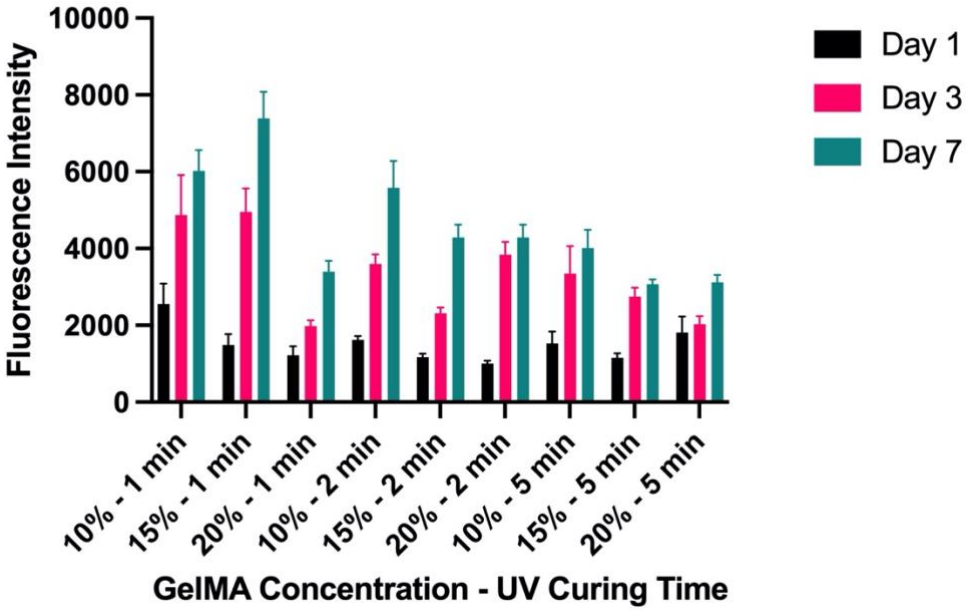

Figure 3. 6. The metabolic activity of ATDC-5 cells cultured in 3D GelMA scaffolds with different concentrations and UV curing time.

All GelMA groups demonstrated a similar trend, increasing metabolic activity from day 1 to day 7 of incubation. 1-minute curing time showed the highest metabolic activity, suggesting the effect of UV exposure duration on cell growth. Data is presented as mean ± SD.

3.3.4.2. Live Cell Visualisation

Live cell visualisation was performed to confirm the cell viability on GelMA samples. On day 1, 10% and 15% GelMA groups generally showed visually brighter green fluorescence representing the live cells than the 20% GelMA group (figure 3.7). At the same time, red fluorescence representing the dead cells was seen in GelMA groups exposed to 5-minute UV light. However, living cells were more visible on day 3 and 7 in the 5-minute curing time groups (figure 3.8 and figure 3.9). This progression was not visible in 20% GelMA groups. Fewer living cells were observed in all 20% GelMA groups on day 3 and 7, regardless of the UV exposure time. Regarding progressive cell proliferation, the 10% and 15% GelMA groups with 1-minute curing times showed more dense colony formation of ATDC5 cells on day 7 of incubation than on day 3.

Day 1

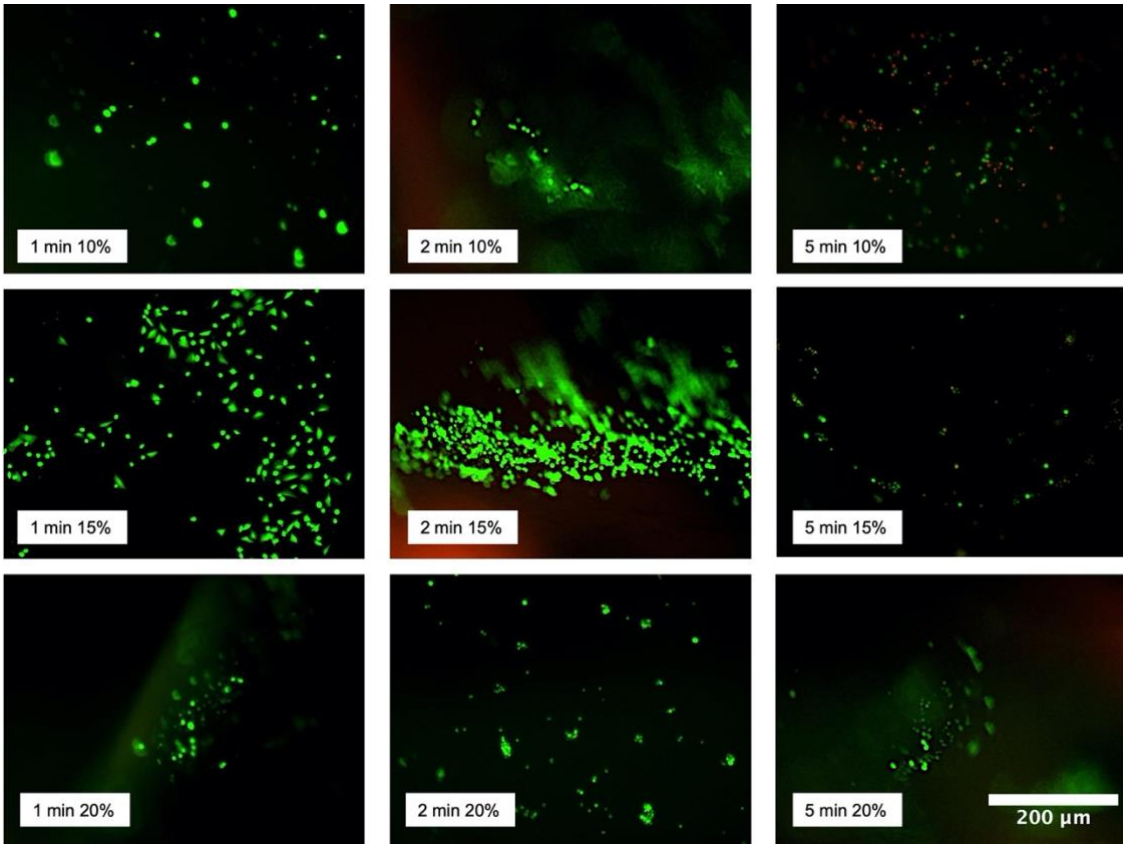

Figure 3. 7. Live and Dead fluorescence images of ATDC-5 cells seeded on GelMA with different concentrations and UV curing time on day 1.

Dead cells represented by red fluorescence were visible on 10% GelMA + 5-minute curing. The 5-minute curing group demonstrated fewer living cells than GelMA with a shorter curing duration. Scale bars = 200 μm.

Day 3

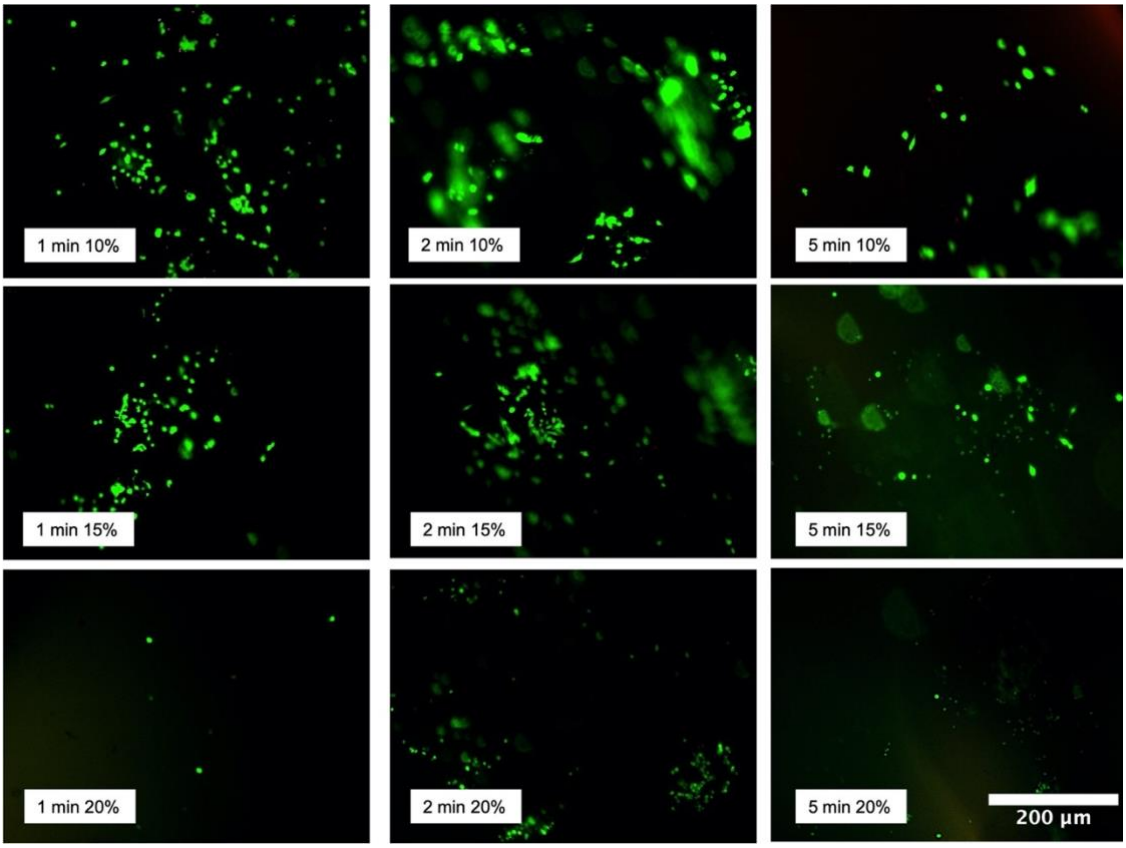

Figure 3. 8. Live and Dead fluorescence images of ATDC-5 cells seeded on GelMA with different concentrations and UV curing time at day 3.

Living cells were mostly visible in 10% and 15% GelMA groups, regardless of the curing time. In 20% GelMA groups, more living can be observed on 2-minute curing than in other curing durations. Scale bars = 200 μm.

Day 7

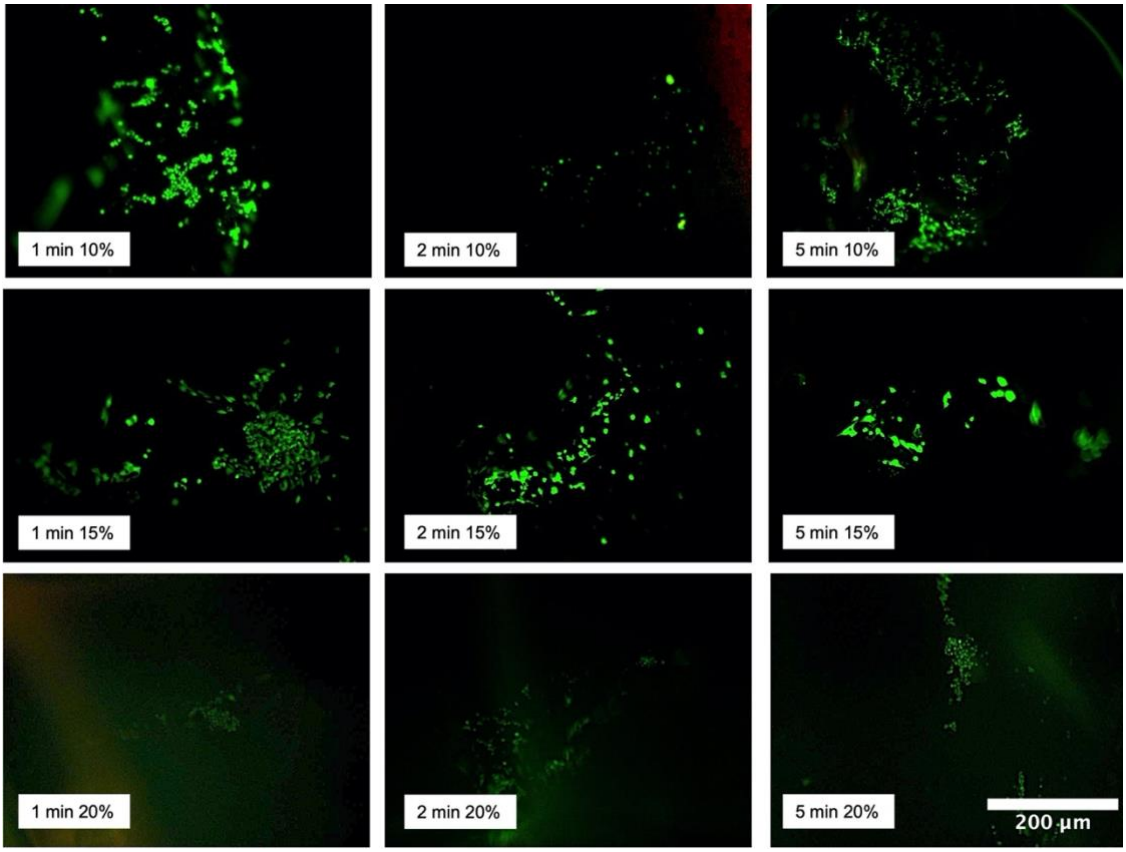

Figure 3. 9. Live and Dead fluorescence images of ATDC-5 cells seeded on GelMA with different concentrations and UV curing time at day 7.

Cell colonies were visible on day 7 of cell culture in all GelMA concentrations and curing time, suggesting the rebound of cells after the exposure to UV light and manipulation during cell seeding, Scale bars = 200 µm.

3.3.4.3. Degradation Rate

Based on the cell viability evaluation, the 20% GelMA group showed the lowest metabolic activity and less visible live cells according to live/dead assay. Therefore, 10% and 15% GelMA were analysed further for the rest of the experiments since these groups demonstrated better cytocompatibility.

GelMA scaffolds degraded to approximately 70% of the initial weight over eight weeks when immersed in the PBS (figure 3.10). There was no significant difference in degradation rate between 10% and 15% GelMA. A sharp decrease in GelMA samples' remaining weight can be observed during the first two weeks of incubation. The scaffolds degraded slowly afterwards, with around 10% of mass loss within the following six weeks.

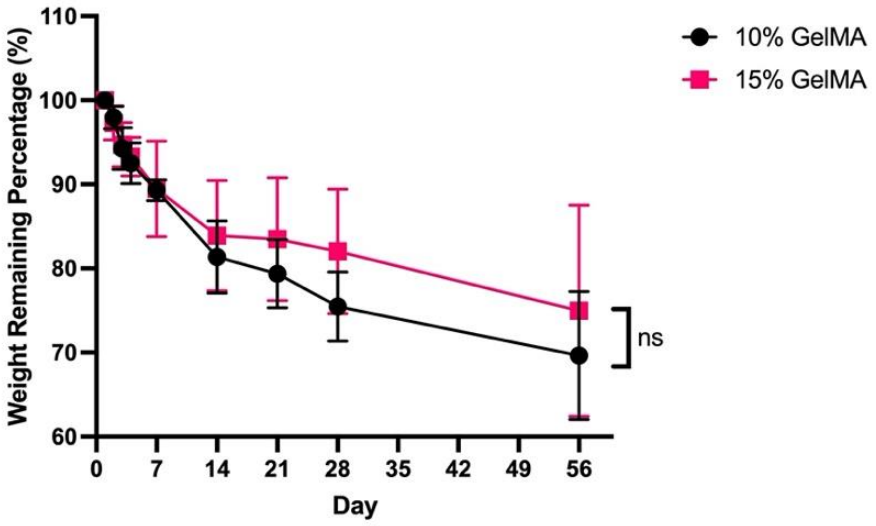

Figure 3. 10. The degradation rate of GelMA scaffolds with different concentrations.

A sharp decrease in GelMA scaffold weight, amounting to 10% mass loss, was observed within the initial 7 days of the degradation test. Beyond day 14, the degradation rate slowed, resulting in a total mass loss of 20% throughout the 42-day course. Data is presented as mean ± SD. NS = not significant.

3.3.5. Cell Differentiation

3.3.5.1. Metabolic Activity

HADSC were used to investigate the chondrogenic properties of GelMA. The metabolic activities of hADSC incubated in growth and chondrogenic media were also compared. As can be seen from figure 3.11, 10% GelMA groups generally showed higher metabolic activity than 15% GelMA. However, the 3D cell culture in chondrogenic media showed a different pattern than the growth media culture. The metabolic activity of hADSC on both GelMA groups steadily increased during the 14-day incubation in the growth media and showed the highest metabolic activity at day 14. On the other hand, hADSC cultured in chondrogenic media showed the highest metabolic activity on day 7 for 10% GelMA and on day 3 for 15% GelMA. The metabolic activity then continued to decrease for the 15% GelMA group.

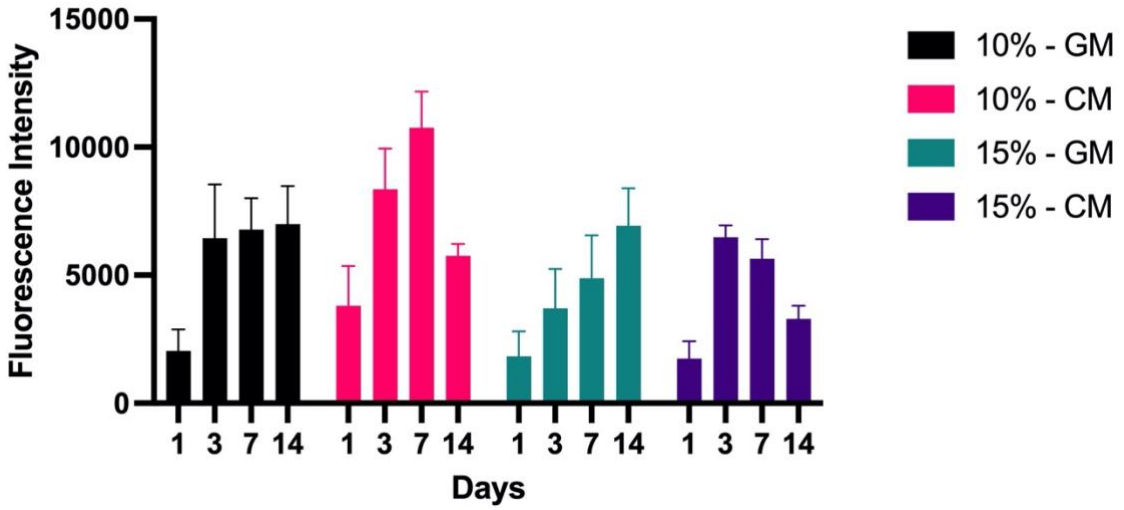

Figure 3. 11. The metabolic activity result of hADSC cultured on 3D GelMA scaffolds incubated in different media.
Different trend of metabolic activity can be observed between hADSCs incubated in GM and CM. GM groups metabolic activity peak at day 14, whilst CM group peaked earlier at day 7. 10% GelMA group demonstrated higher metabolic activity compared to 15% GelMA group.
GM: growth media, CM: chondrogenic media. Data is presented as mean ± SD.

3.3.5.2. Glycosaminoglycan Evaluation

The alcian blue staining images showed different intensities of staining between different media (figure 3.12). 3D GelMA cell culture incubated in chondrogenic media demonstrated stronger positive staining than growth media ones. Dark blue spots were more visible on GelMA in chondrogenic media. The intensity was generally stable during the 21 days of incubation, and no noticeable difference between 10% and 15% GelMA was seen.

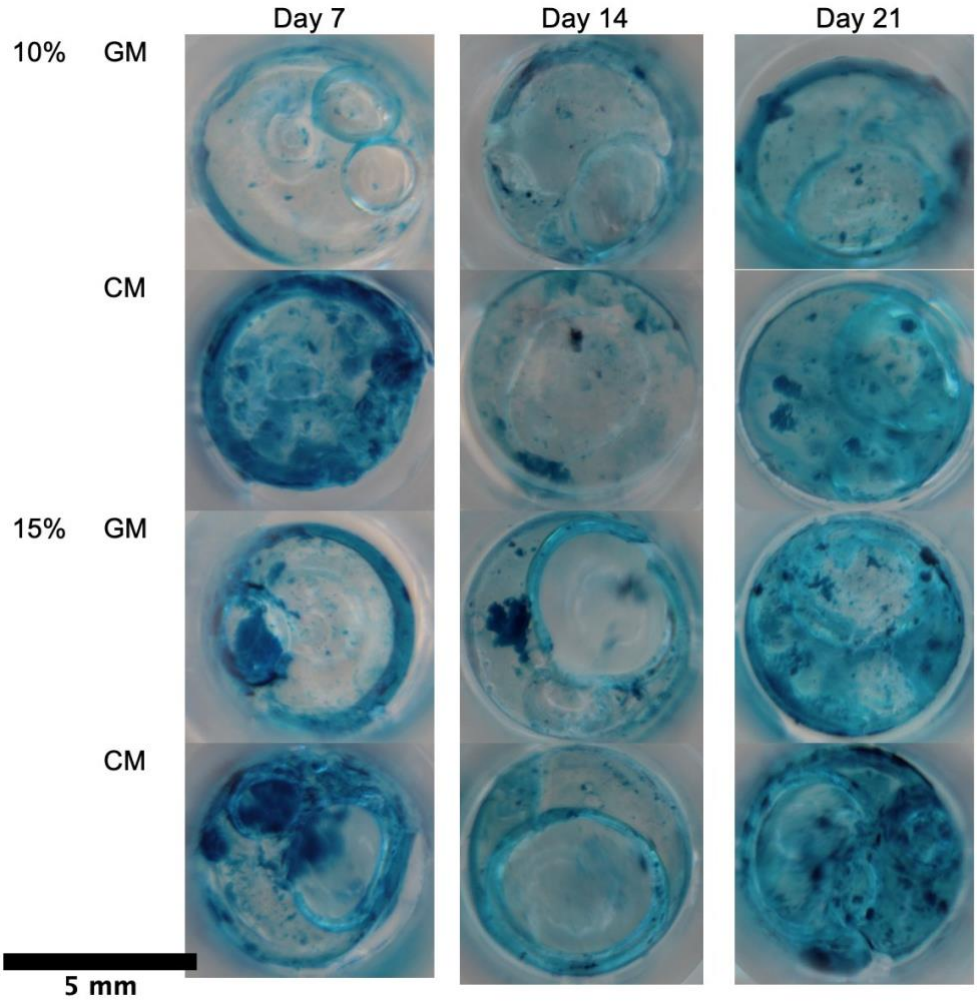

Figure 3. 12. Alcian Blue staining results of hADSC cultured on 3D GelMA scaffolds.

Qualitative evaluation of alcian blue staining showed positive dark blue staining on the GelMA scaffold, indicating the presence of GAG. Scale bar = 5 mm

3.3.5.3. Protein Expression

Sox9 protein expression was detected from day 7 on 10% GelMA and relatively more visible on day 21 (figure 3.13). The expression of Sox9 on 15% GelMA on day 7 was less intense than 10% GelMA. However, on day 14 and day 21, 15% GelMA demonstrated a similar expression of Sox9, with the strongest expression visible on day 21. Both 10% and 15% GelMA showed expression of Collagen 2 protein since day 7. The expression was also detected on day 14 and day 21 (figure 3.14).

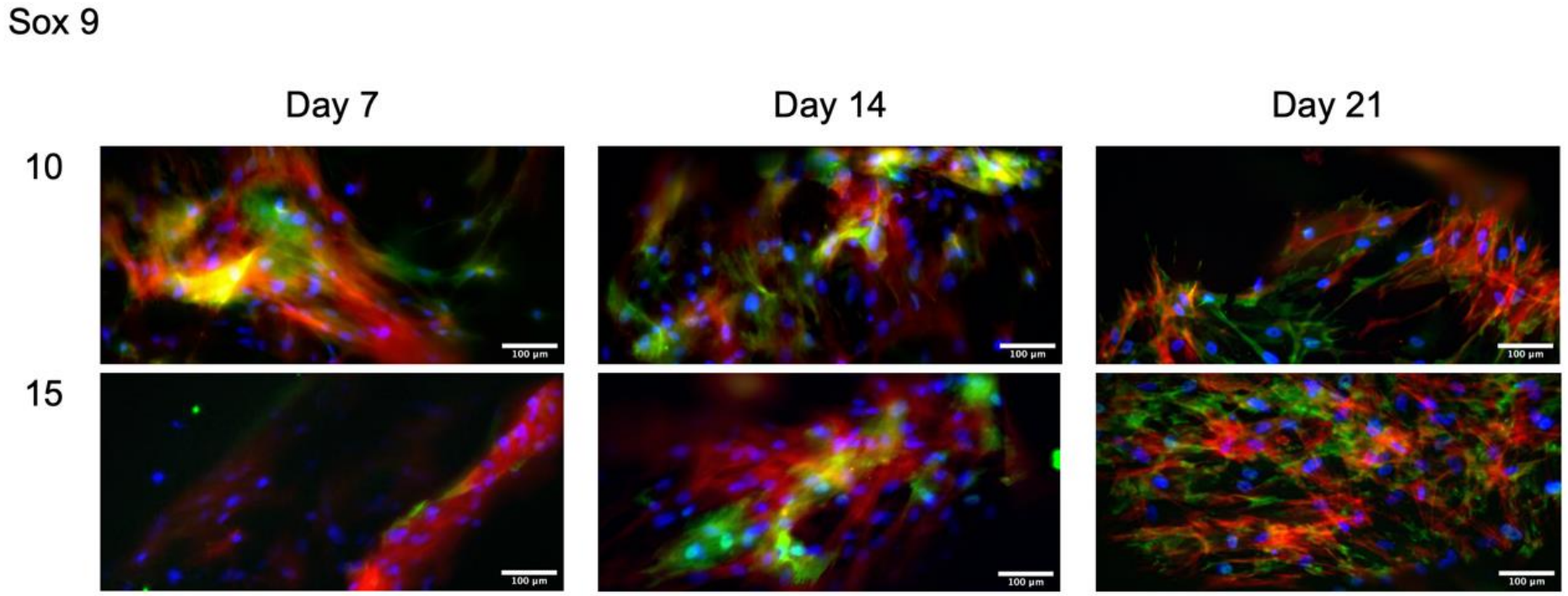

Figure 3. 13 Immunofluorescence images of Sox9 staining in hADSC cultured on 3D GelMA scaffold with different concentrations.

Sox9 expression was visible since day 7 on the 10% GelMA group and remained detected until day 21. 15% GelMA showed Sox9 expression on day 14 and 21. Sox9 (green), DAPI staining on nuclei (blue), and Phalloidin on F-Actin (red). Scale bars: 100 µm.

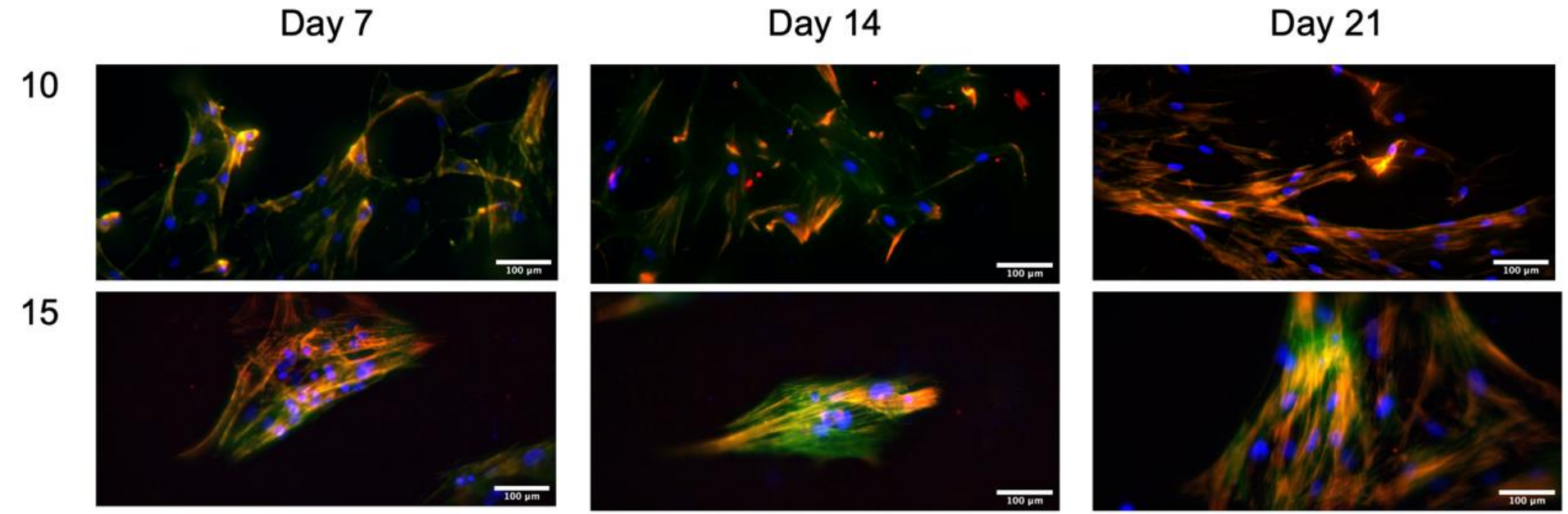

Figure 3. 14 Immunofluorescence images of Collagen II staining in hADSC cultured on 3D GelMA scaffold with different concentrations.

Col II was detected on the cell's cytoskeleton and superimposed with the F-Actin staining. The expression was visible from day 7 until day 21. Collagen II (red), DAPI staining on nuclei (blue), and Phalloidin on F-Actin (green). Scale bars: 100 µm.

3.3.5.4. Gene Expression

Sox9 gene expression increased by approximately 2-fold from day 7 to day 14 of the incubation period. The expression then decreased on day 21. The sox9 gene expression was not significantly different between 10% and 15% GelMA (figure 3.15).

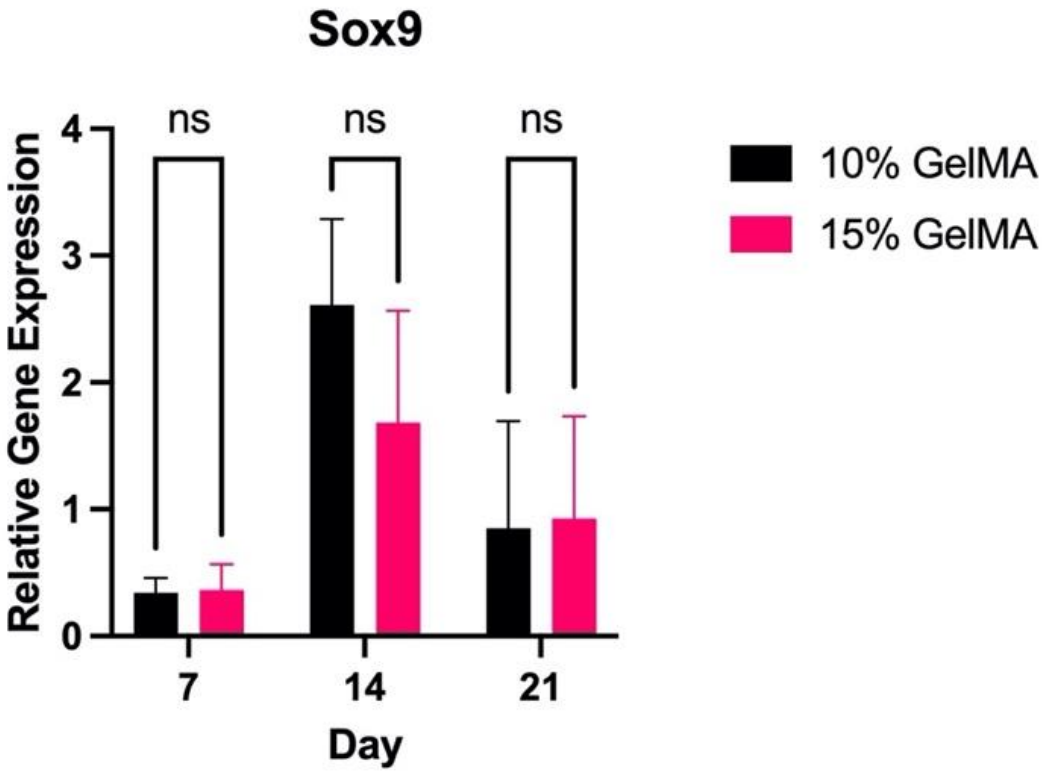

Figure 3. 15. Gene expression of hADSC culture on 3D GelMA scaffolds.

Compared to the control, Sox9 gene expression was lower on day 7. It increased around 2-fold on day 14. There was no significant difference between the 10% and 15% GelMA groups. Data is presented as mean ± SD. NS = Not significant.

3.4. Discussion

GelMA has been widely used for soft tissue engineering, such as neural, corneal, and placental tissue, due to its tunability (Ding, Illsley and Chang, 2019; Ye *et al.*, 2020; Barroso *et al.*, 2022). As a result, various GelMA products are currently commercially available. Since different types of soft tissue have different physical properties, it is important to tune GelMA according to the tissue that will be engineered. Bovine GelMA was chosen in this experiment based on reports that found polymerised bovine GelMA displaying higher compressive modulus than porcine-derived GelMA (Pahoff *et al.*, 2019; Suvarnapathaki *et al.*, 2019). At the time of writing, bovine GelMA has yet to be extensively investigated and commercially available as much as Porcine-derived GelMA. Therefore, this chapter aimed to optimise bovine GelMA to fabricate a cytocompatible 3D cartilage scaffold with native tissue-like mechanical properties. The optimisation process involved comparing essential crosslinking parameters that included different GelMA concentrations and UV curing durations, resulting in different rheological, mechanical, and biological properties. The resulting GelMA scaffold from those parameters that showed more similarity to native cartilage tissue was explored further.

FTIR results of the bovine GelMA mixture showed compounds expected to be identified in the GelMA. Gelatin presence was confirmed in figure 3.2, along with the bond between gelatin and methacrylic anhydride. Furthermore, the rheological properties of the GelMA mixture were analysed to determine which temperature and concentration enable optimum cartilage layer fabrication.

Similar to gelatin, GelMA is thermosensitive. Therefore, its viscosity changed according to the temperature. Figure 3.3. illustrates the viscosity change from the standard storage temperature at 4 °C to the human body temperature at

37 °C. From this result, it can be concluded that GelMA was easier to manipulate at temperatures above 25 °C. It also demonstrates Newtonian behaviour at these temperatures (figure 3.4). This Newtonian behaviour makes GelMA a versatile bio-ink that can be printed by SLA or DLP, which requires such properties (Lim *et al.*, 2018). Lower viscosity at 37°C also makes cell encapsulation possible since it has been reported that solutions with high viscosity may decrease cell viability (Kong, Smith and Mooney, 2003; Lee *et al.*, 2016). Higher viscosity requires a higher shear force to mix the cell with the solutions, which exposes higher stress to cells and reduces their viability (Mondal *et al.*, 2019). As shown in figure 3.3, 20% and 15% GelMA groups still had higher viscosities than 10% GelMA at 37 °C, which might affect gel manipulation, resulting in different cell viability and mechanical properties.

GelMA solutions became solid after light polymerisation. Figure 3.5 shows that all polymerised GelMA scaffolds had compressive moduli similar to native human cartilage compressive modulus (Beck *et al.*, 2016). The results also showed that the higher the GelMA concentration, the higher the compressive modulus, similar to previous studies that have found that increasing GelMA concentration increased its stiffness (Lin *et al.*, 2018). The 20% GelMA demonstrated a higher compressive modulus than other groups in every UV exposure time. This might be caused by the increasing availability of cross-linkable methacryoyls group in GelMA with higher concentration (Lee *et al.*, 2016). Regarding curing time, figure 3.5 reveals that the 1-minute UV irradiation group generally had higher compressive modulus than the 2- and 5-minute groups. This result suggested that increasing UV curing time made GelMA less stiff. It has been demonstrated that UV light can activate free radical polymerisation and cleave the polymeric network into soluble polymer fragments

(Scheiger and Levkin, 2020). The cleaving of the polymeric network or photodegradation requires more prolonged UV irradiation, which occurred in this experiment.

Longer UV exposure has also been reported to reduce cell viability (Monteiro *et al.*, 2018). Figure 3.6 reveals that ATDC5 cells proliferated more slowly when exposed to longer UV irradiation, mainly on higher GelMA concentrations. Although a higher concentration of GelMA might help with mechanical properties, the dense polymeric network might interfere with cell proliferation (Rajabi *et al.*, 2021). More covalent bonds lead to GelMA formation with low porosity and rigidity, limiting cell growth (Yin *et al.*, 2018). Cell spreading was also affected by longer UV crosslinking time and higher GelMA concentrations. Denser network properties were found to disturb cell migration and cell-to-cell interaction (Pepelanova *et al.*, 2018). Scaffold architecture also affects oxygen and nutrient diffusion, influencing cell viability (Pepelanova *et al.*, 2018). Figure 3.7 reveals that dead cells were visible in 20% GelMA groups 24 hours after the crosslinking. The higher viscosity of 20% GelMA, which requires a higher force to mix living cells with the gel, could be attributed to this result. Dead cells were observed on 20% GelMA regardless of UV curing time, indicating concentration significantly affected cell viability. However, the cells were found to recover and spread on every GelMA group on day 3 and 7, with 10% GelMA + 1 minute curing time group demonstrating a progressive cell-to-cell contact and colony formation from day 1 to day 7 (figure 3.8 and figure 3.9). This live cell visualisation result mirrored the metabolic activity trend where lower GelMA concentration showed increased metabolic activity from day 1 to day 7. As mentioned, softer hydrogels could accommodate cell spreading better than thicker gels.

However, figure 3.10 reveals that softer scaffolds with lower GelMA concentrations demonstrated a degradation rate similar to scaffolds with higher GelMA concentrations. Previous studies have shown that GelMA's degree of functionalisation (DoF) is a major factor that affects the degradation rate (X. Li *et al.*, 2016; Pepelanova *et al.*, 2018). The higher the degree of methacryloyl substitution of the gelatin, the higher the degree of functionalisation. This can be done by introducing a higher volume of methacrylic anhydride during the GelMA synthesis. GelMA scaffolds with the same gelatin concentration but different DoF exhibited different stiffness. High DoF increased the cross-linking network's density, resulting in a slower degradation process. Although the mixture had different GelMA concentrations in this experiment, the same lyophilised GelMA with 80% DoF was used. Therefore, the degradation rate was not significantly different among the experimental groups. Rapid degradation might promote the dedifferentiation of chondrocytes due to the down-regulated gene expression of collagen II and aggrecan (X. Li *et al.*, 2016). Furthermore, a higher degradation rate could be a disadvantage in maintaining the chondrocyte phenotype.

Based on rheological and mechanical properties and cytocompatibility, 10% GelMA and 15% GelMA with 1-minute UV crosslinking time were further evaluated for their ability to support cell differentiation by performing 3D cell culture with hADSC. GelMA with encapsulated hADSC were incubated in growth and chondrogenic media to analyse the metabolic activity pattern. Figure 3.11 reveals a different pattern of hADSC metabolic activity in chondrogenic and growth media. The metabolic activity decreased on day 7 in the chondrogenic environment compared to those incubated in growth media, which continued to increase on day 7 and day 14. The decreased metabolic activity in chondrogenic media incubation signalled the shift from cell proliferation to differentiation. Stem

cells are known to reduce their metabolic activities during differentiation (Westhauser *et al.*, 2019). It has been reported that when cells undergo proliferation and reach enough cell-to-cell contact, they will withdraw from the cell cycle, stop the proliferation and start chondrogenesis (Dexheimer, Frank and Richter, 2012). Chondrogenesis starts with chondroprogenitor cells producing the extracellular matrix component, such as proteoglycan and collagen type II (Dexheimer, Frank and Richter, 2012). Since metabolic activity is related to cell proliferation, the decrease of metabolic activity of hADSC on GelMA incubated in chondrogenic media marked the start of chondrogenesis, whilst those in growth media were still proliferating at the same time point.

This result aligned with the Sox9 gene expression of hADSC embedded in GelMA. Both 10% and 15% GelMA demonstrated upregulated Sox9 gene expression on day 14, compared to the hADSC on the tissue culture plate as the control (figure 3.15). Sox9 or SRY-box 9 is a transcription factor mediating stem cells' differentiation into chondrocytes (Chen *et al.*, 2021). Its combination with Collagen II and ACAN can activate Sox9 gene expression and induce ECM synthesis (Chen *et al.*, 2021). Sox9 has been confirmed to be abundant in chondroprogenitor cells, similar to the findings in figure 3.13. Figure 3.13 shows that the expression of Sox9 protein on GelMA scaffolds was detected from day 7, and its intensity increased on day 14 and day 21. Sox9 expression is essential at the start of differentiation and a later stage due to its role in cell survival and maintaining the expression of other cartilage markers, such as Collagen II (Lefebvre and Dvir-Ginzberg, 2017).

The expression of the Collagen II protein itself was visible on day 7 of incubation, the same as the Sox9 expression (figure 3.14). Collagen II is a major component of ECM, along with aggrecan (ACAN). Collagen II is an essential

signalling molecule regulating chondrocyte proliferation and differentiation, whilst reduced ACAN expression has been reported to affect the early stage of chondrogenesis and prevent its progression (Hodax *et al.*, 2019; Lian *et al.*, 2019). The finding of positive staining of alcian blue on GelMA scaffolds indicated the presence of ACAN (figure 3.12). The relatively strong intensity of the staining suggested that hADSC were able to produce the required amount of ACAN to promote chondrogenic differentiation, which was confirmed by the protein expression of Collagen II and Sox9. The expression of the classic chondrogenesis markers on GelMA indicated that GelMA provides a supportive environment for stem cells to undergo chondrogenic differentiation. The fact that there was upregulated Sox9 gene expression on GelMA compared to the tissue culture plate incubated in the same chondrogenic media suggested that GelMA could also promote chondrogenesis of stem cells.

The chemical structure of GelMA plays an important role in GelMA's cytocompatibility and chondrogenic properties. Its gelatin component is derived from collagen, a major component of cartilage tissue. The polymeric structure of gelatin has natural cell-binding motifs such as Arg-Gly-Asp (RGD) that can facilitate cell adhesion and interaction between cells and scaffolds (Dong *et al.*, 2019). In addition, the methacrylamide component of GelMA provides stability since it is less prone to mature crosslinking and contributes to tunability since it is photo-cross-linkable (Hölzl *et al.*, 2022). This tunability also affects the stiffness of GelMA, which is known to influence cellular behaviour (X. Li *et al.*, 2016).

This chapter explores different factors that might affect important properties of GelMA as a material for cartilage tissue engineering. Hydrogels, particularly natural ones, are known to have weak mechanical properties, which is undesirable for musculoskeletal tissue. Therefore, different GelMA

concentrations and UV curing times were investigated in this chapter to find the balance between cytocompatibility and mechanical properties. It was found that 10% and 15% GelMA and 1 minute UV crosslinking time demonstrated cytocompatibility to chondrogenic cells, promoted chondrogenic differentiation, and had tissue-like mechanical properties as a cartilage layer scaffold.

Several limitations emerged from the experiments in this chapter. Notably, the absence of alcian blue quantification primarily stems from the complexities of releasing alcian blue from the GelMA. The experiments also faced limitations in targeting specific proteins and genes due to a restricted timeframe for optimisation and unforeseen disruptions in the availability of reagents. Col II gene expression assay was performed but did not result in valid data, which required redoing the assay or changing the primers. These constraints impacted the investigation's depth and highlighted the need for future research to address the limitations.

3.5. Conclusions

This chapter has described the optimisation of GelMA for cartilage tissue engineering. GelMA scaffolds with mechanical properties similar to native human cartilage were successfully fabricated using bovine-derived GelMA, and GelMA concentration and UV cross-link time influenced GelMA's cytocompatibility and mechanical properties. Although higher stiffness might benefit the scaffold stability, the dense network could negatively affect cell viability. Therefore, it is essential to determine the optimum GelMA parameters that demonstrate a balance between desirable mechanical properties and favourable cytocompatibility. The scaffold with the lowest GelMA concentration and the shortest curing time in this study had shown good cytocompatibility with a

compressive modulus that is still within the range of native cartilage compressive modulus. In addition, chondrogenic differentiation markers such as Sox9, Collagen II, and ACAN were expressed by stem cells encapsulated in the GelMA scaffold. Taking into account the results and limitations mentioned, the subsequent study will proceed with 10% GelMA and 1-minute curing as the cartilage layer scaffold.

Chapter 4. Bilayer Scaffold Development: Combining the Bone Layer (CSMA-2) and Cartilage Layer (GelMA)

4.1. Introduction

Articular cartilage and subchondral bone form the osteochondral unit. This structure can transfer the load during the weight-bearing movement and joint motion (Goldring and Goldring, 2016). Osteochondral defects affect the joints' subchondral bone and cartilaginous component integrity, compromising its function. Trauma, diseases, and excessive loading can cause this defect, which remains asymptomatic until further degeneration occurs (Lesage *et al.*, 2022).

Patients with moderate and severe osteochondral lesions usually complain about joint pain, swelling, locking, or crepitation. Physical examination may find tenderness on the joint. Radiological examinations, particularly with MRI, can determine the lesion location, size, bone marrow involvement, fracture lines, and subchondral plate deformities (Jacob, Shimomura and Nakamura, 2020). Various treatments have been developed to preserve the joint and avoid extensive joint replacement surgery. Smaller lesions can benefit from osteochondral fragment fixation and osteochondral autologous graft (OAT) treatments. However, larger defects require osteochondral allograft transplant (OCA) due to the limited volume of available autografts (Haber *et al.*, 2019). Osteochondral allografts can be fresh, fresh frozen, or cryopreserved. The OCA graft's freshness influences the cells' viability (Lai *et al.*, 2022). The disadvantages of this surgical technique include immunogenicity and graft mismatching (Doyle *et al.*, 2021).

The tissue engineering approach has emerged to address these medical challenges. The stratified architecture of the osteochondral unit has inspired the development of biomimetic layered scaffolds for tissue engineering. At least two layers are needed to provide different microenvironments for cells to develop the bone and cartilage neo-tissue (Lesage *et al.*, 2022). Subchondral bone has been reported to have stiffness ranging from 1.6 to 3.9 GPa, whilst cartilage tissue is significantly softer, with compressive modulus varying from 0.1 to 6.2 MPa (Lesage *et al.*, 2022). Previous studies evaluating bilayer scaffolds observed better outcomes compared to single-layer implants in different in vivo experiments (Lesage *et al.*, 2022).

The osseous part of the biomimetic osteochondral scaffolds is usually fabricated by combining synthetic polymers and bioactive inorganic materials. This combination is known to stimulate the osteogenesis of stem cells (Mahapatra *et al.*, 2019). The bony layer of the scaffold also should be able to provide structural support. On the other hand, the chondral layer requires a different approach to provide the chondrogenic environment for cells. Although synthetic polymers are also used to fabricate the cartilage layer, the requirement for bone-like mechanical properties is not applicable. Softer biomaterials can be used for the chondral layer.

As discussed in previous chapters, the 3D-printed CSMA-2 structure showed promising results as a bone layer scaffold. CSMA-2 monomers were suitable for vat polymerisation 3D printing that can fabricate complex architectures like the trabecular structure of bone. 3D-printed CSMA-2 gyroid scaffolds demonstrated good mechanical properties, and the stiffness of the scaffolds resembled native bone compressive modulus. These CSMA-2 scaffolds could also support cell proliferation and osteogenic differentiation of hADSC.

Osteogenic markers such as RUNX2, OPN, and OCN were found to be expressed by the stem cells seeded on the scaffolds (Verisqa *et al.*, 2022). The gyroid scaffold also allowed angiogenesis and bone ingrowth after implantation in animal studies (Owji *et al.*, 2022).

Based on the results in Chapter 3 - Cartilage layer development, engineered gelatin methacrylate or GelMA, was found to have mechanical properties similar to native cartilage tissue after exposure to UV light. Cell encapsulation was also possible due to its low viscosity at 37°C. Different chondrogenic progenitor cells were found to proliferate when embedded within crosslinked GelMA, confirming its cytocompatibility. Furthermore, GelMA provided a favourable environment for stem cell chondrogenic differentiation, resulting in the expression of important chondrogenic proteins such as Sox9 and Collagen II. GelMA's flowability, photo curability and tunability allow combining them as the chondral layer with 3D-printed CSMA-2 as the osseous layer.

Since CSMA-2 and GelMA showed encouraging results, a bilayer scaffold that combines these biomaterials is expected to have favourable physical, mechanical, and biological properties.

Therefore, the objectives of this chapter were as follows:

1. Fabrication of bilayer osteochondral scaffold with GelMA for the cartilage layer and CSMA-2 for the bone layer
2. Cytocompatibility evaluation of different GelMA and CSMA-2 combinations for the bilayer scaffolds
3. Simulation of bilayer scaffold preconditioning for clinical application

4.2. Materials and Methods

4.2.1. Bilayer Scaffold Fabrication

4.2.1.1. Computer-Aided Design

The bilayer scaffold design was a modification of the gyroid design used for the bone layer. Through a series of trials and errors, a porous circular wall was incorporated on top of the gyroid part to secure the GelMA in place as the cartilage layer (figure 4.1). The circular frame is expected to contain the liquid GelMA before UV irradiation, given its high flowability at working temperature. The constructs were designed with CAD software (Meshmixer, Autodesk, San Francisco, CA, USA). The cartilage layer height was set at 2 mm and a wall thickness of 0.2 mm, whilst the bone layer height was 3 mm. The diameter of the scaffold was 6 mm. The final CAD proved printable and stable among other bilayer scaffold prototypes.

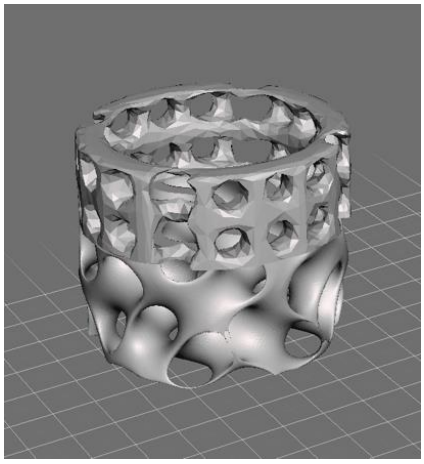

Figure 4. 1. Computer-aided design (CAD) of the bilayer scaffold.

Gridlines = 1 mm.

4.2.1.2. 3D Printing

The frame of bilayer constructs was made by 3D printing a CSMA-2 mixture, without and with hydroxyapatite (CSMA-2 10HA and CSMA-2 0HA), using a Nobel Superfine DLP 3D printer (XYZ Printing, New Taipei City, Taiwan). A slicing software (XYZware Nobel, XYZ Printing, Taiwan) was used to slice the design and determine the printing setup. The base setup's curing time was 19 seconds with 60 $W.m^{-2}$ power intensity. The curing time for the intermediate and model setups was 8.3 seconds with 53 $W.m^{-2}$ power intensity. All the setups used 15% of the power level and 0.25 $mm.s^{-1}$ for the speed at 20 °C. After the printing was finished, the samples were washed with 99% methanol (Merck, Kenilworth, NJ, USA) for 5–10 minutes to remove the uncured monomer, then left to dry, followed by a post-curing process with a UV chamber (XYZ Printing, New Taipei City, Taiwan) for 1 minute at level 3 intensity. After the 3D printed bone layer was ready, GelMA solution was pipetted into the top circular frame and light cured with 405 nm UV light (UV curing chamber, XYZprinting, Taiwan) for 1 minute.

4.2.2. Bilayer Scaffold In Vitro Studies

4.2.2.1. Co-culture

Two types of cells were used for the co-culture experiment. ATDC5 (cell type) for the cartilage layer (top) and MC3T3-E1 (pre-osteoblast cell) for the bone layer (bottom) were obtained from Sigma-Aldrich. ATDC5 and MC3T3-E1 were cultured with DMEM F12 (Gibco), 10% FBS (Gibco), and 1% penicillin/streptomycin (P/S) (Sigma-Aldrich). The cells were incubated at 37 °C and 5% CO_2. The 3D-printed scaffolds were sterilised with 70% alcohol for 15 minutes, washed with sterile PBS (Gibco) twice, and left to dry. UV light sterilisation was then performed for 15 min on each side. The 3D-printed samples

were soaked with a complete medium and placed in the incubator for 24 hours before the cell seeding. After removing the medium, passage 5 MC3T3-E1 cells were seeded to the bottom layer of the scaffold (gyroid structure) and incubated for 1 hour. Meanwhile, the GelMA solution was filtered for sterilisation and then pipetted to the top layer of the 3D-printed scaffold. ATDC5 cells were seeded into the GelMA mixture, and the well plates were exposed to 405 nm UV light in a UV chamber (XYZ Printing, New Taipei City, Taiwan) for 1 minute. The seeding density was 4 x 10^4 cells for each scaffold layer. The cell density calculation was based on a similar study of co-culture in bilayer scaffolds (Xue et al., 2019). Fresh complete medium was added afterwards, and the medium was changed every 2–3 days.

4.2.2.2. Cell Tracking

Cell trackers were added to the cell culture to check whether the right cells resided on the designated layer. PKH26 (Sigma-Aldrich) with red colour was used to stain ATDC5 cells, and Qtracker 525 (Invitrogen) with green colour was used for staining MC3T3-E1 cells. PKH staining for ATDC5 was performed by adding the pre-prepared dye solution to the cell suspension treated by Diluent C. The cell and dye suspension were then incubated for 5 minutes with periodic mixing, and the staining was stopped by adding serum. Dye was removed by centrifuge and washing the cells with a complete medium. After the wash, cells were resuspended in a fresh medium and ready for the cell culture. For MC3T3-E1 staining, the Qtracker 525 working solution was mixed with complete media and then added to the cell culture flask for 45-60 minutes of incubation at 37 ºC. After incubation, cells were washed twice with a complete medium and ready for cell seeding.

Cell visualisation after cell seeding was performed using an Aurox Clarity confocal imaging system (Aurox, Oxfordshire, UK) with an Olympus BX51 microscope (Olympus, Southall, Middlesex, UK), pco.edge 4.2 camera, CoolLED pE-4000 light source (CoolLED, Andover, UK) and Visionary software (Aurox, Oxfordshire, UK).

4.2.2.3. Cell Viability

Cell viability was evaluated by analysing the metabolic activity of the 3D co-culture. Alamar blue 10% (v/v) (Invitrogen, Thermo Fisher, USA) was added to each well and incubated for 4 hours at 37 °C. Biotek FLx800 microplate reader was used to read the fluorescence intensity with 540/35 and 600/40 excitation/emission wavelengths. Four samples were prepared for each scaffold group.

4.2.3. Preconditioning Simulation

4.2.3.1. Dynamic Culture Bioreactor Setup

The bioreactor setup consisted of a perfusion chamber, tubing, peristaltic pumps, and a media reservoir (figure 4.2). A perfusion plate (Alvetex, Durham, UK) was used as the perfusion chamber. The chamber has one inlet and one outlet connected to tubing (Bioprene, ID 1.6 mm) to allow dynamic circulation. 100 ml of complete media consisting of DMEM F12 (Gibco), 10% FBS (Gibco), 1% Antibiotic-Antimycotic (HyClone), and Primocin (Invivogen) was perfused at a 1 $ml.min^{-1}$ flow rate with a peristaltic pump (120S Watson Marlow, Cornwall, United Kingdom).

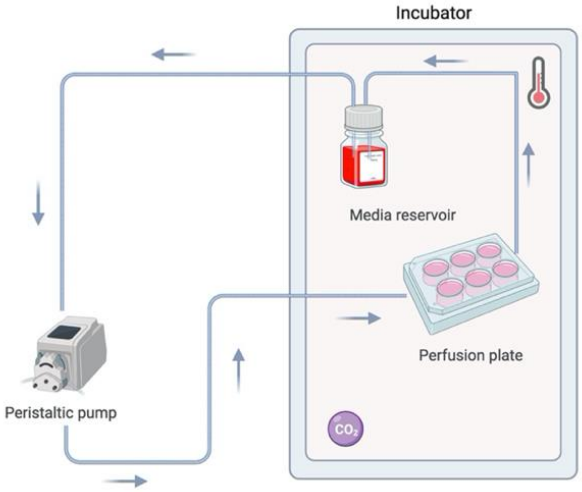

Figure 4. 2. Schematic illustration of the perfusion bioreactor.

The image was created with Biorender.

4.2.3.2. Co-Culture

ATDC5 cells were seeded on the top layer or GelMA with $1x10^5$ cells/layer, whilst MC3T3-E1 cells were seeded on the bottom layer with $1x10^5$ cells/layer. The co-culture was conducted for 4 weeks. For static co-culture, the scaffolds were placed in a 6-well plate. The media was changed every 3 days in the static cultures, and the media in the dynamic bioreactor culture was changed every 7 days.

4.2.3.3. Histological Evaluation

The scaffolds were removed from the culture and washed with PBS. They were fixed in 10% buffered formalin and kept at room temperature before preparing the sample. The samples underwent alcohol dehydration, clearing with xylene and embedded in paraffin wax. The scaffolds were sectioned to 5 μm using a rotary microtome. The sliced samples were mounted on slides and stained with hematoxylin and eosin (H&E).

4.2.3.4. Glycosaminoglycan Evaluation

Alcian blue 0.1% (Sigma Aldrich) staining was performed to evaluate the glycosaminoglycan of the bilayer scaffold. The fixed samples were washed using PBS three times. Next, alcian blue staining solution was added to the samples and incubated for 30 minutes at room temperature. Excess staining was removed by washing the samples with PBS several times. The stained samples were photographed using a Canon EOS camera 1300D, Nikon lens AF Micro NIKKOR 55 mm, 1:2.8, and EOS Utility software 3.0.

4.2.3.5. Calcium Deposits

After the alcian blue staining, alizarin red staining (Sigma Aldrich) was performed to evaluate any calcium deposited in the co-culture of the 3D printed scaffold. The stained samples were washed with PBS, and a 2% w/v alizarin red staining solution was added to the scaffold samples. The samples were incubated for 30 minutes at room temperature. The staining was then removed by washing the scaffold using PBS (Gibco). The stained scaffolds were photographed using a Canon EOS camera 1300D, Nikon lens AF Micro NIKKOR 55 mm, 1:2.8, and EOS Utility software 3.0.

4.3. Results

4.3.1. 3D Printing

Bilayer scaffolds were successfully fabricated by 3D printing CSMA-2 as the bone layer (figure 4.3). The scaffold was cylindrical with 6 mm diameter and 5 mm height. The layers can be easily identified with translucent solid GelMA on top and the porous opaque 3D-printed CSMA-2 layer on the bottom. The bilayer scaffold visually mimicked the macroscopic physical appearance of the osteochondral unit.

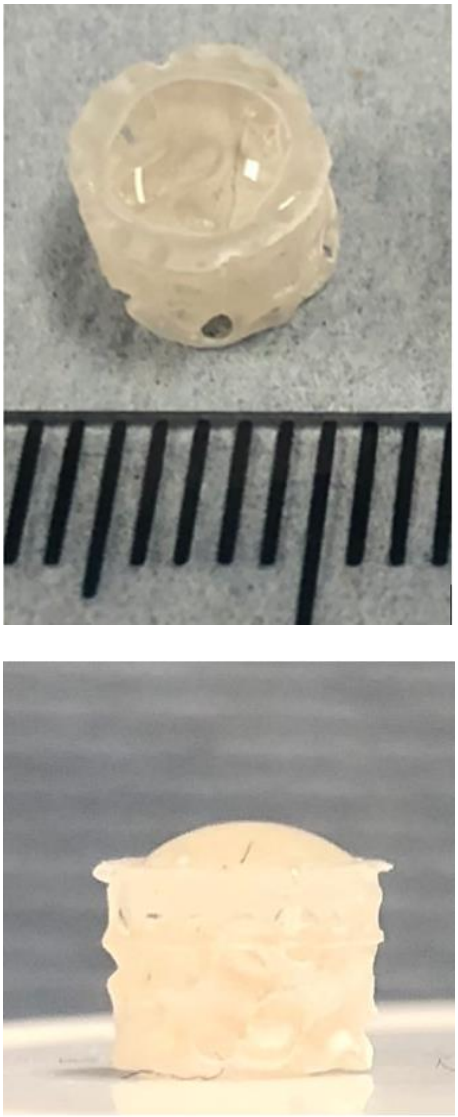

Figure 4. 3. The physical appearance of the GelMA/CSMA-2 Bilayer scaffold.

Lines = 1 mm.

4.3.2. Co-Culture Cell Tracking

Figure 4.4 shows ATDC5 cells were successfully encapsulated in GelMA as the top layer of the scaffold, whilst MC3T3-E1 cells were found to reside on the CSMA2 bottom layer. The confocal images confirmed that the cells were not mixed even after 24 hours of seeding.

Top layer

ATDC5 (red)

Bottom layer

MC3T3-E1

(green)

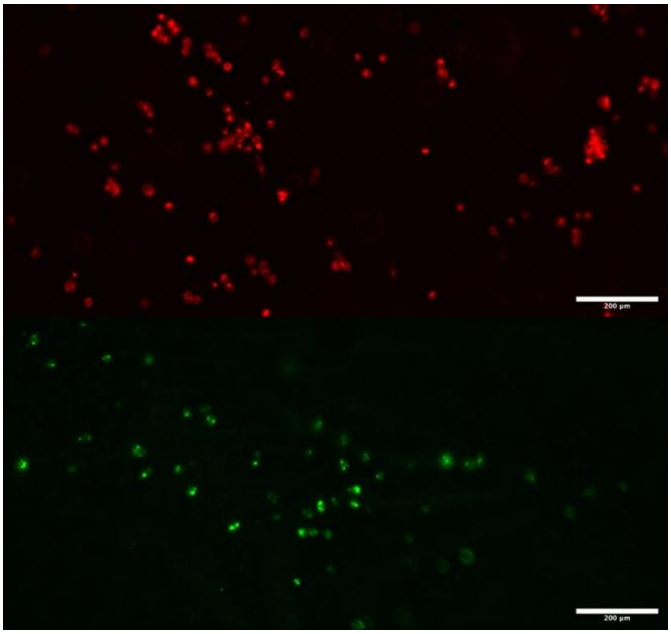

Figure 4. 4. Cell tracking images reveal the location of ATDC5 and MC3T3-E1 cells after the cell seeding. There was no visible cell mixing after the cell seeding. The cells were residing on their designated layer. Scale bars are 200 μm.

4.3.3. Co-culture Cell Viability

The 10% GelMA + CSMA-2 0HA group demonstrated the highest metabolic activity among the groups (figure 4.5). In addition, both bilayer scaffolds group with CSMA-2 0HA as the bottom layer showed a consistent and significant increase in metabolic activity from day 1 to day 7. On the other hand, 10% GelMA + CSMA- 2 10 HA showed decreasing metabolic activity on day 3 with a slight increase on day 7. 15% GelMA + CSMA-2 10 HA metabolic activity also demonstrated a slight decrease on day 3, then peaked on day 7.

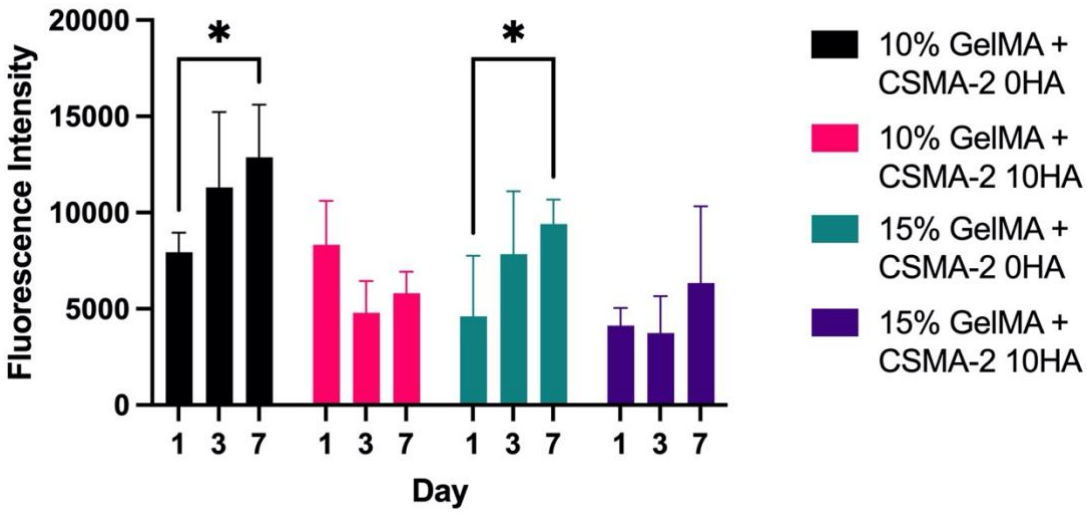

Figure 4. 5. Metabolic activity of ATDC5 and MC3T3-E1 on the bilayer scaffolds.

*The bilayer scaffold with CSMA-2 0HA demonstrated a steady increase of metabolic activity, with day 7 showing the highest cell growth. Data is presented as mean ± SD. * = p <0.05.*

4.3.4. Preconditioning Simulation

Histological analysis was carried out to evaluate neo-tissue formation on the scaffolds. After 7 and 28 days of culture, cells were visible in the cartilage layer of the scaffolds cultured with static and dynamic conditions (figure 4.6). Due to the histological processing, the 10% GelMA layer tended to separate from the bone layer. Due to the sample longitudinal cutting direction, the cells on the bone layer cannot be visualised since the histological slide shows the internal structure of the scaffold's bone layer.

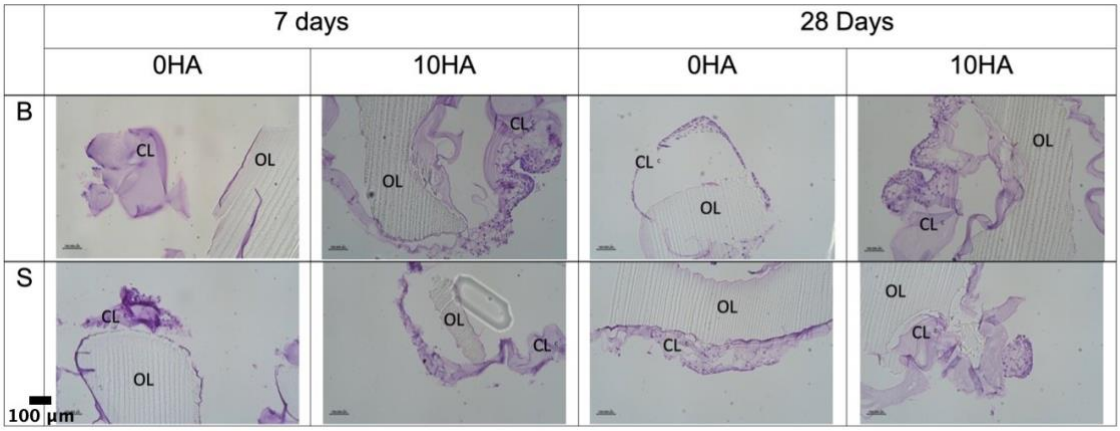

Figure 4. 6. Hematoxylin and Eosin (HE) staining of the bilayer scaffolds after the preconditioning simulation. The sections were cut longitudinally,

Scaffold B = Bioreactor, S = Static, CL = Chondral Layer, OL = Osseous Layer. Scale bars = 100 µm.

Figure 4.7 shows that the bilayer scaffolds stained positive for alcian blue. The scaffolds' top layer exhibited bright blue with some darker blue spots. The tissue-like network structure was also visible in every scaffold group. There were no observable differences in the staining intensity between static and dynamic cultures.

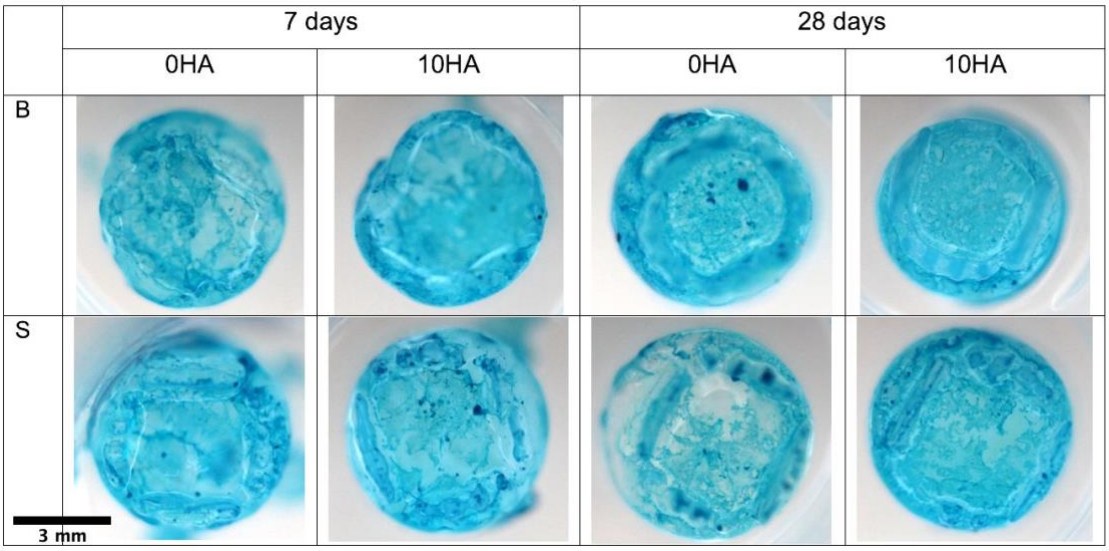

Figure 4. 7. Alcian blue staining of the GelMA/CSMA-2 bilayer scaffolds at 7 and 28 days of preconditioning simulation.

B = Bioreactor, S = Static. Scale bar is 3 mm.

The gross comparison of scaffold stained via alizarin red showed positive results (figure 4.8). All scaffold groups demonstrated dark red staining after 7 days and 28 days of static and dynamic culture. The intensity was relatively similar among the scaffold groups, without or with HA content.

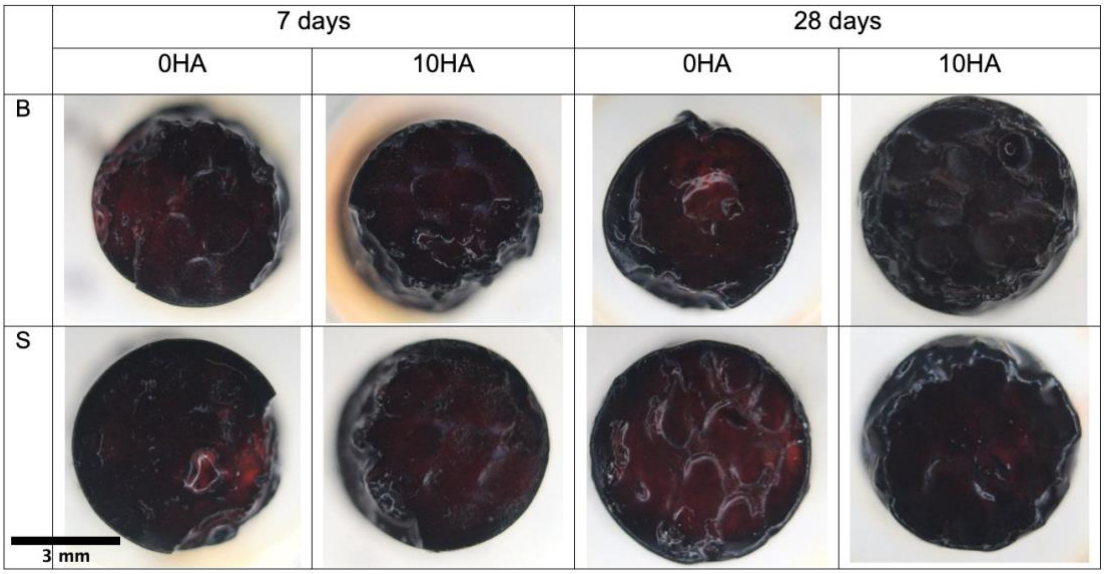

Figure 4. 8. Alizarin red staining of the GelMA/CSMA-2 bilayer scaffolds at 7 and 28 days of preconditioning simulation.

B = Bioreactor, S = Static. Scale bar is 3 mm.

4.4. Discussion

The need to fabricate a bilayer scaffold arose from the distinct environmental requirement for bone and cartilage regeneration owing to the differences in their native structure. The composite osteochondral unit provides suitable physical architectures that allow specific cells, such as osteoblasts on the osseous layer and chondrocytes in the chondral layer, to function accordingly. This chapter aimed to replicate the physical environment of the osteochondral unit by combining optimised GelMA as the cartilage substitute and CSMA-2 as the bone scaffold material. Both GelMA and CSMA-2 demonstrated cytocompatibility and could support chondrogenic and osteogenic differentiation of stem cells, respectively. The multi-material approach was used in this chapter since native osteochondral tissue is a multiphasic structure. A layered scaffold was found to have better outcomes than a single-layer scaffold based on the in vivo experiment results (Lesage *et al.*, 2022).

As mentioned in Chapter 2 - Bone Layer Development, 3D printed CSMA-2 scaffolds showed acceptable physical and mechanical properties. The high compressive modulus and slow degradation of CSMA-2 scaffolds have the potential to support cartilage regeneration. It has been reported that decreased mechanical properties of degradable subchondral scaffolds could provide inferior mechanical support and weaken the newly regenerated cartilage structure (Yang *et al.*, 2021). Therefore, a strong CSMA-2 layer was made as the base of the osteochondral scaffold. The bone layer was fabricated using the DLP method since it offers the possibility of mimicking the complex architecture of biological tissue that can be superior to extrusion-based printing (Lim *et al.*, 2018). However, due to the vat polymerisation mechanism, multi-material 3D printing with DLP is still challenging. The DLP technique was successfully combined with

FDM to fabricate an osteochondral scaffold (Gong *et al.*, 2020). The layers were 3D printed separately and glued together using light-cured GelMA. The adhesive properties of GelMA allowed its adherence to solid material, including ex vivo organs such as the lung, heart, and cornea (Assmann *et al.*, 2017; Barroso *et al.*, 2022; Davis *et al.*, 2022).

Based on these previous studies, it was hypothesised that GelMA could also adhere to other tissues like bone, enabling a straightforward combination with CSMA-2 scaffold. Using the same principle as Gong et al., GelMA was pipetted into the top layer of 3D-printed CSMA-2 and UV-cured for 1 minute. The combination of 3D printing and utilisation of flowable GelMA resulted in a bilayer scaffold. After several trials, this method of creating the chondral layer resulted in a cohesive bilayer scaffold, compared to fabricating the scaffold entirely by 3D printing (figure 4.3). The bond between CSMA-2 and GelMA was possible due to the hydrophilicity of CSMA-2, which allowed GelMA, a hydrogel, to adhere to the bone layer. It has been known that hydrophilic materials have higher maximum adhesion forces and longer adhesion duration compared to hydrophobic ones (Lou *et al.*, 2018). The final result of the fabrication process was a cylindrical scaffold of 6 mm in diameter and 5 mm in height. The cylinder shape was chosen since it is a shape that is commonly used for osteochondral allografts. The thickness of the scaffolds followed the ideal OCA harvest thickness range (Lai *et al.*, 2022).

Although each material had been evaluated individually for its biological properties, the co-culture experiments were performed to observe the bilayer scaffold's properties to host chondrogenic and osteogenic progenitor cells simultaneously. Different cell seeding techniques were used to place the right cells in their suitable environment. ATDC5 was encapsulated in the GelMA

solution and then crosslinked via UV irradiation, whilst MC3T3-E1 was seeded on the solid 3D-printed CSMA-2 scaffolds. These methods were chosen to establish well-defined bone and cartilage layers. Cell trackers were applied to each cell type before the cell seeding to visualise their location during the co-culture. Figure 4.4 reveals that the cells resided on their respective layers following the cell seeding. This is important due to the different tissue expected to form on each layer after the implantation. The presence of osteoblasts on the chondral layer can lead to ossification, which is an unwanted event in cartilage regeneration, except for calcified cartilage and tidemark (Zhang *et al.*, 2018). These layers were not specifically designed and fabricated in this chapter. Thus, maintaining the correct cell in the right layer is essential and possible with this biomimetic bilayer scaffold.

The result of the alamar blue assay of the co-culture correlated with the result of the individual layers. The CSMA-2 0HA and 10% GelMA bilayer showed the highest metabolic activity compared to other combinations. This was similar to the bone layer metabolic activity trend on CSMA-2 0HA and in 10% GelMA for the cartilage layer separately. Since it has been suggested that CSMA-2 with HA content induce earlier osteogenic differentiation of hADSC, the same influence can also be found in the co-culture study where metabolic activity was lower on the scaffold with HA.

Due to the promising 7-day co-culture result, long-term co-cultures with higher cell density were performed. The co-culture aimed to simulate in vitro preconditioning prior to in vivo implantation. It has been suggested that mechanical preconditioning can improve the maturation of engineered tissue and implant integration (Vukasovic *et al.*, 2019). Furthermore, preconditioning stem cells with a chondrogenic medium and dynamic culture in a bioreactor improved

cell viability and enhanced chondrogenic differentiation after the in vivo implantation (Lin *et al.*, 2017). Dynamic culture with a simple perfusion bioreactor system was also conducted along with a static counterpart. Perfusion bioreactors have been reported to induce ECM mineralisation (Zhao *et al.*, 2018).

The osteoinductive optimum flow rate was reported to be varied within 0.5 – 5 $ml.min^{-1}$ (Zhao *et al.*, 2018). The flow rate in this experiment was set at 1 $ml.min^{-1}$. To closely mimic the native tissue, high cell density is essential to establish cell-to-cell interactions (You *et al.*, 2023). These interactions promote a mature and functional neo-tissue formation (You *et al.*, 2023). Tissue-like networks were found on bilayer scaffolds seeded with higher cell density, regardless of the culture conditions. The H&E staining results demonstrated the presence of encapsulated cell colonies in the GelMA layers after 28 days, indicating the occurrence of cell-to-cell networks in the culture.

To support the H&E staining results, alcian blue and alizarin red stainings were also performed. Gross examination of the stained scaffolds can provide information regarding the chondrogenic and osteogenic properties, respectively (Lu *et al.*, 2017; Yu *et al.*, 2020). The GelMA cartilage layer showed positive staining with alcian blue, indicating the presence of GAG, a vital component of the extracellular matrix (Pahoff *et al.*, 2019). Positively stained tissue-like networks were also visible on the scaffolds. This result suggested that GelMA were able to provide a three-dimensional environment that could promote cartilage tissue regeneration. However, further evaluations are necessary to assess the chondrogenic properties of GelMA in vivo. The other challenge that needs to be addressed is the separation of the layers during the sectioning.

The preconditioning simulation results also demonstrated calcium deposition on the osseous layer of the scaffolds. The scaffolds were positively

stained by alizarin red, regardless of the culture period and conditions. The individual CSMA-2 bone layer scaffold in Chapter 2 showed similar positive alizarin red results. The cell density seemed to affect the mineralisation more than the dynamic culture. Although further investigations are needed, this result indicated the role of high-cell-density culture in the maturation of osteogenic progenitor cells, MC3T3-E1.

Furthermore, the high cell density has been known to have a vital role in mimicking the physiological shift from the proliferation phase to the non-proliferation phase of differentiation (Nasello *et al.*, 2020). The mineral deposition is also considered a late osteogenic differentiation marker (Fu *et al.*, 2017). The positive alizarin red staining suggested that MC3T3-E1 entered the mineralisation phase to deposit calcium into the ECM. Since it has been reported that scaffold-free high-density seeding of cells on top of osteoinductive scaffolds results in a neo-tissue formation (Ng, Bernhard and Vunjak-Novakovic, 2016), the same cellular event might occur in the GelMA and CSMA-2 bilayer scaffold, particularly with the support provided by the 3D materials.

The bilayer scaffolds remained stable after 4 weeks of dynamic co-culture in a perfusion bioreactor. The scaffold's chondral and osseous layers were still intact without showing separation, although constantly exposed to shear force in the bioreactor. This result indicated the structural integrity of the GelMA/CSMA-2 scaffold. The arginine-glycine-aspartic acid (RGD) residues in gelatin contribute to GelMA binding capability to native tissues (Kulkarni *et al.*, 2022). Furthermore, it has been reported that GelMA can form chemical bonds between different surfaces due to the presence of its methacrylic groups (Giannoni *et al.*, 2011). GelMA adhesion properties were found to be water-resistant since no separation was observed during the dynamic incubation period of up to 4 weeks. The ability

to maintain adhesion in a wet environment is an essential bio-adhesive property since implants are constantly exposed to the body fluid (Liu *et al.*, 2018).

Moreover, the swelling properties of GelMA as a hydrogel were not found to be a significant factor that affected the bonding stability in vivo (Liu *et al.*, 2018). Although the bilayer scaffolds remained intact for 28 days for static and dynamic cultures, the layers were prone to separation during the sectioning for histological analysis. A better adhesion method might be beneficial to improve the structural integrity. This might include a better scaffold design that can increase the adhesion of the bone and cartilage layers.

This chapter is subject to several significant limitations. Firstly, the challenge of fabricating the calcified cartilage and tidemark within the scaffold led to their absence, posing the accurate replication of native osteochondral tissue architecture. The absence of mechanical stimulations in the simple bioreactor, such as artificial cyclic loading, limited the study's capacity to emulate physiological conditions. Co-culturing was also conducted with animal cell lines that could share the same growth media that perfused the scaffold with a single inlet and outlet. Another substantial limitation was the lack of quantitative analysis, which is crucial for a comprehensive evaluation of the scaffold's performance and characteristics. These limitations are attributed to the challenges of developing a multi-layered scaffold within a limited timeframe.

4.5. Conclusions

The bilayer scaffold was successfully fabricated by combining a 3D-printed CSMA-2 layer and GelMA. The CSMA-2 and GelMA layers were found to bond and withstand long-term in vitro evaluation, indicating their acceptable structural integrity. The bilayer scaffold could mimic the osteochondral unit physically, showing the identifiable chondral and osseous layers. Different cell types could be seeded to replicate the biological properties of the bone and cartilage tissue. The metabolic activity result of ATDC5 and MC3T3-E1 co-culture suggested viable cells can be maintained during the 7-day period. The long-term high cell density co-culture demonstrated positive alcian blue and alizarin red staining, marking the presence of important ECM components and calcium deposition. The 3D environment provided by the bilayer scaffolds during the precondition simulation was shown to support cell-cell interactions that led to cell maturation and neo-tissue formation. The current findings, although constrained, provide a valuable bilayer scaffold prototype. Further in vitro and in vivo evaluations are needed to confirm these findings and to optimise the development of a bilayer scaffold with the combination of novel and widely used biomaterials.

Chapter 5. In Vivo Studies: Angiogenesis and New Bone Formation

5.1. Introduction

Unlike GelMA, which has been investigated widely and is commercially available, the CSMA-2 polymer used as the bone layer material in this thesis has not been studied extensively since it is a novel biomaterial. Chapter 2 - Bone Layer Development outlined that CSMA-2 polymer had suitable rheological properties for 3D printing, particularly with the vat polymerisation methods such as SLA and DLP. HA addition as the filler did not significantly compromise the viscosity, allowing the 3D printing of a complex gyroid structure with an HA percentage of up to 10%.

Although HA incorporation did not affect the 3D printing process, 3D printing results showed different results. The surface morphology of 3D-printed CSMA-2 revealed different roughness depending on the HA percentage. CSMA-2 0HA scaffolds demonstrated a relatively smooth surface, whilst scaffolds with HA addition had a rough and irregular surface morphology. Higher hydrophilicity was exhibited by 3D-printed CSMA-2 with HA content. A similar trend was also followed by the mechanical properties of the gyroid scaffolds, with HA-incorporated scaffolds showing significantly higher compressive modulus.

On the other hand, some in-vitro studies demonstrated different results. Cell proliferation related to cell metabolic activity was higher in CSMA-2 0HA groups than in CSMA-2 5HA and 10 HA scaffolds, whilst late osteogenic marker gene expression was higher in scaffold groups with HA. In summary, HA content influenced the physical and biological properties of 3D-printed CSMA-2 scaffolds.

To confirm and evaluate these properties further, in vivo studies are essential. Osteogenic and angiogenic properties are also crucial for the evaluation of bone substitutes. The osteogenicity of the bone tissue engineering scaffold allows the new bone formation to restore the defect by recruiting stem cells from the surrounding tissue and promoting cell differentiation (Won *et al.*, 2020). Bone regeneration is also supported by angiogenesis, particularly in larger defects. A scaffold's pore size and interconnectivity have been reported to affect vascularisation and tissue repair eventually (Won *et al.*, 2020).

The gyroid structure has been reported to have high porosity and controllable pore size, allowing better cell proliferation (Alizadeh-Osgouei *et al.*, 2021; He, Liu and Rudd, 2021). This structure was successfully 3D printed by using CSMA-2 polymer. A prior study also revealed that a light-cured CSMA-2 scaffold enables angiogenesis on CAM ex vivo assay, supporting the angiogenic potential of the polymer (Owji *et al.*, 2022). The same study included another form of bioceramic, beta-tricalcium phosphate (β-TCP). Compared to HA, β-TCP is less stable and has lower mechanical properties (Bal *et al.*, 2020). It might not be the best candidate to improve the scaffold’s mechanical properties, particularly for the healing process of the load-bearing bone.

Bone healing starts with the inflammatory response from the damaged tissue, which includes cytokine release from the immune cells (Shegarfi and Reikeras, 2009). Revascularisation then occurs along with the recruitment of mesenchymal stem cells. This process leads to soft callus development and continues with the development of fibrous tissue into fibrocartilage, followed by hyaline cartilage and, subsequently, hard callus (He, Liu and Rudd, 2021). The initial anabolic phase of bone repair demonstrates an increase in tissue volume

caused by the recruitment and differentiation of stem cells into bone and vascular tissue (Einhorn and Gerstenfeld, 2014).

The catabolic phase occurs in the second week of bone repair, where the callus tissue volume reduces due to resorption (Wang and Yeung, 2017). Bone remodelling is the synergistic anabolic and catabolic phase of cartilage resorption by osteoclasts and the secondary bone formation by osteoblasts (Wang and Yeung, 2017). The bone marrow structure for hematopoietic tissue is formed during this period (Stucker *et al.*, 2020). Vascular remodelling occurs at the end of the catabolic phase (Einhorn and Gerstenfeld, 2014).

Therefore, the objectives of this chapter were as follows:

1. Evaluation of the tissue response after the implantation of 3D-printed CSMA-2 scaffold.
2. Evaluation of angiogenic properties of the 3D-printed CSMA-2 scaffold post-implantation.
3. Evaluation of new bone tissue formation involved in bone healing after implanting the 3D-printed CSMA-2 scaffold.

5.2. Materials and Methods

5.2.1. Scaffold Preparation

Gyroid bone scaffolds were 3D printed using CSMA-2, according to the same method in Chapter 2—Bone Layer Development. The scaffolds were fabricated with and without adding 10% w/w HA. The scaffolds were 6 mm in diameter and 6 mm in height for the subcutaneous model (Won *et al.*, 2020). To observe the bone remodelling, scaffolds with 5 mm diameter and 2 mm in size were 3D printed. Before the implantation, the samples were sterilised by ethylene oxide (EO) gas.

5.2.2. Scaffold implantation

Small animal models used in this study were 6-week-old (subcutaneous model) and 10-week-old (calvaria model) male Sprague-Dawley (SD) rats housed in a 20 – 24°C fixed temperature with 30 – 70% humidity environment. The nutrients comprised standard pellet foods and water. Light and dark cycles, 12 hours each, were also provided.

Before the surgical procedure, the rats were anaesthetised by 2.5% isoflurane (Forane, Choongwae Pharma, South Korea) in a 2:1 mixture of nitrous oxide: oxygen. After hair removal, the surgical area was wiped with iodine and 70% ethanol, and then the skin was incised using a surgical blade.

To perform the subcutaneous tissue compatibility model implantation, 20 mm incisions were made to each dorsal side of the rats. Six sites for subcutaneous pockets were created using Metzenbaum scissors and blunt dissection on the back, laterally from the spine of each rat. The total number of animals used in the subcutaneous mode was 4 animals.

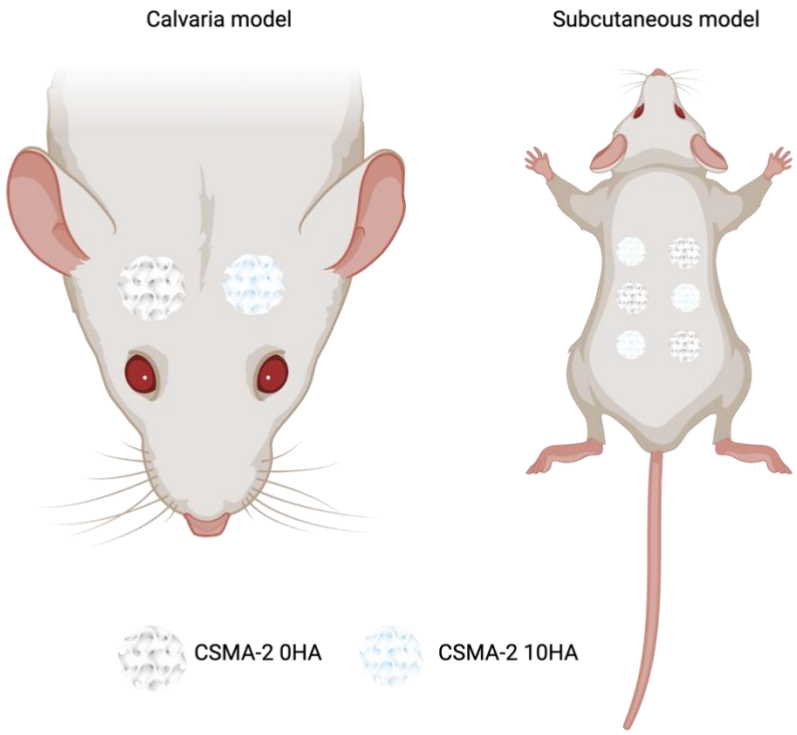

Figure 5. 1. Schematic illustration of scaffold implantation on calvaria and subcutaneous model, following the 3R principle.

In the calvaria model, 2 samples were placed on either side of the rat parietal bone. In the subcutaneous model, a total of 6 samples were placed on the dorsal side of the rat.
The images were created with Biorender.

A rat calvaria critical-size defect model was used for the bone regeneration analysis. Two 5 mm calvaria defects positioned on either side of the parietal bone were produced in each rat using a dental handpiece and a 5 mm trephine bur under cooling conditions with sterile saline. Before implantation, the defect sites were randomly allocated to experimental groups (Sham, CSMA-2 0 HA and CSMA-2 10 HA). The number of animals used in calvaria model was 6 animals.

After the implantation, the skin was sutured with non-absorbable sutures (4-0 Prolene, Ethicon, Germany), and the subcutaneous model was sacrificed at 1, 7, 14, 21 days, while the calvaria model was sacrificed after 6 weeks by carbon dioxide inhalation.

5.2.3. Scaffold Evaluation

The tissue surrounding the implant was harvested and fixed in 10% neutral buffered formalin for 24 hours at room temperature.

The subcutaneous models were immersed in 10 - 30% sucrose solution for one day and stored at -80°C in an optimal cutting temperature compound (Tissue-Tek, Sakura, USA). The frozen blocks were sectioned into 8 µm slices using a cryostat microtome (OOO, Leica, Germany). The sliced samples were mounted on slides and stained with Hematoxylin and Eosin (H&E) to analyse tissue fibrosis and neovascularisation.

New bone formation on the calvaria model was first visualised with a micro-CT scanner (Skyscan 1176, Skyscan, Belgium). The bone formation was measured in a cylindrical region of interest based on the 3D images reconstructed using the Skyscan program. Bone volume (BV), bone surface (BS), bone volume/tissue volume (BV/TV), and bone surface density (BSD) were analysed quantitatively.

The samples were decalcified with rapid Cal solution for histology and immunohistochemistry analysis. The decalcified samples were dehydrated using a serial ethanol regime and xylene and embedded in a paraffin solution. The paraffin blocks were sectioned into 5 µm slices using a semi-automated rotary microtome (RM2245, Leica, Germany). The sliced samples were mounted on slides and stained with H&E, Masson's Trichrome (MT), and Bone Morphogenetic Protein (BMP, Invitrogen, USA) to analyse osteogenesis and neovascularisation. Images were obtained using a slide scanner (VS200, Olympus, Japan) and analysed using an Olympus image viewer (Olyvia, Olympus. Japan).

An aluminium 1mm filter was used in the scanning setting of the CT (Skyscan 1176, Bruker) equipment program. Depending on the density of the

tissue, non-filter, aluminium filters (0.5, 1), aluminium-copper filters, and copper filters can be configured. When conducting analysis, the lower and upper grey thresholds were set to match the area of the old bone density. The analysis area of the lower and high vertical position was set after aligning the defect bottom horizontally.

5.2.4. Statistical Analysis

The data are presented in the form of mean ± standard deviation. The results were statistically analysed using one-way analysis of variance (ANOVA) at a 95% confidence interval with Tukey's post hoc test using GraphPad Prism 10.

5.2.5. Ethics Statement

This study was conducted following ARRIVE guidelines. The animal study was reviewed and approved by the Dankook University Ethics Committee (DKU-18-032).

5.3. Results

5.3.1. Angiogenesis

On day 1 post-implantation, CSMA-2 0HA and 10HA samples did not show visible blood vessel formation (figure 5.2A). The blood vessels were visible on day 7 samples, as shown in figure 5.2B. The angiogenesis started from the scaffolds' peripheral area on day 7 and progressed into the internal porous structure on day 14 and 21, as figure 5.2C and 5.2B reveal. The capillary blood vessels with various diameters were found to penetrate the gyroid structure of CSMA-2 10HA scaffolds more than CSMA-0HA groups. Both scaffold groups demonstrated close contact of the scaffolds with the connective tissue and newly formed blood vessels.

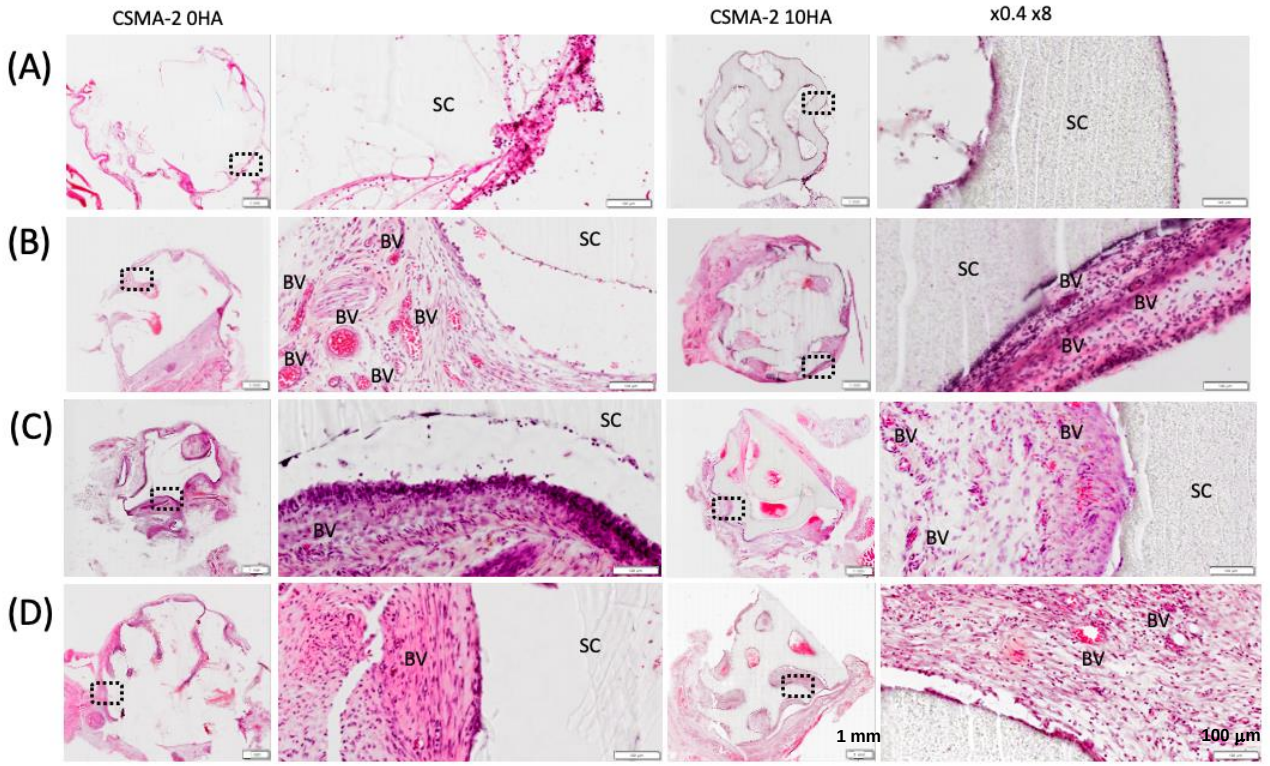

Figure 5. 2. Angiogenesis on CSMA-2 0HA and 10HA scaffolds implanted in rat subcutaneous model.

(A) 1 day, (B) 7 days, (C) 14 days and (D) 21 days. H&E stain shows histological low and high magnification images of the interface between connective tissue, blood vessels (BV), and scaffold (SC). Scale bars are 1 mm on lower magnification and 100 µm on higher magnification.

Fibrous capsule formation was evaluated to analyse the tissue response to the scaffolds. CSMA-2 0HA scaffolds induced thicker fibrotic capsules at earlier time points, days 1 and 7 (figure 5.3). For CSMA-2 10HA groups, day 14 samples showed the thickest capsule that decreased on day 21. The fibrosis capsule thickness was not significantly different among the groups in the following days.

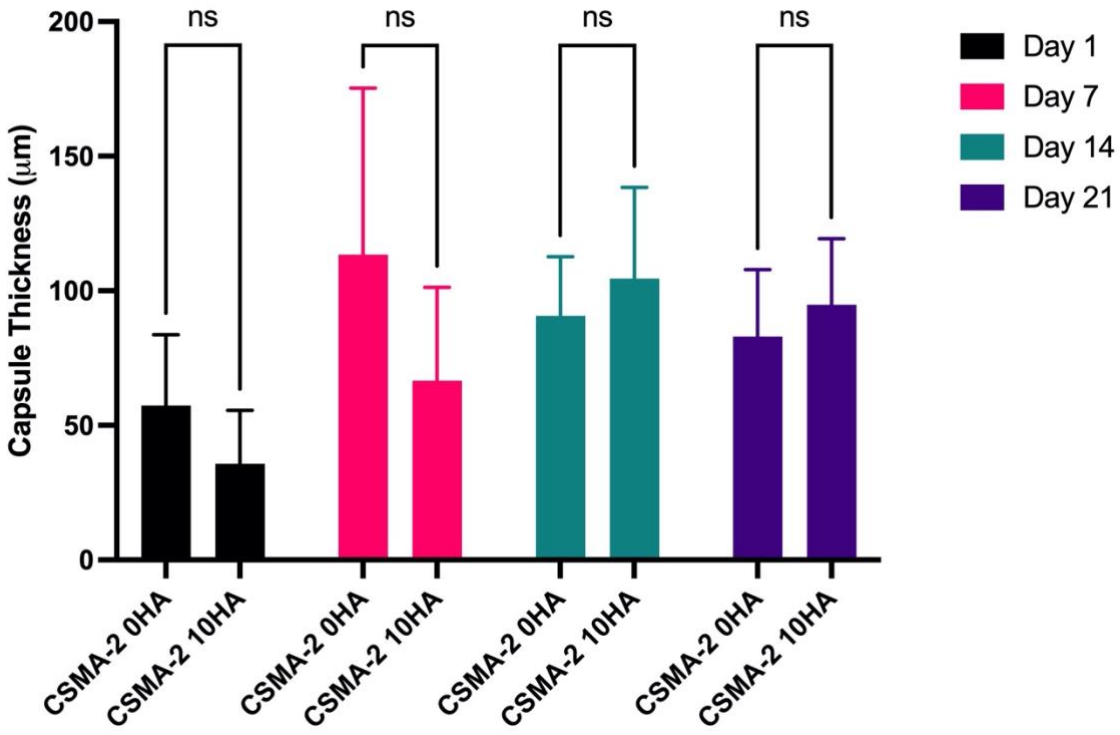

Figure 5. 3. Quantification of the thickness of the fibrous capsule.

There was no significant difference in capsule thickness between CSMA-2 0HA and 10HA. the thickness reaches its peak on Day 7 for CSMA-2 0HA and Day 14 for the CSMA-10HA scaffold. Data is presented as mean ± SD. NS = Not significant.

5.3.2. New Bone Formation

Histological analysis was performed to evaluate new bone formation on the rat calvaria critical size defect 6 weeks after implantation. This time point was chosen to evaluate the early-stage healing and ossification where newly formed woven bone can be detected on the peripheral area of the defect (Cooper et al., 2010; Naguib et al., 2023). New bone tissue was visible in every surgical group, with sham surgery as the control group showing relatively thin tissue compared to the defect with scaffold implantation (figure 5.4). Blood vessels were also seen to penetrate CSMA-2 0HA and 10 HA samples whilst not being noticeable in the sham surgery group (figure 5.4). Masson's trichrome (MT) staining images confirmed the new bone formation, with the blue stain indicating the abundant new collagen fibres.

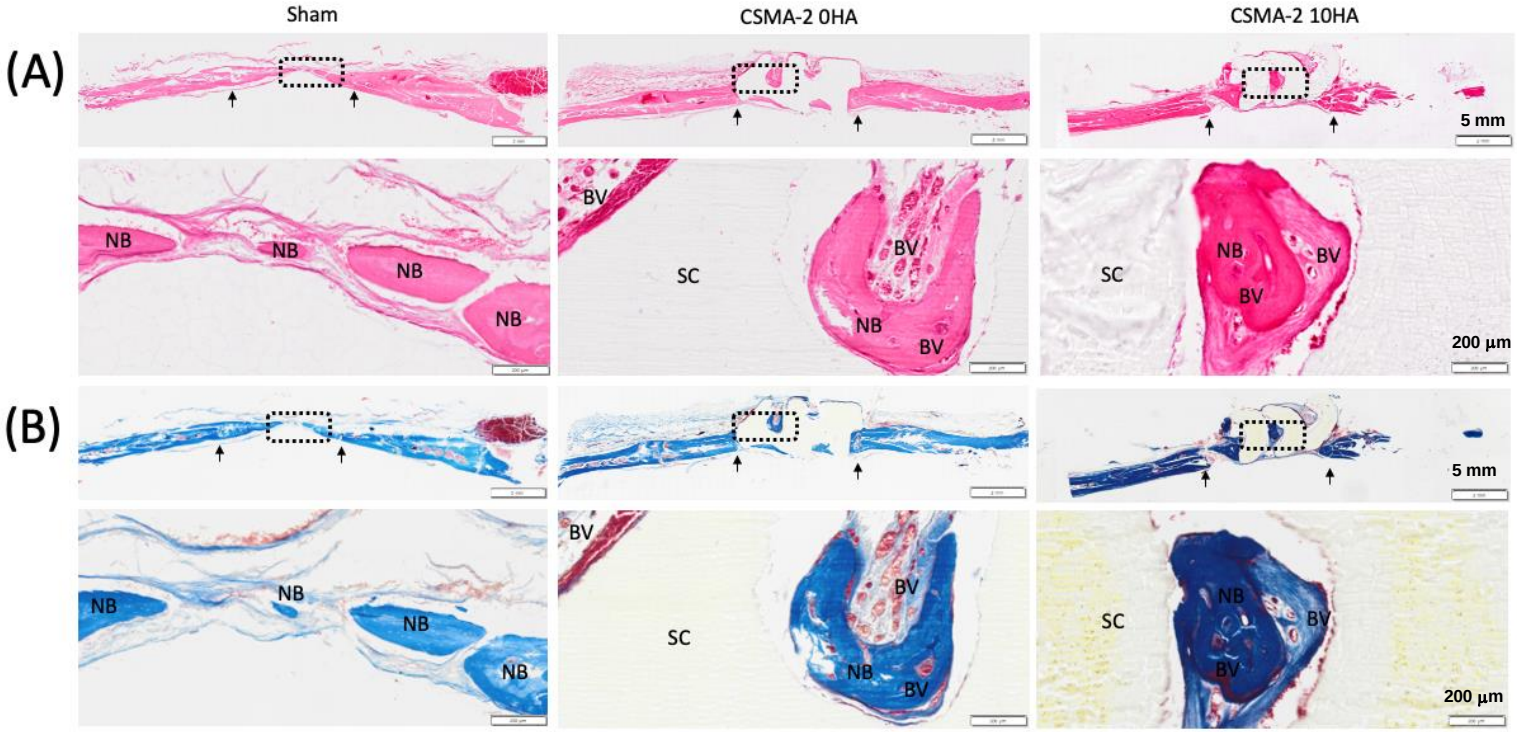

Figure 5. 4. Histological images of the new bone formation on the rat calvaria model.

(A) H&E stain showing the new bone formation and angiogenesis (B) MT staining images at low and high magnification show positive collagen bundle staining (dark blue). New bone (NB), scaffold (SC), blood vessels (BV) and black arrows indicate the margins of the bone defect site. Scale bars are 5 mm on lower magnification and 200 μm on higher magnification.

X-ray and micro-CT images revealed hard tissue formation in the defect (figure 5.5B and 5.5C). The quantified new bone volume was higher in the CSMA-2 10HA group than in CSMA-2 0HA, with volumes of approximately 8 mm^3 and 6 mm^3, respectively. Both scaffold groups showed higher bone surface than the sham surgery group, roughly 80 mm^2 for CSMA-2 0HA and 110 mm^2 for CSMA-2 10 HA (figure 5.6). CSMA-2 10 HA samples also demonstrated the highest bone volume fraction (BV/TV) and bone surface density (figure 5.6), whilst CSMA-2 0HA showed the lowest value of those new bone formation parameters among the surgical groups. The bone volume fraction of CSMA-2 10HA was around 18%, not significantly different to the sham surgery control group.

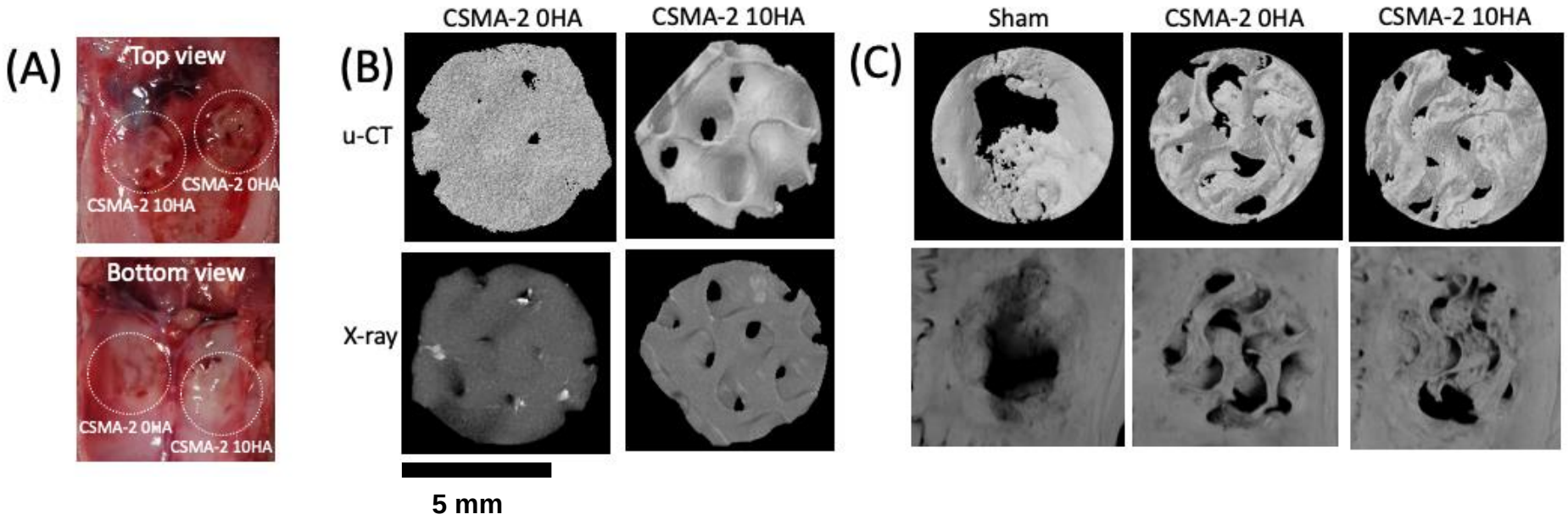

Figure 5. 5. The osteogenic capacity of the CSMA-2 0HA, CSMA-10HA implanted in rat calvaria defect model for six weeks.

(A) Optical images showing implanted CSMA-2 scaffold. (B) 3D scaffold μ-CT images. (C) μ-CT images were taken to reveal the new bone. Scale bar = 5 mm.

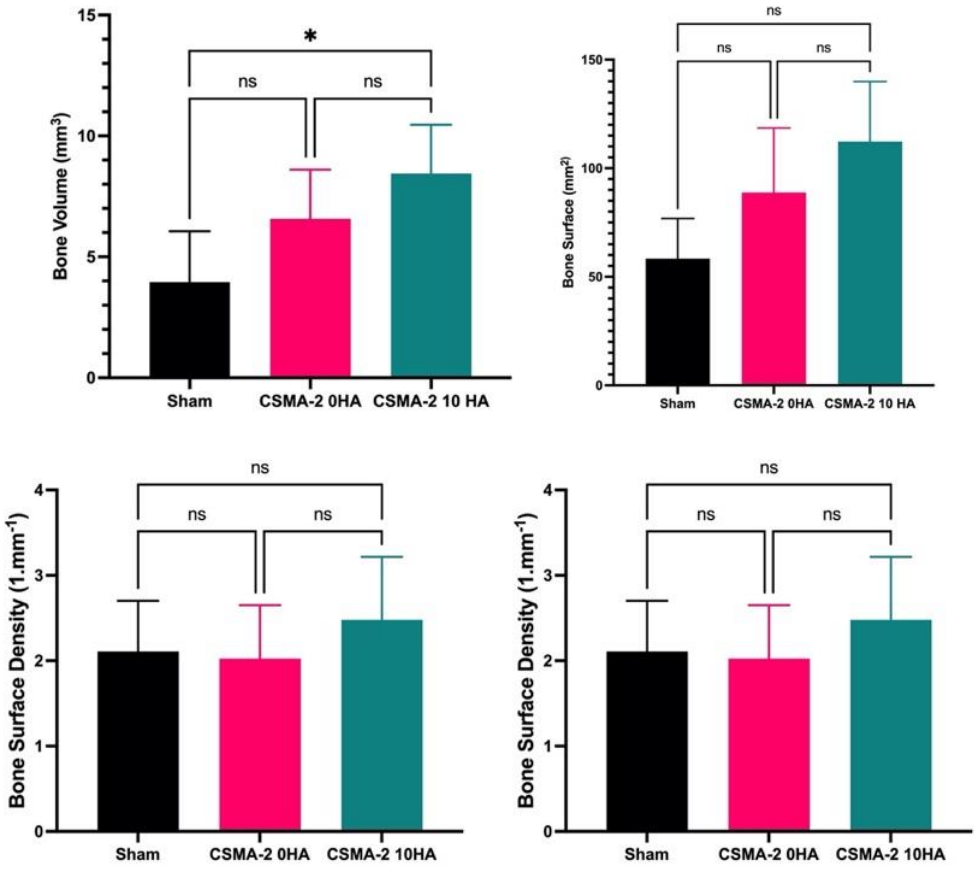

Figure 5. 6. µ-CT quantitative analyses of the calvaria model bone volume

*(BV), bone surface (BS), bone volume/tissue volume (BV/TV) and bone surface density (BSD). Data is presented as mean ± SD. NS= not significant. * = $p < 0.05$. There was no statistically significant difference in quantitative bone formation, except for CSMA-2 10HA bone volume compared to the sham groups.*

New bone tissue formation was also observed using immunohistochemical Bone morphogenetic protein-2 (BMP-2) staining. Positive staining of BMP-2 can be seen from the brownish colour on the images (figure 5.7A). The sham surgery control group showed slight positive staining of BMP-2 compared to the scaffold groups. Sporadic positive staining can be seen on CSMA-2 0HA groups. Positive staining was also visible on the porous structure of CSMA-2 10HA scaffolds. Quantitative analysis of BMP-2 staining revealed that the highest positive cells were found on the CSMA-2 10HA scaffold, followed by the CSMA-2 0HA scaffold and the sham surgery group (figure 5.7B).

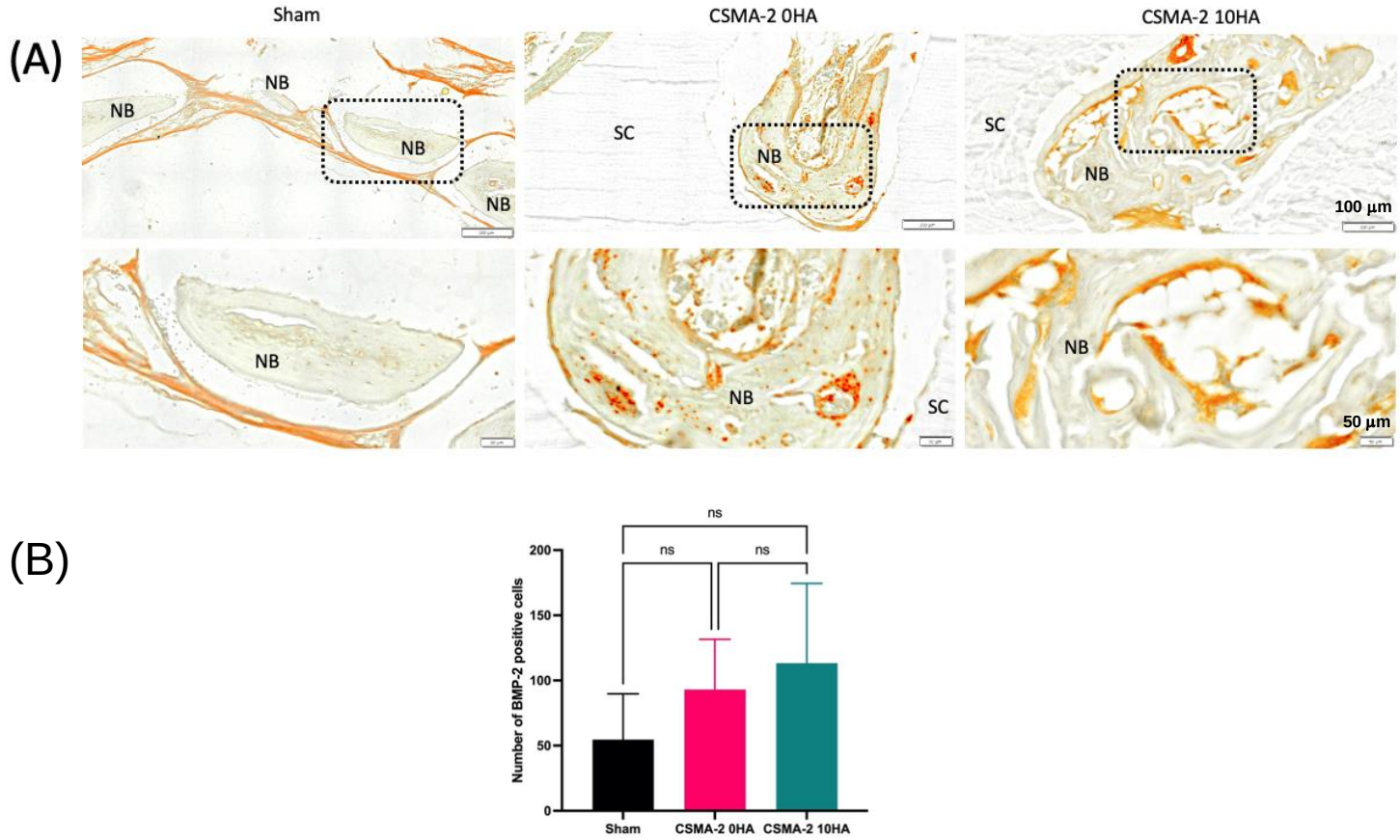

Figure 5. 7. Immunohistochemical expression of BMP-2 protein at the newly formed bone area in the calvaria defect.

Scale bars are 4 mm on lower magnification and 200 μm on higher magnification.
A. Immunohistochemical images show positive BMP-2 staining on the new bone formation area. B. Quantification of BMP-2 expression by the cells. Data is presented as mean $\pm$ SD. NS = not significant.

5.4. Discussion

As shown in figure 5.2A, the connective tissue was visible from day 1 post-implantation. The tissue can be seen to infiltrate the porous structure of the 3D-printed gyroid scaffold, indicating the adequate pore size for inducing necessary tissue response in the initial anabolic phase of bone healing. The increase in fibrotic tissue volume also can be observed after the implantation of the 3D-printed gyroid scaffolds in the subcutaneous model (figure 5.3). The presence of the fibrosis capsule indicated the initial stages of bone healing. The soft callus and the following fibrous tissue are usually developed around day 5-10 and day 10-16 of the healing process, respectively (Einhorn and Gerstenfeld, 2014; Wang and Yeung, 2017). In this study, the fibrotic capsule was the thickest at day 7 on CSMA-2 0HA scaffolds and day 14 for the CSMA-2 10HA groups. These findings are in line with the normal wound healing timeline.

The presence of fibrous connective tissue also leads to the fibrovascular phase, where vascular remodelling occurs (Bahney *et al.*, 2019). Figure 5.2B reveals the presence of blood vessels on day 7 after the surgical implantation, marking the fibrovascular phase. Angiogenesis and vasculogenesis occur in this phase (Bahney *et al.*, 2019). Angiogenesis forms new blood vessels by sprouting them from the existing vasculature, whilst blood vessels in vasculogenesis are formed by in situ endothelial progenitor cells (EPC) (Bahney *et al.*, 2019). Angiogenesis comprises endothelial cell sprouting, branching, lumen formation, and remodelling (Boopathy and Hong, 2019). As revascularisation grows into the injured area and the collagen matrix is laid down, the repair phase follows the fibrovascular phase for a couple of weeks (Maruyama *et al.*, 2020). Blood vessels are still visible in the repair phase since vascularisation is essential for new bone formation. A strong relationship between angiogenesis and osteogenesis has

been reported in previous studies (Bobbert and Zadpoor, 2017; Grosso *et al.*, 2017). Alteration in revascularisation can compromise bone healing, resulting in osteonecrosis and non-union fractures.

This relationship also applies to bone tissue engineering. One of the significant clinical challenges of bone substitute implantation is maintaining the cell viability in the core of the graft, which depends on the vascularisation from the host (Grosso *et al.*, 2017). The lack of vascular networks inside the graft can lead to poor oxygen supply, nutrient transport, and cell death. Further blood vessel infiltration can be seen in figure 5.2C and 5.2D. The gyroid structure with approximately 400 μm pore size diameter was found to provide a favourable environment for vascular remodelling, as shown by the presence of blood vessels in the inner structure of the 3D-printed scaffolds.

In accordance with these results, several studies have reported the angiogenic properties of the gyroid structure, noting the pore size and interconnectivity to have essential roles in the blood vessel (Qi *et al.*, 2022; Wu *et al.*, 2022; Li *et al.*, 2023). Scaffolds with 200 - 300 μm pore diameter demonstrated the formation of large blood vessels vascular network with deep penetration depth (Wu *et al.*, 2022). Additionally, pore geometry has been reported to affect neovascularisation. Scaffolds with hexagonal pores showed significantly slower angiogenesis than the gyroid scaffolds (Wu *et al.*, 2022). This finding is consistent with newer studies, which showed enhanced HUVEC migration and tube formation in gyroid scaffolds compared to cubic and cylindrical pore scaffolds (Li *et al.*, 2023).

Several factors could cause these results; one of them is the influence of biomaterials on the Hippo pathway YAP (Yes-associated protein)/ TAZ (transcriptional coactivator with PDZ-binding motif) (Boopathy and Hong, 2019).

YAP/TAZ pathway has been reported to regulate endothelial cell proliferation, migration, and viability (Boopathy and Hong, 2019). YAP/TAZ directly binds to the TEAD family and RUNX family of transcription factors. The interaction of YAP/TAZ with TEAD1 increases the expression of the ANKRD1 gene, leading to the proliferation and angiogenesis of stem cells (Lee *et al.*, 2019). Furthermore, osteogenesis is also increased by the binding of YAP/TAZ to the RUNX2 (Lee *et al.*, 2019). Therefore, angiogenesis and osteogenesis can be mediated by the YAP/TAZ pathway.

YAP/TAZ acts as a mechanotransducer, affecting the cell response to the physical microenvironment (Brusatin *et al.*, 2018). YAP and TAZ use the physical cues on the cells and convert them into transcriptional responses (Kovar, Bierbaumer and Radic-Sarikas, 2020). Physical structures, like the pore curvature of the gyroid design, were found to activate the YAP/TAZ pathway (Li *et al.*, 2023). This finding is consistent with another study that demonstrated the activation of the YAP/TAZ pathway by the shallow curvature of the scaffold micropore with a larger diameter (>200 μm)(Swanson *et al.*, 2022). The larger pores also showed robust vascularisation in the subcutaneous animal model (Swanson *et al.*, 2021). The blood vessel infiltration in larger micropores was deeper than those with smaller diameters (Swanson *et al.*, 2021). Furthermore, the diameter of the blood vessels was also higher in larger pores. Thus, these results indicated positive cell and tissue modulation by the scaffold pore size and geometry.

The favourable gyroid architecture was accurately 3D printed using the isosorbide-based polymer CSMA-2. Isosorbide is used as a cardiovascular medicine in isosorbide dinitrate (ISDN) or isosorbide mononitrate (ISMN) form. Previous studies revealed that ISMN could promote angiogenesis in vitro and in

zebrafish embryo models, suggesting its potential to treat angiogenesis-related diseases (Lv, Liu and Qin, 2020). Isosorbide was also incorporated into a composite scaffold for vascular regeneration. The combination of PLGA and poly(isosorbide sebacate) (PISEB) was shown to be cytocompatible with HUVEC and showed pro-angiogenic gene expression (Śmiga-Matuszowicz *et al.*, 2023). Moreover, CSMA-2 demonstrated an angiogenic response that can be observed via the CAM assay (Owji *et al.*, 2022).

In addition, bioceramics such as beta-tricalcium phosphate (β-TCP) have shown angiogenic properties by promoting angiogenesis in HUVEC. β-TCP was found to engage with the PI3K/Akt/eNOS axis to promote vascularisation (Nosrati *et al.*, 2021). Other studies with HA as the bio-ceramic component demonstrated compatibility with HUVEC, increased expression of VEGF, and formation of tubular networks (Dixit *et al.*, 2022). These in vitro results suggested the angiogenic properties of HA. Similarly, CAM assay results from heparinised chitosan/hydroxyapatite scaffold implantation showed vascular formation, regardless of the amount of loaded heparin (Nájera-Romero, Yar and Rehman, 2020). This finding indicated the role of HA in angiogenesis by interacting with molecules from microvascular cells and modulating their behaviour (Nájera-Romero, Yar and Rehman, 2020). Therefore, the combination of the 3D printing material and architecture was able to promote the necessary vascularisation for bone regeneration.

The 3D-printed CSMA-2 gyroid scaffolds also facilitated bone growth in critical size defects, as seen in figure 5.5A, 5.5B, and 5.5C. Compared to the sham surgery group, the new bone formation was significantly higher in CSMA-2 10HA scaffold groups. This microCT result corroborated the findings in the previous work, which demonstrated a significant difference in BV/TV between the

gyroid scaffold, commercial graft, and the sham after 6 weeks of implantation (Zhu *et al.*, 2021). The gyroid structure provides a more concave structure, which is more favourable for tissue formation than the convex (Zhu *et al.*, 2021). The smooth surface transition in the gyroid also allows better cell spreading.

Furthermore, cell spreading has been reported to increase YAP/TAZ accumulation in the cell nucleus and activate their transcription (Caliari *et al.*, 2016). YAP/TAZ is a co-regulator of transcription factors essential for bone homeostasis (Lee *et al.*, 2019). They promote stem cell expansion and control osteogenic or chondrogenic differentiation in response to biomechanical and biochemical stimulation (Kovar, Bierbaumer and Radic-Sarikas, 2020). The 3D-printed CSMA-2 gyroid scaffolds provided a favourable physical environment to activate the YAP/TAZ pathway with their stiffness and curvatures. The interaction between cells and scaffold then leads to the upregulation of YAP/TAZ and their binding to RUNX2, resulting in increased bone growth.

Compared to scaffolds without HA, those with HA showed greater new bone formation, as shown in figure 5.6. HA is a naturally occurring and the most stable form of calcium phosphate, constituting most of the human bone's inorganic component (Jeong *et al.*, 2019). It is able to bond to the bone chemically, shows low toxicity and inflammatory response, and stimulates bone growth by influencing osteoblast behaviour (Jang *et al.*, 2017). HA comprises only calcium and phosphate ions, resulting in no adverse reaction when implanted in the human body (Kattimani, Kondaka and Lingamaneni, 2016). HA-based bone graft implantation has been reported to demonstrate bone formation in various animal models (Kim, Kim and Moon, 2016; Jang *et al.*, 2017). New bone formation was observed in the canine alveolar socket as early as 4 weeks post-implantation of different HA forms (Jang *et al.*, 2017). Bone regeneration also

occurred in rat calvaria critical-size defects implanted with commercial HA products (Kim, Kim and Moon, 2016; da Silva Pires *et al.*, 2021).

It has been known that HA coating can improve implant integration with bone (Kattimani, Kondaka and Lingamaneni, 2016). After the implantation, the HA surface is covered rapidly by proteins and other biomolecules, leading to the precipitation of calcium phosphate crystal growth or crystal morphology alterations (Wang *et al.*, 2017). The surface roughness resulting from HA crystals provided a suitable environment for osteogenic differentiation in a YAP/TAZ-dependent manner (Brusatin *et al.*, 2018). Progenitor cells, such as stem cells, can sense the topography through contact with the material surface, forming lamellipodia and filopodia (Oladapo, Zahedi and Adeoye, 2019; Ramaswamy *et al.*, 2021). The topographical information allows filament maturation and forms focal adhesion that induces a specific cellular function (Ramaswamy *et al.*, 2021). The focal adhesion properties are usually related to actin contractility and Ras homolog family member A (RhoA). RhoA and Rho-associated kinase (ROCK) pathway activation leads to cell spreading. As mentioned before, cell spreading promotes osteogenic differentiation. Focal adhesion kinases (FAK) can also activate the Ras pathway that stimulates the ERK signalling cascade, resulting in the expression of osteogenic markers such as COL I and OCN (Bal *et al.*, 2020).

The interaction between cells and biomaterials is based on the complex biomolecular interaction between the surfaces (Gu *et al.*, 2019). The biological influence of a biomaterial on cells results from functional protein adsorption and conformational change of the adsorbed target protein caused by the biomaterial properties. One of the most important proteins in bone regeneration is Bone morphogenetic protein-2 (BMP-2). BMP-2 is a transforming growth factor β (TGF-β) superfamily member. It plays a role in the formation, growth,

development, and reconstruction of bone and cartilage. It is also capable of stimulating non-osteogenic cells to differentiate into osteoblasts. BMP-2 is essential for organ development in the embryonic stage, such as digit formation and cardiogenesis (Halloran, Durbano and Nohe, 2020). Many cells, including osteocytes and osteoblasts, express BMP, contributing to the ossification process in adults. BMP-2 binds with the SER-THR receptor and initiates the osteoblast differentiation signal cascade. The binding induces Smad family recruitment and phosphorylation, particularly Smad1/5/8 (Wei *et al.*, 2020).

It has been reported that BMP-2-induced osteogenic differentiation is dependent on cell shape, cytoskeletal tension, matrix stiffness, and cell-ligand interactions (Wei *et al.*, 2020). These factors also affect the previously mentioned YAP/TAZ pathway. YAP/TAZ is known to read the cytoskeletal tension, which induces the YAP/TAZ nuclear localisation and crosstalk with the BMP-2 signalling pathway (Wei *et al.*, 2020). Previous studies revealed that the knockdown of YAP/TAZ resulted in ALP activity, whilst the recovery of YAP/TAZ increased the ALP (Wei *et al.*, 2020). Thus, tension-activated YAP/TAZ was found to regulate BMP-2 signalling and osteogenic differentiation.

Figure 5.5 reveals the influence of 3D-printed CSMA-2 on BMP-2-induced bone regeneration. Without adding exogenous BMP-2, such as FDA-approved RhBMP2, all groups showed positive BMP-2 expression. Moreover, the CSMA-2 10HA showed the highest BMP-2 positive cells. This result was in accordance with the highest bone volume and fibrous capsule thickness found in the CSMA-2 10HA groups. BMPs have been documented to play a role in bone regeneration by recruiting mesenchymal cells and differentiating them into bone cells (Garrison *et al.*, 2010). BMPs also contribute to bone matrix production and vascularisation (Garrison *et al.*, 2010).

Furthermore, BMP-2 was found to regulate the expression of other BMPs (Dumic-Cule *et al.*, 2018). In a mouse fracture healing study, BMP-2 was found to initiate the repair cascade, showing the peak of its mRNA expression 24 hours after the injury (Dumic-Cule *et al.*, 2018). In the human study, BMP-2 expression increased in the endochondral ossification area (Dumic-Cule *et al.*, 2018). These findings explain the expression of endogenous BMP-2 in all groups after 6 weeks of surgery, including the sham surgery group.

It has been documented that there is a strong affinity between HA and BMP-2 protein (Lu *et al.*, 2015). Previous studies investigated the interaction between the protein's functional groups and HA's calcium ions (Lu *et al.*, 2015). Several factors, including the specific structural characteristics of the protein and HA's surface properties, also influence the adsorption of BMP-2 onto the HA (Lu *et al.*, 2015). BMP-2 demonstrated a positive charge, resulting in the electrostatic attraction between HA and BMP-2 and further adsorption of BMP-2 on the HA surface (Lu *et al.*, 2015). The same studies also suggested the presence of hydrogen bonds between HA and BMP-2 based on FTIR experiments (Lu *et al.*, 2015).

Additionally, extracellular Ca^{2+} ions have been reported to enhance BMP-2 effects on OCN, RUNX2, and osterix expressions in a calvarial critical-size defect model (Aquino-Martínez *et al.*, 2017). The interaction between extracellular Ca^{2+} and BMP-2 in osteoblasts was found to be induced by the calcium-dependent transcription factor NFATc1 of BMP-2 (Aquino-Martínez *et al.*, 2017). In the same study, exposure of Ca^{2+} ions to the cell culture also increased BMP-2, BMP-4, and Axin2 gene expression, confirming the positive relationship between calcium and BMP-2 (Aquino-Martínez *et al.*, 2017). Ca^{2+}

and BMP-2 then cooperatively stimulate the osteogenic differentiation of the osteoblast (Aquino-Martínez *et al.*, 2017).

These studies and findings, to some degree, support the in vivo results in this chapter. The results indicated that HA content in the CSMA-2 10HA scaffolds increases BMP-2 expression and new bone formation compared to the CSMA-2 0HA group. This result might be caused by the exposure of extracellular Ca^{2+} from the scaffold to the progenitor cells residing in the surrounding host tissue, which induced the BMP-2 secretion and greater new bone formation in vivo.

The limitation of this in vivo study includes the absence of power calculation when determining the number of animals. The study also did not perform analysis on the isolated cartilage layer and bilayer scaffold. Pre-seeding the scaffold with cells was not performed due to the limited time and complexity of the experiment.

5.5. Conclusions

This chapter describes the result of in vivo experiments to evaluate the biocompatibility of the 3D-printed CSMA-2 scaffold. The scaffolds were implanted in the subcutaneous model to evaluate the tissue response and in the rat calvaria critical size defect model for the bone formation analysis. The subcutaneous model results showed a favourable tissue response that includes angiogenesis and fibrous tissue, indicating the early wound healing process. The critical size defect model results demonstrated the new bone formation confirmed by micro-CT imaging and immunohistochemistry. The combination of CSMA-2 as the 3D printing material and gyroid as the 3D structure was found to support essential events of bone healing, which are angiogenesis and osteogenesis.

Chapter 6. General Discussions and Conclusions

6.1. Research Objectives

Joints are essential anatomical parts that enable humans to move and carry out daily activities. Human joints have a composite structure formed by articular cartilage and subchondral bone known as the osteochondral unit. The function of this stratified structure includes shock absorber and load transfer during weight bearing and joint motion (Yan *et al.*, 2015). The damage to both layers of the osteochondral unit can cause a reduced range of movement, pain, limitation in daily activities, and a decreased quality of life.

Extensive osteochondral defects require tissue replacement, and osteochondral allograft (OCA) transplantation is the gold standard for larger injuries involving bone and cartilage layers (Husen *et al.*, 2022). Nevertheless, like any other allografts, OCA has major disadvantages, including limited donor tissue availability, graft-tissue mismatch, donor tissue viability, and risk of disease transmission (Matthews *et al.*, 2022).

To provide an alternative solution, a tissue engineering approach can be utilised by developing suitable biomaterials for each layer of the osteochondral tissue and then combining them. This study chose the multi-phasic method to create a specific bone and cartilage tissue environment, mimicking the osteochondral tissue layers. Moreover, with the emergence of personalised medicine, patient-specific implants are made possible by 3D printing methods.

Therefore, the objectives of this thesis are as follows:

1. Development of a 3D-printed biomimetic bilayer osteochondral scaffold for tissue engineering and reconstructive surgery of the joint
2. Development, optimisation, and characterisation of the scaffold's bone layer
3. Development, optimisation, and characterisation of the scaffold's cartilage layer
4. Simulation of bilayer scaffold preconditioning for clinical applications.

6.2. Summary of Key Findings

The 3D-printed biomimetic bilayer scaffolds were successfully fabricated using a novel polymer CSMA-2 as the bone layer and GelMA as the cartilage layer. CSMA-2 is an isosorbide-based polymer with widely used methacrylate as its functional group. The bicyclic structure of isosorbide contributes to the mechanical properties of polymerised CSMA-2 (Nonque *et al.*, 2020), and its optical transparency allows light-based polymerisation (Lai *et al.*, 2019). CSMA-2 was chosen due to its printability with lithography-based 3D printing techniques, particularly DLP, that enable the fabrication of a biomimetic bone scaffold with the gyroid computer-aided design. The advantages of DLP 3D printing are a faster printing process and the possibility of fabricating non-conventional pore curvatures (Petcu *et al.*, 2018; Wu *et al.*, 2022). CSMA-2 showed suitable rheological properties for vat polymerisation methods, regardless of the HA addition up to 10% w/w. The range of viscosity shown by the CSMA-2 groups (below 1 Pa.s) was within the acceptable material viscosity for the vat polymerisation printing, such as SLA and DLP (below 10 Pa.s) (Voet *et al.*, 2018). The low viscosity shown by CSMA-2 allowed the recoating mechanism of the

liquid resin between the last 3D printed model and the resin tank surface, enabling the 3D printing of the biomimetic gyroid structure.

The 3D-printed gyroid scaffold showed good shape fidelity by demonstrating a similar 3D-printed structure as the CAD and mechanical properties within the reported range of human trabecular bone. The scaffolds also demonstrated cytocompatibility with relevant cell lines, such as MC3T3-E1 and hADSC. Osteogenic differentiation of the stem cells was found to occur in the bone layer scaffold, indicated by osteogenic marker expression RUNX2, OPN, OCN, and calcium deposition. CSMA-2 was able to support cell growth and differentiation with HA addition, showing an earlier and higher gene expression of osteogenic differentiation marker as described in Chapter 2. These in vitro results were confirmed further by the in vivo study of the 3D-printed CSMA-2 scaffold in Chapter 5. Favourable tissue response, angiogenesis, and new bone formation were visible after the implantation of the scaffolds on the small animal preclinical model. CSMA-2 with 10% w/w HA content (CSMA-2 10HA) showed similar osteogenic properties in vitro and in vivo, with higher bone volume and BMP-2 expression post-implantation. Therefore, CSMA-2 has the potential to be the 3D-printing material for patient-specific implants, particularly for load-bearing bone defects.

GelMA was chosen as the cartilage layer material to create a bilayer scaffold, among other hydrogels. It has been widely used for tissue engineering due to its favourable biological properties and tunable physical characteristics. The source of gelatin can be porcine, bovine, and fish. This study used bovine GelMA based on previous studies that reported similar mechanical properties of bovine GelMA to native cartilage (Pahoff *et al.*, 2019). GelMA's tunability enabled the fabrication of a stand-alone cartilage layer scaffold and a composite bilayer

scaffold with GelMA as the cartilage layer. The GelMA was optimised to determine the most suitable concentration and cross-linking parameters to provide cartilage tissue-like properties, as explored in Chapter 3. Different GelMA concentrations and UV irradiation times exhibited mechanical properties within the known native cartilage tissue mechanical properties range. Lower GelMA concentration led to lower viscosity, which is easier to manipulate and combine with the 3D-printed CSMA-2. The rheological analysis also revealed the optimum working temperature of GelMA at 37°C. In addition, higher concentrations and longer UV irradiation reduced cell viability. Based on their mechanical properties and cell viability, 10% and 15% GelMA with 1-minute UV curing time were chosen for the differentiation assays. There was no significant difference in the expression of chondrogenic markers, Sox9 and Collagen II among 10% and 15% GelMA scaffolds.

Since the results of the individual layers were promising, a bilayer scaffold was fabricated by combining GelMA and CSMA-2. After several trials, a combination of 3D-printed CSMA-2 with light-cured GelMA was found to be the most cohesive and stable, as explored in Chapter 4. To investigate whether the bilayer scaffolds can simultaneously support the growth of bone cells and cartilage cells, a co-culture in vitro study was performed on the bilayer scaffolds. Pre-osteoblast MC3T3-E1 and chondrogenic cells ATDC-5 were seeded on the bone and cartilage layer, respectively. In a short-term culture period, the cells were found to reside on their assigned layers, indicating a suitable environment for different layers of osteochondral tissue. The combination of CSMA-2 0HA and 10% GelMA showed the highest metabolic activity, similar to the result of the single-layer cytocompatibility study. Long-term cell cultures in different settings, static and dynamic in a simple perfusion bioreactor, were conducted to simulate

the preconditioning on clinical application with 10% GelMA and CSMA-2 0HA and 10HA. The bilayer scaffold showed positive chondrogenic and osteogenic differentiation staining, indicating a suitable environment for osteochondral tissue regeneration. In addition, the bilayer scaffolds can maintain their structural integrity during the 4-week dynamic and static co-culture period, showing the strong and stable bond between GelMA and CSMA-2. Therefore, the results in Chapter 4 suggested the potential of bilayer scaffold for future clinical application.

6.3. Limitations and Future Works

The osteochondral unit is a complex and intricate structure to be replicated artificially. Numerous biomaterials and technologies have been investigated to provide satisfactory scaffold-based tissue engineering solutions for osteochondral repair. At the moment of writing, the reconstruction of the gradient structure of osteochondral tissue remains challenging. This study tried to provide a mechanically strong, biocompatible, and customisable bone layer to support cartilage tissue repair with limited regenerative capacity. Collagen-derived GelMA was chosen to help facilitate cartilage repair due to its resemblance to ECM, tunability, and adhesive properties. Several trials were carried out to combine different materials and create a biomimetic and durable composite scaffold. The combination of GelMA/CSMA-2 maintained its integrity during long-term dynamic cell culture, indicating its durability and capacity to remain stable in a physio-mimetic condition. Although the scaffolds fabricated in this study showed promising results as independent and composite layers, some limitations can be explored further to develop an improved osteochondral scaffold.

The main limitations of this study are as follows:

1. The bilayer scaffold was fabricated by combining 3D printing and manual deposition of the material. An ideal setup will be 3D printing both layers by changing the material for the next layer, combining different 3D printing methods, or using a more sophisticated 3D printing machine. A fully 3D-printed bilayer scaffold might allow for better matching of the recipient site anatomy.
2. The in vivo study did not include the single-layer cartilage and bilayer osteochondral scaffolds. Preconditioning with cells in the bioreactor before the in vivo implantation was also not performed in this study. Even though GelMA has been widely investigated compared to CSMA-2, the in vivo study for the cartilage layer can help to optimise GelMA as the chondrogenic material. Cartilage regeneration is more challenging to predict since the nature of native cartilage shows limited regenerative capacity. Cell encapsulation in the GelMA might improve cartilage tissue regeneration and implant integration. Preconditioning with high cell density is expected to enhance new tissue formation.
3. The absence of bioactive substances. Cartilage tissue healing is known to be limited compared to bone, and bioactive substances like growth factors might be needed to improve cartilage regeneration.

Therefore, future work related to this study might include the following:

1. Exploration of 3D printing methods to fabricate a fully customisable osteochondral scaffold for a better patient-specific implant.
2. Further investigation of the bilayer scaffold's mechanical properties to confirm and improve its integrity during the joint motion.
3. In vivo study to evaluate GelMA as the chondral layer and the potential to incorporate cells or growth factors to improve cartilage repair.
4. In vivo study to evaluate GelMA/CSMA-2 bilayer scaffold in a critical-size osteochondral defect with cellular preconditioning before the implantation.

6.4. Conclusions

It can be concluded that CSMA-2 and GelMA demonstrated remarkable potential as biomaterials for bone and cartilage tissue engineering. The combination of these materials and the innovative employment of DLP 3D printing was able to fabricate a biomimetic bilayer osteochondral scaffold. The initial outcomes were promising, showcasing tissue-like physical attributes and robust mechanical properties, all while demonstrating satisfactory in vivo biocompatibility. Although the present study has unveiled a series of favourable findings, it is essential to acknowledge its current limitation. To further elevate these already encouraging results, there exists an opportunity for more in-depth exploration and comprehensive evaluation. Future studies could involve preclinical large animal models and human clinical trials. Hence, this development could contribute to transformative osteochondral repair, tissue engineering, and regenerative medicine.

References

Abe, T., Takahashi, S. and Fukuuchi, Y. (2002). 'Reduction of Alamar Blue, a novel redox indicator, is dependent on both the glycolytic and oxidative metabolism of glucose in rat cultured neurons'. *Neuroscience Letters*. Elsevier, 326 (3), pp. 179–182.

Abueidda, D. W., Elhebeary, M., Shiang, C. S. (Andrew), Pang, S., Abu Al-Rub, R. K. and Jasiuk, I. M. (2019). 'Mechanical properties of 3D printed polymeric Gyroid cellular structures: Experimental and finite element study'. *Materials and Design*. Elsevier Ltd, 165.

Alizadeh-Osgouei, M., Li, Y., Vahid, A., Ataee, A. and Wen, C. (2021). 'High strength porous PLA gyroid scaffolds manufactured via fused deposition modeling for tissue-engineering applications'. *Smart Materials in Medicine*. Elsevier, 2, pp. 15–25.

Aquino-Martínez, R., Artigas, N., Gámez, B., Luis Rosa, J., Ventura, F. and Cray, J. J. (2017). 'Extracellular calcium promotes bone formation from bone marrow mesenchymal stem cells by amplifying the effects of BMP-2 on SMAD signalling'. *PLoS ONE*, 12 (5), pp. 1–14.

Assmann, A., Vegh, A., Ghasemi-Rad, M., Bagherifard, S., Cheng, G., Sani, E. S., Ruiz-Esparza, G. U., Noshadi, I., Lassaletta, A. D., Gangadharan, S., Tamayol, A., Khademhosseini, A. and Annabi, N. (2017). 'A highly adhesive and naturally derived sealant'. *Biomaterials*. Elsevier Ltd, 140, pp. 115–127.

Bagheri, A. and Jin, J. (2019). 'Photopolymerization in 3D Printing'. *ACS Applied Polymer Materials*.

Bahney, C. S., Zondervan, R. L., Allison, P., Theologis, A., Ashley, J. W., Ahn, J., Miclau, T., Marcucio, R. S. and Hankenson, K. D. (2019). 'Cellular biology of fracture healing'. *Journal of Orthopaedic Research*, 37 (1), pp. 35–50.

Bakhtiary, N., Liu, C. and Ghorbani, F. (2021). 'Bioactive Inks Development for Osteochondral Tissue Engineering: A Mini-Review'. *Gels (Basel, Switzerland)*. Gels, 7 (4).

Bal, Z., Kaito, T., Korkusuz, F. and Yoshikawa, H. (2020). 'Bone regeneration with hydroxyapatite-based biomaterials'. *Emergent Materials*. Emergent Materials, 3 (4), pp. 521–544.

Barroso, I. A., Man, K., Robinson, T. E., Cox, S. C. and Ghag, A. K. (2022). 'Photocurable GelMA Adhesives for Corneal Perforations'. *Bioengineering*. MDPI, 9 (2).

Baruffaldi, D., Palmara, G., Pirri, C. and Frascella, F. (2021). '3D Cell Culture: Recent Development in Materials with Tunable Stiffness'. *ACS Applied Bio Materials*. American Chemical Society, 4 (3), pp. 2233–2250.

Beck, E. C., Barragan, M., Tadros, M. H., Gehrke, S. H. and Detamore, M. S. (2016). 'Approaching the Compressive Modulus of Articular Cartilage With a Decellularized Cartilage-Based Hydrogel'. *Acta biomaterialia*. NIH Public Access, 38, p. 94.

Bedell, M. L., Torres, A. L., Hogan, K. J., Wang, Z., Wang, B., Melchiorri, A. J., Grande-Allen, K. J. and Mikos, A. G. (2022). 'Human gelatin-based composite hydrogels for osteochondral tissue engineering and their adaptation into bioinks for extrusion, inkjet, and digital light processing bioprinting'. *Biofabrication*. IOP Publishing, 14 (4), p. 045012.

Bedi, A., Foo, L. F., Williams, R. J. and Potter, H. G. (2010). 'The Maturation of Synthetic Scaffolds for Osteochondral Donor Sites of the Knee: An MRI and T2-Mapping Analysis'. *Cartilage*. SAGE Publications, 1 (1), p. 20.

Bobbert, F. S. L. and Zadpoor, A. A. (2017). 'Effects of bone substitute architecture and surface properties on cell response, angiogenesis, and structure of new bone'. *Journal of Materials Chemistry B*. Royal Society of Chemistry, pp. 6175–6192.

Boopathy, G. T. K. and Hong, W. (2019). 'Role of Hippo Pathway-YAP/TAZ signaling in angiogenesis'. *Frontiers in Cell and Developmental Biology*, 7 (APR), pp. 1–12.

Briggs, D. T., Sadr, K. N., Pulido, P. A. and Bugbee, W. D. (2015). 'The Use of Osteochondral Allograft Transplantation for Primary Treatment of Cartilage Lesions in the Knee'. *Cartilage*. SAGE Publications, 6 (4), p. 203.

Brusatin, G., Panciera, T., Gandin, A., Citron, A. and Piccolo, S. (2018). 'Biomaterials and engineered microenvironments to control YAP/TAZ-dependent cell behaviour.' *Nature Materials*. Nature Publishing Group, 17 (12), pp. 1063–1075

Caliari, S. R., Vega, S. L., Kwon, M., Soulas, E. M. and Burdick, J. A. (2016). 'Dimensionality and spreading influence MSC YAP/TAZ signaling in hydrogel environments'. *Biomaterials*. Elsevier, 103, pp. 314–323.

Carluccio, M., Ziberi, S., Zuccarini, M., Giuliani, P., Caciagli, F., Di Iorio, P. and Ciccarelli, R. (2020). 'Adult mesenchymal stem cells: is there a role for purine receptors in their osteogenic differentiation?' *Purinergic Signalling 2020 16:3*. Springer, 16 (3), pp. 263–287.

Cassidy, J. W., Roberts, J. N., Smith, C. A., Robertson, M., White, K., Biggs, M. J., Oreffo, R. O. C. and Dalby, M. J. (2014). 'Osteogenic lineage restriction by osteoprogenitors cultured on nanometric grooved surfaces: The role of focal adhesion maturation'. *Acta Biomaterialia*. Elsevier, 10 (2), pp. 651–660.

Chen, H., Han, Q., Wang, C., Liu, Y., Chen, B. and Wang, J. (2020). 'Porous Scaffold Design for Additive Manufacturing in Orthopedics: A Review'. *Frontiers in Bioengineering and Biotechnology*. Frontiers Media S.A., p. 609.

Chen, H., Tan, X. N., Hu, S., Liu, R. Q., Peng, L. H., Li, Y. M. and Wu, P. (2021). 'Molecular Mechanisms of Chondrocyte Proliferation and Differentiation'. *Frontiers in Cell and Developmental Biology*. Frontiers Media S.A. doi: 10.3389/fcell.2021.664168.

Chia, H. N. and Wu, B. M. (2015). 'Recent advances in 3D printing of biomaterials'. *Journal of Biological Engineering*, 9 (1), pp. 1–14.

Da Conceicao Ribeiro, R., Pal, D., Ferreira, A. M., Gentile, P., Benning, M. and Dalgarno, K. (2018). 'Reactive jet impingement bioprinting of high cell density gels for bone microtissue fabrication'. *Biofabrication*. IOP Publishing, 11 (1), p. 015014.

Cooper, G. M., Mooney, M. P., Gosain, A. K., Campbell, P. G., Losee, J. E. and Huard, J. (2010). 'Testing the critical size in calvarial bone defects: Revisiting the concept of a critical-size defect'. *Plastic and Reconstructive Surgery*, 125 (6), pp. 1685–1692.

Cross, M. J. and Spycher, J. (2008). 'Cementless fixation techniques in joint replacement'. *Joint Replacement Technology*, pp. 190–211.

Davis, K. A., Gottipatti, A., Peng, H., Donahue, R., Chelvarajan, L., Cahall, C., Tripathi, H., Al-Darraji, A., Ye, S., Abdel-Latif, A. and Berron, B. J. (2022). 'Gelatin coating enhances therapeutic cell adhesion to the infarcted myocardium via ECM binding'. *PLOS ONE*. Public Library of Science, 17 (11), p. e0277561.

Delcogliano, M., de Caro, F., Scaravella, E., Ziveri, G., De Biase, C. F., Marotta, D., Marenghi, P. and Delcogliano, A. (2014). 'Use of innovative biomimetic scaffold in the treatment for large osteochondral lesions of the knee'. *Knee Surgery, Sports Traumatology, Arthroscopy*. Springer Verlag, 22 (6), pp. 1260–1269.

Deligianni, D. D., Katsala, N. D., Koutsoukos, P. G. and Missirlis, Y. F. (2000). 'Effect of surface roughness of hydroxyapatite on human bone marrow cell adhesion, proliferation, differentiation and detachment strength'. *Biomaterials*. Elsevier, 22 (1), pp. 87–96.

Dexheimer, V., Frank, S. and Richter, W. (2012). 'Proliferation as a Requirement for In Vitro Chondrogenesis of Human

van Dijk, C. N., Reilingh, M. L., Zengerink, M. and van Bergen, C. J. A. (2010). 'Osteochondral defects in the ankle: why painful?' *Knee Surgery, Sports Traumatology, Arthroscopy*. Springer, 18 (5), p. 570.

Ding, H., Illsley, N. P. and Chang, R. C. (2019). '3D Bioprinted GelMA Based Models for the Study of Trophoblast Cell Invasion'. *Scientific Reports*, 9 (1), pp. 1–13.

Dixit, K., Kulanthaivel, S., Agarwal, T., Pal, K., Giri, S., Maiti, T. K. and Banerjee, I. (2022). 'Gum tragacanth modified nano-hydroxyapatite: An angiogenic-osteogenic biomaterial for bone tissue engineering'. *Ceramics International*. Elsevier, 48 (10), pp. 14672–14683.

Dong, Z., Yuan, Q., Huang, K., Xu, W., Liu, G. and Gu, Z. (2019). 'Gelatin methacryloyl (GelMA)-based biomaterials for bone regeneration'. *RSC Advances*. Royal Society of Chemistry, pp. 17737–17744.

Doyle, S. E., Snow, F., Duchi, S., O'connell, C. D., Onofrillo, C., Di Bella, C. and Pirogova, E. (2021). '3D Printed Multiphasic Scaffolds for Osteochondral Repair: Challenges and Opportunities'. *International Journal of Molecular Sciences 2021, Vol. 22, Page 12420*. Multidisciplinary Digital Publishing Institute, 22 (22), p. 12420.

Duchi, S., Onofrillo, C., O'Connell, C. D., Blanchard, R., Augustine, C., Quigley, A. F., Kapsa, R. M. I., Pivonka, P., Wallace, G., Di Bella, C. and Choong, P. F. M. (2017). 'Handheld Co-Axial Bioprinting: Application to in situ surgical cartilage repair'. *Scientific Reports*. Nature Publishing Group, 7 (1), pp. 1–12.

Dumic-Cule, I., Peric, M., Kucko, L., Grgurevic, L., Pecina, M. and Vukicevic, S. (2018). 'Bone morphogenetic proteins in fracture repair'. *International Orthopaedics*. International Orthopaedics, 42 (11), pp. 2619–2626

Einhorn, T. A. and Gerstenfeld, L. C. (2014). 'Fracture healing: mechanisms and interventions'. *Nature Reviews Rheumatology 2014 11:1*. Nature Publishing Group, 11 (1), pp. 45–54.

Feltri, P., Solaro, L., Di Martino, A., Candrian, C., Errani, C. and Filardo, G. (2022). 'Union, complication, reintervention and failure rates of surgical techniques for large diaphyseal defects: a systematic review and meta-analysis'. *Scientific Reports*. Nature Publishing Group UK, 12 (1), pp. 1–14.

Fernandez de Grado, G., Keller, L., Idoux-Gillet, Y., Wagner, Q., Musset, A. M., Benkirane-Jessel, N., Bornert, F. and Offner, D. (2018). 'Bone substitutes: a review of their characteristics, clinical use, and perspectives for large bone defects management'. *Journal of Tissue Engineering*. SAGE Publications, 9.

Flaibani, M., Luni, C., Sbalchiero, E. and Elvassore, N. (2009). 'Flow cytometric cell cycle analysis of muscle precursor cells cultured within 3D scaffolds in a perfusion bioreactor'. *Biotechnology Progress*. American Chemical Society (ACS), 25 (1), pp. 286–295.

Frese, L., Dijkman, P. E. and Hoerstrup, S. P. (2016). 'Adipose Tissue-Derived Stem Cells in Regenerative Medicine'. *Transfusion Medicine and Hemotherapy*. Karger Publishers, 43 (4), p. 268.

Fu, C., Bai, H., Hu, Q., Gao, T. and Bai, Y. (2017). 'Enhanced proliferation and osteogenic differentiation of MC3T3-E1 pre-osteoblasts on graphene oxide-impregnated PLGA–gelatin nanocomposite fibrous membranes'. *RSC Advances*. The Royal Society of Chemistry, 7 (15), pp. 8886–8897.

Fu, J. N., Wang, X., Yang, M., Chen, Y. R., Zhang, J. Y., Deng, R. H., Zhang, Z. N., Yu, J. K. and Yuan, F. Z. (2022). 'Scaffold-Based Tissue Engineering Strategies for Osteochondral Repair'. *Frontiers in Bioengineering and Biotechnology*, 9 (January), pp. 1–21.

Fuchs, R. K., Warden, S. J. and Turner, C. H. (2009). 'Bone anatomy, physiology and adaptation to mechanical loading'. *Bone Repair Biomaterials*. Woodhead Publishing, pp. 25–68.

Fuentes-Mera, L., Camacho, A., Engel, E., Pérez-Silos, V., Lara-Arias, J., Marino-Martínez, I. and Peña-Martínez, V. (2019). 'Therapeutic Potential of Articular Cartilage Regeneration using Tissue Engineering Based on Multiphase Designs'. in *Cartilage Tissue Engineering and Regeneration Techniques*. IntechOpen.

Garrison, K. R., Shemilt, I., Donell, S., Ryder, J. J., Mugford, M., Harvey, I., Song, F. and Alt, V. (2010). 'BMP for fracture healing in adults Garrison Cochrane Review'. *Cochrane Database Syst Rev*, (6).

Gaspar, D. A., Gomide, V. and Monteiro, F. J. (2012). 'The role of perfusion bioreactors in bone tissue engineering.' *Biomatter*, 2 (4), pp. 167–175.

Germain, L., Fuentes, C. A., van Vuure, A. W., des Rieux, A. and Dupont-Gillain, C. (2018). '3D-printed biodegradable gyroid scaffolds for tissue engineering applications'. *Materials & Design*. Elsevier, 151, pp. 113–122.

Giannoni, P., Lazzarini, E., Ceseracciu, L., Barone, A. C., Quarto, R. and Scaglione, Si. (2011). 'Design and characterization of a tissue-engineered bilayer scaffold for osteochondral tissue repair'. *Journal of Tissue Engineering and Regenerative Medicine*, (November 2012), pp. 1182–1192.

Goldring, S. R. and Goldring, M. B. (2016). 'Changes in the osteochondral unit during osteoarthritis: structure, function and cartilage–bone crosstalk'. *Nature Reviews Rheumatology 2016 12:11*. Nature Publishing Group, 12 (11), pp. 632–644.

Gong, L., Li, J., Zhang, J., Pan, Z., Liu, Y., Zhou, F., Hong, Y., Hu, Y., Gu, Y., Ouyang, H., Zou, X. and Zhang, S. (2020). 'An interleukin-4-loaded bi-layer 3D printed scaffold promotes osteochondral regeneration'. *Acta Biomaterialia*. Elsevier, 117, pp. 246–260.

Groen, W. M., Diloksumpan, P., van Weeren, P. R., Levato, R. and Malda, J. (2017). 'From intricate to integrated: Biofabrication of articulating joints'. *Journal of Orthopaedic Research*. John Wiley and Sons Inc., 35 (10), pp. 2089–2097.

Grosso, A., Burger, M. G., Lunger, A., Schaefer, D. J., Banfi, A. and Di Maggio, N. (2017). 'It takes two to tango: Coupling of angiogenesis and osteogenesis for bone regeneration'. *Frontiers in Bioengineering and Biotechnology*. Frontiers Media S.A., 5 (NOV), p. 291271.

Gu, H., Xue, Z., Wang, M., Yang, M., Wang, K. and Xu, D. (2019). 'Effect of Hydroxyapatite Surface on BMP-2 Biological Properties by Docking and Molecular Simulation Approaches'. *Journal of Physical Chemistry B*, 123 (15), pp. 3372–3382.

Gu, L., Li, T., Song, X., Yang, X., Li, S., Chen, L., Liu, P., Gong, X., Chen, C. and Sun, L. (2020). 'Preparation and characterization of methacrylated gelatin/bacterial cellulose composite hydrogels for cartilage tissue engineering'. *Regenerative Biomaterials*. Oxford University Press, 7 (2), p. 195.

Gu, Y., Zhang, L., Du, X., Fan, Z., Wang, L., Sun, W., Cheng, Y., Zhu, Y. and Chen, C. (2018). 'Reversible physical crosslinking strategy with optimal temperature for 3D bioprinting of human chondrocyte-laden gelatin methacryloyl bioink'. *Journal of Biomaterials Applications*. SAGE Publications Ltd, 33 (5), pp. 609–618.

Guo, J. B., Liang, T., Che, Y. J., Yang, H. L. and Luo, Z. P. (2020). 'Structure and mechanical properties of high-weight-bearing and low-weight-bearing areas of

hip cartilage at the micro- And nano-levels'. *BMC Musculoskeletal Disorders*. BioMed Central, 21 (1), pp. 1–9.

Haber, D. B., Logan, C. A., Murphy, C. P., Sanchez, A., Laprade, R. F. and Provencher, M. T. (2019). 'OSTEOCHONDRAL ALLOGRAFT TRANSPLANTATION for the KNEE: POST-OPERATIVE REHABILITATION'. *International Journal of Sports Physical Therapy*. North American Sports Medicine Institute, 14 (3), p. 487.

Halloran, D., Durbano, H. W. and Nohe, A. (2020). 'Developmental review bone morphogenetic protein-2 in development and bone homeostasis'. *Journal of Developmental Biology*, 8 (3), pp. 28–30.

He, L., Liu, X. and Rudd, C. (2021). 'Additive-manufactured Gyroid Scaffolds of Magnesium Oxide, Phosphate Glass Fiber and Polylac'. *Polymers*, 13 (2), pp. 1–21.

Hodax, J. K., Quintos, J. B., Gruppuso, P. A., Chen, Q., Desai, S. and Jayasuriya, C. T. (2019). 'Aggrecan is required for chondrocyte differentiation in ATDC5 chondroprogenitor cells'. *PLOS ONE*. Public Library of Science, 14 (6), p. e0218399.

Holmes, B., Zhu, W., Li, J., Lee, J. D. and Zhang, L. G. (2015). 'Development of novel three-dimensional printed scaffolds for osteochondral regeneration'. *Tissue Engineering - Part A*. Mary Ann Liebert Inc., 21 (1–2), pp. 403–415.

Hölzl, K., Fürsatz, M., Göcerler, H., Schädl, B., Žigon-Branc, S., Markovic, M., Gahleitner, C., Hoorick, J. Van, Van Vlierberghe, S., Kleiner, A., Baudis, S., Pauschitz, A., Redl, H., Ovsianikov, A. and Nürnberger, S. (2022). 'Gelatin methacryloyl as environment for chondrocytes and cell delivery to superficial cartilage defects'. *Journal of Tissue Engineering and Regenerative Medicine*. John Wiley and Sons Ltd, 16 (2), pp. 207–222.

Husen, M., Custers, R. J. H., Hevesi, M., Krych, A. J. and Saris, D. B. F. (2022). 'Systematic review Size of cartilage defects and the need for repair: a systematic review ☆'. *Journal of Cartilage & Joint Preservation*, 2, p. 100049.

Hwang, P. W. and Horton, J. A. (2019). 'Variable osteogenic performance of MC3T3-E1 subclones impacts their utility as models of osteoblast biology'. *Scientific Reports*. Nature Publishing Group, 9 (1), pp. 1–9.

Jacob, G., Shimomura, K. and Nakamura, N. (2020). 'Osteochondral Injury, Management and Tissue Engineering Approaches'. *Frontiers in Cell and Developmental Biology*. Frontiers Media S.A., 8, p. 1118.

Jang, S. J., Kim, S. E., Han, T. S., Son, J. S., Kang, S. S. and Choi, S. H. (2017). 'Bone Regeneration of Hydroxyapatite with Granular Form or Porous Scaffold in Canine Alveolar Sockets'. *In Vivo*. International Institute of Anticancer Research, 31 (3), p. 335.

Jeong, J., Kim, J. H., Shim, J. H., Hwang, N. S. and Heo, C. Y. (2019). 'Bioactive calcium phosphate materials and applications in bone regeneration'. *Biomaterials research*. Biomaterials Research, 23 (4), pp. 1–11.

Jia, G., Huang, H., Niu, J., Chen, C., Weng, J., Yu, F., Wang, D., Kang, B., Wang, T., Yuan, G. and Zeng, H. (2021). 'Exploring the interconnectivity of biomimetic hierarchical porous Mg scaffolds for bone tissue engineering: Effects of pore size distribution on mechanical properties, degradation behavior and cell migration ability'. *Journal of Magnesium and Alloys*. Elsevier.

Jiang, G., Li, S., Yu, K., He, B., Hong, J., Xu, T., Meng, J., Ye, C., Chen, Y., Shi, Z., Feng, G., Chen, W., Yan, S., He, Y. and Yan, R. (2021). 'A 3D-printed PRP-GelMA hydrogel promotes osteochondral regeneration through M2 macrophage polarization in a rabbit model'. *Acta Biomaterialia*. Elsevier, 128, pp. 150–162.

Jin, H., Zhuo, Y., Sun, Y., Fu, H. and Han, Z. (2019). 'Microstructure design and degradation performance in vitro of three-dimensional printed bioscaffold for bone tissue engineering'. *Biomaterials Selection and Performance Deterioration-Research Article Advances in Mechanical Engineering*, 11 (10), pp. 1–10.

Kantaros, A., Chatzidai, N. and Karalekas, D. (2016). '3D printing-assisted design of scaffold structures'. *International Journal of Advanced Manufacturing Technology*, 82 (1–4), pp. 559–571.

Kanwar, S. and Vijayavenkataraman, S. (2021). 'Design of 3D printed scaffolds for bone tissue engineering: A review'. *Bioprinting*. Elsevier B.V.

Kattimani, V. S., Kondaka, S. and Lingamaneni, K. P. (2016). 'Hydroxyapatite–-Past, Present, and Future in Bone Regeneration'. *https://doi.org/10.4137/BTRI.S36138*. SAGE PublicationsSage UK: London, England, 7, p. BTRI.S36138.

Kawane, T., Qin, X., Jiang, Q., Miyazaki, T., Komori, H., Yoshida, C. A., Matsuura-Kawata, V. K. dos S., Sakane, C., Matsuo, Y., Nagai, K., Maeno, T., Date, Y., Nishimura, R. and Komori, T. (2018). 'Runx2 is required for the proliferation of osteoblast progenitors and induces proliferation by regulating Fgfr2 and Fgfr3'. *Scientific Reports 2018 8:1*. Nature Publishing Group, 8 (1), pp. 1–17.

Key Facts | Overview | Transplant Safety | CDC. (no date). Available at: https://www.cdc.gov/transplantsafety/overview/key-facts.html

Kim, R. W., Kim, J. H. and Moon, S. Y. (2016). 'Effect of hydroxyapatite on critical-sized defect'. *Maxillofacial Plastic and Reconstructive Surgery*. Springer, 38 (1).

Komori, T. (2019). 'Regulation of proliferation, differentiation and functions of osteoblasts by runx2'. *International Journal of Molecular Sciences*, 20 (7).

Komori, T. (2020). 'What is the function of osteocalcin?' *Journal of Oral Biosciences*. Elsevier, 62 (3), pp. 223–227.

Kon, E., Filardo, G., Perdisa, F., Venieri, G. and Marcacci, M. (2014). 'Clinical results of multilayered biomaterials for osteochondral regeneration'. *Journal of Experimental Orthopaedics*, 1 (1), pp. 1–8.

Kong, H. J., Smith, M. K. and Mooney, D. J. (2003). 'Designing alginate hydrogels to maintain viability of immobilized cells'. *Biomaterials*. Elsevier BV, 24 (22), pp. 4023–4029.

Kovar, H., Bierbaumer, L. and Radic-Sarikas, B. (2020). 'The YAP/TAZ Pathway in Osteogenesis and Bone Sarcoma Pathogenesis'. *Cells 2020, Vol. 9, Page 972*. Multidisciplinary Digital Publishing Institute, 9 (4), p. 972.

Kulkarni, N. S., Chauhan, G., Goyal, M., Sarvepalli, S. and Gupta, V. (2022). 'Development of gelatin methacrylate (GelMa) hydrogels for versatile intracavitary applications'. *Biomaterials Science*. Royal Society of Chemistry, 10 (16), pp. 4492–4507.

Lai, W. C., Bohlen, H. L., Fackler, N. P. and Wang, D. (2022). 'Osteochondral Allografts in Knee Surgery: Narrative Review of Evidence to Date'. *Orthopedic Research and Reviews*, 14 (August), pp. 263–274.

Lai, W., Su, L., Zhang, M., Yan, J. and Wu, G. (2019). 'Tuning the optical clarity of glass fiber-reinforced polycarbonates by reactive blending with alternatives from biorenewable isosorbide'. *Journal of Polymer Science Part A: Polymer Chemistry*. John Wiley & Sons, Ltd, 57 (15), pp. 1670–1681.

Lai, Y. S., Chen, W. C., Huang, C. H., Cheng, C. K., Chan, K. K. and Chang, T. K. (2015). 'The effect of graft strength on knee laxity and graft in-situ forces after posterior cruciate ligament reconstruction'. *PLoS ONE*. Public Library of Science, 10 (5).

Lammel-Lindemann, J., Dourado, I. A., Shanklin, J., Rodriguez, C. A., Catalani, L. H. and Dean, D. (2020). 'Photocrosslinking-based 3D printing of unsaturated polyesters from isosorbide: A new material for resorbable medical devices'. *Bioprinting*. Elsevier, 18, p. e00062.

Langhans, S. A. (2018). 'Three-dimensional in vitro cell culture models in drug discovery and drug repositioning'. *Frontiers in Pharmacology*, 9 (JAN), pp. 1–14.

Law, A. M. K., Rodriguez de la Fuente, L., Grundy, T. J., Fang, G., Valdes-Mora, F. and Gallego-Ortega, D. (2021). 'Advancements in 3D Cell Culture Systems for Personalizing Anti-Cancer Therapies'. *Frontiers in Oncology*. Frontiers Media SA, 11.

Law, K.-Y. (2014). 'Definitions for Hydrophilicity, Hydrophobicity, and Superhydrophobicity: Getting the Basics Right'. *Journal of Physical Chemistry Letters*, 5 (4), pp. 686–688.

Lee, B. H., Lum, N., Seow, L. Y., Lim, P. Q. and Tan, L. P. (2016). 'Synthesis and characterization of types A and B gelatin methacryloyl for bioink applications'. *Materials*. MDPI AG, 9 (10), p. 797.

Lee, E., Ko, J. Y., Kim, J., Park, J. W., Lee, S. and Im, G. Il. (2019). 'Osteogenesis and angiogenesis are simultaneously enhanced in BMP2-/VEGF-transfected adipose stem cells through activation of the YAP/TAZ signaling pathway'. *Biomaterials Science*. The Royal Society of Chemistry, 7 (11), pp. 4588–4602.

Lefebvre, V. and Dvir-Ginzberg, M. (2017). 'SOX9 and the many facets of its regulation in the chondrocyte lineage'. *Connective Tissue Research*, 58 (1), pp. 2–14.

Lesage, C., Lafont, M., Guihard, P., Weiss, P., Guicheux, J. and Delplace, V. (2022). 'Material-Assisted Strategies for Osteochondral Defect Repair'. *Advanced Science*. John Wiley and Sons Inc, 9 (16).

Li, J., Chen, G., Xu, X., Abdou, P., Jiang, Q., Shi, D. and Gu, Z. (2019). 'Advances of injectable hydrogel-based scaffolds for cartilage regeneration'. *Regenerative Biomaterials*, 6 (3), pp. 129–140.

Li, N., Song, J., Zhu, G., Li, X., Liu, L., Shi, X. and Wang, Y. (2016). 'Periosteum tissue engineering—a review'. *Biomaterials Science*. The Royal Society of Chemistry, 4 (11), pp. 1554–1561.

Li, X., Chen, S., Li, J., Wang, X., Zhang, J., Kawazoe, N. and Chen, G. (2016). '3D culture of chondrocytes in gelatin hydrogels with different stiffness'. *Polymers*. MDPI AG, 8 (8).

Li, Y., Li, J., Jiang, S., Zhong, C., Zhao, C., Jiao, Y., Shen, J., Chen, H., Ye, M., Zhou, J., Yang, X., Gou, Z., Xu, S. and Shen, M. (2023). 'The design of strut/TPMS-based pore geometries in bioceramic scaffolds guiding osteogenesis and angiogenesis in bone regeneration'. *Materials Today Bio*. The Author(s), 20 (January), p. 100667.

Lian, C., Wang, X., Qiu, X., Wu, Z., Gao, B., Liu, L., Liang, G., Zhou, H., Yang, X., Peng, Y., Liang, A., Xu, C., Huang, D. and Su, P. (2019). 'Collagen type II suppresses articular chondrocyte hypertrophy and osteoarthritis progression by promoting integrin β1−SMAD1 interaction'. *Bone Research 2019 7:1*. Nature Publishing Group, 7 (1), pp. 1–15.

Lim, K. S., Levato, R., Costa, P. F., Castilho, M. D., Alcala-Orozco, C. R., Van Dorenmalen, K. M. A., Melchels, F. P. W., Gawlitta, D., Hooper, G. J., Malda, J. and Woodfield, T. B. F. (2018). 'Bio-resin for high resolution lithography-based biofabrication of complex cell-laden constructs'. *Biofabrication*, 10 (3).

Lin, C. C. and Anseth, K. S. (2013). *The Biodegradation of Biodegradable Polymeric Biomaterials*. Third Edit. *Biomaterials Science: An Introduction to Materials: Third Edition*. Third Edit. Elsevier.

Lin, C. H., Su, J. J. M., Lee, S. Y. and Lin, Y. M. (2018). 'Stiffness modification of photopolymerizable gelatin-methacrylate hydrogels influences endothelial differentiation of human mesenchymal stem cells'. *Journal of Tissue Engineering and Regenerative Medicine*. John Wiley & Sons, Ltd, 12 (10), pp. 2099–2111.

Lin, L., Chow, K. L. and Leng, Y. (2009). 'Study of hydroxyapatite osteoinductivity with an osteogenic differentiation of mesenchymal stem cells'. *Journal of Biomedical Materials Research Part A*. John Wiley & Sons, Ltd, 89A (2), pp. 326–335.

Lin, S., Lee, W. Y. W., Feng, Q., Xu, L., Wang, B., Man, G. C. W., Chen, Y., Jiang, X., Bian, L., Cui, L., Wei, B. and Li, G. (2017). 'Synergistic effects on mesenchymal stem cell-based cartilage regeneration by chondrogenic preconditioning and mechanical stimulation'. *Stem Cell Research and Therapy*. Stem Cell Research & Therapy, 8 (1), pp. 1–12. doi: 10.1186/s13287-017-0672-5.

Lin, T. H., Wang, H. C., Cheng, W. H., Hsu, H. C. and Yeh, M. L. (2019). 'Osteochondral tissue regeneration using a tyramine-modified bilayered plga scaffold combined with articular chondrocytes in a porcine model'. *International Journal of Molecular Sciences*. MDPI AG, 20 (2).

Lin, X., Patil, S., Gao, Y. G. and Qian, A. (2020). 'The Bone Extracellular Matrix in Bone Formation and Regeneration'. *Frontiers in Pharmacology*, 11 (May), pp. 1–15.

Litwic, A., Edwards, M. H., Dennison, E. M. and Cooper, C. (2013). 'Epidemiology and Burden of Osteoarthritis'. *British medical bulletin*. Europe PMC Funders, 105 (1), p. 185.

Liu, B., Wang, Y., Miao, Y., Zhang, Xinyu, Fan, Z., Singh, G., Zhang, Xingying, Xu, K., Li, B., Hu, Z. and Xing, M. (2018). 'Hydrogen bonds autonomously powered gelatin methacrylate hydrogels with super-elasticity, self-heal and underwater self-adhesion for sutureless skin and stomach surgery and E-skin'. *Biomaterials*. Elsevier Ltd, 171, pp. 83–96.

Lou, L., Qiu, Y., Ji, F. and Zhu, X. (2018). 'The influence of surface hydrophilicity on the adhesion properties of wet fabrics or films to water'. *Textile Research Journal*. SAGE Publications Ltd, 88 (1), pp. 108–117.

Lu, Y., Zhang, S., Liu, X., Ye, S., Zhou, X., Huang, Q. and Ren, L. (2017). 'Silk/agarose scaffolds with tunable properties: Via SDS assisted rapid gelation'. *RSC Advances*. Royal Society of Chemistry, 7 (35), pp. 21740–21748.

Lu, Z., Huangfu, C., Wang, Y., Ge, H., Yao, Y., Zou, P., Wang, G., He, H. and Rao, H. (2015). 'Kinetics and thermodynamics studies on the BMP-2 adsorption onto hydroxyapatite surface with different multi-morphological features'. *Materials Science and Engineering: C*. Elsevier, 52, pp. 251–258.

Lv, H., Liu, B. and Qin, Y. (2020). 'Isosorbide mononitrate promotes angiogenesis in embryonic development of Zebrafish'. *Genetics and Molecular Biology*, 43 (3), pp. 1–7.

Ma, B., Zhang, S., Liu, F., Duan, J., Wang, S., Han, J., Sang, Y., Yu, X., Li, D., Tang, W., Ge, S. and Liu, H. (2017). 'One-Dimensional hydroxyapatite nanostructures with tunable length for efficient stem cell differentiation regulation'. *ACS Applied Materials and Interfaces*. American Chemical Society, 9 (39), pp. 33717–33727.

Ma, S., Tang, Q., Feng, Q., Song, J., Han, X. and Guo, F. (2019). 'Mechanical behaviours and mass transport properties of bone-mimicking scaffolds consisted of gyroid structures manufactured using selective laser melting'. *Journal of the Mechanical Behavior of Biomedical Materials*. Elsevier Ltd, 93, pp. 158–169.

Mahapatra, C., Kim, J. J., Lee, J. H., Jin, G. Z., Knowles, J. C. and Kim, H. W. (2019). 'Differential chondro- and osteo-stimulation in three-dimensional porous scaffolds with different topological surfaces provides a design strategy for biphasic osteochondral engineering'. *Journal of Tissue Engineering*. SAGE Publications Ltd, 10.

Manapat, J. Z., Chen, Q., Ye, P. and Advincula, R. C. (2017). '3D Printing of Polymer Nanocomposites via Stereolithography'. *Macromolecular Materials and Engineering*. John Wiley & Sons, Ltd, 302 (9), p. 1600553.

Martin, I., Miot, S., Barbero, A., Jakob, M. and Wendt, D. (2007). 'Osteochondral tissue engineering'. *Journal of Biomechanics*, pp. 750–765.

Maruyama, M., Rhee, C., Utsunomiya, T., Zhang, N., Ueno, M., Yao, Z. and Goodman, S. B. (2020). 'Modulation of the Inflammatory Response and Bone Healing'. *Frontiers in Endocrinology*. Frontiers Media S.A., 11, p. 542565.

Matthews, J. R., Brutico, J., Heard, J., Chauhan, K., Tucker, B. and Freedman, K. B. (2022). 'Comparison of clinical outcomes following osteochondral allograft transplantation for osteochondral versus chondral defects in the knee'. *Knee Surgery and Related Research*. BioMed Central, 34 (1), pp. 1–7.

Medvedeva, E. V., Grebenik, E. A., Gornostaeva, S. N., Telpuhov, V. I., Lychagin, A. V., Timashev, P. S. and Chagin, A. S. (2018). 'Repair of damaged articular cartilage: Current approaches and future directions'. *International Journal of Molecular Sciences*. MDPI AG.

Melchels, F. P. W., Barradas, A. M. C., Van Blitterswijk, C. A., De Boer, J., Feijen, J. and Grijpma, D. W. (2010). 'Effects of the architecture of tissue engineering scaffolds on cell seeding and culturing'. *Acta Biomaterialia*, 6 (11), pp. 4208–4217.

Migliorini, F., La Padula, G., Torsiello, E., Spiezia, F., Oliva, F. and Maffulli, N. (2021). 'Strategies for large bone defect reconstruction after trauma, infections or tumour excision: a comprehensive review of the literature'. *European Journal of Medical Research*. BioMed Central, 26 (1), pp. 1–10.

Mondal, A., Gebeyehu, A., Miranda, M., Bahadur, D., Patel, N., Ramakrishnan, S., Rishi, A. K. and Singh, M. (2019). 'Characterization and printability of Sodium alginate -Gelatin hydrogel for bioprinting NSCLC co-culture'. *Scientific Reports 2019 9:1*. Nature Publishing Group, 9 (1), pp. 1–12.

Mondal, D., Diederichs, E. and Willett, T. L. (2022). 'Enhanced Mechanical Properties of 3D Printed Nanocomposites Composed of Functionalized Plant-Derived Biopolymers and Calcium-Deficient Hydroxyapatite Nanoparticles'. *Frontiers in Materials*, 9 (February), pp. 1–12.

Monteiro, N., Thrivikraman, G., Athirasala, A., Tahayeri, A., França, C. M., Ferracane, J. L. and Bertassoni, L. E. (2018). 'Photopolymerization of cell-laden gelatin methacryloyl hydrogels using a dental curing light for regenerative dentistry'. *Dental Materials*, 34 (3), pp. 389–399.

Moser, S. C. and van der Eerden, B. C. J. (2019). 'Osteocalcin — A versatile bone-derived hormone'. *Frontiers in Endocrinology*. Frontiers Media S.A., 10 (JAN), p. 794.

Naguib, G. H., Abd El-Aziz, G. S., Almehmadi, A., Bayoumi, A., Mira, A. I., Hassan, A. H. and Hamed, M. T. (2023). 'Evaluation of the time-dependent osteogenic activity of glycerol incorporated magnesium oxide nanoparticles in induced calvarial defects'. *Heliyon*. Elsevier Ltd, 9 (8).

Nájera-Romero, G. V., Yar, M. and Rehman, I. U. (2020). 'Heparinized chitosan/hydroxyapatite scaffolds stimulate angiogenesis'. *Functional Composite Materials 2020 1:1*. SpringerOpen, 1 (1), pp. 1–15.

Nakamura, A., Dohi, Y., Akahane, M., Ohgushi, H., Nakajima, H., Funaoka, H. and Takakura, Y. (2009). 'Osteocalcin secretion as an early marker of osteogenic differentiation of rat mesenchymal stem cells'. *Tissue Engineering - Part C: Methods*. Mary Ann Liebert Inc., 15 (2), pp. 169–180.

Nasello, G., Alamán-Díez, P., Schiavi, J., Pérez, M. Á., McNamara, L. and García-Aznar, J. M. (2020). 'Primary Human Osteoblasts Cultured in a 3D Microenvironment Create a Unique Representative Model of Their Differentiation Into Osteocytes'. *Frontiers in Bioengineering and Biotechnology*. Frontiers Media S.A., 8, p. 336.

Naujoks, C., Meyer, U., Wiesmann, H. P., Jäsche-Meyer, J., Hohoff, A., Depprich, R. and Handschel, J. (2008). 'Principles of cartilage tissue engineering in TMJ reconstruction'. *Head and Face Medicine*, 4 (1).

Ng, J., Bernhard, J. and Vunjak-Novakovic, G. (2016). 'Mesenchymal stem cells for osteochondral tissue engineering'. in *Methods in Molecular Biology*. Humana Press Inc., pp. 35–54.

Nguyen, A. K., Goering, P. L., Reipa, V. and Narayan, R. J. (2019). 'Toxicity and photosensitizing assessment of gelatin methacryloyl-based hydrogels photoinitiated with lithium phenyl-2,4,6-trimethylbenzoylphosphinate in human primary renal proximal tubule epithelial cells'. *Biointerphases*. American Vacuum Society, 14 (2), p. 021007.

Nguyen, T. T., Hu, C. C., Sakthivel, R., Nabilla, S. C., Huang, Y. W., Yu, J., Cheng, N. C., Kuo, Y. J. and Chung, R. J. (2022). 'Preparation of gamma poly-glutamic acid/hydroxyapatite/collagen composite as the 3D-printing scaffold for bone tissue engineering'. *Biomaterials research*. Biomater Res, 26 (1).

NICE. (2017). *National clinical guideline for the care and management of osteoarthritis in adults*.

Nonque, F., Sahut, A., Jacquel, N., Saint-Loup, R., Woisel, P. and Potier, J. (2020). 'Isosorbide monoacrylate: a sustainable monomer for the production of fully bio-based polyacrylates and thermosets'. *Polymer Chemistry*. The Royal Society of Chemistry, 11 (43), pp. 6903–6909.

Nosrati, H., Aramideh Khouy, R., Nosrati, A., Khodaei, M., Banitalebi-Dehkordi, M., Ashrafi-Dehkordi, K., Sanami, S. and Alizadeh, Z. (2021). 'Nanocomposite scaffolds for accelerating chronic wound healing by enhancing angiogenesis'. *Journal of Nanobiotechnology 2021 19:1*. BioMed Central, 19 (1), pp. 1–21.

Oladapo, B. I., Zahedi, S. A. and Adeoye, A. O. M. (2019). '3D printing of bone scaffolds with hybrid biomaterials'. *Composites Part B: Engineering*. Elsevier Ltd, 158, pp. 428–436.

Olivares-Navarrete, R., Lee, E. M., Smith, K., Hyzy, S. L., Doroudi, M., Williams, J. K., Gall, K., Boyan, B. D. and Schwartz, Z. (2017). 'Substrate Stiffness Controls Osteoblastic and Chondrocytic Differentiation of Mesenchymal Stem Cells

without Exogenous Stimuli'. *PLOS ONE*. Edited by A. van Wijnen. Public Library of Science, 12 (1), p. e0170312.

Onderková, A. and M. Kalaskar, D. (2023). '3D bioprinting for auricular reconstruction: A review and future perspectives'. *International Journal of Bioprinting*. AccScience Publishing, 0 (0), p. 0898.

Onofrillo, C., Duchi, S., O'Connell, C. D., Blanchard, R., O'Connor, A. J., Scott, M., Wallace, G. G., Choong, P. F. M. and Di Bella, C. (2018). 'Biofabrication of human articular cartilage: A path towards the development of a clinical treatment'. *Biofabrication*. Institute of Physics Publishing, 10 (4), p. 045006.

Otto, I. A., Levato, R., Webb, W. R., Khan, I. M., Breugem, C. C. and Malda, J. (2018). 'Progenitor cells in auricular cartilage demonstrate cartilage-forming capacity in 3D hydrogel culture'. *European Cells and Materials*, 35, pp. 132–150.

Owji, N., Aldaadaa, A., Cha, J.-R., Shakouri, T., Garcia, E., Kim, H.-W. and Knowles, J. C. (2019). 'Synthesis, Characterisation and 3D Printing of an Isosorbide Based, Light Curable, Degradable Polymer for Potential Application in Maxillofacial Reconstruction'. *ACS Biomaterials Science & Engineering*. American Chemical Society (ACS).

Owji, N., Mandakhbayar, N., Cha, J. R., Padalhin, A. R., Erdogan, Z. K., Aldaadaa, A., Shakouri, T., Sawadkar, P., Frost, O., Kim, H. W., García-Gareta, E. and Knowles, J. C. (2022). 'Inclusion of calcium phosphate does not further improve in vitro and in vivo osteogenesis in a novel, highly biocompatible, mechanically stable and 3D printable polymer'. *Scientific Reports 2022 12:1*. Nature Publishing Group, 12 (1), pp. 1–16.

Ozturk, B., Cobanoglu, N., Cetin Dr., A. R. and Gunduz, B. (2013). 'Conversion degrees of resin composites using different light sources'. *European Journal of Dentistry*. Dental Investigations Society, 7 (1), p. 102.

Pahoff, S., Meinert, C., Bas, O., Nguyen, L., Klein, T. J. and Hutmacher, D. W. (2019). 'Effect of gelatin source and photoinitiator type on chondrocyte redifferentiation in gelatin methacryloyl-based tissue-engineered cartilage constructs'. *Journal of Materials Chemistry B*. Royal Society of Chemistry, 7 (10), pp. 1761–1772.

Pearce, C. J., Gartner, L. E., Mitchell, A. and Calder, J. D. (2012). 'Synthetic osteochondral grafting of ankle osteochondral lesions'. *Foot and Ankle Surgery*. Elsevier, 18 (2), pp. 114–118.

Pepelanova, I., Kruppa, K., Scheper, T. and Lavrentieva, A. (2018). 'Gelatin-Methacryloyl (GelMA) Hydrogels with Defined Degree of Functionalization as a Versatile Toolkit for 3D Cell Culture and Extrusion Bioprinting'. *Bioengineering*. Multidisciplinary Digital Publishing Institute (MDPI), 5 (3).

Petcu, E. B., Midha, R., McColl, E., Popa-Wagner, A., Chirila, T. V. and Dalton, P. D. (2018). '3D printing strategies for peripheral nerve regeneration'. *Biofabrication*. Institute of Physics Publishing.

Polo-Corrales, L., Latorre-Esteves, M. and Ramirez-Vick, J. E. (2014). 'Scaffold design for bone regeneration.' *Journal of nanoscience and nanotechnology*, 14 (1), pp. 15–56.

Pouran, B., Arbabi, V., Bleys, R. L., René van Weeren, P., Zadpoor, A. A. and Weinans, H. (2017). 'Solute transport at the interface of cartilage and subchondral bone plate: Effect of micro-architecture'. *Journal of Biomechanics*. Elsevier Ltd, 52, pp. 148–154.

Qi, D., Su, J., Li, S., Zhu, H., Cheng, L., Hua, S., Yuan, X., Jiang, J., Shu, Z., Shi, Y. and Xiao, J. (2022). '3D printed magnesium-doped β-TCP gyroid scaffold with osteogenesis, angiogenesis, immunomodulatin properties and bone regeneration capability in vivo'. *Biomaterials Advances*. Elsevier, 136, p. 212759.

Rajabi, N., Rezaei, A., Kharaziha, M., Bakhsheshi-Rad, H. R., Luo, H., Ramakrishna, S. and Berto, F. (2021). 'Recent Advances on Bioprinted Gelatin Methacrylate-Based Hydrogels for Tissue Repair'. *Tissue Engineering - Part A*, 27 (11–12), pp. 679–702.

Ramaswamy, Y., Roohani, I., No, Y. J., Madafiglio, G., Chang, F., Zhang, F., Lu, Z. and Zreiqat, H. (2021). 'Nature-inspired topographies on hydroxyapatite surfaces regulate stem cells behaviour'. *Bioactive Materials*. Elsevier, 6 (4), pp. 1107–1117.

Razafiarison, T., Holenstein, C. N., Stauber, T., Jovic, M., Vertudes, E., Loparic, M., Kawecki, M., Bernard, L., Silvan, U. and Snedeker, J. G. (2018). 'Biomaterial surface energy-driven ligand assembly strongly regulates stem cell mechanosensitivity and fate on very soft substrates'. *Proceedings of the National Academy of Sciences of the United States of America*. National Academy of Sciences, 115 (18), pp. 4631–4636.

Riccio, C., Civera, M., Grimaldo Ruiz, O., Pedullà, P., Rodriguez Reinoso, M., Tommasi, G., Vollaro, M., Burgio, V. and Surace, C. (2021). 'Effects of Curing on Photosensitive Resins in SLA Additive Manufacturing'. *Applied Mechanics*, 2 (4), pp. 942–955.

Roberts, T. T. and Rosenbaum, A. J. (2012). 'Bone grafts, bone substitutes and orthobiologics: The bridge between basic science and clinical advancements in fracture healing'. *Organogenesis*. Taylor & Francis, 8 (4), p. 114

Rogina, A., Antunović, M., Pribolšan, L., Caput Mihalić, K., Vukasović, A., Ivković, A., Marijanović, I., Ferrer, G. G., Ivanković, M. and Ivanković, H. (2017). 'Human Mesenchymal Stem Cells Differentiation Regulated by Hydroxyapatite Content within Chitosan-Based Scaffolds under Perfusion Conditions'. *Polymers*. Multidisciplinary Digital Publishing Institute (MDPI), 9 (9).

Roohani-Esfahani, S. I., Newman, P. and Zreiqat, H. (2016a). 'Design and Fabrication of 3D printed Scaffolds with a Mechanical Strength Comparable to Cortical Bone to Repair Large Bone Defects'. *Scientific Reports*. Nature Publishing Group, 6 (October 2015), pp. 1–8.

Roohani-Esfahani, S. I., Newman, P. and Zreiqat, H. (2016b). 'Design and Fabrication of 3D printed Scaffolds with a Mechanical Strength Comparable to

Cortical Bone to Repair Large Bone Defects'. *Scientific Reports 2016 6:1*. Nature Publishing Group, 6 (1), pp. 1–8.

Rose, J. C. and De Laporte, L. (2018). 'Hierarchical Design of Tissue Regenerative Constructs'. *Advanced Healthcare Materials*, 7 (6).

Ruijtenberg, S. and van den Heuvel, S. (2016). 'Coordinating cell proliferation and differentiation: Antagonism between cell cycle regulators and cell type-specific gene expression'. *Cell Cycle*. Taylor & Francis, 15 (2), p. 196.

Rutkovskiy, A., Stensløkken, K.-O. and Vaage, I. J. (2016). 'Osteoblast Differentiation at a Glance'. *Medical Science Monitor Basic Research*. International Scientific Information, Inc., 22, p. 95.

Santos-Beato, P., Midha, S., Pitsillides, A. A., Miller, A., Torii, R. and Kalaskar, D. M. (2022). 'Biofabrication of the osteochondral unit and its applications: Current and future directions for 3D bioprinting'. *Journal of Tissue Engineering*. SAGE Publications Ltd.

Saxon, D. J., Luke, A. M., Sajjad, H., Tolman, W. B. and Reineke, T. M. (2020). 'Next-generation polymers: Isosorbide as a renewable alternative'. *Progress in Polymer Science*. Pergamon, 101, p. 101196.

Saxon, D. J., Nasiri, M., Mandal, M., Maduskar, S., Dauenhauer, P. J., Cramer, C. J., Lapointe, A. M. and Reineke, T. M. (2019). 'Architectural Control of Isosorbide-Based Polyethers via Ring-Opening Polymerization'. *Journal of the American Chemical Society*. American Chemical Society, 141 (13), pp. 5107–5111.

Scheiger, J. M. and Levkin, P. A. (2020). 'Hydrogels with Preprogrammable Lifetime via UV-Induced Polymerization and Degradation'. *Advanced Functional Materials*, 30 (26).

Schmidleithner, C. and Kalaskar, D. M. (2018). 'Stereolithography'. in *3D Printing*. InTech.

Schoonraad, S. A., Fischenich, K. M., Eckstein, K. N., Crespo-Cuevas, V., Savard, L. M., Muralidharan, A., Tomaschke, A. A., Uzcategui, A. C., Randolph, M. A., McLeod, R. R., Ferguson, V. L. and Bryant, S. J. (2021). 'Biomimetic and mechanically supportive 3D printed scaffolds for cartilage and osteochondral tissue engineering using photopolymers and digital light processing'. *Biofabrication*. IOP Publishing, 13 (4), p. 044106.

Schuurman, W., Levett, P. A., Pot, M. W., van Weeren, P. R., Dhert, W. J. A., Hutmacher, D. W., Melchels, F. P. W., Klein, T. J. and Malda, J. (2013). 'Gelatin-methacrylamide hydrogels as potential biomaterials for fabrication of tissue-engineered cartilage constructs'. *Macromolecular Bioscience*, 13 (5), pp. 551–561.

Schwab, A., Levato, R., D'Este, M., Piluso, S., Eglin, D. and Malda, J. (2020). 'Printability and Shape Fidelity of Bioinks in 3D Bioprinting'. *Chemical Reviews*. American Chemical Society, 120 (19), pp. 11028–11055.

Seo, S. J., Mahapatra, C., Singh, R. K., Knowles, J. C. and Kim, H. W. (2014). 'Strategies for osteochondral repair: Focus on scaffolds'. *Journal of Tissue Engineering*, 5 (X).

Shakouri, T., Cha, J. R., Owji, N., Haddow, P., Robinson, T. E., Patel, K. D., García-Gareta, E., Kim, H. W. and Knowles, J. C. (2020). 'Comparative study of photoinitiators for the synthesis and 3D printing of a light-curable, degradable polymer for custom-fit hard tissue implants'. *Biomedical Materials*. IOP Publishing, 16 (1), p. 015007

Shaukat, U., Rossegger, E. and Schlögl, S. (2022). 'A Review of Multi-Material 3D Printing of Functional Materials via Vat Photopolymerization'. *Polymers*, 14 (12).

Shegarfi, H. and Reikeras, O. (2009). 'Review article: bone transplantation and immune response'. *Journal of orthopaedic surgery (Hong Kong)*. J Orthop Surg (Hong Kong), 17 (2), pp. 206–211.

Sherman, S. L., Garrity, J., Bauer, K., Cook, J., Stannard, J. and Bugbee, W. (2014). 'Fresh osteochondral allograft transplantation for the knee: Current concepts'. *Journal of the American Academy of Orthopaedic Surgeons*. Lippincott Williams and Wilkins, pp. 121–133.

Shirai, M. (2014). 'Photocrosslinkable polymers with degradable properties'. *Polymer Journal*. Nature Publishing Group, pp. 859–865.

Shyh-Chang, N. and Ng, H. H. (2017). 'The metabolic programming of stem cells'. *Genes & Development*. Cold Spring Harbor Laboratory Press, 31 (4), pp. 336–346.

da Silva Pires, J. L., de Carvalho, J. J., Dos Santos Pereira, M. J., da Silva Brum, I., Rosa Nascimento, A. L., Dos Santos, P. G. P., Frigo, L. and Fischer, R. G. (2021). 'Repair of Critical Size Bone Defects Using Synthetic Hydroxyapatite or Xenograft with or without the Bone Marrow Mononuclear Fraction: A Histomorphometric and Immunohistochemical Study in Rat Calvaria'. *Materials 2021, Vol. 14, Page 2854*. Multidisciplinary Digital Publishing Institute, 14 (11), p. 2854.

Sirova, M., Vlierberghe, S. Van, Matyasova, V., Rossmann, P., Schacht, E., Dubruel, P. and Rihova, B. (2014). 'Immunocompatibility evaluation of hydrogel-coated polyimide implants for applications in regenerative medicine'. *Journal of Biomedical Materials Research - Part A*, 102 (6), pp. 1982–1990.

Śmiga-Matuszowicz, M., Włodarczyk, J., Skorupa, M., Czerwińska-Główka, D., Fołta, K., Pastusiak, M., Adamiec-Organiściok, M., Skonieczna, M., Turczyn, R., Sobota, M. and Krukiewicz, K. (2023). 'Biodegradable Scaffolds for Vascular Regeneration Based on Electrospun Poly(L-Lactide-co-Glycolide)/Poly(Isosorbide Sebacate) Fibers'. *International Journal of Molecular Sciences*, 24 (2).

Sophia Fox, A. J., Bedi, A. and Rodeo, S. A. (2009). 'The basic science of articular cartilage: Structure, composition, and function'. *Sports Health*, 1 (6), pp. 461–468.

Stucker, S., Chen, J., Watt, F. E. and Kusumbe, A. P. (2020). 'Bone Angiogenesis and Vascular Niche Remodeling in Stress, Aging, and Diseases'. *Frontiers in Cell and Developmental Biology*. Frontiers Media S.A., 8, p. 602269. doi: 10.3389/FCELL.2020.602269/BIBTEX.

Suvarnapathaki, S., Nguyen, M. A., Wu, X., Nukavarapu, S. P. and Camci-Unal, G. (2019). 'Synthesis and characterization of photocrosslinkable hydrogels from bovine skin gelatin'. *RSC Advances*. Royal Society of Chemistry, 9 (23), pp. 13016–13025.

Swanson, W. B., Omi, M., Woodbury, S. M., Douglas, L. M., Eberle, M., Ma, P. X., Hatch, N. E. and Mishina, Y. (2022). 'Scaffold Pore Curvature Influences MSC Fate through Differential Cellular Organization and YAP/TAZ Activity'. *International Journal of Molecular Sciences*. MDPI, 23 (9), p. 4499.

Swanson, W. B., Omi, M., Zhang, Z., Nam, H. K., Jung, Y., Wang, G., Ma, P. X., Hatch, N. E. and Mishina, Y. (2021). 'Macropore design of tissue engineering scaffolds regulates mesenchymal stem cell differentiation fate'. *Biomaterials*. Elsevier, 272, p. 120769

Szustak, M. and Gendaszewska-Darmach, E. (2021). 'Nanocellulose-Based Scaffolds for Chondrogenic Differentiation and Expansion'. *Frontiers in Bioengineering and Biotechnology*, 9 (August), pp. 1–34.

Tamaddon, M., Wang, L., Liu, Z. and Liu, C. (2018). 'Osteochondral tissue repair in osteoarthritic joints: clinical challenges and opportunities in tissue engineering'. *Bio-Design and Manufacturing*. Springer, pp. 101–114.

Tejeda-Alejandre, R., Charles, R., Patel, P., Lammel-Lindemann, J., Dourado, I. A., Catalani, L. H., Rodriguez, C. A. and Dean, D. (2022). 'The mechanical reliability of vat photopolymerization 3D printing of isosorbide-derived polyester porous tissue engineering scaffolds.' *Procedia CIRP*. Elsevier, 110 (C), pp. 117–121.

Temple, J., Velliou, E., Shehata, M. and Lévy, R. (2022). 'Current strategies with implementation of three-dimensional cell culture: the challenge of quantification'. *Interface Focus*. The Royal Society , 12 (5).

Tihan, T. G., Ionita, M. D., Popescu, R. G. and Iordachescu, D. (2009). 'Effect of hydrophilic–hydrophobic balance on biocompatibility of poly(methyl methacrylate) (PMMA)–hydroxyapatite (HA) composites'. *Materials Chemistry and Physics*. Elsevier, 118 (2–3), pp. 265–269.

Timmer, M. D., Ambrose, C. G. and Mikos, A. G. (2003). 'Evaluation of thermal- and photo-crosslinked biodegradable poly(propylene fumarate)-based networks'. *Journal of biomedical materials research. Part A*. J Biomed Mater Res A, 66 (4), pp. 811–818.

Ulici, V., Chen, A. F., Cheng, A. W. M. and Tuan, R. S. (2022). 'Anatomy, Cartilage'. *Hip Joint Restoration*. StatPearls Publishing, pp. 15–22.

Verisqa, F., Cha, J. R., Nguyen, L., Kim, H. W. and Knowles, J. C. (2022). 'Digital Light Processing 3D Printing of Gyroid Scaffold with Isosorbide-Based Photopolymer for Bone Tissue Engineering'. *Biomolecules*, 12 (11), pp. 1–19.

Viti, F., Landini, M., Mezzelani, A., Petecchia, L., Milanesi, L. and Scaglione, S. (2016). 'Osteogenic Differentiation of MSC through Calcium Signaling Activation: Transcriptomics and Functional Analysis'. *PLoS ONE*, 11 (2), p. 148173.

Voet, V. S. D., Strating, T., Schnelting, G. H. M., Dijkstra, P., Tietema, M., Xu, J., Woortman, A. J. J., Loos, K., Jager, J. and Folkersma, R. (2018). 'Biobased Acrylate Photocurable Resin Formulation for Stereolithography 3D Printing'.

Vukasovic, A., Asnaghi, M. A., Kostesic, P., Quasnichka, H., Cozzolino, C., Pusic, M., Hails, L., Trainor, N., Krause, C., Figallo, E., Filardo, G., Kon, E., Wixmerten, A., Maticic, D., Pellegrini, G., Kafienah, W., Hudetz, D., Smith, T., Martin, I., Ivkovic, A. and Wendt, D. (2019). 'Bioreactor-manufactured cartilage grafts repair acute and chronic osteochondral defects in large animal studies'. *Cell Proliferation*, 52 (6), pp. 1–14

Wang, Q., Wang, M., Lu, X., Wang, K., Fang, L., Ren, F. and Lu, G. (2017). 'Effects of atomic-level nano-structured hydroxyapatite on adsorption of bone morphogenetic protein-7 and its derived peptide by computer simulation'. *Scientific Reports 2017 7:1*. Nature Publishing Group, 7 (1), pp. 1–14.

Wang, Shenqiang, Zhao, Sheng, Yu, Jicheng, Gu, Zhen, Zhang, Yuqi, Wang, S, Zhao, S, Yu, J, Gu, Z and Zhang, Y. (2022). 'Advances in Translational 3D Printing for Cartilage, Bone, and Osteochondral Tissue Engineering'. *Small*. John Wiley & Sons, Ltd, 18 (36), p. 2201869.

Wang, W. and Yeung, K. W. K. (2017). 'Bone grafts and biomaterials substitutes for bone defect repair: A review'. *Bioactive Materials*. Elsevier Ltd, 2 (4), pp. 224–247.

Wanigasekara, J., Carroll, L. J., Cullen, P. J., Tiwari, B. and Curtin, J. F. (2023). 'Three-Dimensional (3D) in vitro cell culture protocols to enhance glioblastoma research'. *PLOS ONE*. Public Library of Science, 18 (2), p. e0276248.

Wei, Q., Holle, A., Li, J., Posa, F., Biagioni, F., Croci, O., Benk, A. S., Young, J., Noureddine, F., Deng, J., Zhang, M., Inman, G. J., Spatz, J. P., Campaner, S. and Cavalcanti-Adam, E. A. (2020). 'BMP-2 Signaling and Mechanotransduction Synergize to Drive Osteogenic Differentiation via YAP/TAZ'. *Advanced Science*. John Wiley and Sons Inc., 7 (15).

Wei, W. and Dai, H. (2021). 'Articular cartilage and osteochondral tissue engineering techniques: Recent advances and challenges'. *Bioactive Materials*. Elsevier, 6 (12), pp. 4830–4855.

Wendt, D., Jakob, M. and Martin, I. (2005). 'Bioreactor-based engineering of osteochondral grafts: From model systems to tissue manufacturing'. *Journal of Bioscience and Bioengineering*. Elsevier, 100 (5), pp. 489–494.

Westhauser, F., Karadjian, M., Essers, C., Senger, A. S., Hagmann, S., Schmidmaier, G. and Moghaddam, A. (2019). 'Osteogenic differentiation of mesenchymal stem cells is enhanced in a 45S5-supplemented β-TCP composite scaffold: an in-vitro comparison of Vitoss and Vitoss BA'. *PLOS ONE*. Public Library of Science, 14 (2), p. e0212799.

Won, J. E., Lee, Y. S., Park, J. H., Lee, J. H., Shin, Y. S., Kim, C. H., Knowles, J. C. and Kim, H. W. (2020). 'Hierarchical microchanneled scaffolds modulate multiple tissue-regenerative processes of immune-responses, angiogenesis, and stem cell homing'. *Biomaterials*. Elsevier Ltd, 227.

Wu, F., Yang, J., Ke, X., Ye, S., Bao, Z., Yang, X., Zhong, C., Shen, M., Xu, S., Zhang, L., Gou, Z. and Yang, G. (2022). 'Integrating pore architectures to evaluate vascularization efficacy in silicate-based bioceramic scaffolds'. *Regenerative Biomaterials*, 9 (December).

Wu, K. H., Mei, C., Lin, C. W., Yang, K. C. and Yu, J. (2017). 'The influence of bubble size on chondrogenic differentiation of adipose-derived stem cells in gelatin microbubble scaffolds'. *Journal of Materials Chemistry B*. Royal Society of Chemistry, 6 (1), pp. 125–132.

Xu, J. H., Li, Z. H., Hou, Y. D. and Fang, W. J. (2015). 'Potential mechanisms underlying the Runx2 induced osteogenesis of bone marrow mesenchymal stem cells'. *American Journal of Translational Research*. e-Century Publishing Corporation, 7 (12), p. 2527.

Xu, S. J., Qiu, Z. Y., Wu, J. J., Kong, X. D., Weng, X. S., Cui, F. Z. and Wang, X. M. (2016). 'Osteogenic Differentiation Gene Expression Profiling of hMSCs on Hydroxyapatite and Mineralized Collagen'. *Tissue Engineering - Part A*. Mary Ann Liebert Inc., 22 (1–2), pp. 170–181.

Xue, R., Chung, B., Tamaddon, M., Carr, J., Liu, C. and Cartmell, S. H. (2019). 'Osteochondral tissue coculture: An in vitro and in silico approach'. *Biotechnology and Bioengineering*, 116 (11), pp. 3112–3123.

Yan, L. P., Oliveira, J. M., Oliveira, A. L. and Reis, R. L. (2015). 'Current Concepts and Challenges in Osteochondral Tissue Engineering and Regenerative Medicine'. *ACS Biomaterials Science and Engineering*. American Chemical Society, 1 (4), pp. 183–200.

Yang, T., Tamaddon, M., Jiang, L., Wang, J., Liu, Ziyu, Liu, Zhongqun, Meng, H., Hu, Y., Gao, J., Yang, X., Zhao, Y., Wang, Y., Wang, A., Wu, Q., Liu, C., Peng, J., Sun, X. and Xue, Q. (2021). 'Bilayered scaffold with 3D printed stiff subchondral bony compartment to provide constant mechanical support for long-term cartilage regeneration'. *Journal of Orthopaedic Translation*. Elsevier, 30, pp. 112–121.

Yang, X., Li, Y., Liu, X., Zhang, R. and Feng, Q. (2018). 'In vitro uptake of hydroxyapatite nanoparticles and their effect on osteogenic differentiation of human mesenchymal stem cells'. *Stem Cells International*. Hindawi Limited, 2018.

Yao, Y., Sha, N. and Zhao, Z. (2019a). 'Highly Concentrated Hydroxyapatite Suspension for DLP Printing'. *IOP Conference Series: Materials Science and Engineering*, 678 (1).

Yao, Y., Sha, N. and Zhao, Z. (2019b). 'Highly Concentrated Hydroxyapatite Suspension for DLP Printing'. *IOP Conference Series: Materials Science and Engineering*. IOP Publishing, 678, p. 012016.

Yazdanpanah, Z., Johnston, J. D., Cooper, D. M. L. and Chen, X. (2022). '3D Bioprinted Scaffolds for Bone Tissue Engineering: State-Of-The-Art and Emerging Technologies'. *Frontiers in Bioengineering and Biotechnology*, 10 (April).

Ye, W., Li, H., Yu, K., Xie, C., Wang, P., Zheng, Y., Zhang, P., Xiu, J., Yang, Y., Zhang, F., He, Y. and Gao, Q. (2020). '3D printing of gelatin methacrylate-based nerve guidance conduits with multiple channels'. *Materials and Design*. Elsevier Ltd, 192, p. 108757.

Yi, H. G., Kim, H., Kwon, J., Choi, Y. J., Jang, J. and Cho, D. W. (2021). 'Application of 3D bioprinting in the prevention and the therapy for human diseases'. *Signal Transduction and Targeted Therapy*. Springer US, 6 (1).

Yin, J., Yan, M., Wang, Y., Fu, J. and Suo, H. (2018). '3D Bioprinting of Low-Concentration Cell-Laden Gelatin Methacrylate (GelMA) Bioinks with a Two-Step Cross-linking Strategy'. *ACS Applied Materials and Interfaces*, 10 (8), pp. 6849–6857.

You, S., Xiang, Y., Hwang, H. H., Berry, D. B., Kiratitanaporn, W., Guan, J., Yao, E., Tang, M., Zhong, Z., Ma, X., Wangpraseurt, D., Sun, Y., Lu, T. Y. and Chen, S. (2023). 'High cell density and high-resolution 3D bioprinting for fabricating vascularized tissues'. *Science Advances*, 9 (8), pp. 1–14.

Yousefi, A. M., Hoque, M. E., Prasad, R. G. S. V. and Uth, N. (2015). 'Current strategies in multiphasic scaffold design for osteochondral tissue engineering: A review'. *Journal of Biomedical Materials Research - Part A*, 103 (7), pp. 2460–2481.

Yu, J., Lee, S., Choi, S., Kim, K. K., Ryu, B., Kim, C. Y., Jung, C. R., Min, B. H., Xin, Y. Z., Park, S. A., Kim, W., Lee, D. and Lee, J. (2020). 'Fabrication of a polycaprolactone/alginate bipartite hybrid scaffold for osteochondral tissue using a three-dimensional bioprinting system'. *Polymers*, 12 (10), pp. 1–16.

Yue, K., Trujillo-De Santiago, G., Mois Es Alvarez, M., Tamayol, A., Annabi, N. and Khademhosseini, A. (2015). 'Synthesis, properties, and biomedical applications of gelatin methacryloyl (GelMA) hydrogels'.

Zeng, Y. S., Hsueh, M. H. and Hsiao, T. C. (2023). 'Effect of ultraviolet post-curing, laser power, and layer thickness on the mechanical properties of acrylate used in stereolithography 3D printing'. *Materials Research Express*. IOP Publishing, 10 (2).

Zhang, J. and Xiao, P. (2018). 'Polymer Chemistry MINIREVIEW 3D printing of photopolymers'. *Polymer Chemistry*, 9.

Zhang, S., Chen, L., Jiang, Y., Cai, Y., Xu, G., Tong, T., Zhang, W., Wang, L., Ji, J., Shi, P. and Ouyang, H. W. (2013). 'Bi-layer collagen/microporous electrospun nanofiber scaffold improves the osteochondral regeneration'. *Acta Biomaterialia*. Elsevier, 9 (7), pp. 7236–7247.

Zhang, Y., Guo, W., Wang, M., Hao, C., Lu, L., Gao, S., Zhang, X., Li, X., Chen, M., Li, P., Jiang, P., Lu, S., Liu, S. and Guo, Q. (2018). 'Co-culture systems-based

strategies for articular cartilage tissue engineering'. *Journal of Cellular Physiology*, 233 (3), pp. 1940–1951

Zhang, Y., Mao, H., Gao, C., Li, S., Shuai, Q., Xu, J., Xu, K., Cao, L., Lang, R., Gu, Z., Akaike, T. and Yang, J. (2016). 'Enhanced Biological Functions of Human Mesenchymal Stem-Cell Aggregates Incorporating E-Cadherin-Modified PLGA Microparticles'. *Advanced Healthcare Materials*. Wiley-VCH Verlag, 5 (15), pp. 1949–1959.

Zhao, F., van Rietbergen, B., Ito, K. and Hofmann, S. (2018). 'Flow rates in perfusion bioreactors to maximise mineralisation in bone tissue engineering in vitro'. *Journal of Biomechanics*. Elsevier, 79, pp. 232–237.

Zhou, H., Wang, Xiaofeng, Wang, Xinyu, Peng, C., Wang, R. and Zhou, K. (2021). 'Principles of dispersing powders for 3d printing'. *Colloids and Interfaces*, 5 (2).

Zhou, L., Fu, J. and He, Y. (2020). 'A Review of 3D Printing Technologies for Soft Polymer Materials'. *Advanced Functional Materials*, 2000187, pp. 1–38.

Zhu, H., Li, M., Huang, X., Qi, D., Nogueira, L. P., Yuan, X., Liu, W., Lei, Z., Jiang, J., Dai, H. and Xiao, J. (2021). '3D printed tricalcium phosphate-bioglass scaffold with gyroid structure enhance bone ingrowth in challenging bone defect treatment'. *Applied Materials Today*. Elsevier, 25, p. 101166.

Zhu, S., Chen, P., Chen, Y., Li, M., Chen, C. and Lu, H. (2020). '3D-Printed Extracellular Matrix/Polyethylene Glycol Diacrylate Hydrogel Incorporating the Anti-inflammatory Phytomolecule Honokiol for Regeneration of Osteochondral Defects'. *American Journal of Sports Medicine*. SAGE Publications Inc., 48 (11), pp. 2808–2818.